Generation of unconventional optical properties in triarylamine-based supramolecular polymers and molecular motors-based nanodevices

Chuan Gao

To cite this version:

Chuan Gao. Generation of unconventional optical properties in triarylamine-based supramolecular polymers and molecular motors-based nanodevices. Other. Université de Strasbourg, 2021. English. NNT : 2021STRAF033 . tel-04741195

HAL Id: tel-04741195
https://theses.hal.science/tel-04741195v1

Submitted on 17 Oct 2024

UNIVERSITÉ DE STRASBOURG

ÉCOLE DOCTORALE 222

UPR 22

THÈSE présentée par :

Chuan GAO

soutenue le : **22 Septembre 2021**

pour obtenir le grade de : **Docteur de l'université de Strasbourg**

Discipline/ Spécialité : Chimie moléculaire- chimie supramoléculaire

Generation of Unconventional Optical Properties in Triarylamine-based Supramolecular Polymers and Molecular Motors-based Nanodevices

THÈSE dirigée par :

M. GIUSEPPONE Nicolas	Professeur, Université de Strasbourg
Mme MOULIN Emilie	Directrice de Recherche, CNRS-Institut Charles Sadron

RAPPORTEURS :

M. HECHT Stefan	Professeur, RWTH Aachen University
M. SURIN Mathieu	Maître de Recherches, Université de Mons

RESUME

Introduction

Les matériaux aux propriétés optiques avancées sont d'un intérêt croissant en raison de leurs applications dans un large éventail de domaines allant des capteurs chimiques et biologiques[1,2] aux dispositifs optoélectroniques[3], voire même à la thérapie biologique[4]. De part leurs propriétés optiques et électroniques particulières, les dérivés de triarylamines (TAAs) sont couramment utilisés dans la fabrication de matériaux optiques comme les diodes électroluminescentes organiques[5] et les transistors à effet de champ organiques[6]. Cependant, la majeure partie des études portant sur les TAAs est limitée à l'état amorphe. En 2010, notre groupe de recherche a décrit pour la première fois que les TAAs mono-substituées par une fonction amide pouvaient s'auto-assembler en polymères supramoléculaires (Figure 1)[7]. Par la suite, les auto-assemblages à base de TAAs ont été étendus à diverses structures moléculaires[8]. De manière intéressante, ces structures supramoléculaires organisées peuvent donner lieu à des propriétés émergentes, telles que des propriétés de conductivité, de guides d'ondes plasmoniques ou encore d’interconnecteurs plasmoniques. A partir de nos recherches précédentes, le premier objectif de ma thèse a été d’élaborer des matériaux optiques à base de TAA présentant une phosphorescence organique pure à température ambiante et des propriétés plasmoniques organiques.

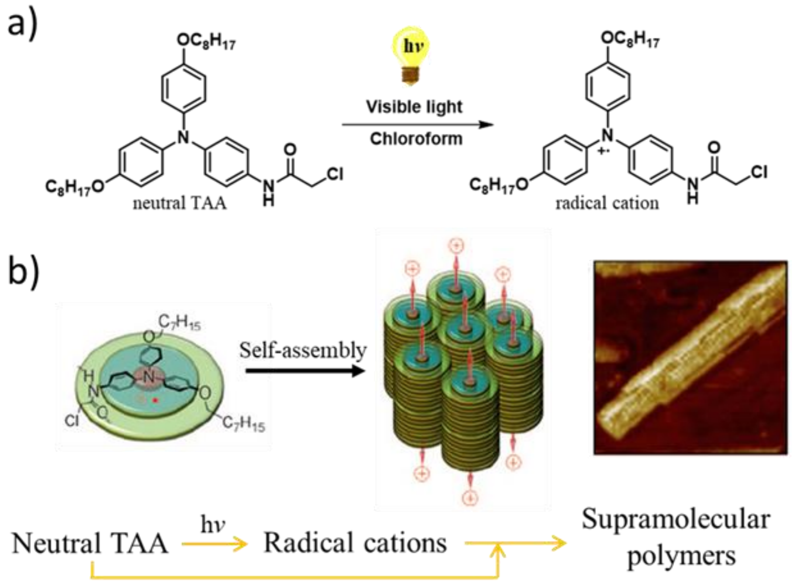

Figure 1. (a) Photo-oxydation de la TAA mono-amide dans le chloroforme sous irradiation à la lumière visible; (b) Représentation schématique de l'auto-assemblage induit par la lumière pour la TAA mono-amide dans le chloroforme. Cette figure est reproduite à partir de la réf.[7]

D'autre part, réguler à la demande le comportement d'absorption et d'émission des dispositifs optiques s’avère souhaitable pour les applications de tous les jours. Actuellement, le développement de dispositifs aux propriétés optiques modulables est principalement basé sur des systèmes sensibles aux stimuli, dans lesquels les propriétés optiques sont généralement modifiées par commutation entre deux états à l’équilibre thermodynamique.[9,10] À notre connaissance, la régulation du comportement optique mettant en jeu des systèmes hors équilibre est rare. En 2015, notre groupe a décrit un nouveau matériau contractile intégrant des moteurs moléculaires stimulables par la lumière comme unités de réticulation au sein de gels chimiques à base de poly(éthylène glycol) (PEG) (Figure 2).[11]

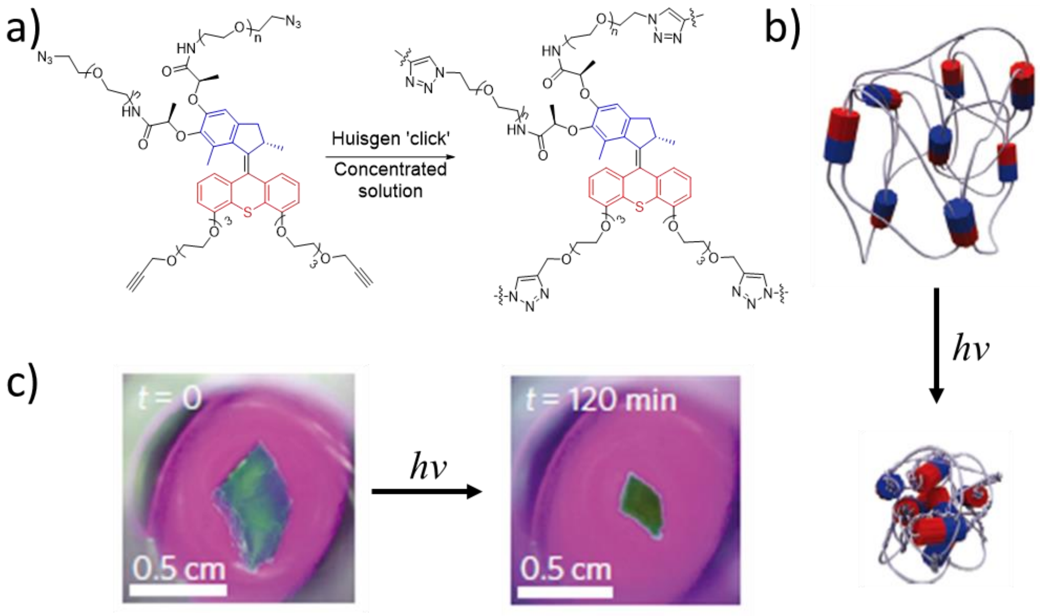

Figure 2. (a) Structure chimique des dérivés polymère-moteur et formation subséquente de réseaux polymères par réaction «click»; (b) Représentation schématique de la contraction induite par la lumière des gels chimiques moteurs/PEG; (c) Images tirées d'un film montrant la contraction macroscopique d'un morceau de gel en fonction du temps. Reproduit à partir de la réf.[11]

Sous irradiation UV à 365 nm, la rotation des moteurs moléculaires induit un enroulement continu des chaînes de polymère, entraînant une contraction macroscopique du gel via une voie hors équilibre. Curieusement, les intensités d'émission du gel avant et après irradiation apparaissent sensiblement différentes. Ainsi, le deuxième objectif de ma thèse vise à mieux comprendre ce phénomène et à l’exploiter davantage pour développer des matériaux aux propriétés optiques modulables.

Résultats et discussions

Projet I: Phosphorescence à température ambiante de polymères supramoléculaires à base de triarylamines

Les matériaux phosphorescents à température ambiante émergent en raison de la longue durée de vie de leur état triplet.[12] Une manière de favoriser la phosphorescence à température ambiante (RTP) consiste à rigidifier les unités phosphorescentes au sein d'une structure polymérique. A partir de nos connaissances sur les structures supramoléculaires auto-assemblées à base de TAA, nous avons conçu et synthétisé une molécule de triarylamine trisamide (**TATA-BrNp**) portant le groupement 4-bromo-1,8-naphtalimide (**BrNp**) comme unité phosphorescente sur l'une de ses chaînes latérales (Figure 3a). Cette molécule est capable de s'auto-assembler en polymères supramoléculaires avec le groupement **BrNp** confiné dans la structure, conduisant au phénomène de RTP.

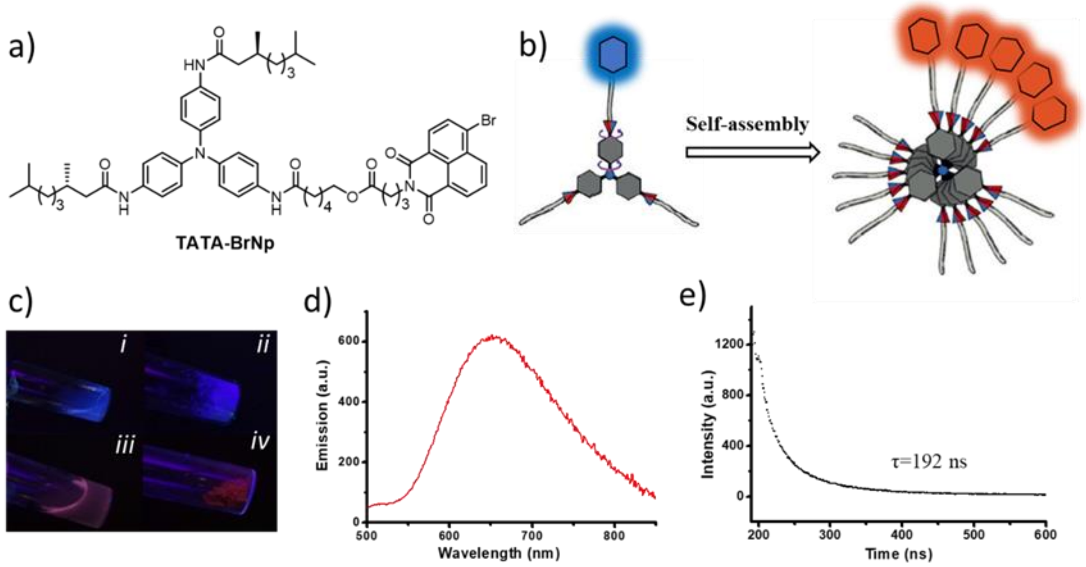

Figure 3. (a) Structure chimique du **TATA-BrNp**; (b) Représentation schématique du RTP induit par auto-assemblage de **TATA-BrNp**; (c) Images de i) **TATA-BrNp** dans THF, ii) **BrNp** à l'état solide, iii) **TATA-BrNp** en suspension dans le toluène, et iv) **TATA-BrNp** à l'état solide sous une lumière de 365 nm; (d) Spectre d'émission de la suspension **TATA-BrNp** dans le toluène à température ambiante; (c) Courbe de décroissance de la durée de vie des émissions de la suspension **TATA-BrNp** dans le toluène à 645 nm.

Comme envisagé, la suspension de **TATA-BrNp** dans le toluène et sa poudre présentent une émission de couleur rouge, tandis que la solution diluée de **TATA-BrNp** dans le THF émet une fluorescence bleue qui est identique à la poudre de **BrNp** pur (Figure 3c). Pour mieux comprendre l'émission de couleur rouge associée à la présence d'agrégats de **TATA-BrNp**, les études de spectroscopie d'émission montrent une large bande d'émission à 652 nm qui est cohérente avec le comportement phosphorescent de **BrNp** décrit dans la littérature (Figure 3d).[13] La durée de vie de cette émission à 645 nm est de 192 ns, ce qui est plus long que la fluorescence typique. En conclusion, ce travail démontre que les propriétés d'auto-assemblage des triarylamines permettent au groupement **BrNP** d'émettre en RTP.

Projet II: Nanoparticules plasmoniques à base de triarylamine trisacétamide (TATA-Ac)

Les nanoparticules métalliques nobles (c'est-à-dire d'or ou d'argent) peuvent donner lieu à une forte bande d'absorption lors de l'interaction avec la lumière incidente en raison de l'oscillation d'électrons libres.[14] Ce comportement optique est défini comme la résonance plasmonique de surface localisée (LSPR), un phénomène rarement observé dans les systèmes organiques purs. Sur la base du comportement métallique des auto-assemblages TATA, nous avons souhaité explorer le comportement plasmonique des nanoparticules à base de triarylamines trisacétamides (**TATA-Ac**).

Nous avons d'abord étudié les propriétés redox du TATA-Ac. Comme le montre la Figure 4b, lors de l'irradiation à la lumière visible d'une solution à 0,5 mM de **TATA-Ac** dans un mélange de MeOH/$CHCl_3$ (1/3), de nouvelles bandes d'absorption à 600-950 nm et 400-500 nm apparaissent et sont attribuées à la formation des radicaux cations et à l'empilement π-π des **TATA-Ac** oxydées. La formation de radicaux a été confirmée par spectroscopie par résonance paramagnétique électronique (RPE) qui montre la présence d'un signal à trois lignes, caractéristique des électrons non appariés localisés sur des atomes d'azote, et dont l'intensité augmente avec le temps d'irradiation (I_{max} après 20 min d'irradiation, Figure 4c).

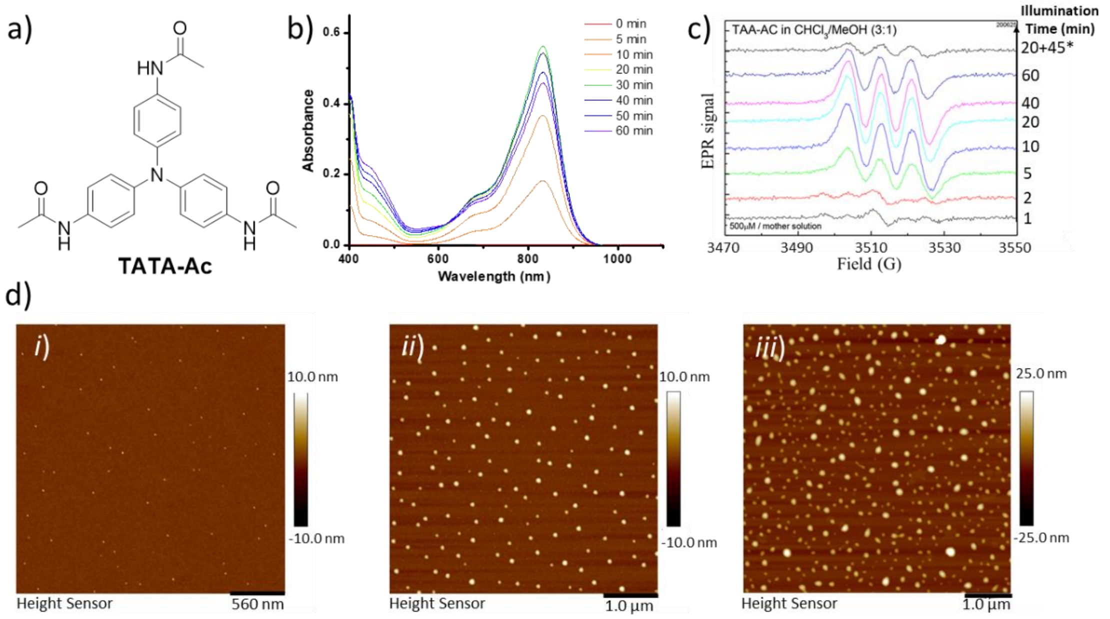

Figure 4. (a) Structure chimique de **TATA-Ac**; (b) Evolution de l'absorbance d'une solution de **TATA-Ac** dans un mélange de MeOH/CHCl3 (1/3) en fonction du temps d'irradiation à la lumière visible; (c) Evolution de du signal RPE d'une solution de **TATA-Ac** dans un mélange de MeOH/CHCl3 (1/3) en fonction du temps d'irradiation à la lumière visible ; (d) Images AFM de nanoparticules de **TATA-Ac** préparées à partir de diverses concentrations de solution mère. i) 5 µM, ii) 20 µM, et iii) 50 µM.

Des nanoparticules organiques de **TATA-Ac** sont obtenues à partir d'une solution mère de 0,5 mM de **TATA-Ac** dans un mélange de MeOH / CHCl3 (1/3), qui a été irradiée pendant 1 h sous lumière visible. La solution mère est ensuite ajoutée dans 10 ml d'acétate d'éthyle conduisant à une suspension de nanoparticules **TATA-Ac** par une approche de précipitation. De façon intéressante, la taille des nanoparticules peut être modifée en ajustant le volume utilisé de solution mère. Ainsi, comme le montre des études de microscopie à force atomique (AFM) (Figure 4d), la taille moyenne des nanoparticules (5 µM, 20 µM et 50 µM) préparées à partir de 0,1 mL, 0,4 mL et 1 mL de solution mère varie de 4,6 nm, à 9,1 nm voire 20 nm, respectivement.

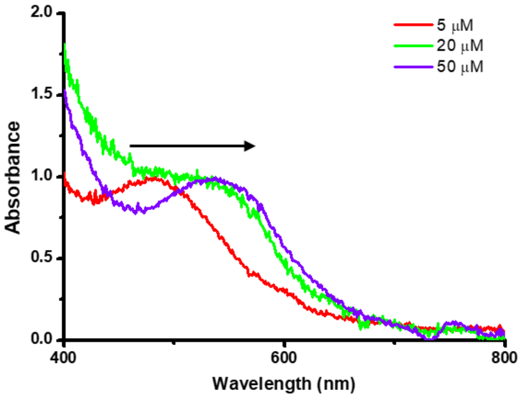

Figure 5. Spectres UV-Vis de nanoparticules **TATA-Ac** issues de différentes concentrations de solution mère.

L'étude du comportement optique des nanoparticules de **TATA-Ac** par spectroscopie UV-Vis montre la présence de bandes d'absorption à 480 nm, 528 nm et 543 nm en fonction de la taille des nanoparticules (Figure 5). Ces bandes n'apparaissent pas dans les auto-assemblages de TATA précédemment étudiées. De plus, le déplacement des bandes d'absorption des nanoparticules vers le rouge pour les plus grosses nanoparticules est cohérent avec le comportement de LSPR des nanoparticules de métaux nobles. Au cours de ce travail, nous avons pu obtenir des nanoparticules organiques de TATA avec différentes tailles puis nous avons commencé d'étudier leurs propriétés LSPR. D'autres caractérisations sont actuellement en cours pour mieux comprendre ce phénomène.

Chapitre III : Couplage plasmonique au sein d'un gel de polymère réticulé par des moteurs moléculaires

Dans le troisième projet, nous avons introduit différentes quantités de nanoparticules d'or (AuNPs) dans des gels de polymères incorporant des moteurs moléculaires *via* une réaction de cycloaddition de Huisgen intermoléculaire «CuAAc» (Figure 6a). L'objectif de ce projet visait à faire varier la bande LSPR des AuNPs en fonction de la contraction du gel sour l'influence du stimulus lumineux (Figure 6b).

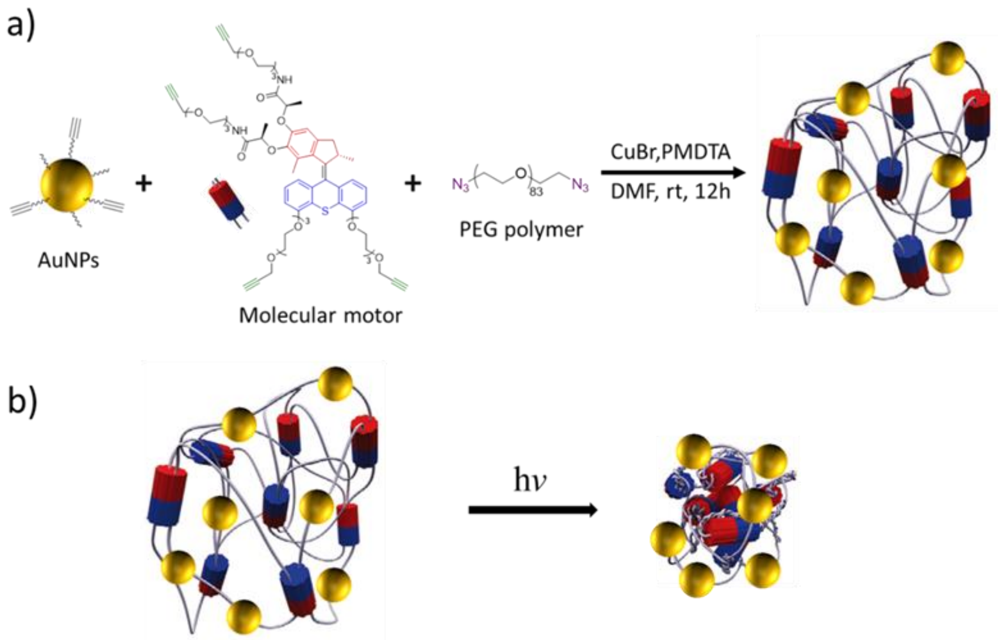

Figure 6. (a) Représentation schématique de la formation d'un gel contenant des moteurs moléculaires et des nanoparticules d'or via une réaction de cycloaddition de Huisgen intermoléculaire ; (b) Représentation schématique de la contraction macroscopique du gel représenté sur le panel (a) et induite par la lumière.

Lors de l'exposition à une irradiation par lumière UV, tous les gels montrent une contraction macroscopique du fait du tressage des chaînes de PEG lié au mouvement rotatif collectif des moteurs moléculaires. Les propriétés plasmoniques de ces gels ont ensuite été étudiées avant et après contraction par spectroscopie UV-Vis. Cependant, malgré plusieurs tentatives, nous n'avons observé aucun décalage de la bande plasmonique dans les gels contractés par rapport à ceux avant irradiation (Figure 7). Ceci pourrait s'expliquer par l'altération limitée de la distance interparticule, qui n'est pas suffisante pour donner lieu au couplage plasmonique des AuNPs.

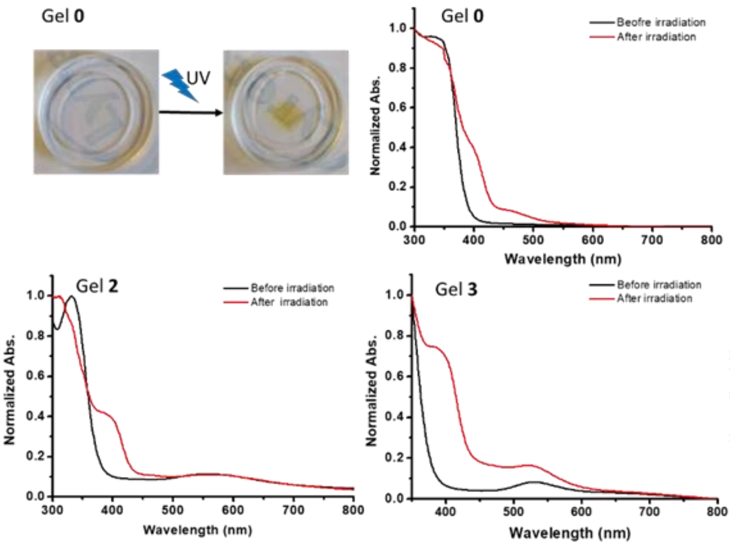

Figure 7. Spectres UV-Vis de gels représentés sur la Figure 6 avant et après irradiation sous lumière UV.

Projet IIII: Amélioration des propriétés d'émissions induites mécaniquement par des moteurs moléculaires en forme de 8

Comme mentionné en introduction, l'intensité d'émission d'un gel de PEG comportant des moteurs moléculaires comme nœuds de réticulation augmente considérablement après irradiation UV. Nous avons supposé que ce phénomène provenait de l'émission induite par l'agrégation (AIE) [15] du moteur moléculaire. Autrement dit, après contraction des gels, le mouvement des moteurs moléculaires est restreint en raison de l'enroulement des chaînes PEG, favorisant ainsi la désintégration radiative des excitons qui conduit à une forte fluorescence. Dans un premier temps, nous avons étudié le comportement AIE du moteur moléculaire **M1** (Figure 8). L'intensité d'émission de **M1** dans un solvant pauvre (90% d'eau) est beaucoup plus forte que dans le THF pur en raison du caractère luminophore AIE typique (AIEgen) de **M1**.

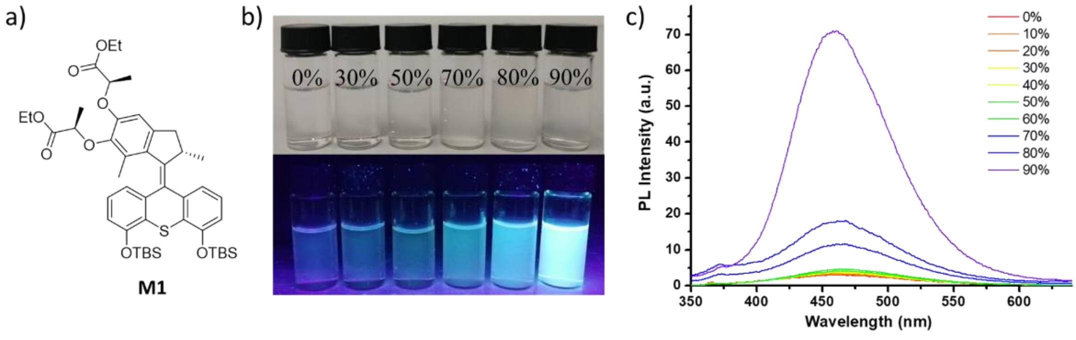

Figure 8. Comportement AIE du moteur moléculaire **M1**. a) Structure chimique de **M1**; (b) Images de **M1** dans différents mélanges THF / % H2O prises en lumière visible (en haut) et sous lumière

UV à 365 nm (en bas); (c) Spectres UV-Vis de **M1** pour différents mélanges THF / % H2O.

Souhaitant tirer parti du comportement AIE du moteur moléculaire, nous avons conçu et synthétisé des moteurs moléculaires en forme de 8 **E1**, **E2** et **E3**, dans lesquels les parties supérieure et inférieure du moteur étaient respectivement liées par des chaînes PEG10000, PEG3000 et PEG300 (Figure 9).

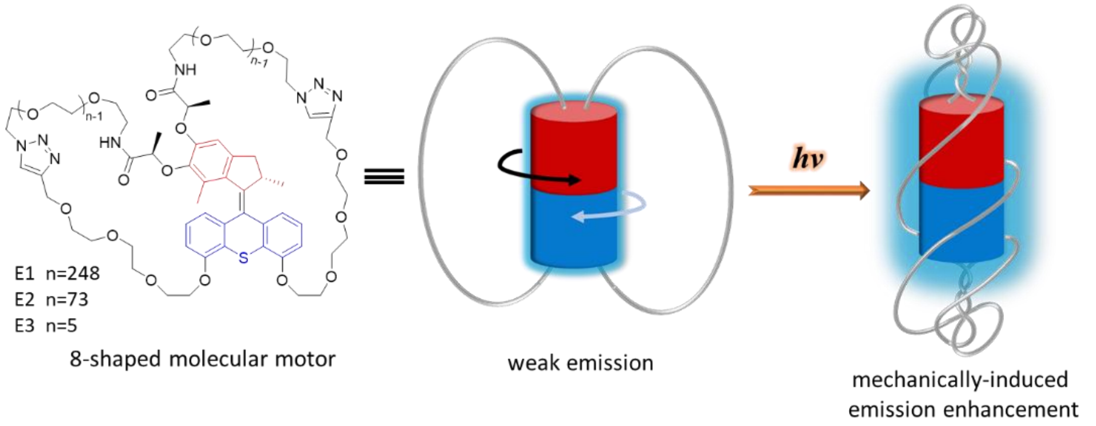

Figure 9. Structure chimique du moteur moléculaire en forme de 8 **E1**, **E2** et **E3**, et représentation schématique de l'amélioration des propriétés d'émission induite mécaniquement.

Après irradiation à 365 nm pendant 130 min, l'intensité d'émission de **E1** et **E2** augmente respectivement de 0,5 et 0,9 fois (Figures 10a-b) et peut s'expliquer par la torsion des chaînes PEG qui limite la désintégration non radiative des moteurs moléculaires. Pour **E3**, après 25 min d'irradiation, l'intensité d'émission augmente considérablement (5 fois, Figure 10c). Cette augmentation est liée à la taille des chaînes PEG beaucoup plus courte que pour **E1** et **E2**, et qui conduit à un état hautement «tendu».

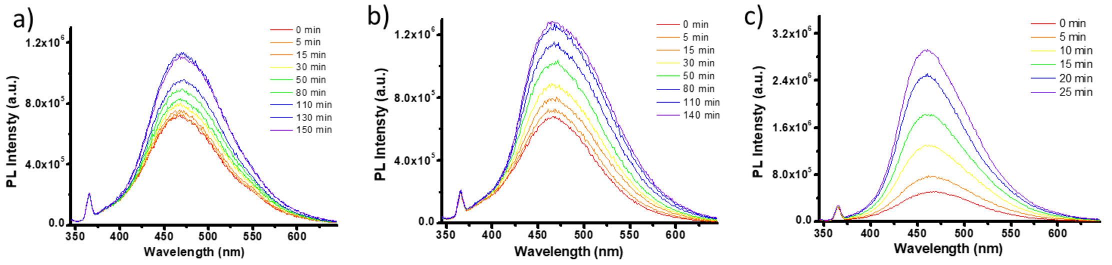

Figure 10. Spectres d'émission de (a) **E1** (0,03 mM), (b) **E2** (0,03 mM) et (c) **E3** (0,025 mM) en solution dans le THF pour différents temps d'irradiation UV à 365 nm.

Comme le montrent les figures 11a-b qui décrivent une modification du spectre UV-Vis et d'une diminution de l'intensité des émissions, l'état « tendu » de **E3** peut se détendre à un état relativement stable après 21 h dans l'obscurité en raison de la déformation conformationnelle. De manière intéressante, 6 minutes de ré-irradiation ultérieure conduisent à une récupération complète des spectres UV-Vis et avec la possibilité de répéter pendant au moins trois cycles ces changements de propriétés (Figure 11c).

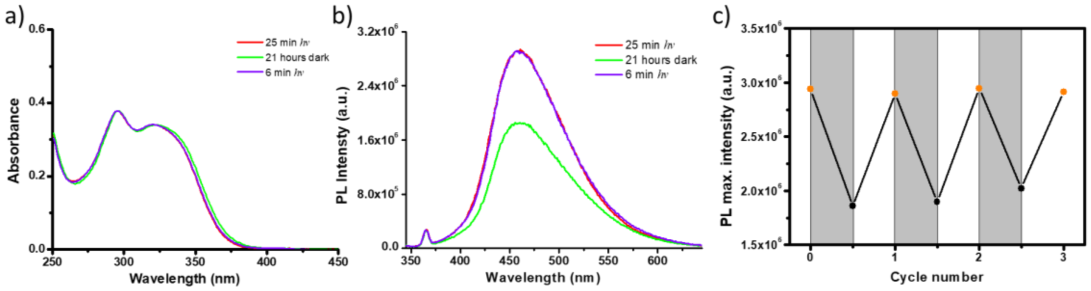

Figure 11. (a-b) Spectres (a) d'absorption UV-Vis et (b) d'émission de **E3** dans le THF (0,025 mM) après 25 min d'irradiation UV (rouge), après 21 h dans l'obscurité (vert), et après ré-irradiation pendant 6 min (violet); (d) Modifications de l'émission maximale au cours de trois cycles d'irradiation / obscurité.

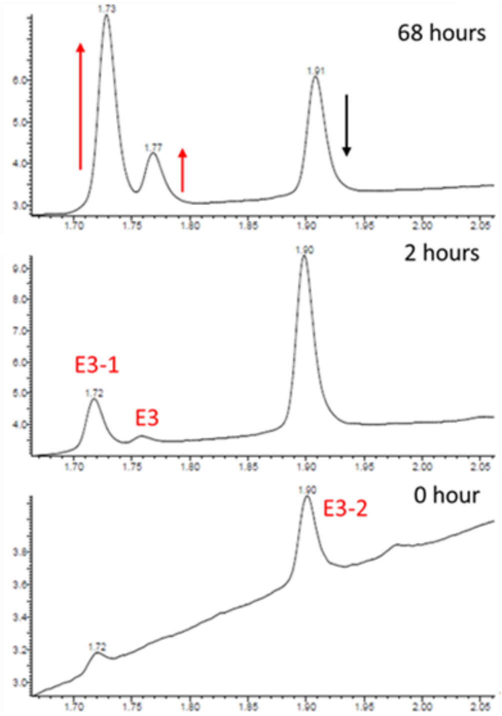

Figure 12. Evolution des chromatogrammes UV d'une solution d'**E3-2** dans l'obscurité à 40°C en fonction du temps.

À des températures plus élevées, **E3-2** peut relaxer en **E3**, comme cela a été mis en évidence par UPLC. Comme le montre la Figure 12, après 68 heures de chauffage à 40 ºC, nous avons observé une diminution de l'intensité d'**E3-2**, accompagnée d'une augmentation de l'intensité d'**E3-1** et l'apparition d'**E3**. Cela signifie que le processus de rotation de **E3** pourrait être complètement inversé via une voie thermiquement activée.

En conclusion, nous avons développé un nouveau système d'émission hors équilibre conçu à partir de moteurs moléculaires et dont l'émission augmente sous irradiation UV. De plus, en utilisant de courtes chaines de PEG, l'intensité d'émission a pu être régulée de manière reversible par irradiation lumineuse et relaxation thermique.

Conclusion générale

En résumé, au cours de ma thèse, j'ai pu mettre au point trois matériaux aux propriétés optiques originales à partir des connaissances du laboratoire sur les dérivés TAA et les moteurs moléculaires. Premièrement, nous avons mis en évidence les propriétés de RTP pour la molécule **TATA-BrNp** à l'état solide notamment en raison de la rigidification du luminophore **BrNp** par les structures auto-assemblées de **TATA-BrNp**. Ensuite, nous avons exploré les propriétés plasmoniques des nanoparticules à base de TATA-Ac, et principalement étudié le comportement de résonance plasmonique de surface localisé. De plus, nous avons exploré le possible couplage plasmonique de AuNPs au sein des gels incorporant des moteurs moléculaires comme unités stimulables, mais nous n'avons pas encore été en mesure d'observer, à l'heure actuelle, ce phénomène. Enfin, inspiré par les propriétés des émissions induites par la lumière d'un gel de moteurs moléculaires, et après avoir révélé le caractère AIE du moteur moléculaire, nous avons mis au point un système d'émission hors équilibre basé sur un moteur moléculaire en forme de 8, dans lequel l'intensité d'émission peut être modulée en contrôlant le temps d'irradiation.

Références

1. Mako, T. L.; Racicot, J. M.; Levine, M. *Chem. Rev.* **2019**, *119* (1), 322–477.
2. Wolffbeis, O. S. *Anal. Chem.* **2006**, *78* (12), 3859–3874.
3. Yu, T.; Liu, L.; Xie, Z.; Ma, Y. *Sci. China Chem.* **2015**, *58* (6), 907–915.
4. Xing, J.; Gong, Q.; Akakuru, O. U.; Liu, C.; Zou, R.; Wu, A. *Nanoscale* **2020**, *12* (48), 24311–24330.
5. Xia, C.; Wang, X.; Lin, J.; Jiang, W.; Ni, Y.; Huang, W. *Synth. Met.* **2009**, *159* (3), 194-200.
6. Sonntag, M.; Kreger, K.; Hanft, D.; Strohriegl, P.; Setayesh, S.; De Leeuw, D. *Chem. Mater.* **2005**, *17* (11), 3031–3039.

7. Moulin, E.; Niess, F.; Maaloum, M.; Buhler, E.; Nyrkova, I.; Giuseppone, N. *Angew. Chem. Int. Ed.* **2010**, *49* (39), 6974–6978.
8. Moulin, E.; Armao, J. J.; Giuseppone, N. *Acc. Chem. Res*. **2019**, *52* (4), 975–983.
9. Liang, E.; Su, F.; Liang, Y.; Wang, G.; Xu, W.; Li, S.; Yang, C.; Tang, J.; Zhou, N. *Chem. Commun*. **2020**, *56* (96), 15169–15172.
10. Wang, Q.; Zhang, Q.; Zhang, Q.-W.; Li, X.; Zhao, C.-X.; Xu, T.-Y.; Qu, D.-H.; Tian, H. *Nat. Commun*. **2020**, *11* (1), 158.
11. Li, Q.; Fuks, G.; Moulin, E.; Maaloum, M.; Rawiso, M.; Kulic, I.; Foy, J. T.; Giuseppone, N. *Nature Nanotech.* **2015**, *10* (2), 161–165.
12. Zhao, W.; He, Z.; Tang, B. Z. *Nat. Rev. Mater.* **2020**, *5* (12), 869–885.
13. Li, D.; Lu, F.; Wang, J.; Hu, W.; Cao, X.-M.; Ma, X.; Tian, H. *J. Am. Chem. Soc.* **2018**, *140* (5), 1916–1923.
14. Willets, K. A.; Van Duyne, R. *Annu. Rev. Phys. Chem.* **2007**, *58*, 267–97.
15. Luo, J.; Xie, Z.; Lam, J. W. Y.; Cheng, L.; Tang, B. Z.; Chen, H.; Qiu, C.; Kwok, H. S.; Zhan, X.; Liu, Y.; Zhu, D. *Chem. Commun.* **2001**, *18*, 1740–1741.

Table of Contents

ACKNOWLEDGMENTS

First of all, I would like to express my profound gratitude to my supervisor, Prof. Nicolas Giuseppone, for giving me the opportunity to join SAMS research group and work in an international environment. I really thank him for the great instructions and support during these four years. What is more, his optimistic spirit encourages me to persevere in research projects.

I would like to thank my co-supervisor, Dr. Emilie Moulin, for her tremendous help for completion of this dissertation. I am grateful for her important suggestions and encouragement in academic and daily life.

I great thank Dr. Andreas Jentzsch Vargas, he taught me so many things in chemistry. I cannot imagine how I could successfully accomplish the project without his support in practical and theoretical aspects.

To Odile Gavat and Marie-Céline Samy-Arlaye, I am grateful for their logistic work for the group, which supported me to conduct experiments orderly.

Of course, I wish to express my gratefulness for other people who give me favor on this work. Thanks for Prof. Mounir Maaloum, for his beautiful AFM images. Thanks to Dr. Gilles Ulrich, for his kind help with optical spectroscopy measurements. Thanks to Dr. Bertrand Vileno, for his help with EPR experiments. Dr. Raul Arenal, for his effort on EELS. Dr. Patrick Kekicheff, for his work with GIWAXS. Guillaume Fleith, for the X-ray scattering experiments. Dr. Jean-Marc Strub, for his help with high-resolution mass and MALDI. Dr. Emeric Wasielewski, for his help with NMR.

I would also like to thank all the other former and current members in SAMS group: Yali, Wenzhi, Damien, Alexis, Melodie, Flavio, Raphaël, Nicolas, Pierre, Erol, Frédéric, Shoichi, Maria, Christian, Alessandro, Dania, Sergio, Joakim, Philippe, Thiebault, Gad, Cris, Lara, Chloé, Jean-Rémy, Ting, Xuyang, and Xiaoqin. Some of you gave me valuable advices for learning in chemistry and language. All the members I met here are nice and they are always willing to help me. I really enjoyed the spare time we talked together about science, food, and life.

The same thanks to all the other members in ICS who helped me a lot during past four years.

A special thanks to the Chinese coffee break team in ICS (Xuyang, Xiaoqin, Wenzhi, Yali, Wenbing, Yazhao, and Da), we visited many places and cooked so much lovely food together. I always could gain inspirations and encouragement from them when I was disappointing.

Finally, I greatly thank to my family. It is my parents' unconditional support and understanding that encouraged me to study abroad. It is their selfless care that gives me comfort when I miss my hometown. I would like to express my special thanks to my two sisters. Their care for my parents has relieved me of worries and enabled me to pursue my dream at ease.

古话说“父母在，不远游，游必有方”，正是我父母无条件的支持与理解鼓励我做出了海外求学的决定。也正是他们无私的关心让我在想念家乡时多了一丝慰藉。特别感谢我的两个姐姐，她们对爸妈的照顾是我打消了心底的顾虑，让我可以安心求学。

Direction de la **recherche**
et de la **valorisation**
Collège **doctoral**
Université de Strasbourg

Déclaration sur l'honneur
Declaration of Honour

J'affirme être informé que le plagiat est une faute grave susceptible de mener à des sanctions administratives et disciplinaires pouvant aller jusqu'au renvoi de l'Université de Strasbourg et passible de poursuites devant les tribunaux de la République Française.

Je suis conscient(e) que l'absence de citation claire et transparente d'une source empruntée à un tiers (texte, idée, raisonnement ou autre création) est constitutive de plagiat.

Au vu de ce qui précède, **j'atteste sur l'honneur que le travail décrit dans mon manuscrit de thèse est un travail original et que je n'ai pas eu recours au plagiat ou à toute autre forme de fraude.**

I affirm that I am aware that plagiarism is a serious misconduct that may lead to administrative and disciplinary sanctions up to dismissal from the University of Strasbourg and liable to prosecution in the courts of the French Republic.

I am aware that the absence of a clear and transparent citation of a source borrowed from a third party (text, idea, reasoning or other creation) is constitutive of plagiarism.

In view of the foregoing, ***I hereby certify that the work described in my thesis manuscript is original work and that I have not resorted to plagiarism or any other form of fraud.***

Nom : GAO   Prénom : Chuan

Ecole doctorale : ED222

Laboratoire : SAMS research group, ICS

Date : 20/12/2021

Signature :

ABSTRACT

Advanced optical materials are of intense interest due to their applications in a wide range of fields, from chemical and biological sensors to optoelectronic devices, even for biological therapy. Thanks to the excellent optical and electronic properties, triarylamine derivatives are extensively exploited in optical materials, such as organic light-emitting diodes and organic field-effect transistors. On the other hand, the unidirectional rotary motion of molecular motors able to achieve mechanical coiling of polymer chains is promising in tunable optical materials. The objective of this work is to make use of triarylamine-based self-assemblies and molecular motors to design and construct unconventional optical materials and nanodevices.

In the first chapter, we aim to develop triarylamine-based supramolecular polymers with room temperature phosphorescence. First, the advance of triarylamine-based supramolecular polymers is introduced. We then demonstrate that triarylamine trisamide bearing a phosphorescent unit is able to form self-assemblies via intermolecular supramolecular interactions in various solvents. As a result of restriction of intramolecular motion of phosphorescent unit, the supramolecular polymers in solid state could emit red phosphorescence.

In the second chapter, triarylamine-based supramolecular nanoparticles with different sizes are prepared via precipitation. After photo-oxidation, these nanoparticles display unusual UV absorption bands, which are absent in neutral nanoparticles. This unique optical behaviour is ascribed to localized surface plasmon resonance. Further investigations will be addressed to get a deeper insight into organic plasmonic nanoparticles.

In the third chapter, we explored the plasmonic coupling in contractile gels made by crosslinking gold nanoparticles, molecular motors, and polymers chains. Light-induced macroscopic contraction of these gels were observed owing to mechanical braiding of polymer networks. While, in present conditions, the regulation of plasmonic coupling is still challenging. The improvement of contraction will be the direction toward our goal.

In the last chapter, taking inspiration from aggregation-induced emission, we developed an emission-tunable system based on 8-shaped molecular motor. Upon UV light irradiation, the emission intensities were enhanced associated with the mechanical coiling of polymer chains.

The influence of solvents and polymer length on emission enhancement was revealed. We then demonstrated that the ‘tensed’ motors can reverse the rotary motion via thermal relaxation process to release elastic energy stored in wound chains, accompanied by decreased fluorescence.

Overall, the work presented in this thesis demonstrates the construction of optical materials by following our previous research on triarylamine and molecular motors. These results provide new insights for the design of novel optical systems.

ABBREVIATIONS AND SYMBOLS

°C	Celsius degree
Å	angstrom
ACQ	aggregation caused quenching
AFM	atomic force miscoscopy
AgNPs	silver nanoparticles
AIE	aggregation induced emission
AIEgens	AIE luminogens
AuNPs	gold nanoparticles
ATP	adenosine triphosphate
BODIPY	4,4-difluoro-4-bora-3a,4a-diaza-s-indacene
CD	circular dichroism
CPL	circularly polarized luminescence
CT	charge transfer
CV	cyclic voltammetry
CuAAC	azide-alkyne Huisgen cycloaddition
d	day
DC	direct current
DCM	dichloromethane
DEA	dissociative electron attachment
DFT	density functional theory
DLS	dynamic light scattering
DMF	dimethylformamide
DMSO	dimethylsulfoxide
EDC	1-ethyl-3-(3-dimethylaminopropyl)carbodiimide
EPR	electron paramagnetic resonance
ESI	electron spray ionization
EELS	electron energy loss spectroscopy
etc.	et cetera
FFTEM	freeze fracture transmission electron microscopy
G	Gibbs free energy
GIWAXS	grazing-incidence wide-angle X-ray scattering
h	hour

HCl	hydrochloric acid
HOBt	hydroxybenzotriazole
HPLC	high-performance liquid chromatograpy
HRMS	high-resolution mass spectroscopy
hv	irradiation with light
IC	internal conversion
ISC	internal system crossing
IR	infrared
IV-CT	inter valence charge transfer
K	kelvin
LSPR	localized surface plasmon resonance
M	molar
MCH	methylcyclohexane
MeCN	acetonitrile
MeOH	methanol
MHz	megahertz
min	minute
mM	millimolar
mm	millimeter
mL	milliliter
MIEE	mechanically-induced emission ehancement
MS	mass spectroscopy
MV	mixed valence
MV-CT	mixed-valence charge transfer
NIR	near infrared
nm	nanometers
NMR	nuclear magnetic resonance
OFET	organic field-effect transistor
OLED	organic light emitting device
PEDOT:PSS	poly(3,4-ethylenedioxythiophene) polystyrene sulfonate
PMDETA	N,N,N′,N″,N″-pentamethyldiethylenetriamine
PEG	poly(ethylene) glycol
PEI	polyethyleneimine
PPh_3	triphenylphosphine

PPT	pre-planarized triarylamine
PSS	photostationary state
ref.	reference
r.t.	room temperature
RTP	room temperature phosphorescence
RIM	restriction of intramolecular motion
RIR	restriction of intramolecular rotation
RIV	restriction of intramolecular vibration
s	second
SAXS	small-angle X-ray scattering
SEM	scanning electron microscopy
S_NAr	aromatic nucleophilic substitution
STEM	scanning transmission electron microscope
TAA	triarylamine
TATA	triarylamine trisamides
TATA-Ac	triarylamine trisacetamide
TBAF	tetra-n-butylammonium fluoride
TBAH	tetrabutylammonium hydroxide
TEA	triethylamine
TEM	transmission electron microscopy
TFA	trifluoroacetic acid
THI	thermal helix inversion
THF	tetrahydrofuran
TLC	thin layer chromatography
TPE	1,1,2,2-tetraphenylethylene
UV	ultraviolet
Vis	visible
UPLC	ultra-performance liquid chromatography
WAXS	wide-angle X-ray scattering
XRD	X-ray diffraction
µM	micromolar
µm	micrometer
µL	microliter
δ	chemical shift
λ	wavelength

Chapter I. Room Temperature Phosphorescence of Triarylamine-based Supramolecular Polymers

1.1 Bibliography

1.1.1 Structure and properties of triarylamines

Over the past 60 years, triarylamine (TAA) derivatives have been investigated in a wide range of fields. For instance, thanks to their fascinating electronic and optical properties, they are extensively exploited in the fabrication of optoelectronic devices, involving organic light emitting diodes (OLEDs)[1], organic field effect transistors (OFETs)[2], organic and perovskite solar cells[3]. For a long time, research on TAA was limited to the amorphous state. In 2010, our group demonstrated that, upon exposure to visible light, TAA derivatives are able to self-assemble into supramolecular polymers by employing Van der Waals, intermolecular hydrogen-bonding and π-π stacking interactions.[4] Since that time, research on TAA-based self-assemblies became a topic full of interest. In addition, TAA-based supramolecular polymers with ordered nanostructures display emergent properties such as high conductivity, unique optical and plasmonic properties.[5]

In this section, structural information and several synthetic approaches towards TAA will be introduced briefly. Then we will discuss the electrochemical properties of TAA involving redox, charge transfer, and conductivity, which is fundamental for optoelectronic materials. With the basic knowledge, we will then illustrate that how TAA monomers form ordered supramolecular polymers via non-covalent bonds.

1.1.1.1 Synthesis and structure of triarylamines

The first synthetic protocol on triarylamine (TAA) was proposed in 1873 by Merz and Weith. As shown in Scheme 1.1a, mixing diphenylamine or aniline with bromobenzene in the presence of potassium at 300 °C yields triphenylamine.[6] In 1907, Goldberg and Nimerovsky succeeded to synthesize the same molecule via a three-step approach,[7] which affords TAA under relatively mild condition. As detailed in Scheme 1.1b, starting from anthranilic acid and bromobenzene, the TAA precursor is obtained via two consecutive copper-catalyzed Ullmann coupling reaction, and then undergoes decarboxylation providing target triphenylamine in 8% yield.

To diversify the family of TAA core, tremendous efforts have been given to explore new and efficient synthetic strategies. Nowadays, the synthesis of TAA rely on three main protocols. The first is copper-catalyzed Ullmann coupling developed by Goldberg and Nimerovsky, which is the oldest but still an efficient method to prepare TAA under relatively mild conditions.[7,8] Alternatively, palladium-catalyzed Buchwald-Hartwig coupling reaction is also extensively used in laboratory to synthesize TAA derivatives.[9] Another possibility is the aromatic nucleophilic substitution (S_NAr) reaction, which access the preparation of TAA derivatives with various substituted side chains.[10]

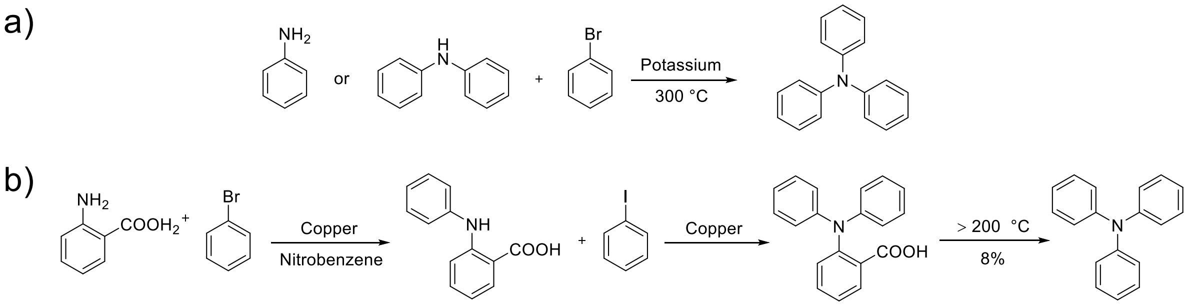

Scheme 1.1 (a) First synthetic protocol of TAA proposed by Merz and Weith; (b) three-step approach towards the synthesis of TAA derived by Goldberg and Nimerovsky. Adapted from ref.[6,7].

As detailed in Figure 1.1a, the TAA core consists of three phenyl rings with a central nitrogen atom. Moreover, from the chemical structure one can see that, similarly to its analogues (e.g. trimethylamine), the TAA core adopts a C_3-symmetric conformation. Crystallographic data of this core suggests a C-N-C angle of around 119.6°, indicating a planar conformation resulting from a sp^2 hybridization (Figure 1.1b).[11] In sharp contrast, the analogue trimethylamine has a tetrahedral C_3-symmetry corresponding to a sp^3 hybridization. To relieve steric hindrance, three phenyl rings are forced to rotate out of the plane of the TAA core adopting a propeller-like shape. According to DFT calculations, dihedral angles between phenyl rings and the plane of the molecule are comprised between 41 and 44° depending on the nature of the substituents at phenyl rings.[1] As a result, TAA core exists either as Δ or as Λ conformations (Figure 1.1c).[12] With energy input, these two enantiomers can transform to each other.

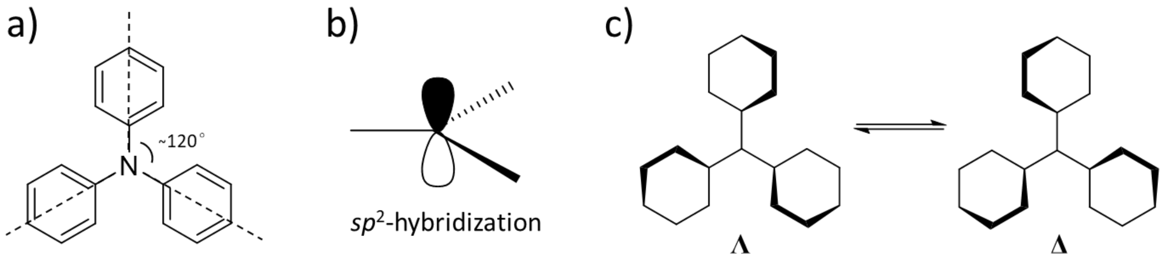

Figure 1.1 (a) Chemical structure of TAA; (b) sp^2 hybridization; (c) Schematic representation of transformation from one enantiomer to the other. The figure is adapted from ref.[12].

1.1.1.2 Electrochemical properties of triarylamines

Redox

Studies on the redox property of simple *para*-substituted TAA derivatives were pioneered by the group of Lambert.[13] Series of molecules bearing electron donating (-OMe) or withdrawing (-Cl) groups were synthesized, and their redox potential was measured by cyclic voltammetry. All tris-*para*-substituted compounds **1-10** exhibit an electrochemical first oxidation potential wave corresponding to the formation of radical cations (Figure 1.2). Interestingly, the nature of the substituents strongly modifies measured redox potentials. For example, the introduction of chlorine atoms increases the oxidation potential, whereas methoxy substituent results in smaller values.

	R_1	R_2	R_3	$E_{1/2}$
1	OMe	OMe	OMe	109
2	Me	Me	Me	332
3	Me	OMe	OMe	180
4	Me	Cl	Cl	576
5	OMe	Me	Me	250
6	OMe	Cl	Cl	463
7	Cl	Me	Me	460
8	Cl	OMe	OMe	290
9	Cl	Cl	Cl	691
10	Cl	OMe	Me	359

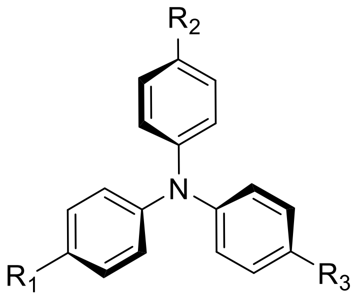

Figure 1.2 First oxidation potentials (mV) of TAA derivatives **1-10** vs. ferrocene (Fc/Fc^+) in CH_2Cl_2 (TBAH). This Figure is adapted from ref.[13].

Audevert and coworkers further investigated the substituent effect on redox potentials of TAA derivatives by introducing diverse functional groups and reached similar conclusion.[14] Electron donating groups (methoxy, methyl, and methoxyphenyl) lower oxidation potential, while electron withdrawing groups (aldehyde, nitrile, or halide) shift the potentials to higher values.

Oxidation of triarylamines in chlorinated solvents

The oxidation of TAA derivatives described above is triggered via an electro-oxidation strategy. Alternatively photo- or chemical oxidation processes can also be used. Compared to chemical oxidants, light is a clean and non-invasive source and proved to be more favoured in practical applications. The first report on photo-oxidation of dates back to 1971, when Richtol and coworkers demonstrated that substituted aromatic amines could form coloured products in chloroform upon UV light irradiation, suggesting oxidation of aromatic amines.[15] Unexpectedly, further studies indicate that the energy of UV light required for photo-oxidation process (3.5 eV) is much less than the ionization potentials of these amines (6.0 - 7.0 eV), suggesting that the additional energy is provided by the heat released by a dissociative electron attachment (DEA) reaction in chloroform (as shown below, the energy is 16 kcal/mol) and the solvation energy of ionic products.

$$\mathrm{CHCl_3} + e^- \longrightarrow \mathrm{CHCl_2^{\bullet}} + \mathrm{Cl^-} \qquad (1)$$

Based on this hypothesis, the entire photo-oxidation process of aromatic amines in halogenated solvents was suggested as such:

$$\mathrm{A} \xrightarrow{h\nu} {}^{1}\mathrm{A}^{*} \tag{2}$$

$$ {}^{1}\mathrm{A}^{*} \longrightarrow \mathrm{A} + h\nu_{f} \tag{3}$$

$$ {}^{1}\mathrm{A}^{*} \longrightarrow {}^{3}\mathrm{A}^{*} \longrightarrow \mathrm{A} \tag{4}$$

$$ {}^{1}\mathrm{A}^{*} + \mathrm{CHCl_3} \longrightarrow \mathrm{A}^{\bullet+} + \mathrm{Cl}^{-} + \mathrm{CHCl}_2^{\bullet} \tag{5}$$

$$ \mathrm{CHCl}_2^{\bullet} + \mathrm{O_2} \longrightarrow \mathrm{CHCl_2O}_2^{\bullet} \tag{6}$$

$$ \mathrm{CHCl_2O}_2^{\bullet} \longrightarrow \mathrm{CHClO} + \mathrm{ClO}^{\bullet} \tag{7}$$

$$ \mathrm{CHClO} \longrightarrow \mathrm{HCl} + \mathrm{CO} \tag{8}$$

$$ \mathrm{ClO}^{\bullet} + \mathrm{CHCl_3} \longrightarrow \mathrm{COCl_2} + \mathrm{HCl} + \mathrm{Cl}^{\bullet} \tag{9}$$

$$ \mathrm{Cl}^{\bullet} + \mathrm{A} \longrightarrow \mathrm{A}^{\bullet+} + \mathrm{Cl}^{-} \tag{10}$$

in which A = substituted aromatic amines, ${}^{1}A^{*}$ = excited singlet state of amines, $A^{\bullet+}$ = radical cation of amines, ${}^{3}A^{*}$ = excited triplet state of amines.

First, excitation of amines induced by UV light takes place, resulting in the formation of excited singlet and triplet states (steps 2-4). Thanks to dissociative electron attachment reaction in chloroform, the excited amines are subsequently oxidized to the radical cations (step 5). Interestingly, the presence of oxygen in chloroform increased the oxidation quantum yield by 2 as opposed to the degassed ones and led to the formation of equivalent amount of HCl after photo-oxidation. Taking account of these observations, a decomposition process of dichloromethyl radicals into chlorine radicals was proposed, which could further oxidize aromatic amines (steps 6-10).

Charge transfer in triarylamines

Charge transfer (CT) can take place both in mixed-valence (MV) and donor-acceptor (D-A) systems. Typically, organic MV systems consist of two chemically identical redox centers but differently charged. As a result, the saturated or unsaturated molecular bridge between two redox centers as electronic coupling medium assists the charge transfer process from one center (donor) to the other (acceptor), associated with the emergence of a characteristic spectral absorption band (intervalence charge-transfer (IV-CT) band). This process is defined as mixed-valence charge transfer (MV-CT).[16] In contrast, redox centers in D-A systems are chemically different. Moreover, charges are allowed to be transferred from an electron-donating group (donor) to an electron-withdrawing group (acceptor).

The Marcus-Hush theory is commonly applied to study MV-CT systems, in which reorganization energy and electronic coupling *V* are used to evaluate charge transfer processes.[16,17,18] According to the strength of the electronic communication between the two redox moieties (electronic coupling *V*), MV-CT systems are divided into three classes.[19] In class I, redox centers are regarded as totally isolated, indicating the absence of electronic communication. It equally means CT process cannot take place. Class II consists of redox centers which are coupled weakly, leading to a partial delocalization of charges between redox centers. In sharp contrast, in class III, redox centers are strongly coupled, resulting in full delocalization of charges. Classes can be determined according to information given by UV-Vis-NIR spectroscopy. As described in the literature, symmetric spectral band refers to class II, while class III typically shows an asymmetric absorption band.[16]

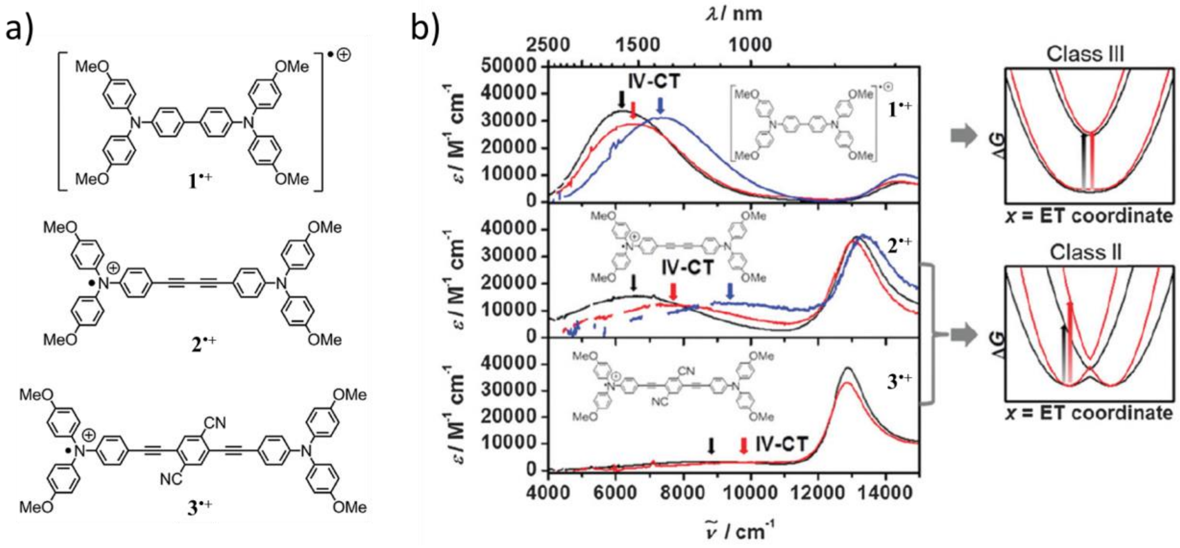

Figure 1.3 (a) Chemical structure of monoradical cations $\mathbf{1}^{\bullet+}$, $\mathbf{2}^{\bullet+}$ and $\mathbf{3}^{\bullet+}$; (b) Vis-NIR absorption spectra of $\mathbf{1}^{\bullet+}$, $\mathbf{2}^{\bullet+}$ and $\mathbf{3}^{\bullet+}$ in CH_2Cl_2 (black), $PhNO_2$ (red) and MeCN (blue). Diagrams on the right hand side corresponds to free energy surface for low (black) and high (red) reorganization energy in class III and II, respectively. This figure is adapted from ref.[20].

For a long time, MV-CT systems were investigated on inorganic and asymmetric systems. Since TAA derivatives exhibit superior redox property and relatively high stability, the research group of Lambert first explored symmetric organic MV-CT systems consisting of TAA moieties. Three TAA dimers **1**, **2**, and **3** were synthesized, in which two identical methoxy substituted TAA centers are linked through different saturated bridges.[20] After undergoing a chemical oxidation process, one TAA moiety in these molecules is oxidized to the monoradical cations $\mathbf{1}^{\bullet+}$, $\mathbf{2}^{\bullet+}$, and $\mathbf{3}^{\bullet+}$ (Figure 1.3a), leading to appearance of IV-CT band in their UV-Vis spectrum.

The spectral profile of the IV-CT band in **1**$^{\bullet+}$ is narrow and asymmetric (Figure 1.3b), suggesting that charges are fully delocalized over TAA moieties through the short bridge. Moreover, its IV-CT band only slightly shifts in different solvents, which is consistent with the signature of class III systems[16]. In contrast, **2**$^{\bullet+}$ and **3**$^{\bullet+}$ with longer bridges display broad and symmetric IV-CT band with significant shifts depending on the solvent, suggesting a class II MV-CT system. (Figure 1.3b).

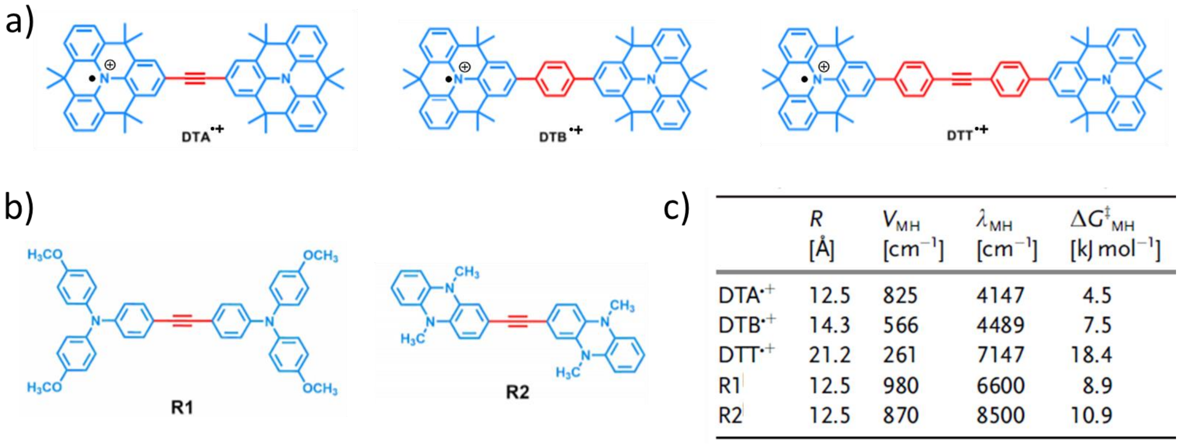

	R [Å]	V_{MH} [cm^{-1}]	λ_{MH} [cm^{-1}]	$\Delta G^{\ddagger}_{MH}$ [kJ mol^{-1}]
DTA$^{\bullet+}$	12.5	825	4147	4.5
DTB$^{\bullet+}$	14.3	566	4489	7.5
DTT$^{\bullet+}$	21.2	261	7147	18.4
R1	12.5	980	6600	8.9
R2	12.5	870	8500	10.9

Figure 1.4 (a) Chemical structures of radical cations **DTA**$^{\bullet+}$, **DTB**$^{\bullet+}$ and **DTT**$^{\bullet+}$, respectively; (b) Chemical structures of analogues R_1 and R_2; (c) Parameters in CT process obtained through NIR absorption spectra and theoretical calculations. V_{MH} represents electronic coupling, λ_{MH} is the reorganization energy in CH_2Cl_2. This figure is reproduced form ref.[21].

Upon oxidation, the conformation of propeller shaped TAAs undergoes a planarization process to stabilize charges. Precisely, C-N bonds become shorter and torsion angles of phenyl rings become smaller than those of neutral TAA[1]. Very recently, Guldi and coworkers demonstrated the planarization process on MV-CT systems.[21] **DTA**, **DTB** and **DTT** were successfully obtained by bridging two “pre-planarized” TAA moieties (**PPT**) via acetylene, *p*-phenylene and tolane, respectively. X-ray crystallographic data suggested that the sum of C-N-C angles are approximately 360°C, suggesting a planarized conformation of **PPT**. Based on information provided by UV-Vis-NIR and EPR experiments on **DTA**$^{\bullet+}$, **DTB**$^{\bullet+}$ and **DTT**$^{\bullet+}$, one can see that these oxidized molecules are class II MV-CT system. Furthermore, the relevant values of reorganization energy and electronic coupling were calculated according to UV-Vis-NIR spectra. As suggested by Figure 1.4c, a longer molecular bridge results in weaker electronic coupling but larger reorganization energy, which is in agreement with the observations by Lambert’s group.[20] Importantly, compared to non-planarized analogues **R1**$^{\bullet+}$ and **R2**$^{\bullet+}$, **DTA**$^{\bullet+}$ displays similar electronic coupling values but much smaller reorganization energy, which is ascribed to the pre-planarization effect.

Conductivities

As described in the redox section, TAA derivatives are prone to be oxidized to generate radical cations at low ionization potentials. Under an external electric field, the formed radicals behave as charge carriers (holes) from one molecule to the neighbored ones in a hopping transport mechanism, giving rise to conductivity. Different from the band transport mechanism in metals, in which free electrons are delocalized over periodic energy bands and transported to conduction band from the valence band, a hole transport process is generally regarded as a sequential redox reaction over TAA molecules (Figure 1.5).[22]

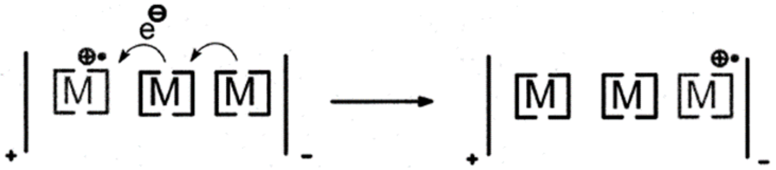

Figure 1.5 Schematic representation of charge transport in a hopping process under an external electric field. This Figure is adapted from ref.[22].

One of the earliest studies on conductivity of TAA derivatives was carried out in 1989 by the group of Shirota.[23] Two starburst molecules **TDATA** and **MTDATA** (Figure 1.6a) were synthesized and a transparent amorphous film was made of **MTDATA**. Under ambient conditions, some **MTDATA**s in the film were oxidized by air generating radical cations, leading to a poor conductivity of 10^{-10} $S\cdot cm^{-1}$. One efficient way to promote conductivity of TAA derivatives consists in doping with *p*-dopants (e.g. $SbCl_5$), which could dramatically enhance conductivities by several orders of magnitude.[24,25] For instance, Grätzel and coworkers found that the conductivity of **Spiro-MeODTA** can be increased by 100-fold upon addition of lithium bis(trifluoromethylsulfonyl)-imide (Li-TFSI) (Figure 1.6b).[26] The underlying mechanism was then elucidated by the research group of Snaith.[27] The large improvement in conductivity was attributed to the involvement of Li-TFSI in the chemical oxidation process. As presented in Figure 1.6c, **Spiro-MOeTAD** is first oxidized by air to form radical cation complex, which subsequently reacts with Li-TFSI affording **Spiro-OMeTAD**$^{\cdot+}$**TFSI**$^{-}$, which is a highly efficient mobile hole in organic matrix.

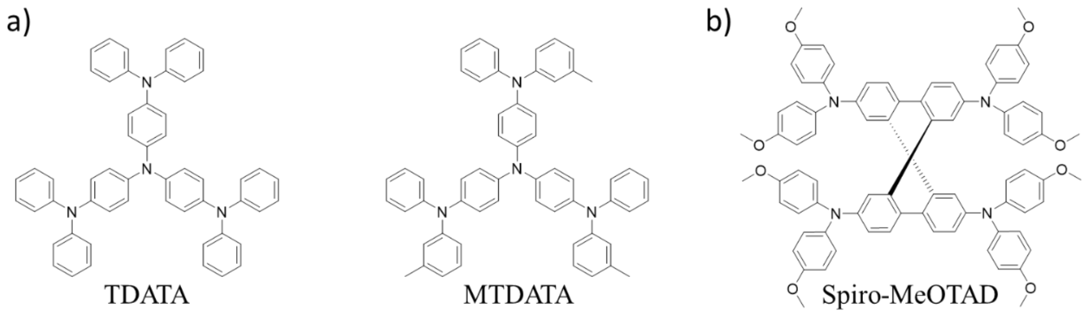

c)

$$\text{Spiro-OMeTAD} + O_2 \leftrightarrow \text{Spiro-OMeTAD}^{\bullet +}\, O_2^{\bullet -}$$

$$\text{Spiro-OMeTAD}^{\bullet +}\, O_2^{\bullet -} + \text{Li-TFSI} \rightarrow \text{Spiro-OMeTAD}^{\bullet +}\, \text{TFSI}^{-} + \text{Li}_x\text{O}_y$$

Figure 1.6 (a) Molecular structures of **TDATA** and **MTDATA**; (b) Molecular structure of **Spiro-MeOTAD**; (c) Chemical oxidation process of **Spiro-OMeTAD** in the presence of oxygen and Li-TFSI. The figure is reproduced from ref.[23,27]

Aforementioned examples were studied in amorphous state, in which conductivities are typically low due to the slow charge carrier mobility. Crystallization can resolve this issue to a certain extent. Furthermore, such defect-free structures enable anisotropic conductivity thanks to the directional charge transport between adjacent molecules.[28,29] For instance, the group of Umeda grew a single crystal of a TAA derivative (Figure 1.7a), and the ordered structure was characterized by X-ray diffraction (XRD).[29] As shown in Figure 1.7b, TAA derivatives prefer a face-to-face stacking along the c-axis rather than along a- or b-axis. As a consequence of higher stacking degree of electron cloud along the c-axis, the conductivity measured in the a- or b-axis are lower than that in the c-axis, indicating an anisotropic conducting behavior (Figure 1.7c).

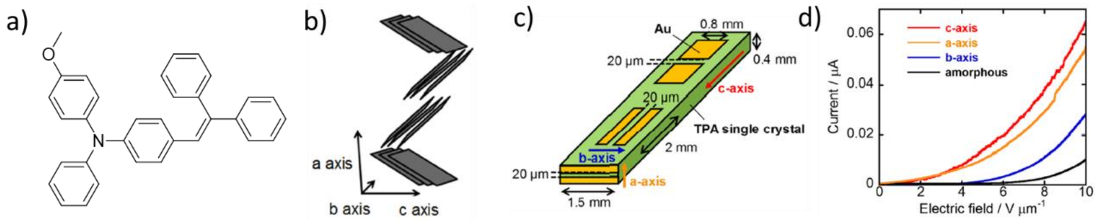

Figure 1.7 (a) Molecular structure of TAA derivative; (b) Schematic diagram of stacking orientation of TAA from panel (a); (c) Schematic representation of a single crystal; (d) *I-V* curves obtained in different axes and on the amorphous state. This figure is adapted from ref.[29].

1.1.2 Triarylamine-based supramolecular polymers

Conventional polymers consist of numerous repeating units that are linked through covalent bonds. On the contrary, in supramolecular polymers, thousands of monomers are connected together through non-covalent bonds, such as hydrogen bonds,[30] π-π stacking,[31] metal coordination,[32] host-guest interactions[33] and so on. Thanks to the dynamical reversibility of non-covalent bonds, supramolecular polymers bring great potentials in advanced materials with emergent functions, recyclable, and stimuli-responsive properties.[34]

Towards this goal, our research group has successfully designed and synthesized several TAA derivatives that can stack into supramolecular polymers in various solvent systems by employing π−π stacking and hydrogen-bonding interactions. In this section, we will present detailed examples to illustrate how TAA derivatives self-assemble into supramolecular structures via non-covalent interactions.

Light-induced supramolecular polymerization

The first discovery in light-triggered supramolecular polymerization of TAA was reported by our research group in 2010.[4] TAA **1** bearing two alkoxy chains and one amide group was synthesized. During characterization by ^{1}H NMR spectroscopy, we observed the disappearance of specific proton signals of TAA **1** in deuterated chloroform after exposure to sunlight for 10 minutes, accompanied by a noticeable change in color. Interestingly, the proton signals reappeared after heating overnight at 60°C. This reversible change was ascribed to the formation and quenching of radicals, which was further confirmed by EPR spectroscopy. As shown in Figure 1.8b, visible light irradiation for 1 hour resulted in the continuous generation of radical cations, and eventually around 11% of molecules were oxidized forming positively charged radical species (A-B). When the solution was placed in the dark for 1 week, the amount of radicals exhibited a slow decay and finally reached plateau (B-C). After heating, no more radicals were observed. Interestingly, in the irradiated solution, we observed the presence of corn-like fibrils which do not exist in non-irradiated solution. This was attributed to the self-assembly of TAA **1** assisted by radical cations (Figure 1.8d).

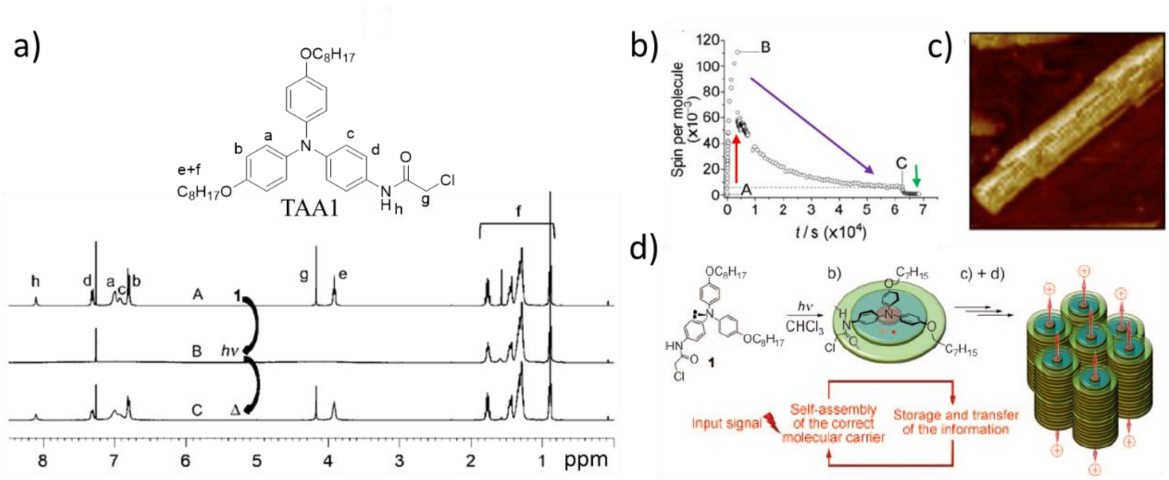

Figure 1.8 (a) Molecular structure of TAA **1** and its ^{1}H NMR spectra (before irradiation, A; and after 10 min irradiation, B; and after subsequent heating overnight at 60°C, C.); (b) Quantitative EPR data in different stages (irradiation, A-B; under dark, B-C; heating at 60°C, C); (c) AFM high resolution image (surface scale 50×50 nm^2); (d) Schematic representation of self-assembly of TAA **1** triggered by visible light in chloroform. This figure is adapted from ref.[4].

Mechanism of light-induced supramolecular polymerization

A combination of practical experiments (UV-Vis-NIR, EPR, and XRD) and theoretical calculations helped us sheding light on the light-triggered self-assembly process of TAA **1** in chloroform solution.[35]

According to all-atomic calculations, one can see that, before photo-oxidation, neutral TAA **1** cannot initiate the self-organization process in an early stage, because the activation energy required for planarization and solvent dissociation is too high (Figure 1.9(II)a). Upon visible light irradiation, a few percent of TAA **1** are oxidized into radical cations, which have a flattened conformation (Figure 1.9(II)b). These flat TAA $\mathbf{1}^{\bullet+}$ radicals interact with chloride ions generating electric dipoles that readily self-assemble into so-called “loose” chains, leaving chloride ions sandwiched between radicals (Figure 1.9(II)c-f). Once these ‘loose’ chains approach a certain length, chloride ions are forced out of the center resulting in the formation of “tight” chains (Figure 1.9(II)g-h). The tight chains are much stable due to the stabilization by optimal aromatic stack, which further form double columnar aggregates via intermolecular hydrogen bonds (Figure 1.9(II)i). As a result, neutral TAA **1** is attracted by double columns via hydrogen bonds and π-π stacking interactions, leading to the formation of large fibrils (Figure 1.9(II)j).

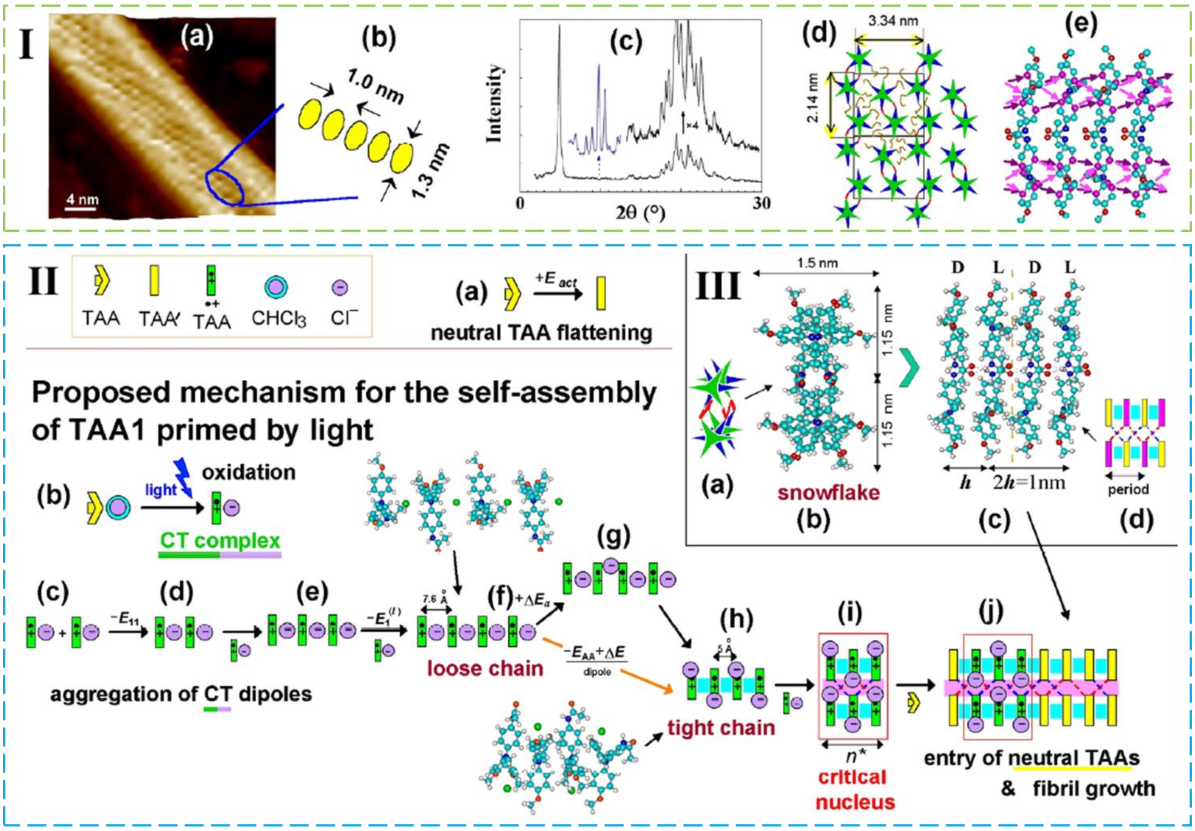

Figure 1.9 TAA fibrils in chloroform after exposure to white light for 1 hour. (I) (a,b) AFM height image; (c) XRD pattern from 10 mM TAA **1** sample (bottom, black) and its magnification in the WAXS range (top, black) and in the SAXS range (top, blue); (d) The proposed internal molecular organization of TAA **1** fibrils based on the XRD; (e) The simulated all-atomic structure of snowflake double column; (II) (a) Spontaneous flattening of isolated neutral TAA molecules; (b) Light induces oxidation of a neutral TAA molecule forming electric dipole; (c,d) Two free radicals $TAA^{•+}$ complexed with Cl^{-} attract each other head-to-tail; (e,f) A growing stack of radical dipoles; (f,g,h) Tightening of the stack; (i) Formation of double-columnar nuclei stabilized by H-bonds between the columns; (j) Growth of the structure by attracting neutral TAA molecules. (III) Molecular arrangements in bicolumnar “snowflake” stacks of neutral TAA. (a) A cartoon showing alternating molecular orientation in the columns; (b) The top view, and (c) the side view of the structure; (d) A cartoon with zigzag chain of H-bonds connecting the columns. This figure is reproduced from ref.[35].

Self-assembly of triarylamine trisamides

In our initial system, light is a necessity to initiate the nucleation step, and intermolecular hydrogen bonds play an important role in the elongation of self-assemblies. As multiple hydrogen bonds can increase the strength of intermolecular interactions between monomers,[30] we considered the introduction of multiple hydrogen bonds in order to the self-assembly of neutral TAA derivatives. To this end, we explored the self-assembling behaviour of triarylamine trisamides (TATA).[36] A symmetric molecule TATA **1** (Figure 1.10a) bearing three long alkyl chains was synthesized in a three-step protocol.

Without light irradiation, TATA **1** can self-assemble into large aggregates in several solvents (chloroform, acetonitrile, acetone, or toluene). Moreover, an organogel was obtained at high concentration. Fibrillar nanostructures with high persistence length were directly observed by freeze fracture transmission electron microscopy (FFTEM) and AFM. By combining X-ray scattering (SAXS and WAXS) and density functional theory (DFT), the molecular arrangement within single columnar fibers as such: seven TATA **1** molecules stacked with a distance of 4.85 Å and dihedral angles of 20° between adjacent molecules to form a helical nanostructure with a longitudinal period of 29.1 Å (Figure 1.10f).

Similar to triarylamines monoamide, in the presence of chloroform, the disappearance of some ^{1}H NMR signals of TATA **1** took place upon visible light irradiation, indicating the photo-oxidation and self-assembly of TATA **1** (Figure 1.10b). The charge transfer process in self-assembled structures was thoroughly investigated by UV-Vis-NIR and EPR spectroscopy. As shown by UV-Vis-NIR experiment (Figure 1.10c), visible light irradiation causes a large absorption band at 1100 nm (Figure 1.10c, d). Considering the absence of MV-CT system, this absorption band is attributed to intermolecular through-space charge transfer. Furthermore, from 0 to 30 minutes, the asymmetry of absorption band at 1100 nm is continuously increasing, indicating a gradual transition of charge transfer from partially delocalized class II to full delocalized class III. Further light irradiation creates a large number of radical cations, resulting in electrostatic repulsion. As a result, charge transfer process adopts class I, in which radicals are localized around nitrogen atom centers.

Although light is not a prerequisite for self-assembly of TATA, SAXS investigation indicates that light irradiation can diminish structural defects in self-assembled nanostructures as evidenced by a 49% increase in correlation length compared to non-irradiated one (Figure 1.10e), which is in agreement with the observation of smoother fibers by AFM (Figure 1.10g, h).

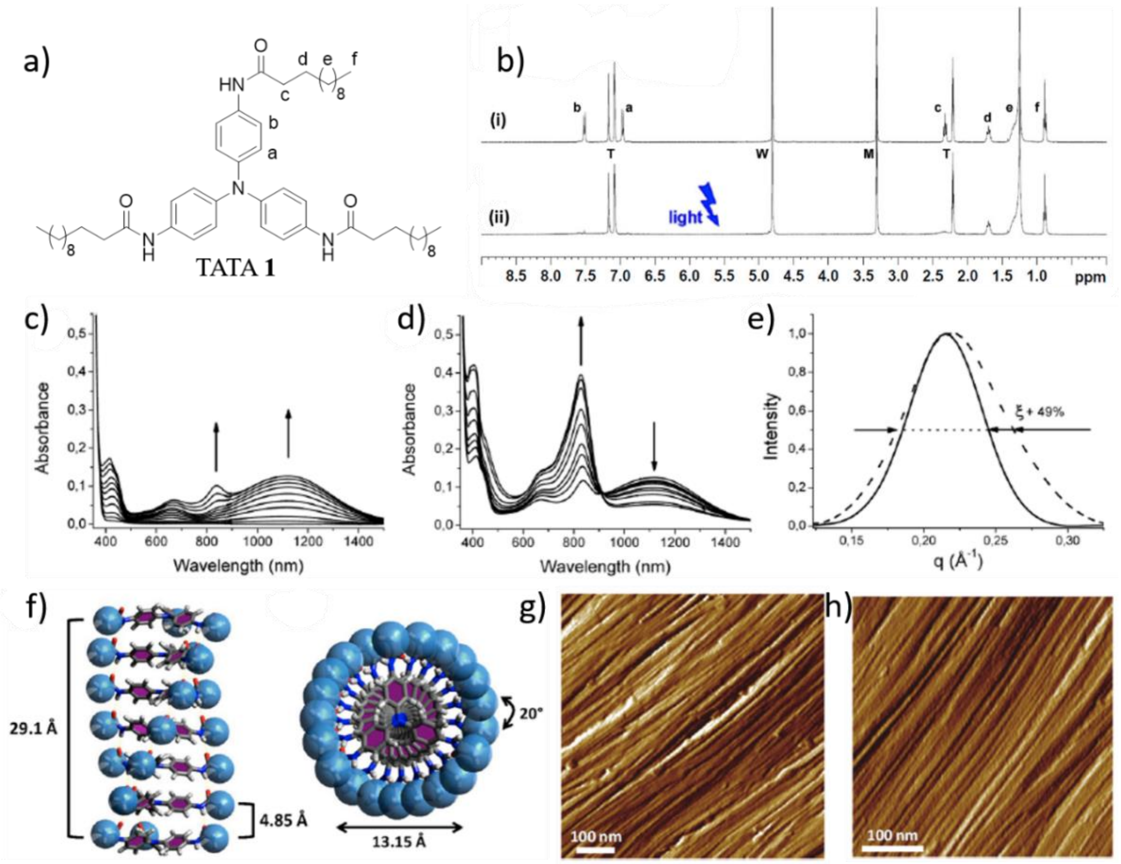

Figure 1.10. Self-assembly of triarylamine trisamide (TATA **1**). (a) Chemical structure of TATA **1**; b) ^{1}H NMR spectra before (i) and after (ii) light irradiation (W, M, and T are the residual resonance peaks for water, methanol, and toluene, respectively); (c,d) UV-Vis-NIR absorption sepctra taken during irradiation in CHCl$_3$; (c) first 6 min of irradiation, (d) 7 to 73 min of irradiation; (e) SAXS of nonirradiated (dotted line) and irradiated (full line) thin films demonstrating a 49% increase in the correlation length; (f) Side view (left) and top view (right) of proposed packing structures of TATA **1**; (g,f) AFM images of TATA **1** before (g) and after (h) 15 min of light irradiation. This figure is reproduced from ref.[36].

Over the last 10 years, our research group reported several stimuli-responsive self-assembling systems involving chemical oxidants, self-assembled fibril seeds,[35] and electric field[37] to induce supramolecular polymerization.

Triarylamine-based chiral supramolecular polymers

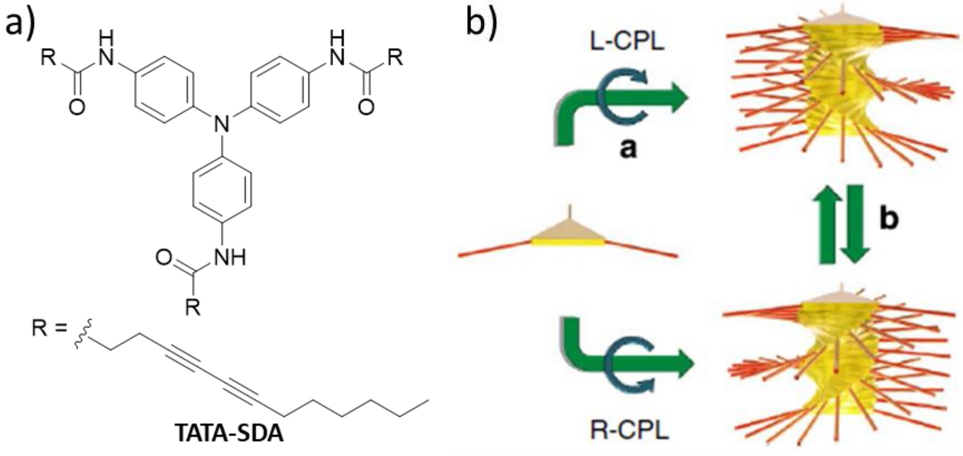

Figure 1.11 (a) Chemical structure of **TATA-SDA**; (b) Supramolecular polymerization of **TATA-SDA** and helices inversion induced by CPL. This figure is reproduced from ref.[38]

As shown before, TAA derivatives containing several amide groups can self-assemble into supramolecular helices. For example, TATA **1** can stack in a racemic mixture of well-defined *P*- and *M*- supramolecular polymers.[36] In 2015, Kim and collaborator reported the formation of *M*- or *P*- helical supramolecular polymers by irradiating the enantiomerically pure **TATA-SDA** (Figure 1.11a) with left-handed or right-handed circularly polarized light (CPL), respectively.5[38] Furthermore, the helicity of one helical supramolecular polymer can undergo reversible switching by irradiating with the opposite CPL (Figure 1.11b). This interesting behavior is explained by the photo-resolution effect of TAA moiety, which forces the TAA core to adopt a single *Δ* or *Λ* conformation dependent on the light direction of CPL.

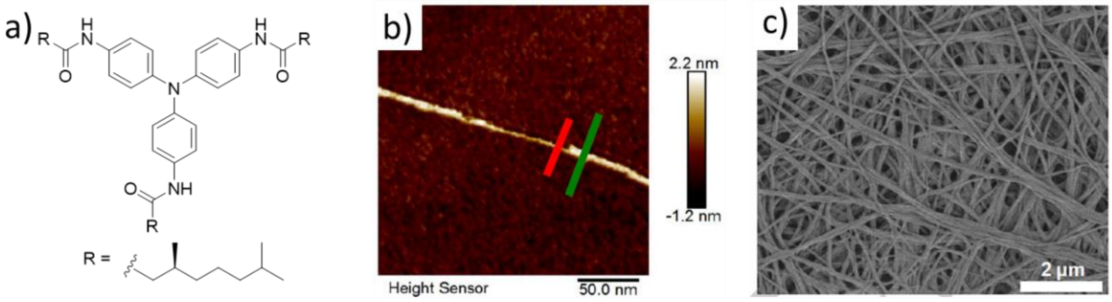

Figure 1.12 (a) Molecular structure of **(*S*)-TATA**; (b) AFM image of **(S)-TATA** single fiber prepared at concentration of 0.1 mM in toluene. This figure is adapted from ref.[39].

Chiral TAA supramolecular polymers were also obtained by introducing stereogenic centers on the side chain of TATA. Recently, our group investigated the self-assembling behavior of chiral

(*S*)-TATA bearing three chiral side chains (Figure 1.12a).[39] Owing to the presence of chiral side chains, **(*S*)-TATA** monomers are able to self-assemble into chiral polymers in different solvents, such as toluene, chloroform, and acetonitrile. As shown in Figure 1.12b, a diluted solution of **(*S*)-TATA** in toluene (0.1 mM) spontaneously stack in single columnar fibers. Increasing the concentration to 1mM led to the formation of fibrillar bundles with lengths over the micron and with diameters up to hundreds of nanometers.

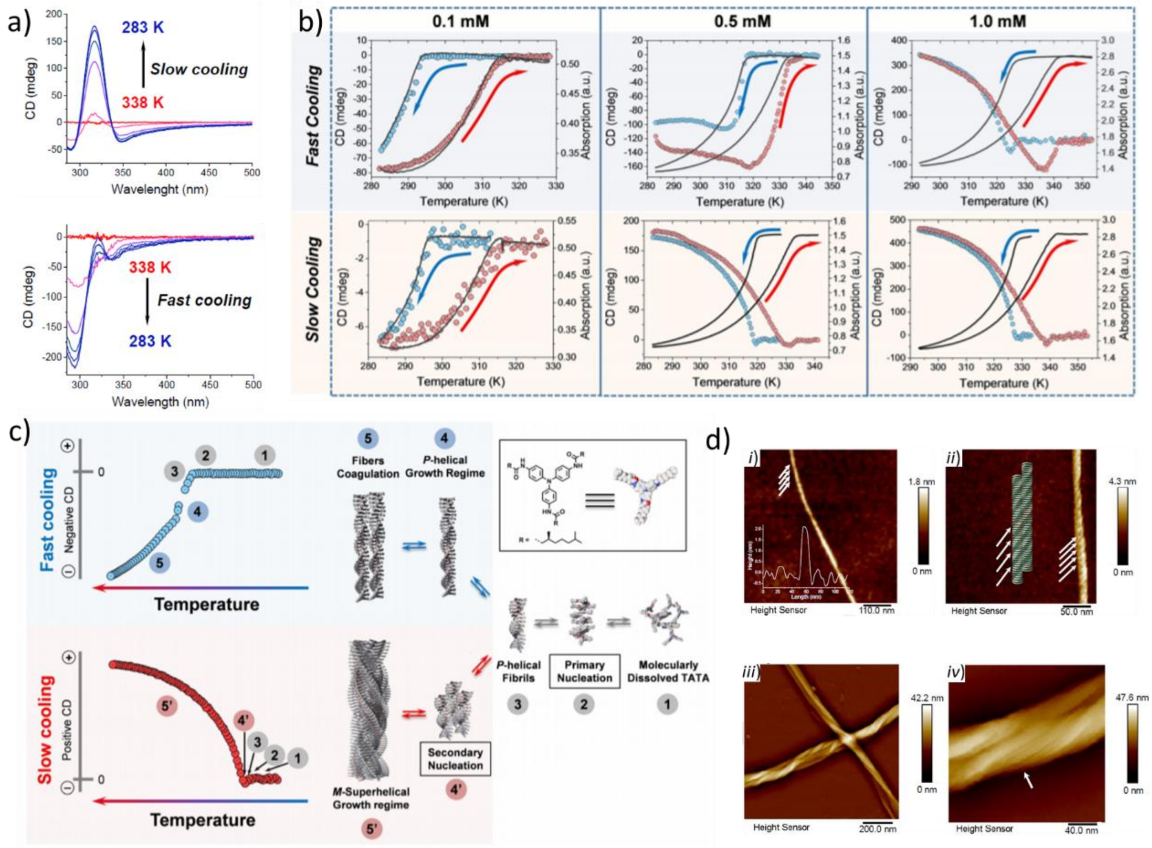

Figure 1.13. (a) Evolution of CD spectrum of **(*S*)-TATA** in toluene (0.5 mM) during slow cooling (top) and fast cooling (bottom); (b) Temperature-dependent CD and UV curves of **(*S*)-TATA** in toluene at different concentrations and for different cooling rates; (c) Proposed self-assembling pathways for **(*S*)-TATA** depending on cooling regime at concentration of 0.5 mM in toluene; (d) AFM images of **(*S*)-TATA** self-assemblies obtained from *i*) a 0.1mM solution in toluene; *ii*) a 0.5 mM solution in toluene at fast cooling rate; *iii*) and *iv*) 0.5 mM solution in toluene in slow cooling regime. In *iv*), only single *P*-helices in larger *M*-superhelices is identified. This figure is adapted from ref.[39].

Further investigation confirmed that the cooling rate and concentration both influence the self-assembling behavior of **(*S*)-TATA**. For example, a 0.5 mM solution of **(*S*)-TATA** in toluene at slow cooling rate (1 K/min) showed positive cotton effect at 315 nm, while, fast cooling regime (10 K/min) afforded negative cotton effect. However, the CD signals of dilute (0.1 mM) or concentrated (1 mM) **(*S*)-TATA** solution in toluene exhibited no dependence on the cooling rate.

According to AFM images for **(*S*)-TATA** self-assemblies (Figure 1.13d), this unusual phenomenon was explained by the hierarchical supramolecular polymerization of **(*S*)-TATA**.

At a concentration of 0.5 mM, the cooling of a hot solution triggers primary nucleation of molecularly dissolved **(*S*)-TATA**, resulting in short *P*-helical fibrils (Figure 1.13c, steps 1-3). Then these fibrils can evolve over two self-assembling pathways: I) at a fast cooling rate, *P*-helical fibrils grow into long *P*-helices which further coagulate into larger fibers with unchanged helicity (Figure 1.13c, steps 4-5); II) In slow cooling regime, ***(S)*-TATA** monomers undergo a second nucleation process, in which short monocolumnar fibrils (*P*-helicity) coagulate into polyfibrillar nuclei thanks to lateral interactions (Figure 1.13c, step 4'). The nuclei subsequently enter in a superhelical growth regime, resulting in the formation of *M*-superhelices (Figure 1.13c, 5'). It is noteworthy that, in a dilute solution (0.1 mM), **(*S*)-TATA** monomers preferentially form *P*-helices with few superhelices at all cooling rate. In sharp contrary, the concentrated solution of **(*S*)-TATA** prefers to form *M*-superhelices via second nucleation process.

According to above-mentioned examples, one can see that the presence of amide bond on side chains of TAA could induce the supramolecular polymerization. On the other hand, diversity in TAA-based self-assembled structures can be obtained by the rational functionalization of its periphery and preparation method.

1.1.3 Organic room temperature phosphorescence

The development of organic luminescent compounds is of interest due to great potential in advanced applications, particularly in biology [40] and energy [41]. According to the spin multiplicity, luminescence emitted from organic compounds is generally classified as fluorescence and phosphorescence. In comparison to fluorescence, phosphorescence displays longer life-time and larger Stoke-shift.[42,43] In past decades, phosphorescent materials have been extensively explored for novel applications, such as data encryption and display,[44,45] chemical sensors, [46] bioimaging, [47] OLED [48] and so on. In this section, the mechanism of phosphorescence emission will be presented, then we will introduce several efficient strategies for enabling room temperature phosphorescence (RTP).

1.1.3.1 Pure organic phosphorescence emission

The photophysical process of electrons in luminophores is detailed in a simplified Jablonski diagram (Figure 1.14).[49] Without energy input, electrons are placed in ground state (S_0). After absorbing energy from light, electrons (S_0) are able to transit to excited singlet state (S_n, n⩾2). Based on Kasha rule, the singlet excitons rapidly decay to the energy-lowest singlet state (S_1) via internal conversion (IC). Then excitons in S_1 are confronted with three competitive channels for the following relaxation. First, the excitons may undergo a non-radiative decay, accompanied by a transition from S_1 to S_0 via IC process. Alternatively, excitons (S_1) can relax to S_0 via radiative decay emitting fluorescence. A comparable channel is spin-flipping to excited triplet state (T_n, n⩾2) via internal system crossing (ISC) process. When the energy difference between T_n and S_1 is small enough, the triplet excitons will go back to singlet state via a reversed ICS process (RICS). Otherwise, a rapid IC will take place, through which excitons (T_n) transfer to energy-lowest triplet state (T_1). Eventually, excitons in T_1 subsequently relax to S_0 via non-radiative decay (molecular vibration and collision), phosphorescence emission or quenching by oxygen or other substances. It should be noted that the transition S_0 from T1 is spin forbidden, associated with transformation of spin multiplicity, thus the lifetime of phosphorescence is relatively longer than fluorescence ($>10^{-8}$s).

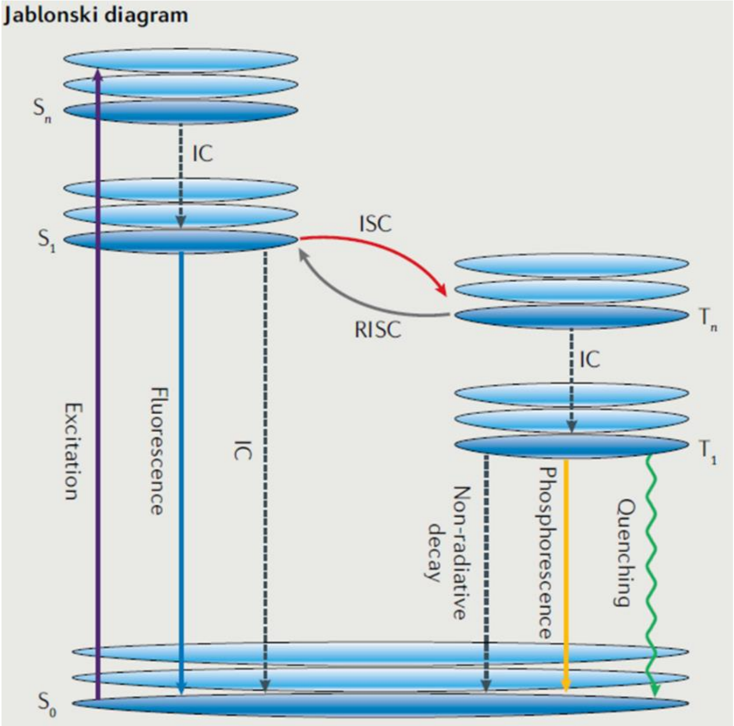

Figure 1.14 Simplified Jablonski diagram that describes photophysical processes in organic molecules. Figure is reproduced from ref.[49].

1.1.3.2 Enhancing organic RTP efficiency

According to the generation of phosphorescence described in Jablonski diagram, one can see that facilitating ISC process and suppressing of non-radiative decay of excitons (T_1) are keys to enhance phosphorescence. To facilitate ISC, chemical modifications by introducing heavy atom, hetero atoms (O, N, S, and P) or aromatic carbonyls have proved to be highly efficient,[49,50] as the incorporation of above substituents can enhance the spin-orbit coupling (SOC) between singlet and triplet states.

On the other hand, suppressing non-radiative decay by embedding phosphorescent units into a rigid matrix could lead to RTP.[49,50,51] Crystallization is a typical method used for organic RTP. However, for certain molecular structures, the tight packing may cause energy transfer or triplet-triplet annihilation thus weakening RTP.

An alternative approach consists in embedding phosphors to amorphous polymers, in which molecular motions of phosphors can be sufficiently suppressed, enhancing radiative decay for phosphorescence. Kim and coworkers doped amorphous poly(vinyl alcohol) (PVA) with phosphor **G1** (Figure 1.15a).[52] Thanks to the combination of halogen bonds and hydrogen bonds, the molecular vibration of **G1** was sufficiently diminished, resulting in a 24% RTP quantum yield. Afterwards, the same research group reported a covalent cross-linking strategy to introduce phosphor into polymeric matrices (Figure 1.15b).[53] The phosphor **DA1** bearing ene units was connected with the diene units on the polymer side chains via Diels-Alder reaction. Compared to non-cross-linked reference compound **Br6A**, the cross-linked **DA1** displays much higher performance in RTP with a quantum yield of 28%.

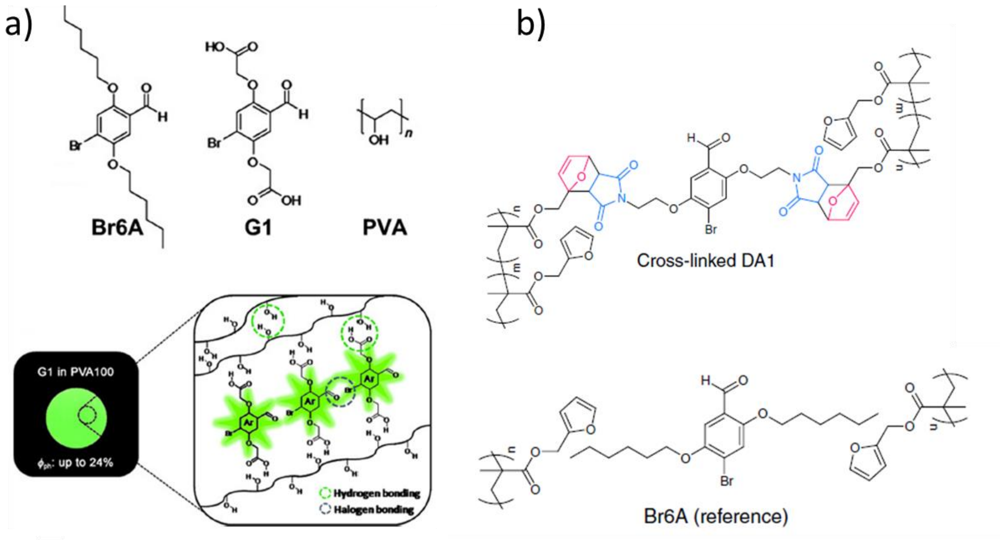

Figure 1.15 (a) Chemical structures **Br6A**, **G1**, and **PVA**, and photography of the thin film made of the mixture of **PVA** and **G1**. The photograph was taken under UV light irradiation; (b) Molecular structures of cross-linked **DA1** and reference **Br6A**. Figure is reproduced from ref.[52,53].

Another comparable strategy enabling RTP relies on host-guest complexation. The confined space in host components are able to rigidify the structure of guest phosphors, which also prevents the aggregation-induced quenching. In this method, a strong RTP can be achieved even in solution. Turro and coworker reported for the first time RTP induced by the complexation of cyclodextrin (CD), in which 1-bromonaphthalene or 1-chloronaphthalene was embedded in the cavity of CD and emitted RTP in degassed aqueous solution.[54] Taking inspiration from host-guest complexation induced RTP, the group of Ma developed a photo-responsive system to regulate RTP (Figure 1.16a).[55] This system consists of modulator **DAYR**, host *β*-CD, and guest phosphor ***α*-BrNp**. Before light irradiation, the cavity of *β*-CD host was occupied by *trans*-**DAYR**, and phosphor ***α*-BrNp** was molecularly dissolved in solvent. Without restriction of non-radiative decay, the RTP was very weak. Upon light irradiation, **DAYR** isomerizes to its cis form and phosphor ***α*-BrNp** replaced **DAYR** in host *β*-CD, leading in RTP enhancement.

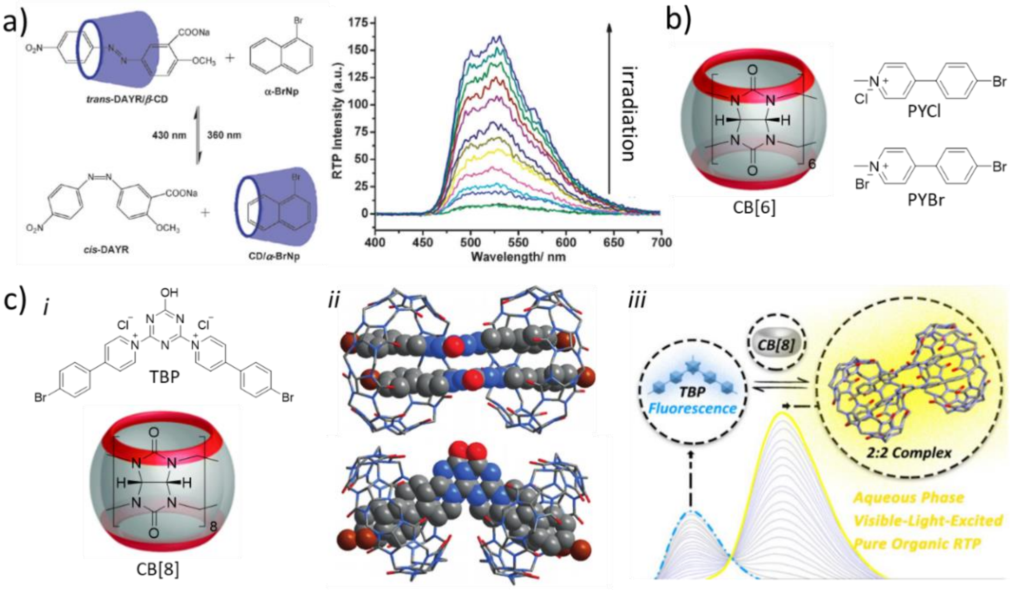

Figure 1.16 (a) Reversible RTP of **CD/DAYR/BrNp** induced by light irradiation; (b) Chemical structures of **CB[6]**, **PYCl**, and **PYBr**; (c) Visible light induced RTP in aqueous solution of **TBP** and **CB[8]**. Figure is reproduced and adapted from ref.[55,56,57].

Cucurbituril (CB) is an ideal host to improve RTP performance as well. Recently, Liu and coworkers reported highly efficient RTP in solid state (Figure 1.16b),[56] in which bromophenyl-methyl-pyridinium (**PY**) with different counterions (Cl^- or Br^-) was encapsulated by host CB[6]. Thanks to the encapsulation, CB[6]/[**PY**] complexes exhibited great improvement in RTP. In particular, the RTP quantum yield of **PYCl**/CB[6] reached up to 81.2% with a 32-fold increase with respect to the pure **PYCl**. By enlarging the cavity of CB, the research group of Ma obtained visible-light-excited RTP in aqueous phase (Figure 1.16c).[57] In an aqueous solution, two **TBP** phosphors were capsulated by two CB[8] hosts forming a 2:2 quaternary complex via dipole-dipole interaction, hydrogen-bonding, and hydrophobic interaction. The complexes not only reduced non-radiative decay of **TBP**, but also shifted absorption wavelength to visible region due to charge-transfer between two adjacent **TBP**. In comparison with pure **TBP**, the emission spectrum of this complex displayed a noteworthy red-shift with long life-time, which is attributed to the RTP of CB[8]/**TBP** complex.

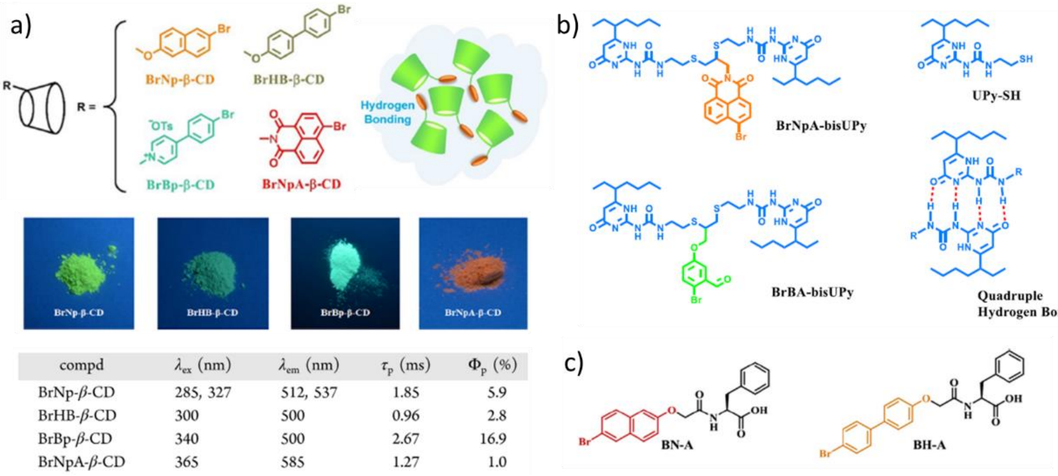

compd	λ_{ex} (nm)	λ_{em} (nm)	τ_p (ms)	Φ_p (%)
BrNp-β-CD	285, 327	512, 537	1.85	5.9
BrHB-β-CD	300	500	0.96	2.8
BrBp-β-CD	340	500	2.67	16.9
BrNpA-β-CD	365	585	1.27	1.0

Figure 1.17 RTP examples of amorphous systems made of metal-free organic small molecules developed by the research group of Ma. Figure is adapted from ref.[58,59,60].

Very recently, various amorphous RTP systems made of metal-free organic small molecules have been developed. The first example was reported in 2018 by the group of Ma,[58] who designed and synthesized four CD derivatives, in which the macrocyclic *β*-CD were modified, with phosphorescent moieties **BrNp**, **BrHB**, **BrBp**, and **BrNpA** (Figure 1.17a). All compounds in amorphous solid state showed RTP with a decent quantum yield. Interestingly, they found that such molecular design does not favor host-guest complexation between CD and phosphors due to steric hindrance. The dominant factor in RTP is intermolecular hydrogen bonds between adjacent CDs. In this case, the stacked CD hosts provide a rigid and isolated space that not only impedes the non-radiative transition from T_1 to S_0, but also prevents encapsulated phosphors from external quenchers (oxygen and other substances). On the basis of above design, they further extended this RTP system by combining phosphors with various hydrogen-bonding moieties, such as amino acid skeleton[59] (Figure 1.17b) and ureidopyrinidinone (upy)[60] (Figure 1.17c).

1.2 TAA-based supramolecular polymers with room temperature phosphorescence

1.2.1 Objectives

As presented in the bibliography section, on one hand, TAA derivatives can spontaneously or passively self-assemble into supramolecular polymers, with well-defined structural features depending on their molecular design. On the other hand, it is challenging to obtain organic room temperature phosphorescence (RTP) due to low internal system crossing (ISC) efficiency and non-radiative decay of triplet excitons. One way to favor organic RTP is to rigidify phosphors, which could be achieved by crystallization, host-guest complexation, and confinement in networks of covalent or supramolecular polymers. Based on these knowledges, we aimed to develop TAA-based supramolecular polymers with organic RTP, as the formation of supramolecular polymer could induce rigidification of phosphors.

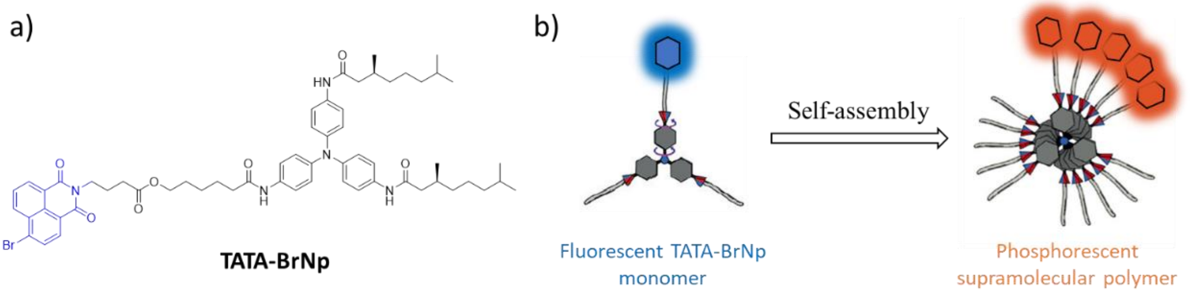

Figure 1.18 (a) Chemical structure of **TATA-BrNp**; (b) Schematic representation of TAA-based supramolecular polymer with RTP.

To this end, we designed and synthesized a triarylamine trisamide molecule (TATA-BrNp) bearing two chiral alkyl side chains and one 4-bromo-1,8-naphthalimide (BrNp) as phosphorescent unit. By employing intermolecular π-π stacking interactions and multiple hydrogen-bonds, the central TATA motif should spontaneously self-assemble to form supramolecular polymers with BrNp confined in the structure. In such configuration, the intramolecular motion of BrNp could be suppressed sufficiently, leading to organic RTP.

1.2.2 Synthesis of TATA-BrNp

The synthesis of TATA-BrNp required the preparation of three building blocks consisting of the chiral chains, TATA motif, and the phosphorescent unit **BrNp**. First, we synthesized carboxylic acid-substituted BrNp **1** according to a protocol previously reported in the literature.[61] A mixture of commercially available 4-bromo-1, 8-naphthalic anhydride and 4-aminobutanoic acid in ethanol was refluxed for 10 hours affording BrNp **1** with 87% yield.

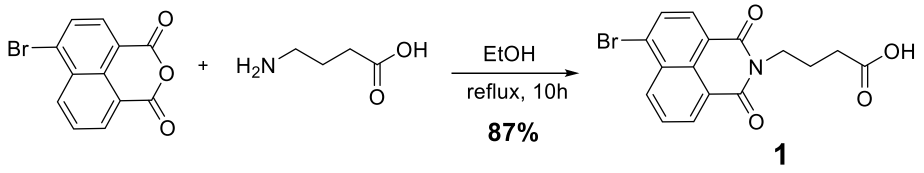

Scheme 1.2 Synthesis of BrNp **1**.

The synthesis of the chiral alkyl chain was started from (*S*)-3,7-dimethyloct-6-en-1-ol.[62] After alkene reduction with palladium on carbon and hydrogen, compound **(*S*)-2** was obtained almost quantitatively. In the presence of pyridinium chlorochromate and periodic acid as oxidants, the hydroxyl group on **(*S*)-2** was oxidized to carboxylic acid affording **(*S*)-3** in excellent yield. Subsequently, a chloroform solution of **(*S*)-3** was refluxed with thionyl chloride for 3 hours providing chiral chain **(*S*)-4** with 99% yield.

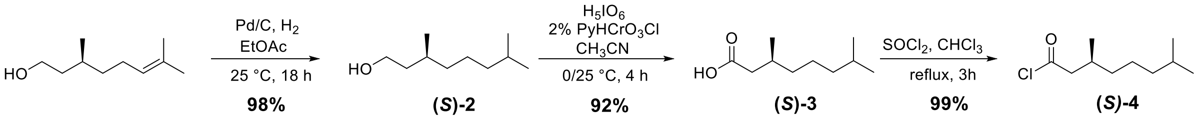

Scheme 1.3 Synthetic route of **(*S*)-4**.

TAA motif **5** was synthesized with a good yield via aromatic nucleophilic substitution reaction between 4-aminoaniline and 4-fluoro-nitrobenzene.[10] The subsequent acylation reaction of compound **5** with 6-bromohexanoyl chloride allowed us to obtain product **6** with 79% yield. Reduction of nitro groups with tin chloride afforded product **7**, which was directly reacted with chiral chain **(*S*)-4** to provide TATA **8** with 73% yield. Finally, carboxylic acid substituted compound **1** was engaged in a nucleophilic substitution reaction with TATA **8** at room temperature for 12 hours, providing final molecule TATA **9** in good yield.

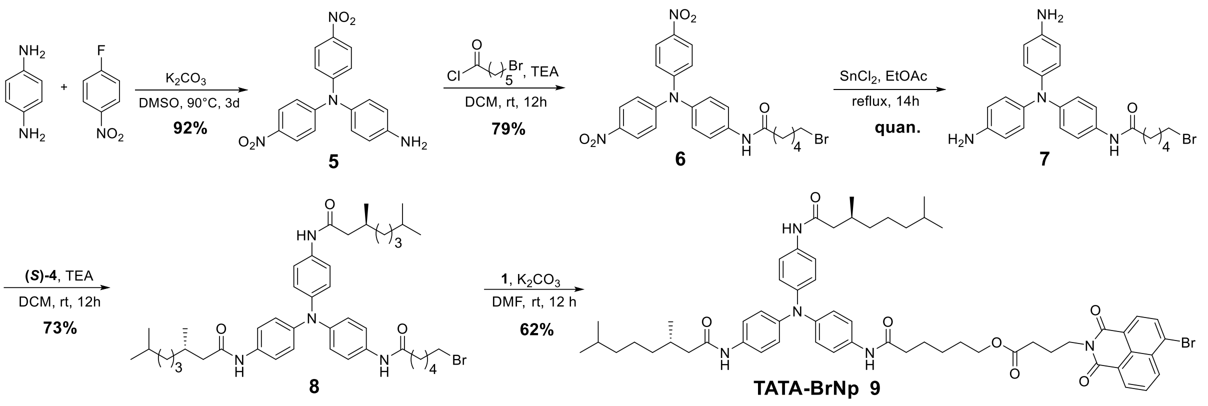

Scheme 1.4 Synthesis of TATA-BrNp **9**.

1.2.3 Optical and structural properties

We then studied the optical properties of BrNp **1**, TATA **8** and TATA-BrNp **9** in dilute solution. As reported in the literature,[63] in THF solution (0.02 mM), phosphor BrNp **1** displays a narrow absorption peak at a wavelength of 355 nm and a broad absorption band at 340 nm with a tiny shoulder around 325 nm. On the contrary, TATA **8** shows a single broad band with a maximum at 324 nm. Similar to TATA **8**, the maximum absorption intensity of TATA-BrNp **9** is located at 324 nm with a shoulder occurring at 355 nm.

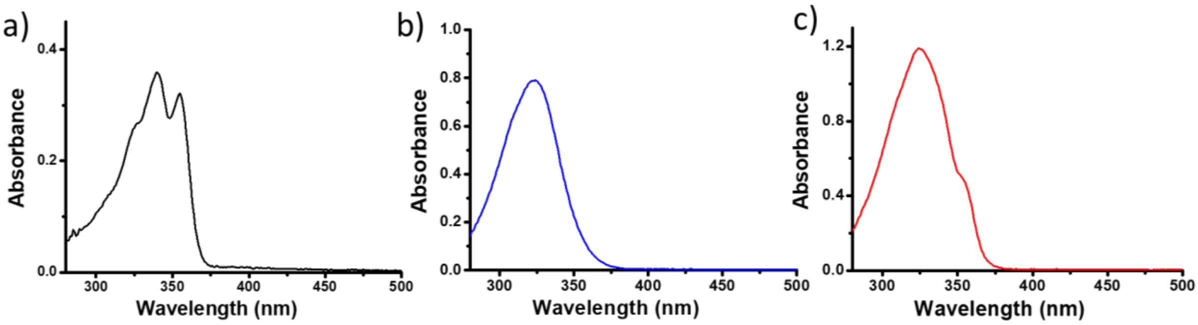

Figure 1.19 Absorption spectrum of 0.02 mM THF solution of (a) BrNp **1**; (b) TATA **8**; and (c) TATA-BrNp **9**.

Then the emission property of these compounds, at room temperature, was investigated. As shown in Figure 1.20a, the emission spectra of phosphor BrNp **1**, TATA **8**, and TATA-BrNp **9** display similar spectral profile ranging from 350 nm to 500 nm with maxima around 395 nm. It is noteworthy that, at room temperature, the non-radiative decay of triplet excitons in dilute solution cannot be diminished efficiently, thus the nature of these emissions is fluorescence rather than phosphorescence.

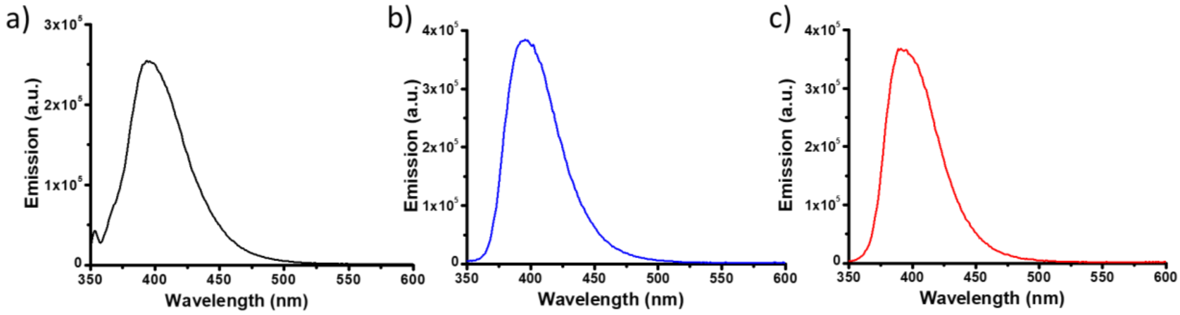

Figure 1.20 Emission spectrum of 0.02 mM THF solution of (a) BrNp **1**; (b) TATA **8**; and (c) TATA-BrNp **9**. (λ_{ex} = 345 nm, 298K)

To gain an insight into phosphorescent characteristics of TATA-BrNp **9**, we carried out experiments on emission at 77 K. At such low temperature, molecules are ‘frozen’ and intramolecular motion is efficiently diminished, leading to phosphorescence. Compared to the emission spectrum recorded at room temperature, TATA-BrNp **9** displays well-defined sharp emission bands at low temperature. Moreover, besides the bands between 370 and 500 nm, a new emission band ranging from 550 to 700 nm is observed, which probably corresponds to the phosphorescence of BrNp **1**. To determine whether or not this new emission band stems from BrNp **1**, we equally recorded the emission spectrum of BrNp **1** at 77K. An emission band at 500-700 nm bearing same spectral profile as TATA-BrNp **9** was observed, verifying our assumption. Intriguingly, BrNp **1** also displays a broad emission band ranging from 400 nm to 550 nm, which is attributed to excimer emission of BrNp **1**.[64]

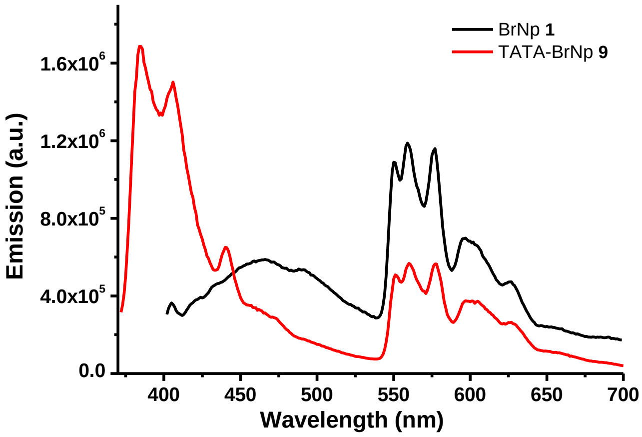

Figure 1.21 Emission spectrum 0.02 mM MTHF solution of BrNp **1** (black line), and TATA-BrNp **9** (red

line). (λ_{ex} = 345 nm, 77K)

The emission spectrum of TATA-BrNp **9** at room temperature shows that, in dilute solution, only fluorescence emission occurs. To achieve RTP, self-assembly of TATA-BrNp **9** is considered mandatory. Thus we turned to investigate the self-assembling behaviour of TATA-BrNp **9** in different solvents. THF, toluene, chlorobenzene, and DMF were considered for the self-assembly process. The self-assemblies were then evaluated by TEM. As shown in Figure 1.22a and 1.22b, in 1 mM chlorobenzene or toluene solution, TATA-BrNp **9** forms thin and soft fibers with a certain amount of amorphous materials. Similarly, in 1 mM THF solution, we also observed self-assembled thin fibers, which interact with each other and further form thick bundles (Figure 1.22c). In sharp contrast, supramolecular polymers observed in 1 mM DMF are much thicker with respect to those in other solvents (Figure 1.22d). Based on these observations, we considered DMF as the solvent of choice to study RTP properties of compound **9**.

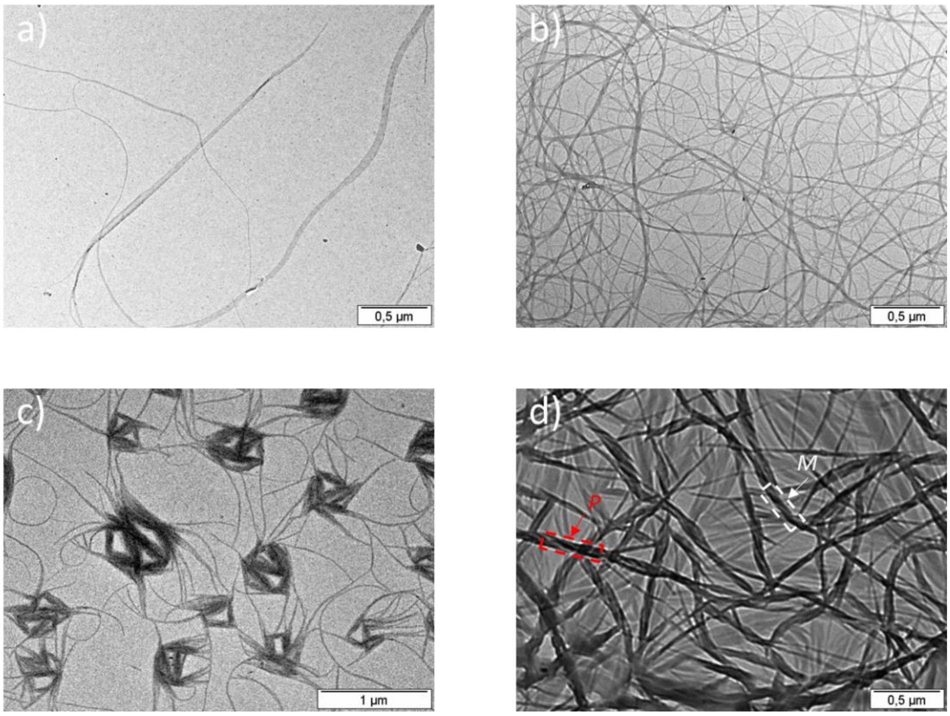

Figure 1.22 TEM images of 1 mM solution TATA-BrNp **9** in different solvents. (a) Chlorobenzene; (b) Toluene; (c) THF; (d) DMF.

The presence of a stereogenic center on the chiral side chains of TATA-BrNp **9** should induce a predominant chirality to the corresponding supramolecular polymers. To verify this hypothesis, we carried out CD experiments with solutions of TATA-BrNp **9** in toluene and DMF. However, only very low CD signals were obtained for these samples (Figure 1.23), suggesting a limited chirality transfer to self-assemblies. This can be explained by the formation of racemic self-assemblies, as evidenced by the co-existence of *M* and *P* supramolecular helices observed in DMF (Figure 1.22 d).

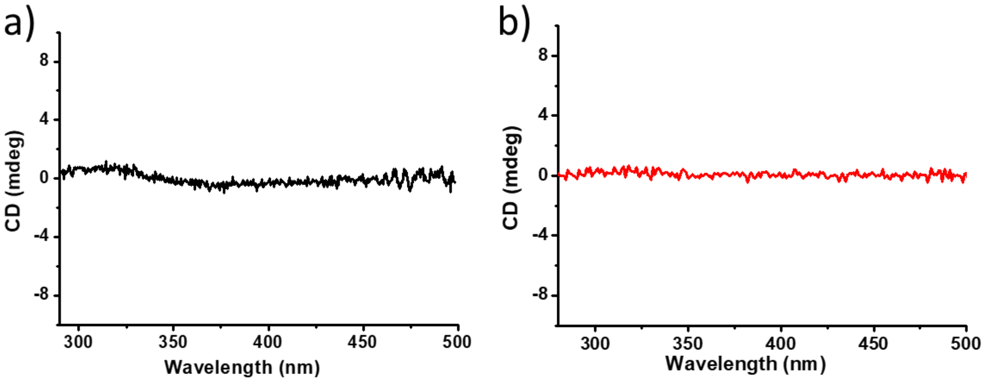

Figure 1.23 CD spectra of 0.1 mM solution of TATA-BrNp **9** in (a) toluene, and (b) DMF.

Although we proved that TATA-BrNp **9** stacks in supramolecular polymers in different solvents, the self-assembled nanostructures in DMF showed higher ordered degree. Regarding our objectives, we believe that these well-organized structures are favoured for RTP, and thus opted to focus the investigation on TATA-BrNp **9** in DMF. To shed light on the structural information on the self-assemblies of TATA-BrNp **9**, small angle X-ray scattering (SAXS) and wide angle X-ray scattering (WAXS) experiments were performed on a powder prepared from a DMF solution. In the wide angle region, series of diffraction peaks were observed, indicating periodically ordered structures at short distances. By applying Bragg diffraction equation, and comparing our data with the known crystalline structure of TAA-based supramolecular polymer previously reported by our group,[36] the peak located at 1.31 $Å^{-1}$ corresponds to a distance of 4.80 Å i.e. between stacked nitrogen centers, and the peak located at 1.94 $Å^{-1}$ corresponding to a distance of 3.23 nm is attributed to the π-π stacking of piled TAA motifs.

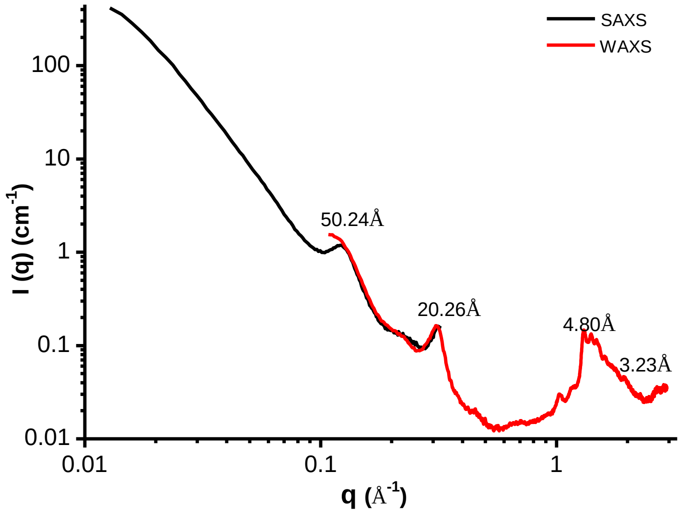

Figure 1.24 SAXS and WAXS of the powder of TATA-BrNp **9** obtained from 1 mM solution in DMF.

With such ordered supramolecular structure in solid state, the non-radiative decay of triplet excitons in BrNp group is expected to be diminished efficiently, resulting in RTP. Under UV light, the powder of TATA-BrNp **9** prepared form DMF solution showed a red emission, as opposed to the blue fluorescence which was observed in its THF solution or BrNp **1** powder. To get a better insight into the red emission, we carried out fluorescence spectroscopy on a TATA-BrNp **9** suspension in toluene (0.1 mg/mL), which was prepared by ultrasonication. Similarly to the emission spectrum of TATA-BrNp **9** solution recorded at 77K, the suspension displayed two emission bands as well (Figure 1.25b), the narrow peak at 420 nm corresponding to the fluorescence of TAA core and BrNp, and the broad band at 550-800 nm probably originating from phosphorescence emission of the BrNp group as the result of TATA-BrNp **9** self-assembly.

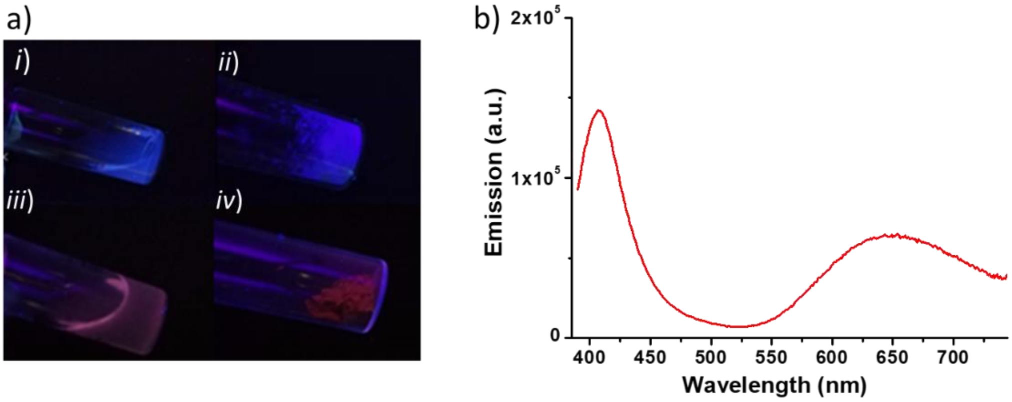

Figure 1.25 (a) Photographs of i) TATA-BrNp **9** solution in THF, ii) powder of BrNp **1**, iii) TATA-BrNp **9** suspension in toluene (0.3 mg/mL), and iv) TATA-BrNp **9** powder prepared from DMF solution. These photographs were taken under 365 nm UV light irradiation; (b) Emission spectrum of TATA-BrNp **9** suspension in toluene (0.1 mg/mL). (λ_{ex} = 345 nm, 298K)

To elucidate the nature of the emission at 550-800 nm, we first tried to record phosphorescence emission spectrum of TATA-BrNp **9** powder in a phosphorescence mode. As described in the examples reported by the research group of Ma,[58,59] the phosphorescence lifetime of BrNp usually ranges from microseconds to milliseconds. So, we set a delay time of 0.1-0.5 ms for parameter settings. However, we did not observe any emission signals despite many attempts, suggesting a short lifetime in our system. We then performed lifetime measurement. The result is shown in Figure 1.26, the lifetime of emission at 645 nm is 192 ns, which is much shorter than previous examples but still in the range of phosphorescence.

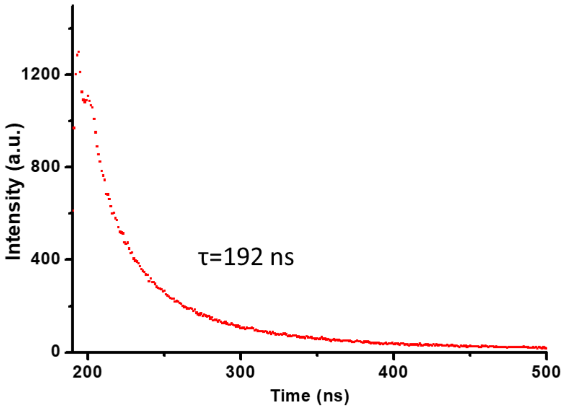

Figure 1.26 Emission intensity decay of TATA-BrNp **9** suspension in toluene. (λ_{em} = 645 nm)

As mentioned in the bibliography section of phosphorescence, phosphorescence emission is typically sensitive to oxygen due to quenching effect. For toluene suspension of TATA-BrNp **9**, degassing for 10 minutes with an argon flow results in a slight emission enhancement at 650 nm, accompanied by a decrease in emission at 400 nm (Figure 1.27), which implies that the emission at 550-800 nm corresponds to phosphorescence.

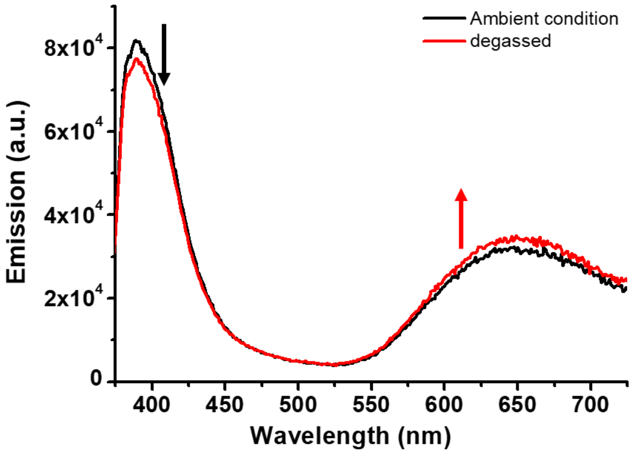

Figure 1.27 Emission spectra of TATA-BrNp **9** suspension at ambient condition (black line), and after degassing with an argon flow.

1.2.4 Conclusion

A triarylamine trisamide derivative TATA-BrNp bearing 4-bromo-1,8-naphthalimide (BrNp) as phosphorescent unit on one of its side chains was designed and synthesized. The optical properties of dilute solution of TATA-BrNp were investigated by UV-Vis and emission spectroscopy. At low temperature, TATA-BrNp could emit red phosphorescence. While, at room temperature, only fluorescence was observed due to non-radiative decay of triplet excitons. By combining intermolecular hydrogen bonding and π-π stacking interactions, TATA-BrNp can self-assemble into supramolecular polymers with BrNP units confined in the structure, which were studied by TEM. Furthermore, using X-ray scattering technique, we confirmed the ordered structure of self-assembled polymers in DMF. Thanks to the restriction of intramolecular motion of BrNp, self-assemblies of TATA-BrNp in solid state displayed red phosphorescence.

Chapter II. Triarylamine-based Supramolecular Nanoparticles for Organic Plasmonics

2.1 Bibliography

2.1.1 Localized surface plasmon resonance

2.1.1.1 Plasmon and localized surface plasmon

A plasmon is a type of quasi-particles, which is described as a collective oscillation of free electrons in metal.[65] Similar to mechanical oscillation, electron gas in metals can coherently oscillate with respect to the fixed positive ionic cores under external electromagnetic of incident light. At metal surfaces, plasmons (surface plasmons) take the form of surface plasmon polaritons (SPPs), which are optically excited and further couple with incident light to propagate along the surface of metals (Figure 2.1). When a surface plasmon is confined in a metal nanospheres, the external electromagnetic field leads to polarization of free electrons, that is, the distribution of free electrons is asymmetric around particles' boundary. Furthermore, thanks to electrostatic attraction between electrons and ionic cores, a linear restoring force occurs resulting in coherent oscillation of free electrons at a resonant frequency, it is defined as localized surface plasmon (LSP).

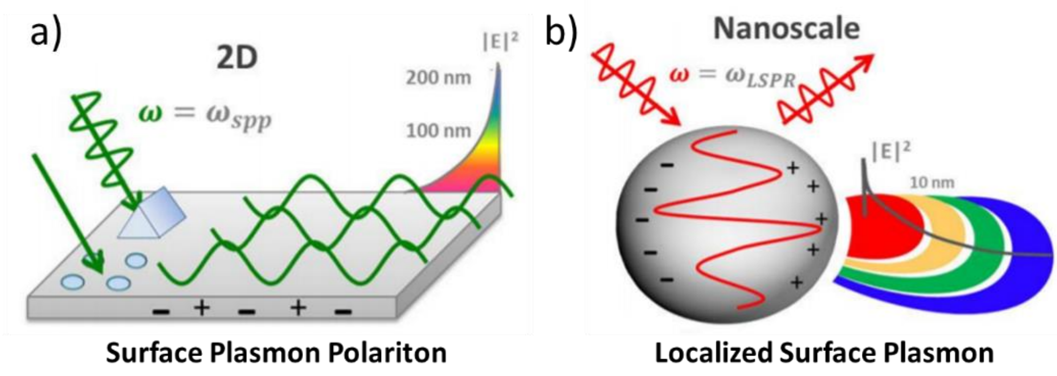

Surface Plasmon Polariton **Localized Surface Plasmon**

Figure 2.1 Schematic representation of (a) surface plasmon polariton, and (b) localized surface plasmon resonance. This figure is adapted from ref.[65].

2.1.1.2 Localized surface plasmon resonance

Once LSPs interact with an incident light bearing the same frequency as LSRs, the oscillation of electrons is extremely enhanced, resulting in an enhancement of local electromagnetic field and in the formation of an intense surface plasmon absorption band. This phenomenon is known as localized surface plasmon resonance (LSPR). The position of a LSPR absorption band is related to the surrounding medium. In principle, increasing the refractive index of the surrounding medium will lead to a redshift in absorption spectra (Figure 2.2a).[66] Thanks to this sensitivity to the environment, LSPR is widely applied in sensing applications. On the other hand, changing the size of nano-object can also modulate the wavelength of the LSPR band. Precisely, smaller nanospheres usually display a blue-shifted LSPR band compared to larger particles (Figure 2.2b).[66]

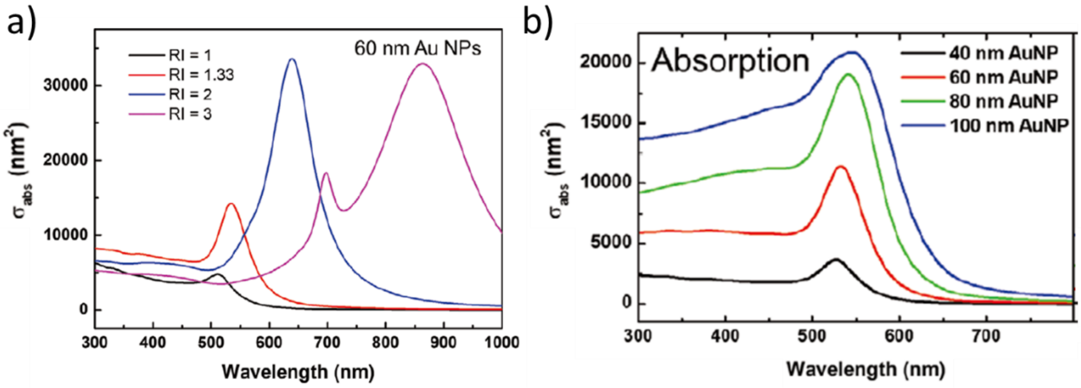

Figure 2.2 (a) Absorption spectra of 60 nm gold nanoparticles (AuNPs) in medium with different refractive indices (RI); (b) Absorption spectra of AuNPs in water with diameter of 40, 60, 80, and 100 nm. This figure is adapted from ref.[66].

As the polarization of electrons is isotropic in metal nanospeheres, only one LSPR band is observed. However, in an anisotropic nanoparticle, multiple LSPR bands may appear at different wavelengths. For example, in a gold nanorod (GNR) the polarization of electrons takes place along longitudinal and transverse directions, showing LSPR bands at wavelength of ~800 and ~500 nm, respectively.[67]

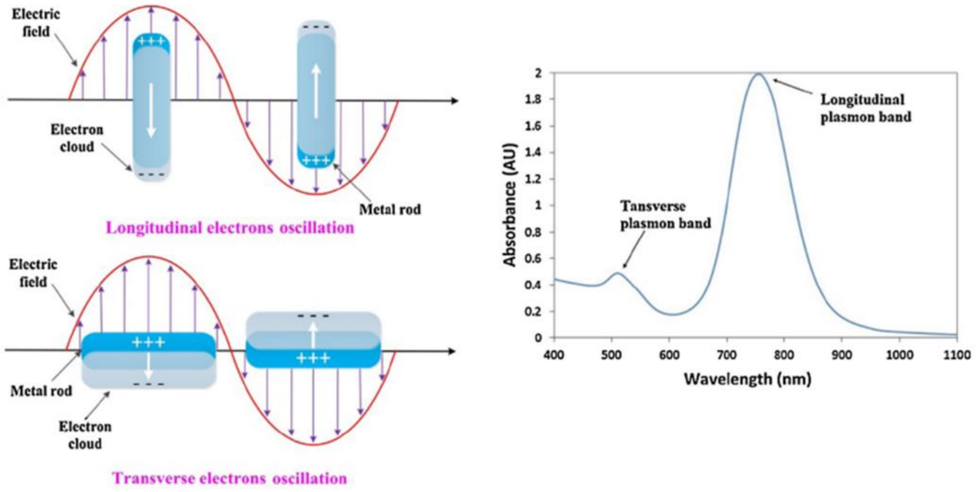

Figure 2.3 Schematic representation of longitudinal and transverse electrons oscillation in GNRs and related LSPR absorption bands. This figure is adapted from ref.[67].

2.1.1.3 Plasmonic nanoparticles

Metals

Conventional plasmonic nanoparticles are made of noble metals, owing to direct current (DC) conductivity and small ohmic losses.[68] For instance gold, silver, copper, and their alloys, display LSPR in the UV and visible region. Among these metals, gold shows high chemical stability and resistance to oxidization. Hence, AuNPs are commonly studied in diverse applications. As silver nanoparticles (AgNPs) owe higher sensitivity to refractive index, they are popularly used in practical sensing applications. With the advances in plasmonic nanoparticles, several drawbacks in metal NPs limit the application in certain fields. For instance, the losses originating from interband transition at optical frequencies and the fixed permittivity of metals limit their functional performance in optical devices.[68] To overcome these disadvantages, alternative materials with LSPR properties have been explored and developed.

Semiconductors

In comparison to noble metals, LSPR materials made of semiconductor (e. g. degenerately doped metal chalcogenides and metal oxide nanocrystals) show relatively lower electron densities (10^{19}-10^{21} cm^{-3}). As a result, LSPR bands in semiconductors are usually located in the NIR or MIR region. However, as the electron density of semiconductors is tunable by controlling doping levels, localization of the LSPR band can be modulated. For example, metal chalcogenides as *p*-type semiconductors are intrinsically doped with Cu (cation) vacancies, which concentration can be regulated by redox or cation exchange methods, leading to shift of LSPR band. Pioneering research on plasmonic property in metal chalcogenides is reported by Durda and coworkers in 2009.[69] This work illustrates how the concentration of charge carriers affect LSPR band. By employing different chemical methods, three $Cu_{2-x}S$ (x = 1, 0.2, 0.03) (Figure 2.4a) nanocrystals with different copper vacancies (holes concentration) were synthesized. By increasing x from 0.03 to 1 a blueshift of the LSPR band occurs (Figure 2.4b). Shortly afterwards, Alivisatos and coworkers demonstrated that the LSPR band is dependent on the size of doped $Cu_{2-x}S$ semiconductors (Figure 2.4c),[70] i.e. increasing the size leads to a redshift of the LSPR band. The group of Feldmann further found that this LSPR behavior exists in the entire family of metal chalcogenides (S, Se, and Te).[71]

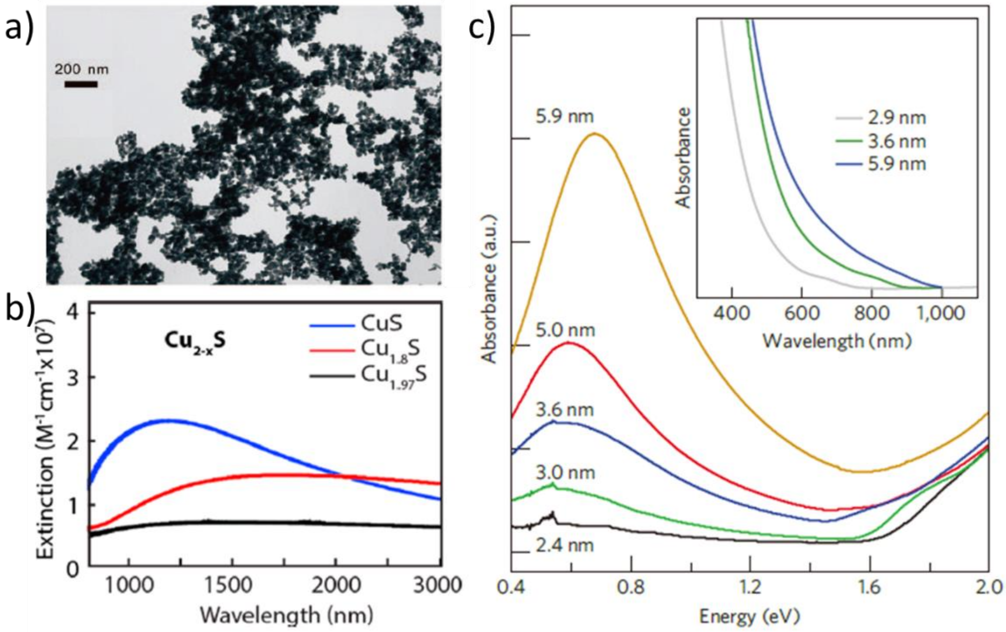

Figure 2.4 LSPR in metal chalcogenides nanoparticles. (a) TEM image of CuS nanospheres. (b) Extinction spectra of $Cu_{2-x}S$ for x = 1, 0.2 and 0.3. (c) Absorbance spectra of $Cu_{2-x}S$ for different sizes. This figure is reproduced from ref.[69,70].

Organic conductive polymers

For a long time, the possibility of using organic materials to fabricate plasmonic nanoparticles was discussed and explored. However, due to the low charge carrier density and difficulties in preparing organic nanoparticles, it has remained a challenging task. Very recently, the research group of Jonsson achieved this goal by using poly(3,4-ethylenedioxythiophene:sulfate) (PEDOT:Sulf), which is a conductive polymer presenting a metallic character and a high electrical conductivity of 5000 $S\cdot cm^{-1}$.[72] Simulation of the extinction spectrum of a nanodisk made of PEDOT:Sulf with a diameter of 500 nm and a thickness of 30 nm shows a LSPR band at 2.9 µm, which is absent in amorphous thin film (Figure 2.5c). In addition, simulation of the optical near-field profile revealed that such unique spectral band in the nanodisk arises from dipolar mode, which leads to field enhancement on the opposite edges of nanodisk (Figure 2.5b). Subsequently, three PEDOT:Sulf arrays containing nanodisks with different sizes were fabricated via top-down colloidal lithographic technique. As presented in Figure 2.5d, increasing the diameter of nanodisks leads to a redshift of the extinction band, indicating the LSPR behavior of these organic nanoparticles.

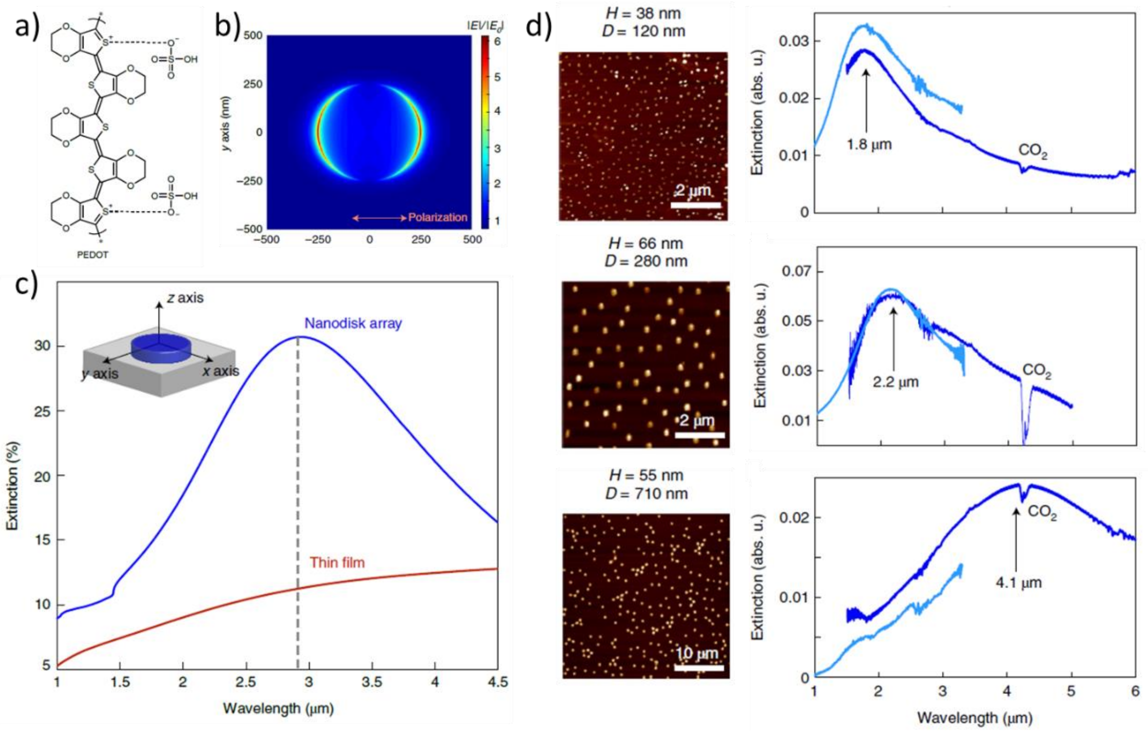

Figure 2.5 (a) Chemical structure of PEDOT:Sulf; (b) Simulated optical near-field profile at the wavelength of 2.9 µm; (c) Simulated optical extinction spectrum of a thin film and a nanodisk array made of PEDOT:Sulf; (d) AFM images of three arrays containing nanodisks with different sizes, and corresponding experimental extinction spectra. This figure is adapted from ref.[72].

Intriguingly, the permittivity of these nanodisks can be modulated reversibly via chemical oxido-reduction using either PEI vapor or H_2SO_4, allowing the LSPR character to be switched on and off on-demand. As detailed in Figure 2.6a-c, upon exposure to PEI vapor, charged PEDOT:Sulf nanodisks are reduced to neutral PEDOT, leading to the disappearance of the LSPR band at 1.9 µm. Further reoxidation with H_2SO_4 results in a recovery of LSPR band due to the reappearance of polaronic charge carriers. As the first example of organic plasmonic nanoparticles, this research opens the door to dynamically shape light at nanoscale by using organic materials.

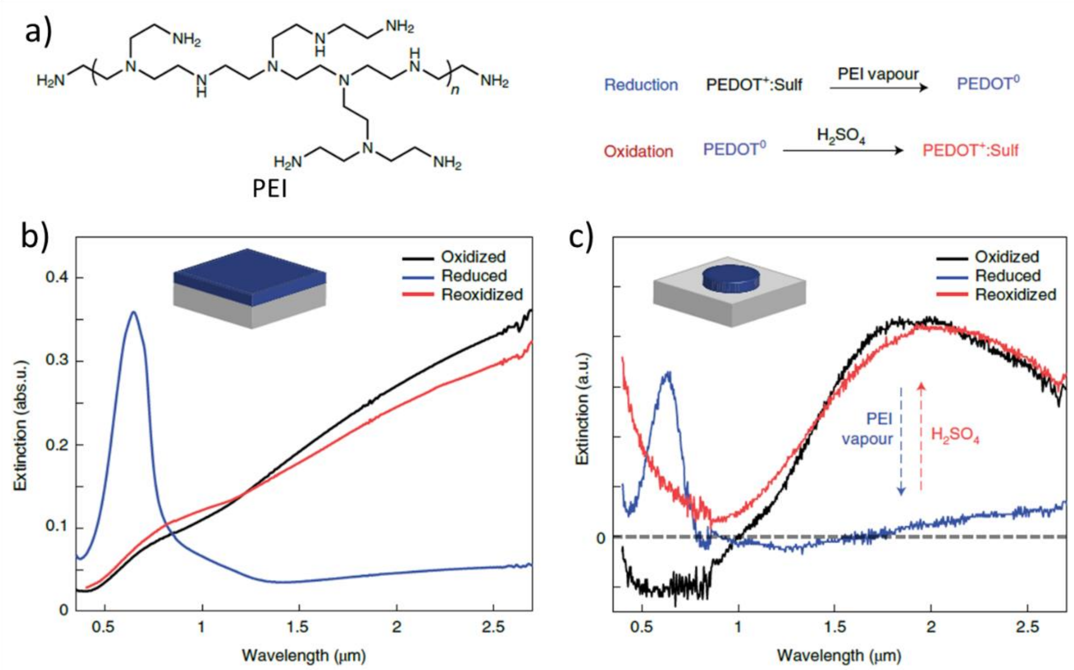

Figure 2.6 (a) Chemical structure of PEI and redox processes of PEDOT:Sulf; (b) Extinction spectra of a PEDOT:Sulf film at different redox state; (c) Extinction spectra of a PEDOT:Sulf nanodisk array at different redox state.

2.1.1.4 Plasmonic coupling

Besides morphology, composition, size, density of charge carriers, and surrounding medium, the inter-particle distance can also dictate LSPR behavior. Precisely, when nanoparticles are in close proximity, free electrons are simply not localized over individual nanoparticles, but delocalized between adjacent nanoparticles. As a result of delocalization, plasmon oscillations of the nanoparticles become coupled through near-field interaction, leading to a redshift of the LSPR (Figure 2.7a), leading to a so-called plasmonic coupling. In this case, the classical electromagnetic theory is not applicable to plasmon resonance mode. To visualize the plasmonic coupling, a plasmon hybridization model was developed, by analogy with the hybridization of atomic orbitals in molecules.[73,74,75] When two nanospheres are closed to each other, the plasmon modes hybridize to form lower energy ‘bonding’ and higher energy ‘antibonding’ coupling modes (Figure 2.7b).[73] In all modes, the out-phase coupling is optically disfavored due to the cancellation of the oppositely oriented dipole moments. Thus, along the direction of the dimer axis, a stable in-phase bonding mode is favored, which explains why a redshift of the LSPR band occurs when decreasing interparticle distance.

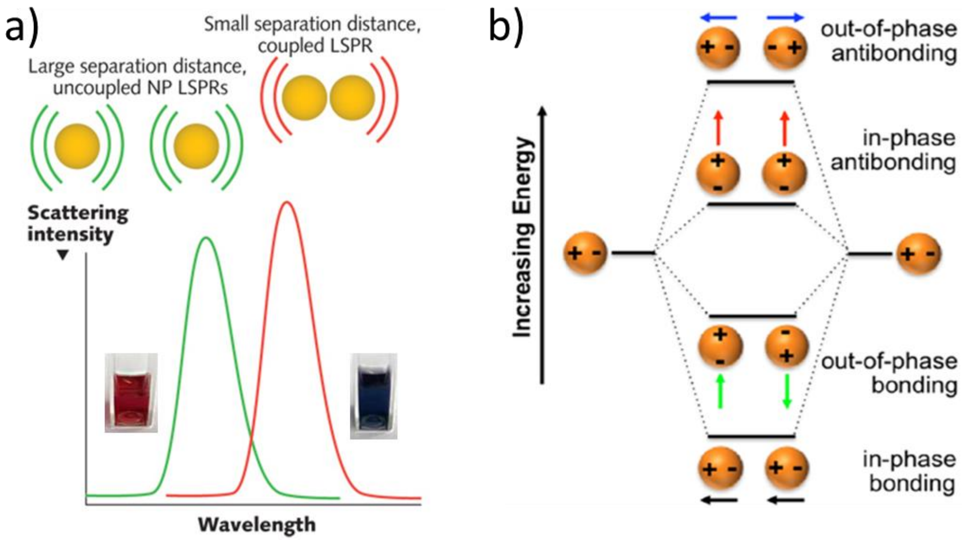

Figure 2.7 (a) Schematic representation of scattering or absorption spectra of individual particles and aggregated particles, insets are photographs of individual AuNPs (red color) and aggregated AuNPs (blue color) solutions; (b) Scheme of the plasmon hybridization model of a symmetric dimer, depicting in-phase/out-of-phase bonding/antibonding combinations of dipole moments. Arrows in the scheme indicate the dipole moments of each individual particles. The figure is adapted from ref.[73].

Experimental studies demonstrate that subtle changes in interparticle distance could result in significant shifts of LSPR bands. In 2007, based on the universal scaling behavior of distance decay of plasmonic coupling, the research group of EI-Sayed proposed a “plasmon ruler equation”.[76] By using electron beam lithography, arrays of gold nanodisk pairs with varying interparticle distance from 2 to 212 nm were obtained (Figure 2.8a). Each nanodisk pair was illuminated by an incident light with opposite polarization directions, either parallel or perpendicular to the interparticle axis. Along the parallel direction, LSPR band showed significant redshift with decreasing the interparticle distance (Figure 2.8b). In sharp contrast, the LSPR band at perpendicular direction slightly blueshifted when reducing interparticle distance (Figure 2.8c). These observations are in agreement with the above-mentioned plasmon hybridization model. Furthermore, they utilized discrete dipole approximation (DDA) method to simulate the LSPR spectra for nanoparticles with different sizes, shapes, and compositions, and then correlated the fractional plasmon shift and the gap/diameter ratio. As conclusion, the fractional plasmon shift for parallel polarization exponentially decays with increasing interparticle distance (Figure 2.8d). In addition, all decay constants are around 0.23. Finally, a plasmon ruler equation for gold nanoparticle pairs was derived:

$$\frac{\Delta\lambda}{\lambda_0} \approx 0.18\,\exp(\frac{-(s/D)}{0.23})$$

In which, $\Delta\lambda/\lambda_0$ is the fractional plasmon shift, s/D corresponds to the ratio of interparticle edge-

edge distance and particle diameter.

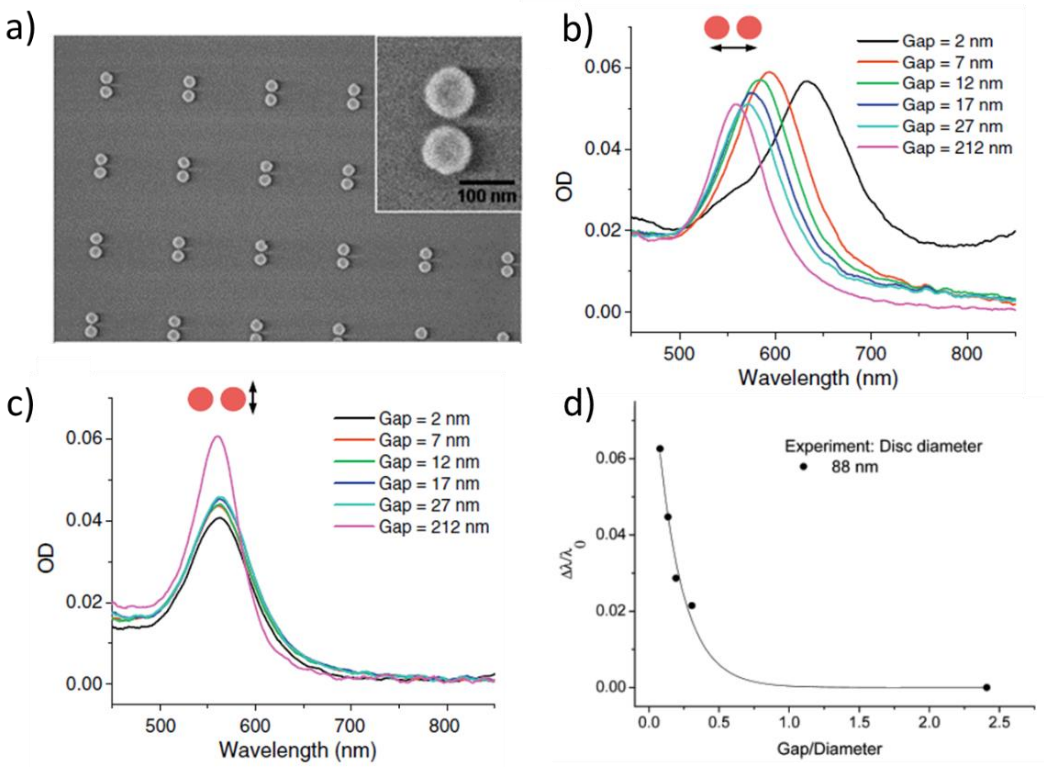

Figure 2.8 (a) SEM image of an array of nanodisk pairs; (b) Microabsorption spectra of gold nanodisk pairs for different interparticle distance using an incident light with a polarization direction parallel to the interparticle axis; (c) Microabsorption spectra of gold nanodisk pairs for different interparticle distance using an incident light with a polarization direction perpendicular to the interparticle axis; (d) Shift of LSPR band in a gold nanodisk pair as a function of the interparticle edge-to-edge distance. This figure is adapted from ref.[76].

Metallic plasmonic nanoparticles have been extensively studied and can enable advanced applications in optics, electronics, catalysis, energy, and biology due to their LSPR properties. However, the fabrication of plasmonic nanoparticles using small organic molecules still remains unexplored.

2.1.2 Conductivity and plasmonic property in triarylamine-based supramolecular polymers

2.1.2.1 Conductivity

As mentioned in the previous chapter, TAA derivatives in the amorphous state commonly present low conductivities, which can be efficiently enhanced by several orders of magnitude by chemical doping. Compared to the amorphous state, conductivities of oxidized TAA-based supramolecular polymers are also greatly enhanced by several orders of magnitude, as originally reported by our research group in 2012.[77] First, a metallic electrode with a nanotrench of 80 nm was immersed in a 1,1,2,2-tetrachloroethane solution of monoamide TAA (Figure 2.9a). In the dark, the trench was open thus exhibiting a very low conductance of nanosiemens (Figure 2.9e). Upon visible light irradiation, one electrode attracted the formed radical cations, initiating an elongation of the supramolecular polymers towards the other electrode, resulting in the bridge of the two separated electrodes by self-assembled nanowires. Thanks to the supramolecular closure of the trench, the conductance dramatically increased by six orders of magnitude (Figure 2.9e). Moreover, nanowires displayed a large conductivity of 5×10^{3} S·m^{-1} and a low interface resistance of 2×10^{-4} Ω·m (Figure 2.9f, g). Unexpectedly, the nanowires manifested a metallic character as determined by a decrease of the resistance value with lowering temperatures. Complementary studies conducted by the group of Sanvito, and relying on theoretical calculations, revealed the charge carrier mobility in our supramolecular nanowires ranges from 0.1 to 12 cm^{2} ·V^{-1}·s^{-1}.[78]

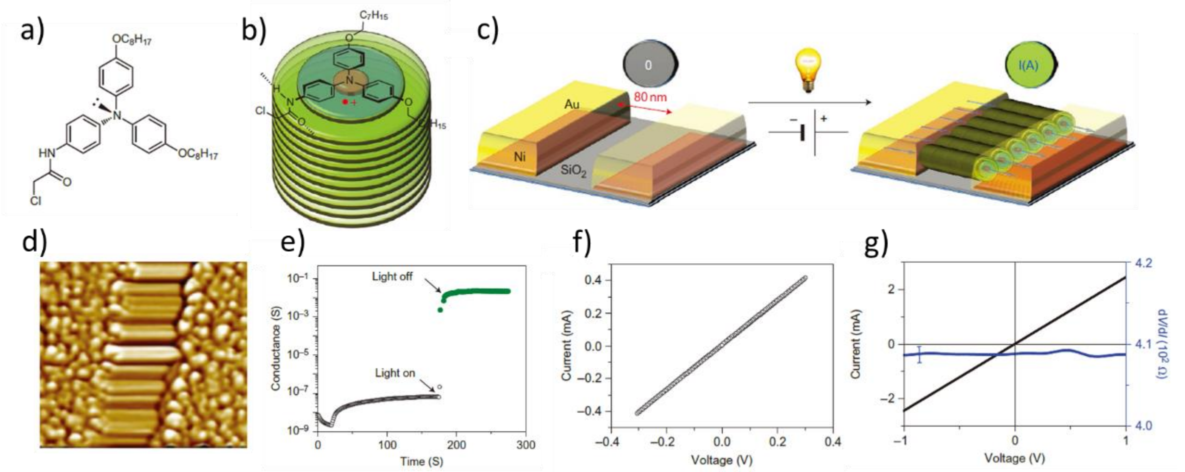

Figure 2.9 (a) Molecular structure of TAA; (b) Schematic representation of light induced self-assembled columnar fiber of TAA; (c) Schematic representation of the light triggered self-assembly process in a nanotrench; (d) AFM image of a nanotrench filled with self-assembled nanowires after light irradiation; (e) Conductance of a nanotrench immersed in a TAA solution in the dark and after light irradiation (over 10s); (f) current-voltage curve measurement on nanotrench filled with oxidized supramolecular nanowires; (g) *I-V* curve measurement performed at 4K and under atmospheric pressure, on nanotrench bridged with nanowires. This figure is adapted from ref.[77].

The metallic behavior was also observed in TATA-based supramolecular polymers.[36,79,80] For instance, a film made of irradiated TATA **1** (Figure 2.10a, b) showed metallic signature as evidenced by a minimum reflectance at a value around 1000 nm, which was previously observed for the conducting conjugated polymers (Figure 2.10c).[36] Resistance and *I*-*V* curve measurements suggest that light irradiation is mandatory to give rise to conducting nanowires. Combining UV-Vis with EPR experiments suggested that the nature of charge carriers in this system is supramolecular polarons that are through-space delocalized over stacked TAA.

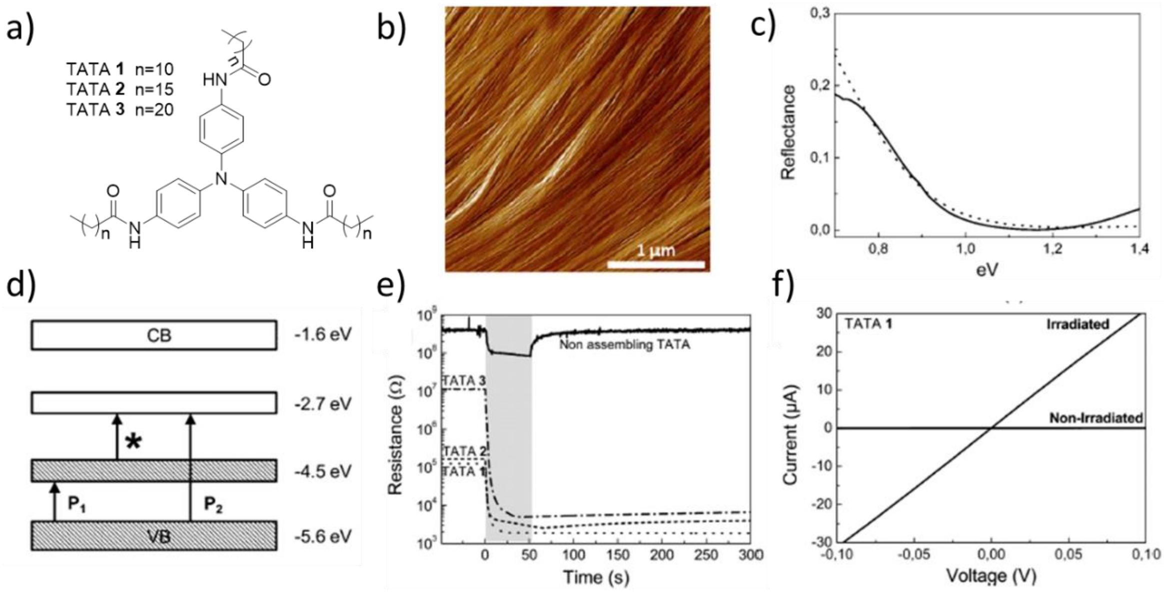

Figure 2.10 (a) Molecular structures of TATA **1**, TATA **2** and TATA **3**; (b) AFM image of self-assembled TATA **1**; (c) Reflectance measured for an irradiated film of TATA **1** (black line), and theoretical fit of the reflectance with the Drude model (dotted line); (d) Energy band diagram of self-assembled TATA **1**; (e) Resistance of sample TATAs as a function of time (gray area represents light irradiation time); (f) *I*-*V* curve measurements of TATA **1** with and without irradiation. This figure is adapted from ref.[36].

2.1.2.2 Plasmonic property

Thanks to the presence of supramolecular polarons, supramolecular polymers of TAA derivatives have been considered as promising materials with plasmonic properties. In 2016, our group demonstrated TAA-based supramolecular polymer can serve as plasmonic interconnects.[79] In the study, TATA terminated with thiol groups TATA-SH was synthesized (Figure 2.11a), and used to cap gold nanoclusters (Figure 2.11b(ii)). The array was then immersed in a chloroform solution of TATA, and then irradiated with visible light for 10 minutes. Subsequent incubation for 1 day resulted in the connection of clusters by supramolecular nanowires (Figure 2.11b(iii)). In this case, hot electrons-holes between nanoclusters and conducting nanowires are coupled, and the excited electrons in gold clusters can migrate to other clusters via the half-filled polaronic band of the TATA supramolecular nanowires, leading to a great enhancement in optical conductivity (Figure 2.11c).

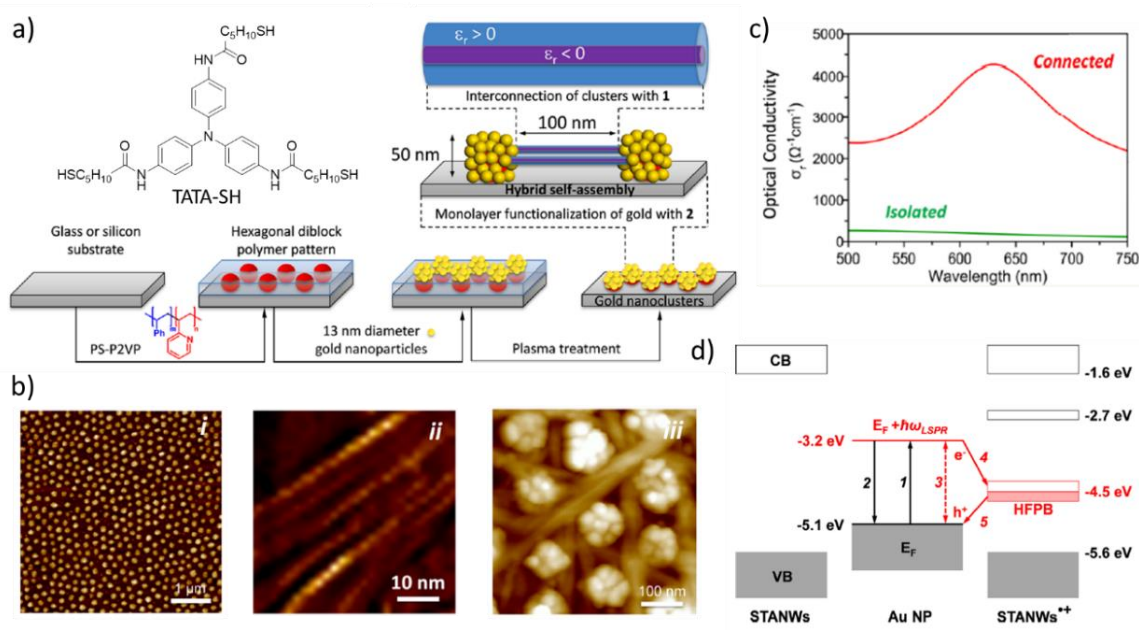

Figure 2.11 (a) Molecular structure of TATA-SH and schematic representation of construction of connected gold nanoclusters array; (b) AFM images of (i) isolated nanoclusters array, (ii) self-assembled TATA single columns and (iii) connected nanoclusters array; (c) Optical conductivity of gold nanoclusters array in the absence (green) and the presence of TATA supramolecular polymers (red); (d) Energetic diagram in neutral supramolecular nanowires, gold nanoclusters and photo-doped supramolecular nanowires. This figure is adapted from ref.[79].

The same year, our group achieved long-range energy transport via plasmonic propagation in TATA-based rigid supramolecular structures.[80] As shown in Figure 2.12c, transparent single crystals of triarylamine trisacetamide (TATA-Ac) were obtained by a differential evaporation method. Afterwards the crystals were oxidized by light irradiation in a suspension of chloroform. Similar to above examples, a film made of oxidized crystals showed three absorption bands at 0.80, 2.17, and 2.74 eV, indicating the presence of supramolecular polarons (metallic signature) (Figure 2.12d). Interestingly, the crystal can transport light with a wavelength of 532 or 785 nm, and it is strongly dependent on the irradiation position of laser. More precisely, only when the laser is positioned at the tip of the crystal, light transport is possible. This observation is against the light transport in luminescent waveguides, which are unselective to the laser position. Taking into account the metallic character of our oxidized crystals, we concluded that the light transport in our system is achieved via plasmonic propagation mechanism, in which the supramolecular polarons couple with incident light and further propagate along crystals. The hypothesis was then thoroughly verified by fluorescence bleaching experiments, from which one can see that the oxidized crystals can transport light, while neutral ones cannot.

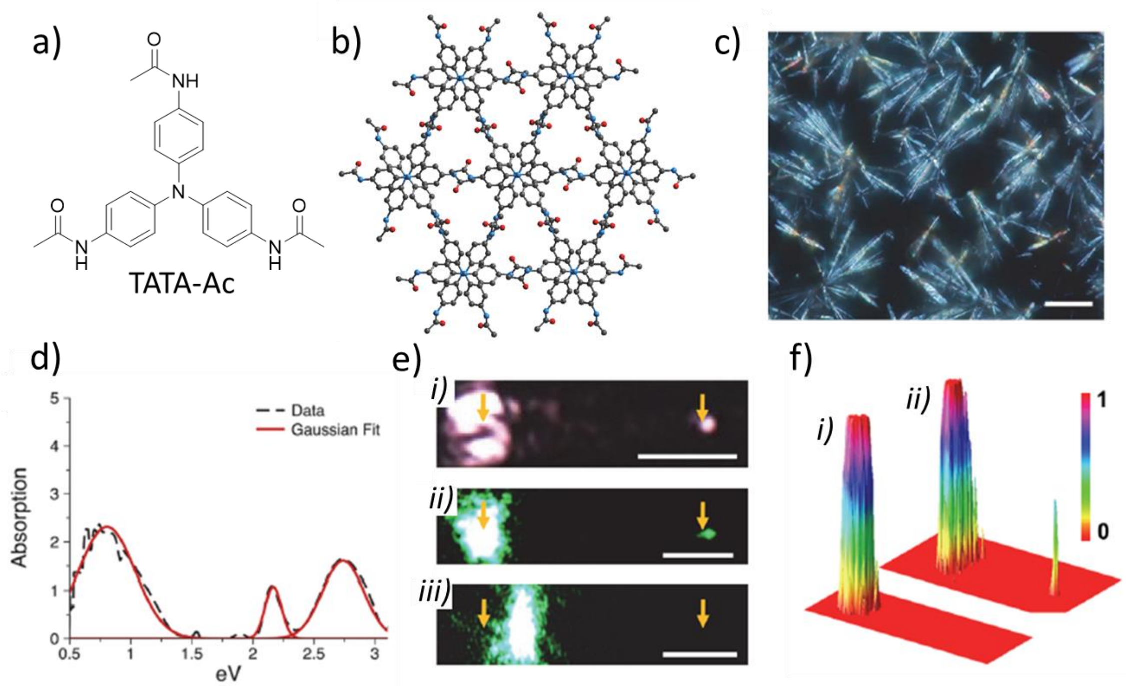

Figure 2.12 (a) Molecular structure of TATA-Ac; (b) Single crystal structures of TATA-Ac; (c) Single crystals observed under crossed polarizers (scale bar=20 µm); (d) Absorption spectrum measured on oxidized crystals and corresponding Gaussian fitting curve; (e) Optical waveguide tests with an incident 785 nm (*i*) or 532 nm (*ii*, *iii*) laser positioned at the tip (*i*, *ii*) or on top (*iii*) of the crystal ; (f) Three dimensional images of light propagation in (*i*) non-oxidized and (*ii*) oxidized single crystals covered with indocyanine dye. This figure is adapted from ref.[80].

2.2 Triarylamine-based plasmonic nanoparticles

2.2.1 Objectives

Manipulating light ranging from UV to NIR region with matters at nanoscale is of great interest in diverse areas such as sensors,[81,82] catalysis,[83,84] biological therapy,[85,86] and material science.[87,88] Till today, such nanomaterials are mainly developed from noble metals and metallic semiconductors. Although organic conducting polymer (PEDOT:Sulf) was reported to be an alternative material, such strategy still keeps being unexplored and it remains of high importance to enrich the family of organic plamonics with other organic materials. As presented in the previous section, our research group has demonstrated the metallic character of self-assembled TAA supramolecular structures. In particular, supramolecular polarons in oxidized single crystals can couple and transport incident light along the nanostructures via plasmonic propagation. Based on this study,[80] we plan to use triarylamine trisacetamide (TATA-Ac) to fabricate supramolecular nanoparticles, and we envisioned that, upon photo-oxidation, the nanoparticles could display LSPR behaviour.

2.2.2 Synthesis

Target molecule TATA-Ac was synthesized according to the protocol previously described in the literature.[80] Starting from compound **5**, palladium-catalyzed reduction of nitro groups afforded the intermediate **10** with 45% yield. Afterwards, compound **10** was engaged in an acylation reaction with acetyl chloride providing TATA-Ac **11** in moderate yield.

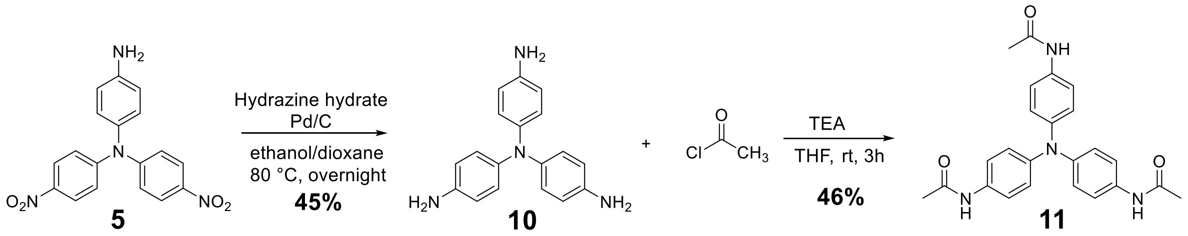

Scheme 2.1 Synthetic route for triarylamine trisamide TATA-Ac **11**.

2.2.3 Photo-oxidation property

As the objective of this project is to determine whether a LSPR behaviour exists in oxidized TATA-Ac nanoparticles, we first investigated the photo-oxidation behaviour of TATA-Ac by ^{1}H NMR spectroscopy (Figure 2.13). A 0.5 mM solution of TATA-Ac in a deuterated methanol:chloroform (1:3) mixture was prepared. Upon exposure of this solution to visible light for 10 minutes, we observed the disappearance of signals corresponding to aromatic and acetamide protons H_a, H_b, and H_c, a phenomenon consistent with our previous studies, which suggests the formation of TATA-Ac radical cations.

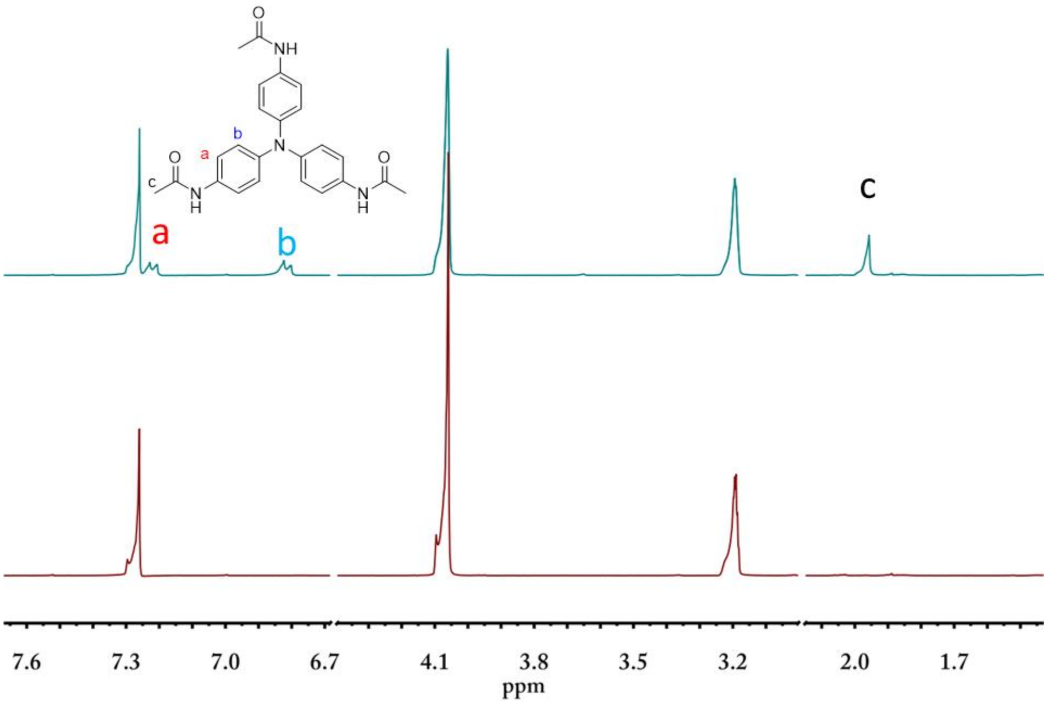

Figure 2.13 ^1H NMR spectra of TATA-Ac **11** in a 3:1 $CDCl_3$:CD_3OD mixture before (top) and after (bottom) visible light irradiation (10 minutes).

Subsequently, we carried out UV-Vis spectroscopy to study the photophysical properties of TATA-Ac **11** in a methanol:chloroform (1:3) mixture. As shown in Figure 2.14a, the UV-Vis spectra as function of irradiation time were recorded. Before visible light irradiation, there is no absorption band observed from 400 to 1000 nm, suggesting the absence of radical cations. However, upon exposure to visible light for 5 minutes, the solution turned from colourless to green and absorption bands at 400 nm, 470 nm, 680 nm, and 840 nm appeared, which are indicative of the formation of radical cations. The absorption bands at 400 nm is attributed to π-π stacking of formed TATA-Ac radical cations. The bands at 680 nm and 840 nm are spectral signature of TATA radicals that are delocalized over the entire π-conjugated skeleton. The absorption band at 470 nm, which was not observed before in other oxidized individual or self-assembled TATA motifs, might stem from Davydov splitting in crystals.[80] Davydov splitting refers to the red-shifted absorption transition due to the splitting of excited state energy levels in *J*-aggregates.[89] From 0 to 20 minutes, the absorption intensities of these four bands continuously increased. However, after 20 minutes, subsequent irradiation led to a decrease in intensities at wavelengths of 680 nm and 840 nm. The decrease can be explained by the recombination of radical cations once radical concentration is up to a certain value.

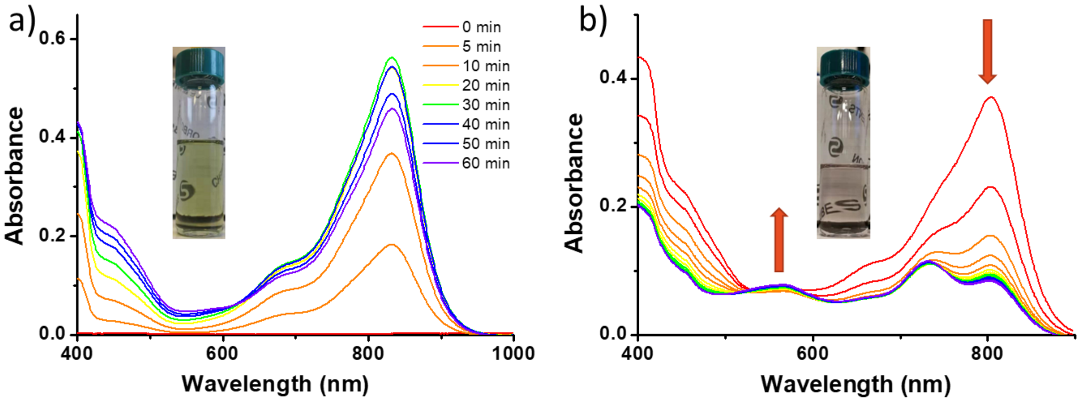

Figure 2.14 (a) UV-Vis spectra of a TATA-Ac solution (0.01 mM, methanol:chloroform (1:3)) as a function of an irradiation time, the inset is photograph of TATA-Ac solution after 1 hour irradiation; (b) Evolution of UV-Vis spectra of irradiated TATA-Ac solution in the dark for 14 hours. Inset shows photograph of TATA-Ac solution after 14 hours under dark.

After 1 hour irradiation, the stability of TATA-Ac radical cations was investigated by recording UV-Vis spectrum over time in the dark. As presented in Figure 2.14b, as time goes on, absorption intensities at 400 nm, 470 nm, 680 nm, and 840 nm keep going down, which indicates a decay of the number of radicals. In sharp contrast, a new absorption band at 566 nm emerges, and its intensity increases gradually. After 14 hours, the solution turned from green to pink, a colour similar to that of plamonic gold nanoparticles (LSPR band at 530 nm). These observations might be explained by the formation of plasmonic TATA-Ac self-assemblies.

The photo-oxidation of TATA-Ac was also studied by EPR spectroscopy. As shown in Figure 2.15, applying visible light irradiation led to the appearance of a three-line patterned signal, characteristic of unpaired electrons localized on nitrogen atom centers. Its intensity increased over time, and reached maximum after 20 minutes, which is slightly faster than what was observed by UV-Vis spectroscopy (Figure 2.14a). Similar to the observations by UV-Vis, subsequent irradiation resulted in quenching of radicals. Using a (2,2,6,6-Tetramethylpiperidin-1-yl)oxyl (TEMPO) standard reference, we determined that the maximum radical cation content in an irradiated TATA-Ac solution is around 4 percent, which subsequently decreased down to 0.4 percent after 45 minutes in the dark (Figure 2.15, 20+40*).

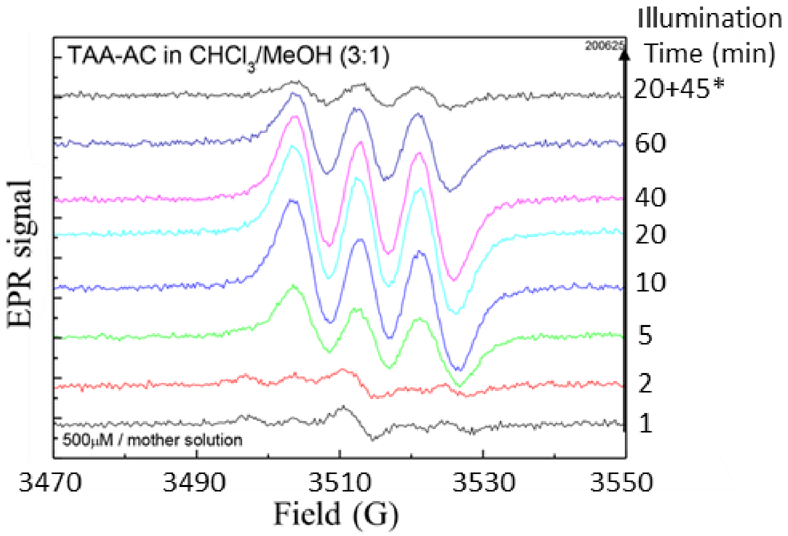

Figure 2.15 Time-dependent EPR spectra of a 0.5 mM TATA-Ac solution in chloroform:methanol (3:1) during visible light irradiation.

2.2.4 Preparation and characterization of TATA-Ac nanoparticles

The photo-oxidation of TATA-Ac, particularly the emergence of an absorption peak at 566 nm, encouraged us to look for plamonic properties in our supramolecular nanoparticles. The fabrication of nanoparticles using TATA-Ac was explored by former PhD student in our research group, Dr Melodie Galerne. At beginning, top-down strategies were employed. First, she managed to grow small single crystals of TATA-Ac via the protocol reported by our group.[80] In addition, by slowly evaporating a 1.5 mM TATA-Ac methanol:ethyl acetate (5:95) mixture, larger single crystals were obtained. With these two crystals in hands, she prepared nanoparticles via tip sonication and grinding of crystals. However, both methods led to aggregation of nanoparticles with a relatively large size.

Nevertheless, we successfully managed to obtain well-dispersed TATA-Ac nanoparticles with an uniform size via a precipitation manner. First, a 0.5 mM mother solution was prepared by dissolving TATA-Ac in a chloroform:methanol (3:1) mixture, which was subsequently irradiated by visible light for 1 hour to generate radical cations. Owing to the high proportion of methanol, no self-assembled nanostructures are present in the freshly prepared mother solution. To obtain nanoparticles with varying sizes, we added 100 µL, 400 µL, and 1 mL of mother solution to 10 mL ethyl acetate, which resulted in nanoparticles with final concentrations of 5 µM, 20 µM, and 50 µM, respectively. To get an insight into the sizes of the formed nanoparticles, we initially performed SEM and TEM imaging experiments. As shown in Figure 2.16a and 2.16b, small nanoparticles were observed by TEM, accompanied by amorphous materials. Similar nanoparticles were found by SEM (Figure 2.16c and 2.16d), which are highly blurred due to the low contrast between the substrate and the nanoparticles. Thus, we could not determine the accurate size of our nanoparticles. We further performed DLS experiments with the solution of nanoparticles, but still did not get convincing results owing to limited concentrations.

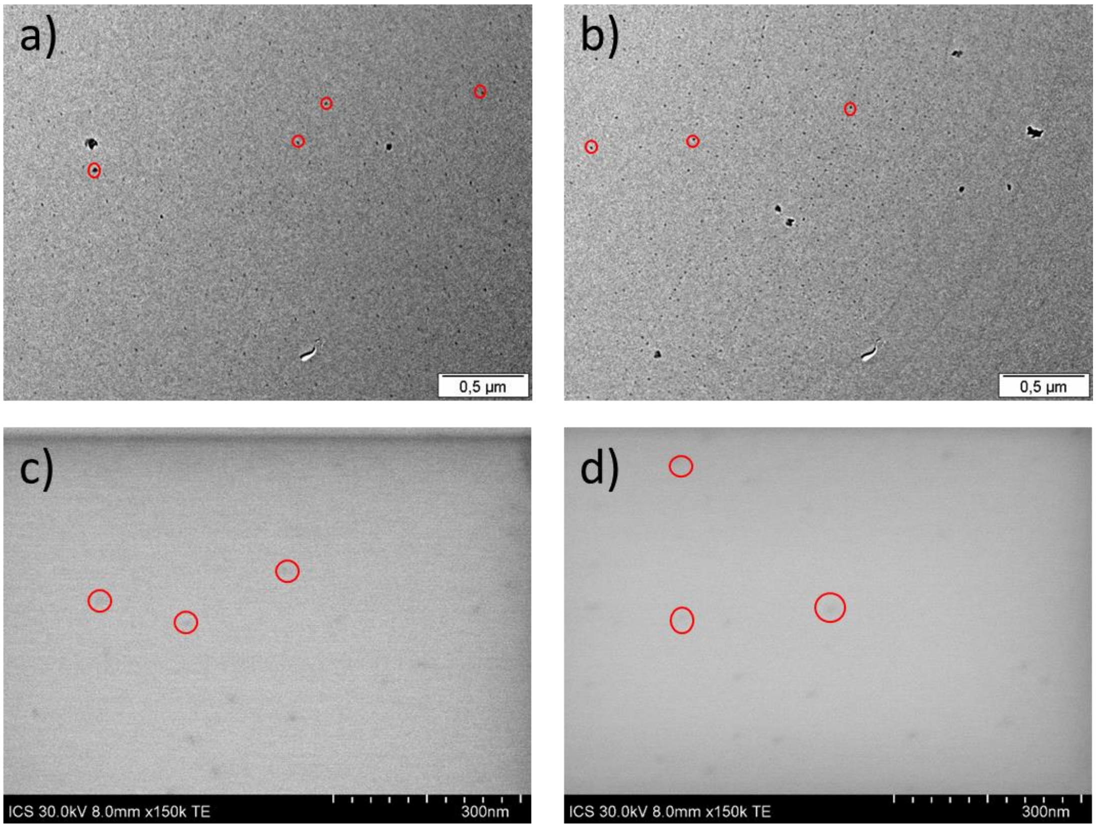

Figure 2.16 TEM images of TATA-Ac nanoparticles with concentrations of 5 µM (a), and 20 µM (b); SEM images of TATA-Ac nanoparticles with concentrations of 5 µM (c), and 20 µM (d).

Information on the sizes of nanoparticles was provided by AFM experiments. As presented in Figure 2.17a and 2.17b, solutions of 5 µM and 20 µM give well-dispersed and uniform nanoparticles with average sizes of 4.6 nm and 9.1 nm, respectively. Although the size distribution in 50 µM solution is relatively wide, the nanoparticles are obviously larger than that of 5 µM and 20 µM. The largest particles show 20 nm in height. These observations confirm that, by varying the volume of mother solution, nanoparticles with different sizes can be obtained after precipitation.

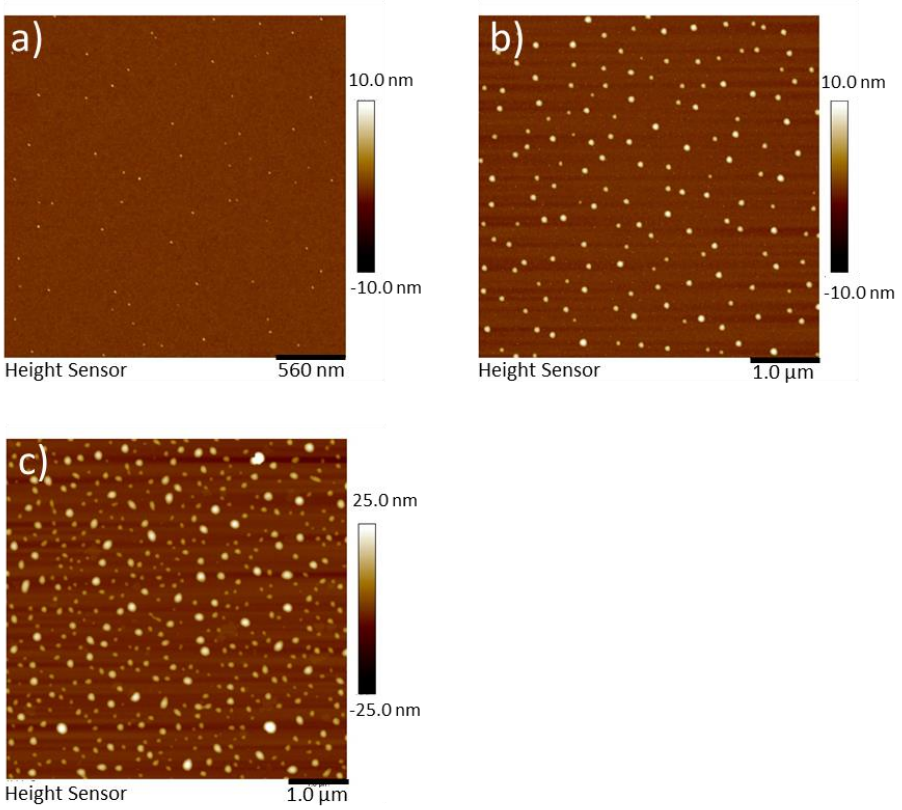

Figure 2.17 AFM images of TATA-Ac nanoparticles with concentrations of 5µM (a), 20 µM (b), and 50 µM (c).

As discussed in the bibliography section, an ordered nanostructure of TAA derivatives is mandatory to achieve high conductivity and plasmonic property. Thus, we carried out X-ray scattering experiments to investigate the structure of TATA-Ac nanoparticles. First, we prepared samples by dropping solutions onto silicon wafer, which were subsequently studied by grazing-incidence wide-angle X-ray scattering (GIWAXS). However, due to issues occurring during deposition, only limited signals were observed, precluding the possibility to get structural information. We then prepared a powder of nanoparticles by evaporating the solvent. Afterwards, the structure was investigated by SAXS and WAXS, from which we can establish whether or not TATA-Ac self-assemble into supramolecular structures. The X-ray scattering pattern shows well-defined peaks (Figure 2.18a), suggesting the crystalline nature of nanoparticles. To get a deep insight into the self-assembled structure, we compared the X-ray diffraction pattern with that of large single crystals obtained by Dr Melodie Galerne. As shown in Figure 2.18c, large single crystals present diffraction peak ratios of 1, $3^{1/2}$, $4^{1/2}$, $7^{1/2}$, $9^{1/2}$, *etc*., indicating a hexagonal packing system (Figure 2.18b). In addition, the peak at 11.48 Å, as first diffraction peak, is considered as the distance between diffractive planes d_{100}. After calculation, one can see that the distance between nitrogen centers of two adjacent columns is 13.256 Å, which is identical with the value given by crystallographic structure (13.254 Å). Compared to these large single crystals, nanoparticles show more diffraction peaks, indicating the presence of multiple structures. In addition, nanoparticles did not show diffraction peak ratios corresponding to a hexagonal system, which might be ascribed to the lattice of torsion. In this case, the diffraction peak corresponding to 4.22 Å corresponds to the distance between two adjacent nitrogen centers in stacked column. Moreover, the strong diffraction peak corresponding to 13.49 Å can be attributed to the distance between nitrogen centers in two adjacent columns.

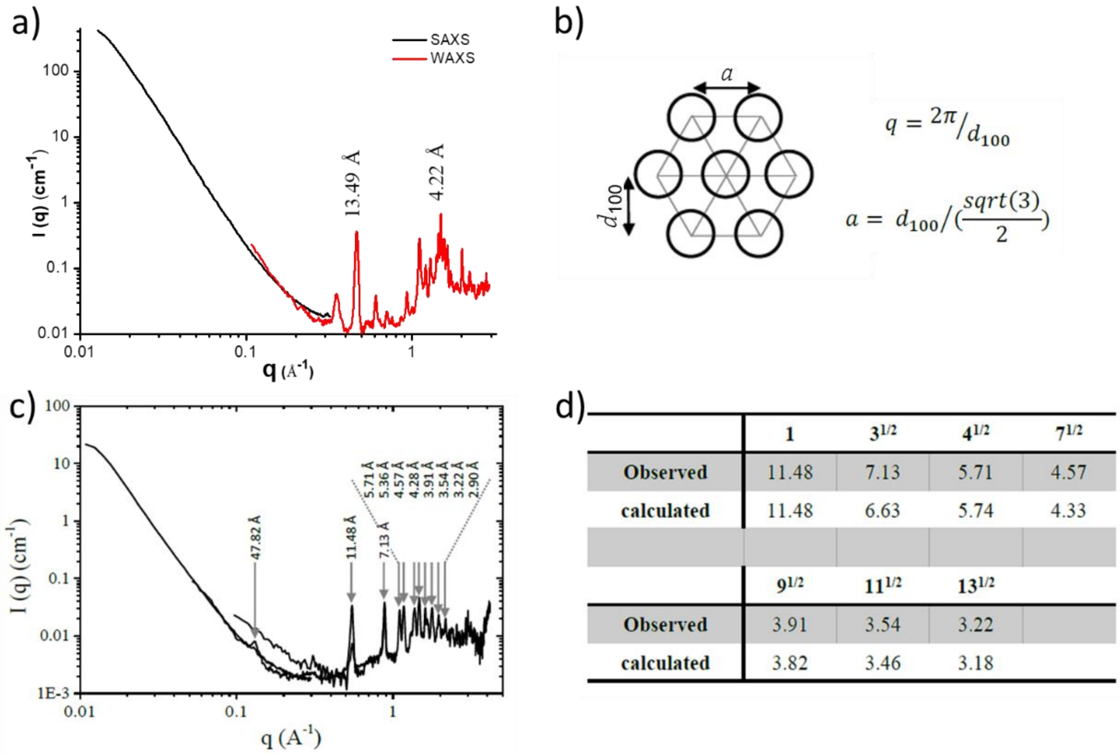

	1	**$3^{1/2}$**	**$4^{1/2}$**	**$7^{1/2}$**
Observed	11.48	7.13	5.71	4.57
calculated	11.48	6.63	5.74	4.33
	$9^{1/2}$	**$11^{1/2}$**	**$13^{1/2}$**	
Observed	3.91	3.54	3.22	
calculated	3.82	3.46	3.18	

Figure 2.18 (a) X-ray scattering spectrum obtained from the powder of TATA-Ac nanoparticles; (b) Schematic representation of a hexagonal packing system, and related equations; (c) X-ray scattering spectrum of the powder of large single crystals; (d) Table summarizing the observed and calculated distances between diffraction planes for a hexagonal system.

As the supramolecular nanoparticles are prepared from an oxidized mother solution of TATA-Ac, without subsequent photo-oxidation, we preliminarily performed UV-Vis spectroscopy with the solution of nanoparticles, aiming at observing a LSPR band. Absorption bands of nanoparticles with concentrations of 5 µM, 20 µM, and 50 µM emerge at 481 nm, 530 nm, and 540 nm, respectively (Figure 2.19a). It is noteworthy that these absorption bands are absent in the oxidized mother solution. Thus we cannot attribute these unusual absorption bands to the electronic transitions occurring in TAA-based supramolecular self-assemblies. More importantly, with increasing size of nanoparticles, a redshift of the absorption band occurs. This phenomenon is highly consistent with LSPR in plasmonic metal nanoparticles.

As the presence of charge carriers is a necessity for LSPR in plasmonic nanoparticles, as a control experiment, we prepared supramolecular nanoparticles (50 µM) from a non-irradiated mother solution, and subsequently recorded their UV-Vis spectra. As presented in Figure 2.19b, no absorption band is observed in these neutral nanoparticles. Upon irradiation for 1 hour, the oxidized nanoparticles show absorption bands at the wavelength of 560 nm, meaning that the absorption band arises from oxidized radical cations. To further quantify the radicals, EPR spectroscopy was carried out on the solution of irradiated nanoparticles. However, due to the concentration limitation, we did not obtain any relevant information. Moreover, we cannot concentrate the solution because, at higher concentration, nanoparticles tend to form into large aggregates.

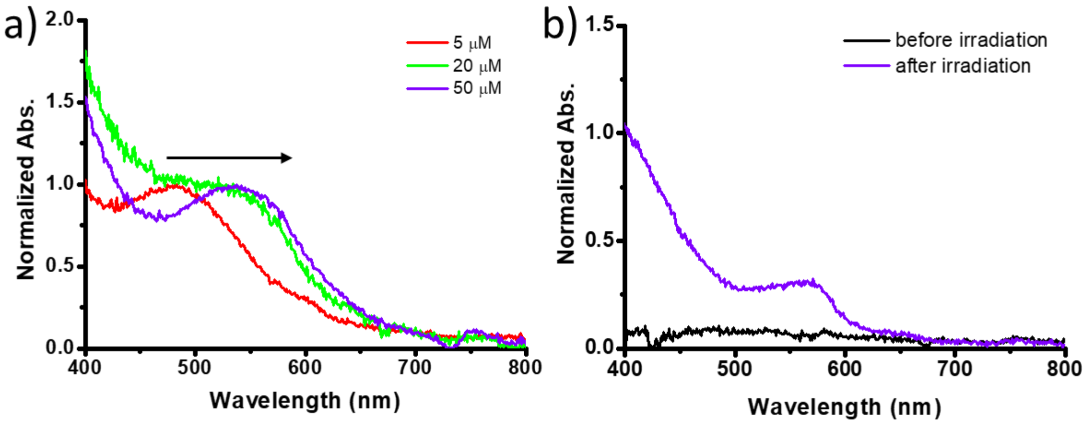

Figure 2.19 (a) UV-Vis spectra of TATA-Ac nanoparticles with concentrations of 5 µM (red), 20 µM (green), and 50 µM (purple); (b) UV-Vis spectra of nanoparticles (50 µM) before (black line) and after (purple line) visible light irradiation.

Electron energy loss spectroscopy (EELS) is a powerful characterization technique extensively used for plasmon detection.[90,91] Experimentally, an electron beam with known kinetic energies is applied to samples. The interaction between electrons of the beam and free electrons in the plasmonic materials leads to plasmon resonance. As a consequence, partial energies of electron beam will be lost, which corresponds to EELS spectrum. In general, the energy loss caused by plasmon excitation is located in low energy-loss region (< 50 eV). Moreover, the electron energy loss signal shift as a function of nanoparticles shape, size, and plasmonic coupling. For solid evidence supporting plasmonic property of our TATA-Ac nanoparticles, we initiated a collaboration with Dr Raul Arenal (University of Zaragoza) on EELS. At the time of writing, the experiment is ongoing.

2.2.5 Conclusion

In this project, we successfully synthesized triarylamine trisacetamide (TATA-Ac) with the objective to construct organic plasmonic nanoparticles. The photo-oxidation property of TATA-Ac was first confirmed. Upon visible light irradiation, we observed the formation of triarylamine radical cations, as evidenced by the disappearance of proton signals in ^{1}H NMR spectrum, the appearance of characteristic absorption bands and EPR signals. After several attempts, we managed to prepare triarylamine-based nanoparticles by precipitating the mother solution of oxidized TATA-Ac from ethyl acetate. Moreover, by regulating the volume of mother solution used for precipitation, the sizes of these nanoparticles can be well varied, which was determined by AFM imaging. X-ray scattering experiments on the powder of nanoparticles revealed a crystalline signature, demonstrating that nanoparticles are formed via hydrogen bonding and π-π stacking interactions between TATA-Ac. Thanks to the presence of radical cations, the oxidized nanoparticles showed unique absorption bands, which were absent in neutral nanoparticles. More importantly, a redshift of this absorption band occurred with increasing the size of our nanoparticles. Thus, we hypothesized that this optical behaviour might stem from the collective oscillation of positive charge carriers in response to light, namely, localized surface plasmon resonance (LSPR). To verify our hypothesis, a collaboration on electron energy loss spectroscopy (EELS) was initiated, and the related work is ongoing. Once the LSPR property is confirmed by EELS, this work will be the first example which achieves LPSR behaviour in supramolecular self-assembled organic nanoparticles.

Chapter III. Tunable Plasmonic Coupling in Motorized Gels

3.1 Artificial molecular motors

In 2016, three chemists, Jean-Pierre Sauvage, Sir J. Fraser Stoddart, and Bernard L. Feringa, were awarded Nobel Prize in chemistry for their pioneering contributions to the design and synthesis of molecular machines (Figure 3.1). Undoubtedly, this recognition fully demonstrates the promising future of molecular machines, and thus encourages more researchers to carry out academic research on artificial molecular machines (AMMs). For nearly thirty years, AMMs with structural complexity have been reported. According to conformational and operational features, AMMs are mainly categorized into two classes: 1) mechanically interlocked molecules (MIMs) including catenanes (Figure 3.1a) and rotaxanes (Figure 3.1b), in which multi-components are linked via mechanical bonds;[92,93,94] 2) molecular motors that can operate out-of-equilibrium under external energy input (Figure 3.1c).[95,96] In this section, molecular motors including development, operation mechanism, and applications up to the macroscopic scale will be briefly presented.

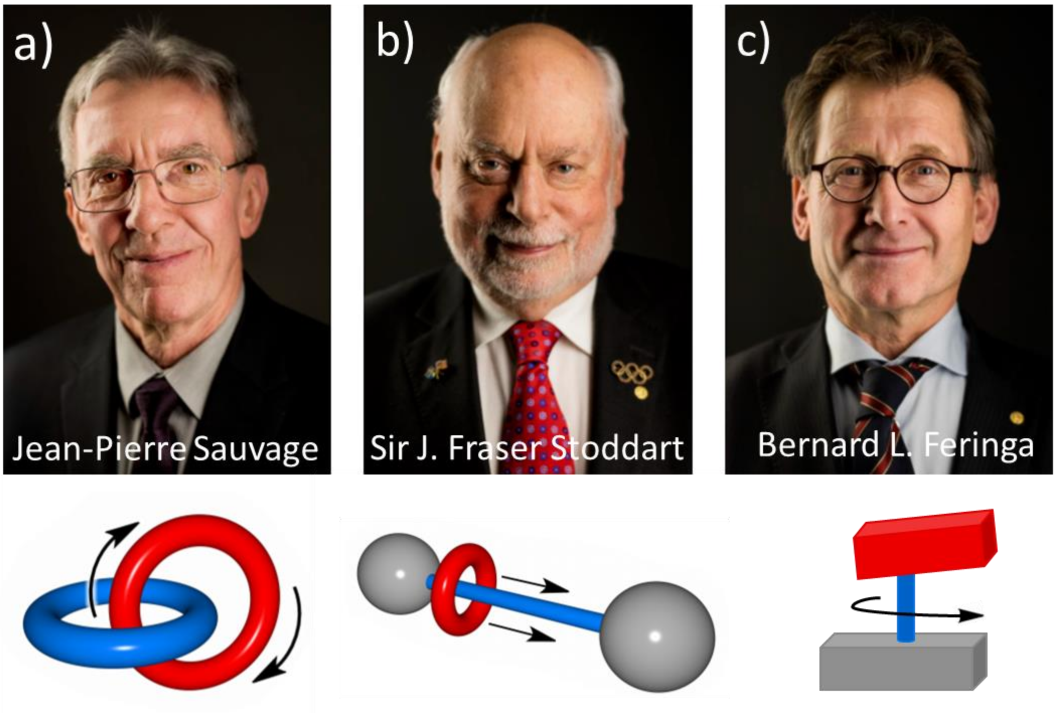

Figure 3.1 2016 Chemistry Nobel Prize winners a) Jean-Pierre Sauvage and a catenane, b) Sir J. Fraser Stoddart and a rotaxane, and c) Bernard L. Feringa and a molecular motor. This Figure is adapted from ref.[97].

In living organisms, molecular motors are ubiquitous, and play important roles in biological events. For example, protein motors involving kinesin, myosin, and dynein powered by ATP can perform mechanical work for muscle contraction and cargo transport.[98] Another impressive example is ATP synthase, as a typical rotary molecular motor, it harness the electrochemical potential energy of a gradient of ions to produce necessary energy (APT) for cellular processes.[99] Taking inspiration from nature, scientists have designed and synthesized artificial molecular motors that, in response to external stimuli, could perform unidirectional rotation and implement diverse tasks in various environment, such as organic solution,[100] aqueous media,[101] surface,[102,103] and confined space (e.g. organic frameworks, polymeric networks, membranes, etc.)[104,105].

Typically, artificial molecular motors can be classified into two types: 1) light driven molecular motors that rotate around a double bond (Figure 3.2a); and 2) chemically fueled molecular motors, in which the rotary motion is accomplished around single bond (Figure 3.2b).

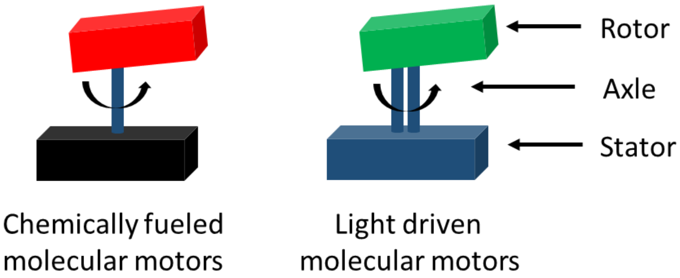

Figure 3.2 Schematic representation of two classes of rotary molecular motors.

3.1.1 Light-driven molecular motors

First generation molecular motors

The first light-driven molecular motor was reported by the research group of Feringa in 1999.[106] The molecular structure is shown in Figure 3.3a, the first generation molecular motor is based on an overcrowded alkene, in which two identical components are linked through a carbon-carbon double bond. The upper half as rotor implement the unidirectional rotation with respect to the lower half. A complete 360° rotation cycle consists of four successive steps, and each step results in a new isomer (Figure 3.3a). (*P*, *P*)-trans-**1** is the most stable among the four isomers due to its "strain-free" conformation, in which two naphthalene rings are away from each other and the methyl substituents adopt an energetically favored axial position. Upon UV light irradiation ($\lambda \geq 280$ nm), *trans-cis* photo-isomerization of (*P*, *P*)-trans-**1** as first step takes place.

In this process, two naphthalene rings are forced to be close, leading to a helix inversion (*P*, *P* → *M*, *M*). Meanwhile, two methyl substituents at stereogenic centers take the energy-unfavored equatorial conformation. As a result, the formed (*M*, *M*)-cis-**2** has a higher conformational strain. The second step is a thermal helix inversion (THI), through which the structural strain is relieved. Precisely, at 20°C one naphthalene ring flips over another one to form stable (*P*, *P*)-cis-**2**, in which the methyl substituents readopt an energetically favored axial orientation. Subsequent UV light irradiation induces the third step (photo-isomerization), resulting in the transformation of (*P*, *P*)-*cis*-**2** to (*M*, *M*)-trans-**1**. By heating at 60°C, (*M*, *M*)-trans-**1** returns to the (*P*, *P*)-trans-**1** via a second THI process. After these four steps, one 360° rotation cycle is completed.

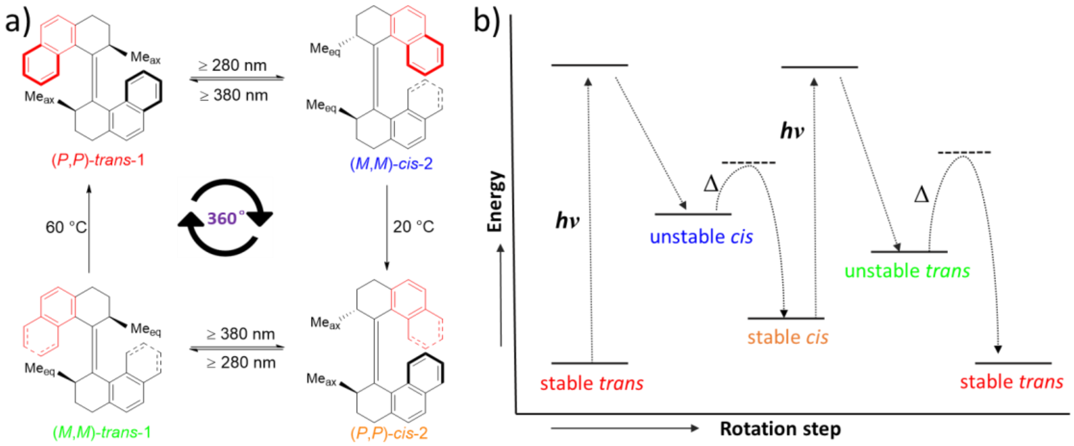

Figure 3.3 (a) Four-step unidirectional 360° rotation for first generation light-driven molecular motor; (b) Energy profile for one rotation cycle. The figure is reproduced from ref.[106].

It should be noted that the configuration of the stereogenic centers governs the conformational strain, thereby dictating the unidirectionality. In addition, the rotation direction is determined by the axial chirality of the stable motors. For instance, molecular motors with *M* helicity rotates in a clockwise direction, whereas *P* helicity results in counterclockwise rotation. To well understand such unidirectional rotation, the energy profile for the four-step 360° rotation is schematically depicted in Figure 3.3b. From the energetic point of view, *trans-cis* photo-isomerization leads to the reversal of configuration in methyl substituents, resulting in unstable isomers that are of higher energy levels. In sharp contrast, THI process forces methyl substituents to readopt an energy-favored axial conformation, affording stable isomers which can be excited again by light irradiation. In doing so, the molecular motor can continuously rotate as long as energy is supplied.

Second generation light-driven molecular motors

The discovery of unidirectional rotary motors opened tremendous opportunities in the development of nanodevices and artificial molecular machines. However, several drawbacks preclude the use of the first generation molecular motors for practical applications. Indeed, such molecular motors featuring two identical halves are difficult to functionalize selectively on their lower or upper half. On the other hand, the different activation energy of the two THI steps leads to the discordant rotation, which is unfavorable in systems performing work. These issues were resolved by the design of second generation light driven molecular motors proposed by Feringa and coworkers (Figure 3.4).[107] This newly designed molecular motor is still based on an overcrowded alkene, but it is composed of two distinct halves and only contains one stereogenic center. Similar to the first generation molecular motors, a complete unidirectional 360° rotation is accomplished through *trans*-*cis* photo-isomerization and THI processes. As anticipated, the two THI steps take place at the same temperature of 60°C. Noteworthily, in the example shown in Figure 3.4, the symmetry of the lower part is broken due to the presence of methoxy substituent, leading to difference in optical properties (absorption and circular dichroism) between the two stable states or the two unstable ones.

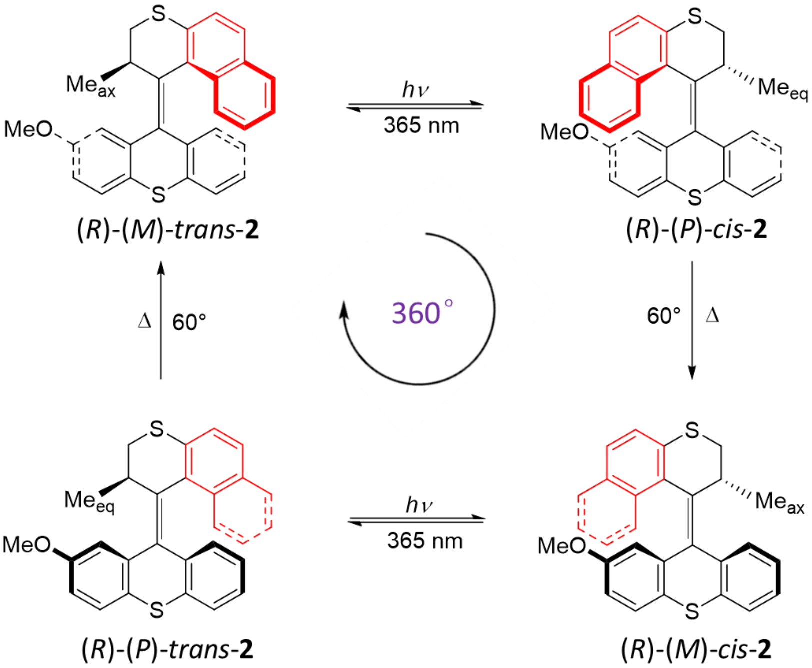

Figure 3.4 A complete 360° rotation for the second generation light-driven molecular motor. This figure is reproduced from ref.[107].

In biological systems, the rotation speed of molecular motors is very high. For example, the rotation speed of F1-ATPase is up to 130 revolutions per second, such high speed can sufficiently counter molecular collisions and vibrations.[108,109] In contrast, the speed in the first second generation molecular motor reported by Feringa is slow as each revolution takes around 400 hours at room temperature,[107] precluding the possibility to perform efficient work. To accelerate the rotation speed of molecular motors, Feringa's group studied the speed of each step. They showed that the photo-isomerization process is extremely fast (on the time scale of picoseconds), while the rate-determining step is the THI process.[110] Lowering the activation energy required for the THI process by varying the nature of bridging atoms, size of rings, substituents efficiently speed up the rotation of molecular motors.[111,112,113] In 2008, a megahertz (MHz) rotation speed was reached at ambient temperature in a molecular motor which contains a rigid five-membered ring on the upper half and a flexible six-membered ring on the lower one.[114] In this configuration, the energy barrier in THI step is efficiently reduced due to a lower steric hindrance. Further investigations revealed the nature of bridging atoms is important for the rotation speed of this second generation molecular motor (Figure 3.5).[115,116,117]

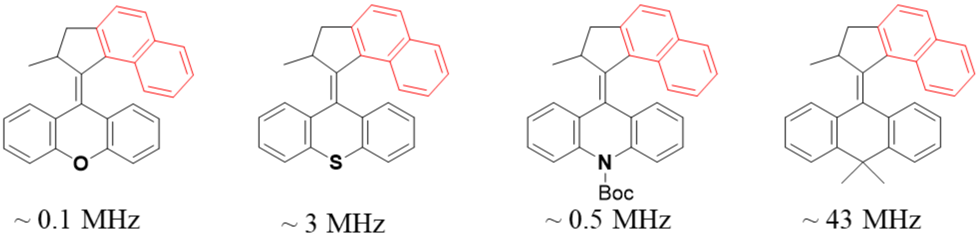

Figure 3.5 Second generation molecular motors with MHz rotation speed. This Figure is reproduced from ref.[115,116,117].

Third generation light-driven molecular motors

The first and the second generation molecular motors are chiral due to the presence of stereogenic centers and axial chirality. In 2015, Feringa and coworkers demonstrated the unidirectional rotation of an achiral molecule,[118] which is defined as third generation light-driven molecular motor.[118,119,120] The molecular design is detailed in Figure 3.6, two enantiomers (*M* and *P* helicity) of a second generation molecular motor are merged to form an overcrowded alkene. The newly formed molecular motor *meso*-(*r*)-**3** possess a plane of symmetry but retains the pseudo-asymmetric carbon at C2 which ensures the unidirectional rotation of each rotor. Based on the analyses of UV/Vis spectra, ^{1}H NMR spectra and thorough theoretical calculations, the rotation process was found to consist in 2 steps (Figure 3.6), UV light irradiation (365 nm, -80°C) induces the first photo-isomerization process, and the system reaches a photostationary state (PSS) involving racemic (*M*)-**3** and (*P*)-**3** in which only one rotor accomplished a quarter rotation. Subsequently, the rotated rotor continues to rotate another quarter turn at room temperature (THI process) to form *meso*-(*r*)-**3'**. This study proves that rotary motion with unidirectionality at the molecular level can be obtained in a genuine achiral molecular motor, and provides important insight into controlling nanoscale movement in order to meet the challenge of designing nanocars.

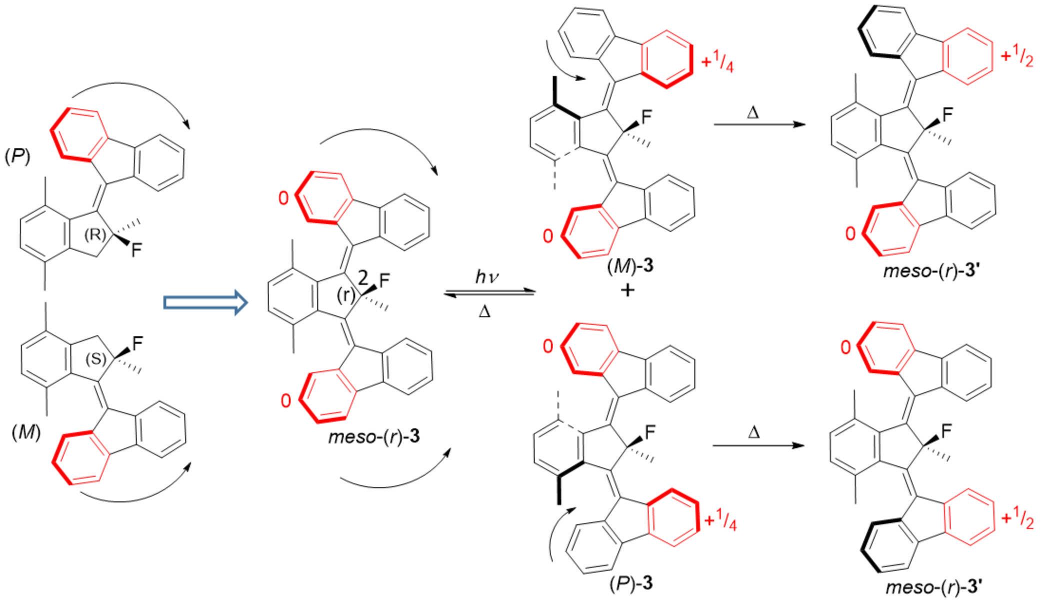

Figure 3.6 Molecular design of third generation light-driven molecular motors and rotation process induced by UV light irradiation and heat. This figure is reproduced from ref.[118].

Other light-driven molecular motors

Apart from molecular motors developed by Feringa, the group of Dube described in 2015 hemithioindigo (HTI) visible light-driven molecular motors,[121,122,123] which are based on an overcrowded alkene comprising a stilbene fragment as upper half and a thioindigo fragment as lower half. The presence of sulfur based stereogenic center (*S* or *R* configuration) and helical chirality (*M* or *P* helicity) warrants the unidirectional 360° rotation around the carbon-carbon double bond.

The underlying working mechanism was unveiled relying on time-resolved absorption spectroscopy and theoretical calculation.[122] Similarly to Feringa's motors, a four-step 360° unidirectional rotation of HTI is achieved via successive photo-isomerization and THI processes (Figure 3.7a). More precisely, upon 460 nm light irradiation at 22 °C, the helical reversal of stable state A proceeds to form unstable B with a 7% photo-isomerization quantum yield. Such low efficiency is attributed to the formation of the triplet excited state of A ($^3A^*$). In the following THI process, B quantitatively transforms by helicity inversion into C in 3 ns. The third step is the formation of D via a second photo-isomerization process. It should be noted that, because of the absence of the formation of a triplet intermediate state, the quantum yield of this step is much higher (24%) as opposed to the first one. Finally, molecular motor D returns to starting A by a second THI process (1.2 ms).

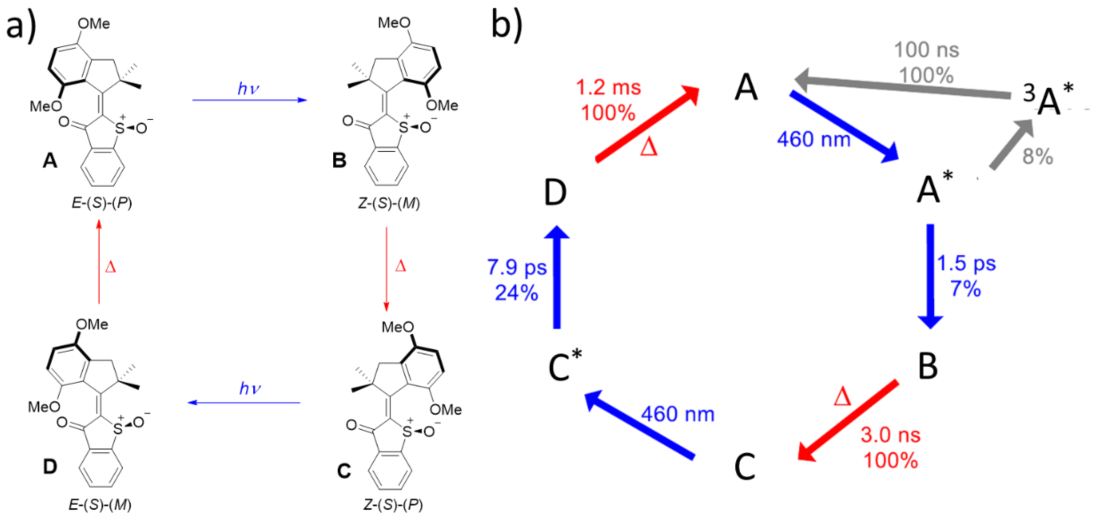

Figure 3.7 (a) Four-step unidirectional 360° rotation for HTI molecular motor; (b) Schematic representation of mechanism for a complete unidirectional 360° rotation depicted according to the time-resolved absorption spectra and theoretical calculation. This figure is reproduced from ref.[122].

In 2006, Lehn suggested that imine-based molecules are able to operate unidirectional rotary motion.[124] 8 years later, his research group reported on the first imine-based molecular motors.[125,126] Thanks to the presence of a stereogenic center, these diaryl-*N*-alkene imine based molecular motors can rotate towards a favored directionality upon exposure to UV light (> 280 nm) (Figure 3.8a). Regarding to the THI process, two possible mechanisms have been proposed: either an in-plane inversion at the nitrogen atom (NI), or a ring-inversion (RI) in which the phenyl rings flip to invert the helicity (Figure 3.8a).

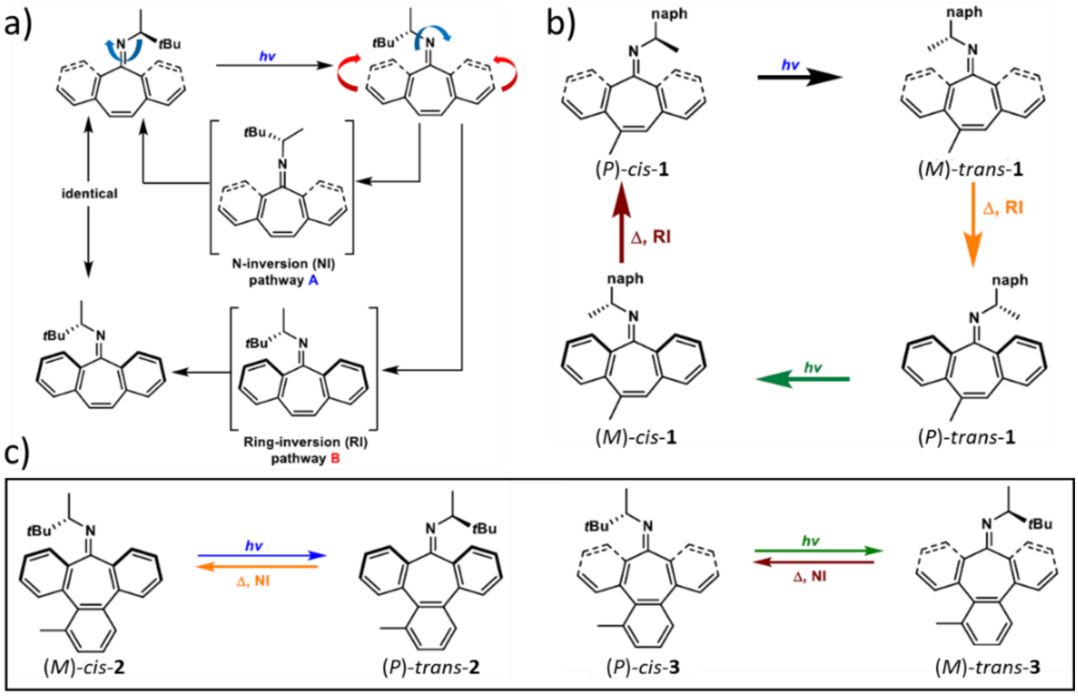

Figure 3.8 (a) Two possible pathways for thermal inversion in imine-based molecular motors; (b) Four-step unidirectional 360° rotation for molecular motor **1**, in which the THI process takes place by the ring-inversion pathway; (c) Two-step unidirectional 360° rotation for molecular motors **2** and **3** with N-inversion pathway. This figure is adapted from ref.[124].

To unambiguously reveal the nature of the THI process, two imine-based molecular motors were synthesized and investigated. In molecular motor **1**, the lower half is relatively flexible. In this case, the THI process takes place by the RI pathway in which the phenyl rings readily flip and invert the helicity (Figure 3.8b). Conversely, the NI pathway is preferential for molecular motors **2** and **3** as the introduction of phenyl ring at tricyclic core dramatically reduces the conformational flexibility of the lower half and concomitantly increases the activation energy of the RI process. (Figure 3.8c).

3.1.2 Chemically-fueled molecular motors

Over the past two decades, molecular motors fueled by chemical energy have also been explored. The first example towards this aim was reported by the group of Kelly,[127] who synthesized a triptycene-based molecule, which however can only implement a 120° unidirectional rotation. One ideal molecule candidate for the formation of unidirectional rotary motors is biaryl-based molecules in which the phenyl rings can undergo sterically hindered rotation around a carbon-carbon single bond.[128,129,130]

Feringa and coworkers first demonstrated the four-step 360° unidirectional rotation of a biaryl-based molecular motor.[129] The starting state of this molecular motor is **1a** in which the rotor (phenyl ring) and stator (naphthalene ring) are locked via a lactone unit. In step 1 and 3, asymmetric ring-opening of the lactone takes place upon addition of chiral auxiliary as reducing agent leading to the rotation of the rotor with high unidirectionality. In step 2 and 4, selective deprotection of the ether bond and subsequent lactonization reaction enable the rotor to forbid the stator realizing further rotation. It is noteworthy that cyclized biaryls **1a** and **1c** exist as a racemic mixture because of the low energy barrier between the two helical conformations. Thus the rotary unidirectionality of this molecular motor is merely 90%.

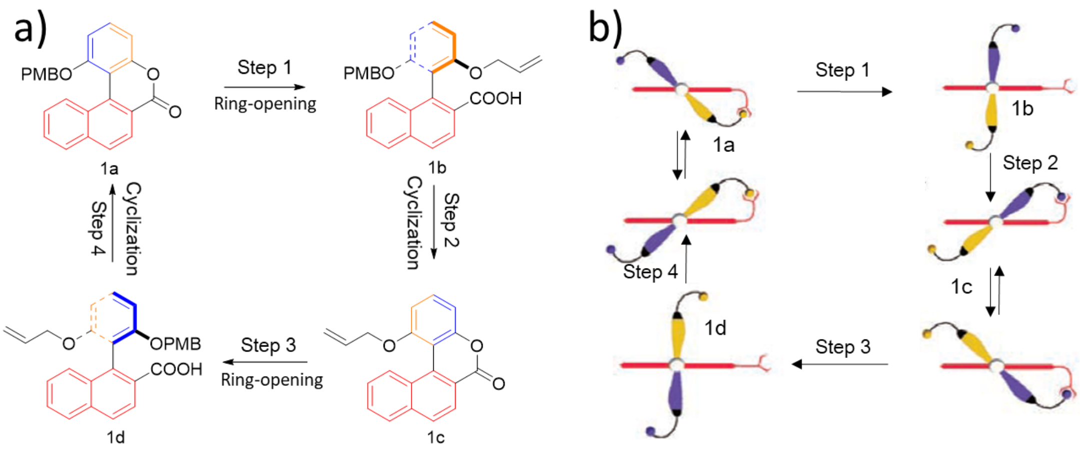

Figure 3.9 (a) Molecular structures and four-step 360° unidirectional rotation of biaryl-based molecular motor (side view); (B) Schematic representation of molecular rotation (top view). This figure is reproduced from ref.[129].

Recently, the unidirectional rotary motion in biaryl-based chemically-fueled molecular motor reached 100 %, as reported by Feringa and collaborators (Figure 3.10).[130] The rotation process is unequivocally established according to the single crystals analyses of each station. Similarly to their initial work, a four-step rotary cycle can be realized via successive cyclization and ring-opening processes. In light-driven molecular motors, the presence stereogenic center at the upper half is used to dictate the rotary directionality. Expanding this design to chemically fueled molecular motors allows to selectively populate one energy-favored conformation in lactonization and ring-opening processes, resulting in a 100% unidirectionality.

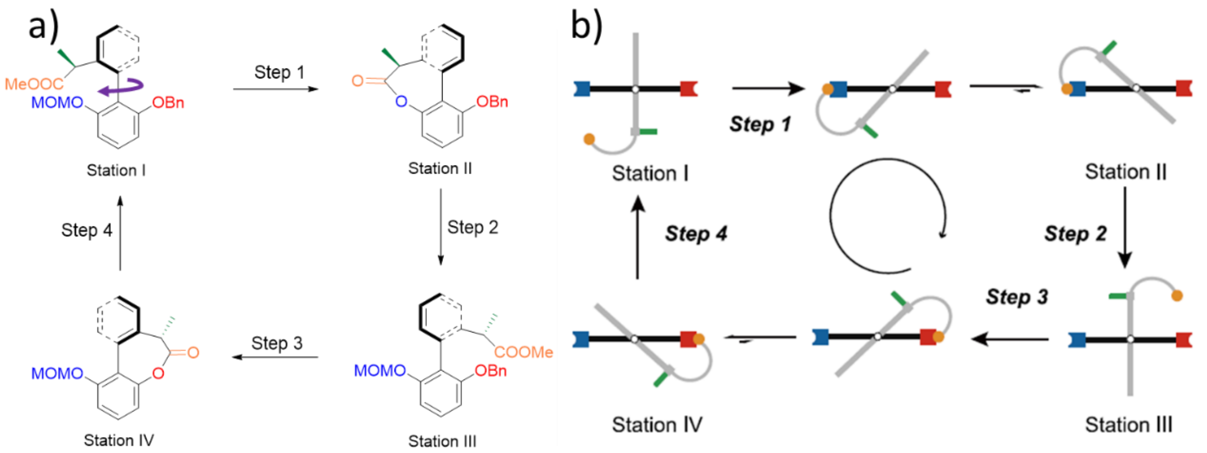

Figure 3.10 A 360˚ rotary motion of biaryl-based molecular motor observed from (a) side view; and (b) top view. This figure is reproduced from ref.[130].

Till today, light-driven or chemically fueled molecular motors with unidirectional and speedy rotary motion have been extensively studied, which opens tremendous opportunities for the applications of molecular machines.

3.1.3 Macroscopic amplification of collective motions induced by molecular motors

The unidirectional rotary motion of molecular motors has been exploited in various areas of nanoscale science, such as molecular nanocar,[131] switchable catalysis,[100,132] and controllable self-assembly.[101, 133] However, making use of such unique rotary motion to perform mechanical work at macroscopic level is a challenging topic.

Based on Feringa’s second generation molecular motor, in 2015, our research group developed a tetrasubstituted molecular motor, [134] in which the upper half and lower half were functionalized with azide-terminated polyethylene glycol (PEG) and alkyne-terminated tri(ethylene glycol), respectively (Figure 3.11a). In a highly diluted solution, figure-eight-shaped molecular motors were obtained via intramolecular Huisgen ‘click’ reaction, which was directly observed by AFM (Figure 3.11b). Under UV light irradiation (366 nm), continuous rotation of molecular motors resulted in braiding of PEG chains. As a result, collapsed coils with smaller dimension were observed (Figure 3.11b). On the other hand, when the reaction was performed in a concentrated condition, preferential intermolecular ‘click’ reaction proceeded and provided chemical polymer gel. In this motorized gel, molecular motors serve as reticulating units connecting the polyethylene glycol (PEG) chains. Upon UV irradiation, a large number of molecular motors were triggered to rotate and subsequently braided PEG chains resulting in macroscopic contraction of the gel (Figure 3.11c). Intriguingly, once contraction of gel reached a certain extent, rupture of the gel happened. This behavior was attributed to the oxidative degradation of molecular motors in their tensed state, leading to a reduction of the double bond into to a single bond. It is worthy to note that, in this system, the energy of light drove the system continuously away from equilibrium, leading to energy storage in the contracted gel.

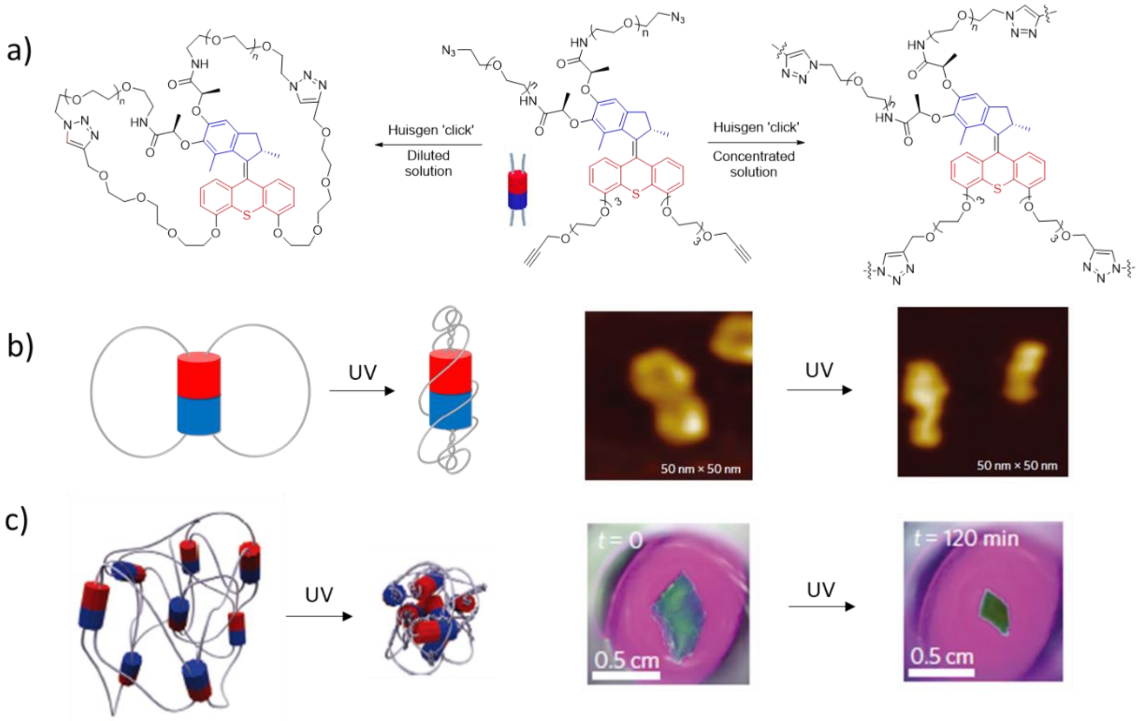

Figure 3.11 (a) Chemical structure of tetrasubstituted molecular motor, eight-figure-shaped molecular motor, and polymeric networks formed via ‘click’ reaction; (b) Schematic representation of braiding of eight-figure-shaped molecular motor, and AFM images before and after UV light irradiation; (c) Schematic representation of the contraction of a motorized gel, and snapshots of a video showing time-dependent contraction of gel upon light irradiation. This figure is adapted from ref.[134].

One limitation associated with the presence of unidirectional molecular motor in the gel, so that the wound PEG chains cannot be unbraided. This means that the contraction of the gel is persistent and that the elastic energy stored cannot be released. In order to solve this issue, the system was optimized by the introduction of a so called “modulator” unit (Figure 3.12a).[135] This modulator is based on a tetrasubstituted diarylethene photoswicth, which can serve as an on-demand elastic releaser for unbraiding the wound PEG chains. Thanks to this rational design, the contraction and expansion of motorized gels are controllable and reversible by applying light with different wavelengths. Precisely, under UV light irradiation, the modulator is in a ‘closed’ form, so the continuous rotation of molecular motors leads to braiding of polymer chains and results in the contraction of the gel. Alternatively, upon irradiation with visible light, rotation of molecular motor is interrupted and the modulator is switched to an ‘open’ form. In this case, the free rotation of carbon-carbon single bond at modulators is triggered, and the elastic energy stored in the wound chains can be released, leading to the expansion of the gel until thermodynamic equilibrium is fully reached (Figure 3.12b). In addition, when visible and UV light are applied together, braiding and unbraiding of the polymer chains will take place concomitantly. Moreover, by adjusting the UV and visible light intensities, braiding and unbraiding rates can be regulated, allowing to modulate the contraction or expansion of the gel.

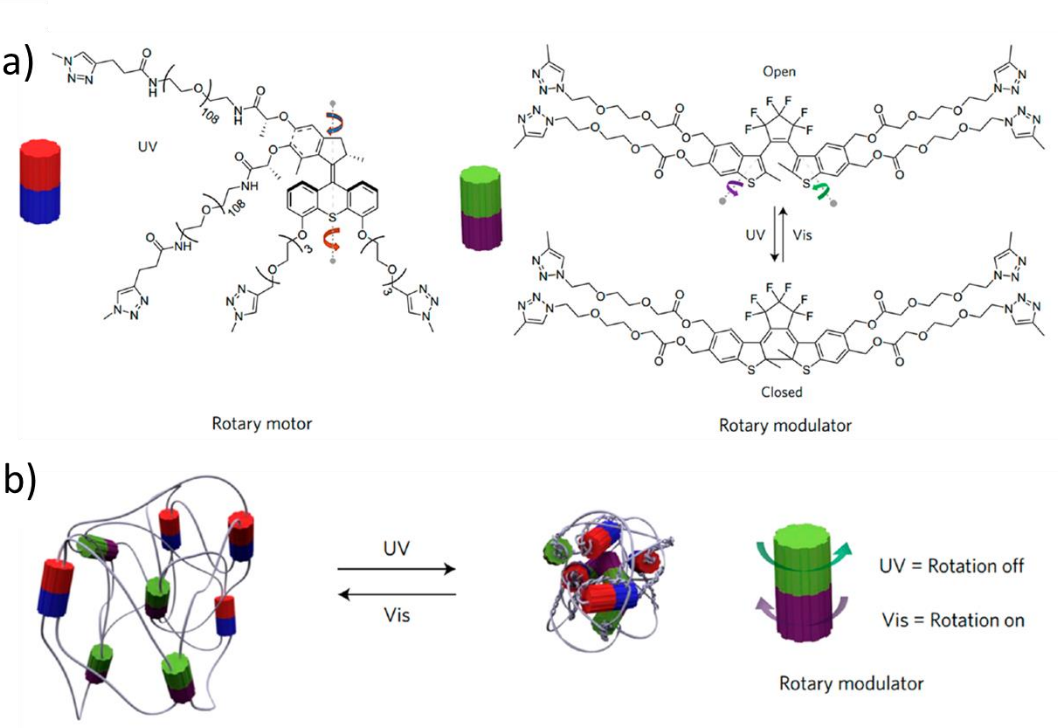

Figure 3.12 (a) Molecular structures of molecular motor and diarylethene based “modulator”; (b) Schematic representation of controllable contraction or expansion of a chemical gel driven by light. This figure is adapted from ref.135.

To amplify the nanoscopic motions in supramolecular structures up to the macroscopic scale, Feringa and coworkers integrated amphiphilic molecular motors (Figure 3.12b) into hierarchical supramolecular self-assembly, which acts as artificial molecular muscles in response to UV light irradiation.[136] As shown in Figure 3.12, molecular motors bearing one dodecyl chain on the upper half and two carboxyl terminated alkyl chains on the lower half can stack into nanofibers in water. Macroscopic gel consisting of aligned bundles of nanofibers is further formed by drawing the aqueous solution of amphiphilic motor into an aqueous solution containing calcium ions.

Upon UV light irradiation, the gel bends towards the direction of the incoming beam (Figure 3.13c). This phototactuation mechanism was unveiled by SAXS. Light irradiation induces the transformation of stable molecular motors to an unstable state that disorders the local packing arrangement in the bundles. Moreover, the bent gel can restore its initial conformation via a heating process in the dark at 50˚C for 3 hours (Figure 3.13c), as a result of the rearrangement of the fibers induced by the recovery of stable molecular motors.

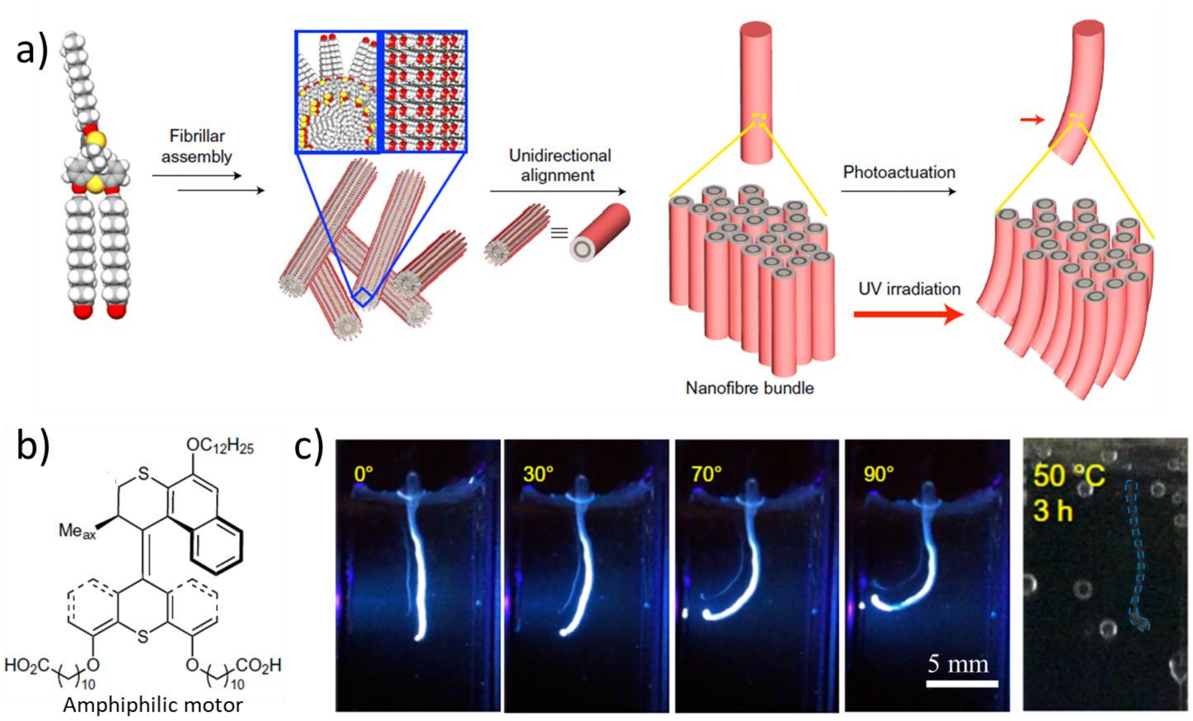

Figure 3.13 (a) Schematic representation of the formation of amphiphilic molecular motor based supramolecular gel and its photoactuation; (b) Molecular structure of amphiphilic molecular motor; (c) Snapshots taken from the video of photoactuation process of supramolecular gel and subsequent recovery at 50˚C in the dark. This figure is adapted from ref.[136].

Very recently, the same group introduced molecular motors into liquid crystalline networks (LCN) reaching a series of sophisticated motion at the macro-level.[137] In this system, cyclopentene-based second generation molecular motors were chosen to serve as chiral LC dopant and stimuli-responsive cross-linker due to their high rotation speed (Figure 3.14a). The LCN material was fabricated from a racemic mixture of molecular motors and a mixture of acrylate-functionalized nematic LC (RM 82, RM 105, and RM 23) via light-initiated polymerization. The formed material displays alignment from homeotropic to parallel. In addition, molecular motors preserve their photochemical and thermal isomerization in the aligned structure. When the homeotropic side of this material was exposed to UV light (365 nm), it instantly bent away from the incident beam, and subsequently returned to the starting position once the light beam was off (Figure 3.14c). The rapid photoactuation process comes from the disordering of the LCN arising from structural deformation induced by molecular motors. In the following study, LCN materials with helical alignment were obtained by employing enatiomerically pure molecular motor as chiral dopant (Figure 3.14b). When the material was irradiated with UV light, the change in chirality of the molecular motor is amplified to the macroscopic level leading to a helical twisting motion, and the twisting direction is dictated by the initial chirality of the molecular motor (Figure 3.14e and 3.14f).

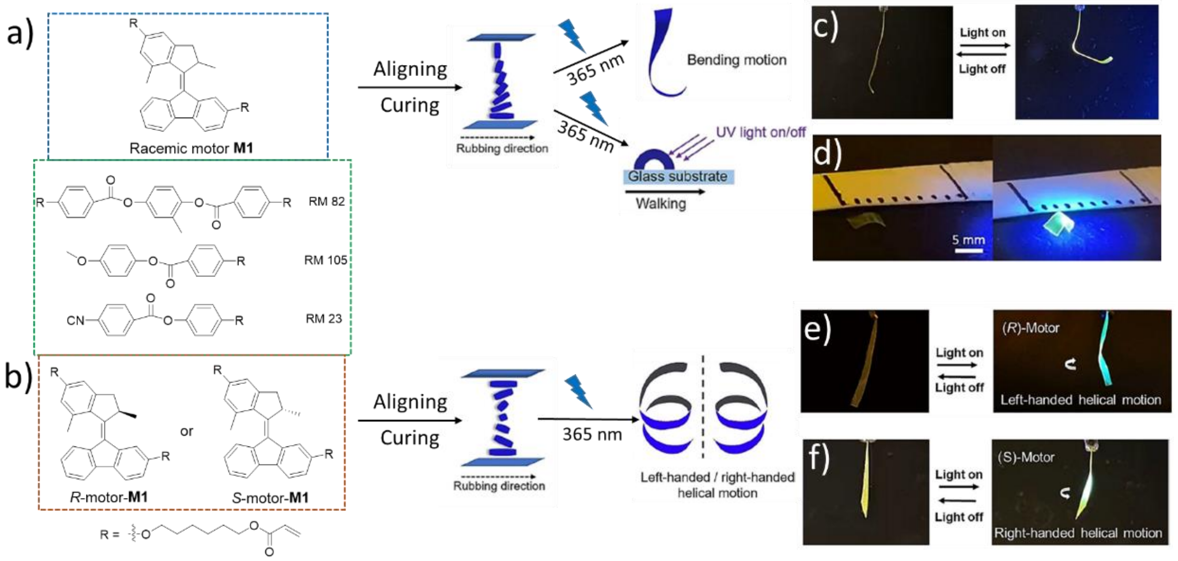

Figure 3.14 (a,b) Molecular structures of (a) bis-functionalized racemic molecular motors, and (b) *R*-motor-**M1** and *S*-motor-**M1**; (c-f) Snapshots taken from videos recording photoactuation processes of gels made of (c, d) racemic molecular motors, and (e, f) enatimerically pure molecular motors. This figure is adapted from ref.[137].

3.2 Photo-responsive systems with tunable plasmonic coupling

As presented in chapter 2, the proximity of plasmonic nanoparticles gives rise to a profound spectral change in the localized surface plasmon resonance (LSPR) band (noticeable red shift and broadening of the band) arising from plasmonic coupling. For this reason, plasmonic nanoparticles have been extensively incorporated into stimuli-responsive systems with tunable optical properties. External stimuli, such as pH,[138] solvent,[139] temperature,[140] and light[141] are capable of regulating interparticle distance, thereby modulating the LSPR behavior at will.

Among all external stimuli, light is particularly attractive as it is noninvasive thus avoiding the pollution of the whole system. On the other hand, switching the light on and off is convenient and instantaneous. In addition, light as stimulus can be selectively and remotely addressed with high spatial and high spatiotemporal resolution.

Based on these advantages, Lin and coworkers achieved the switchable plasmonic coupling of AuNPs involving a photodimerization reaction.[142] As shown in Figure 3.15a, AuNPs were capped with hydrophilic polymers terminated with methylcoumarin (MAMC). Under UV light irradiation (365 nm), a redshift of the LSPR band was observed, indicating aggregation of AuNPs due to the intermolecular [2+2] photodimerization of MAMC (Figure 3.15 b). The solution was then exposed to light at 254 nm, and a recovery of the LSPR band (narrowing and blue shifting) gradually occurred, suggesting a disassembly of aggregates thanks to the photocleavage of MAMC dimers (Figure 3.15c). Remarkably, without the need for external chemicals, the entire system manifested very high stability and reversibility after five irradiation cycles (Figure 3.15d).

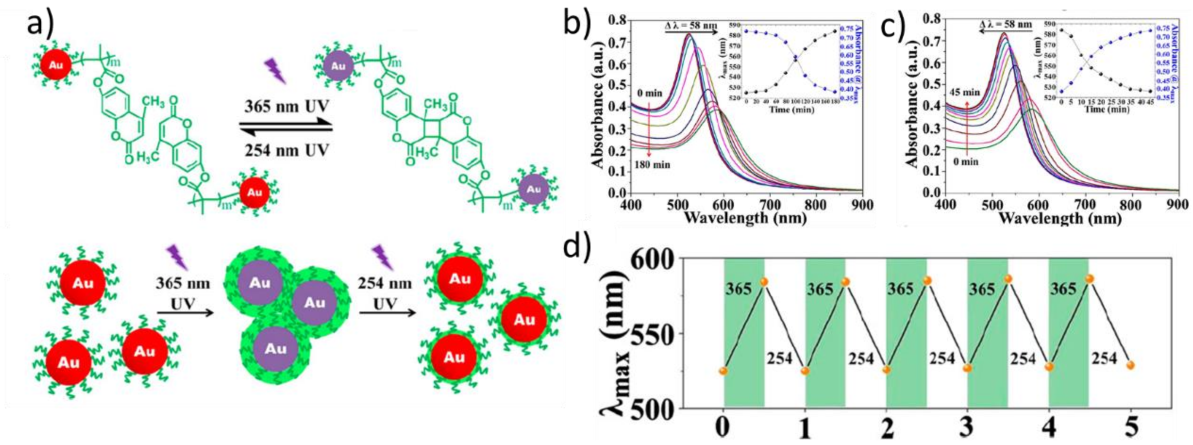

Figure 3.15 (a) Photodimerization and photocleavage reaction of methylcoumarin and schematic representation of light-induced self-assembly and disassembly of PMAMC-capped AuNPs; (b) UV-Vis spectra of AuNPs upon 365 nm UV light irradiation; (c) UV-Vis spectra of AuNPs upon 254 nm UV light irradiation; (d) Reversible photocontrol of the LSPR peak position of PMAMC-capped AuNPs during the self-assembly (green areas) and disassembly (white areas) cycles upon the irradiation with 365 and 254 nm UV light, respectively. This figure is adapted from ref.[142].

The research group of Klajn has extensively explored photo-responsive systems in which self-assembly and disassembly of AuNPs can be directly or indirectly controlled via supramolecular interactions. One impressive methodology was demonstrated in 2015.[143] As illustrated in Figure 3.16a, protonated merocyanine (MCH^+) is added into a solution of photo-inactive AuNPs in order to achieve the indirect control of the AuNPs self-assembly. In the initial state, 11-mercaptoundecanoic acid (MUA) capped AuNPs precipitate due to multiple hydrogen bonds between COOH. Upon irradiation with blue light, MCH^+ transforms to spiropyran and release H^+ that subsequently breaks the hydrogen bonds resulting in a AuNPs suspension. Meanwhile, the color of this solution turns to red accompanied by the appearance of a notable LSPR band on the UV-Vis spectrum. After turning off the light, the color returns to yellow and a blueshift of the LSPR band occurs due to the self-assembly of AuNPs. The reason is that the surface-bound H^+ was captured by the newly formed SP in the dark. Interestingly, the same self-assembly and disassembly processes of AuNPs are also achieved in a thin film of PEG polymers. As shown in Figure 3.16d, thanks to the aggregation and separation of AuNPs, the color of thin film is locally controllable by exposure to light or darkness.

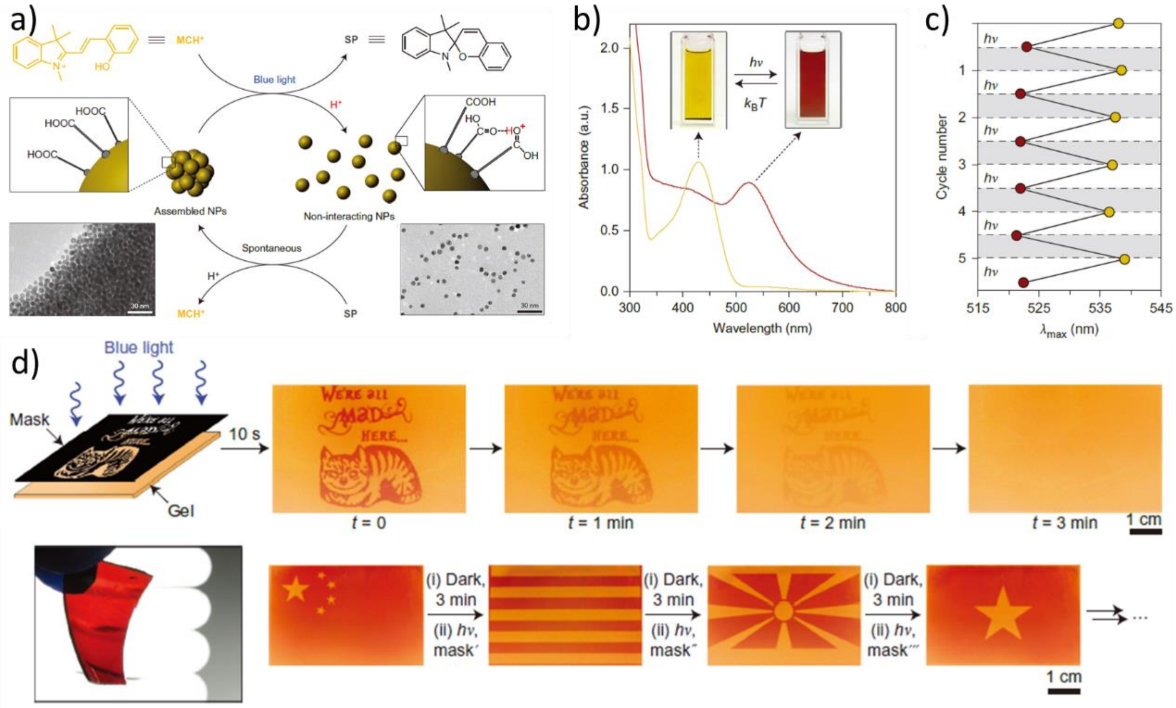

Figure 3.16 (a) Schematic illustration of light-controlled self-assembly and disassembly of MUA-capped AuNPs; (b) UV-Vis spectra of AuNPs solution before (yellow line) and after irradiation (red line); (c) Reversible photocontrol of the LSPR peak position of MUA-capped AuNPs during the self-assembly (white areas) and disassembly (grey areas) cycles. This figure is adapted from ref.[143].

3.3 Regulating plasmonic coupling of AuNPs in motorized gels

3.3.1 Objectives

Based on our understanding of plasmonic coupling and on our knowledge on contractile motorized gels, we envisaged that, by integrating AuNPs into a polymer networks of photo-responsive motors, the regulation of optical properties could be set on-demand. To achieve this goal, we designed a system in which bisazide poly(ethylene glycol) (PEG) polymers, alkyne-functionalized molecular motor, and alkyne-capped AuNPs are integrated into a chemical gel via copper(I)-catalyzed azide-alkyne cycloaddition (CuAAC) reaction (Figure 3.17a). When the gel is exposed to UV light, the interparticle distance between AuNPs could be shorten as the contraction of gel occurs. As a result, plasmonic coupling could be modulated by controlling irradiation time, thereby giving rise to changes in LSPR band (Figure 3.17b).

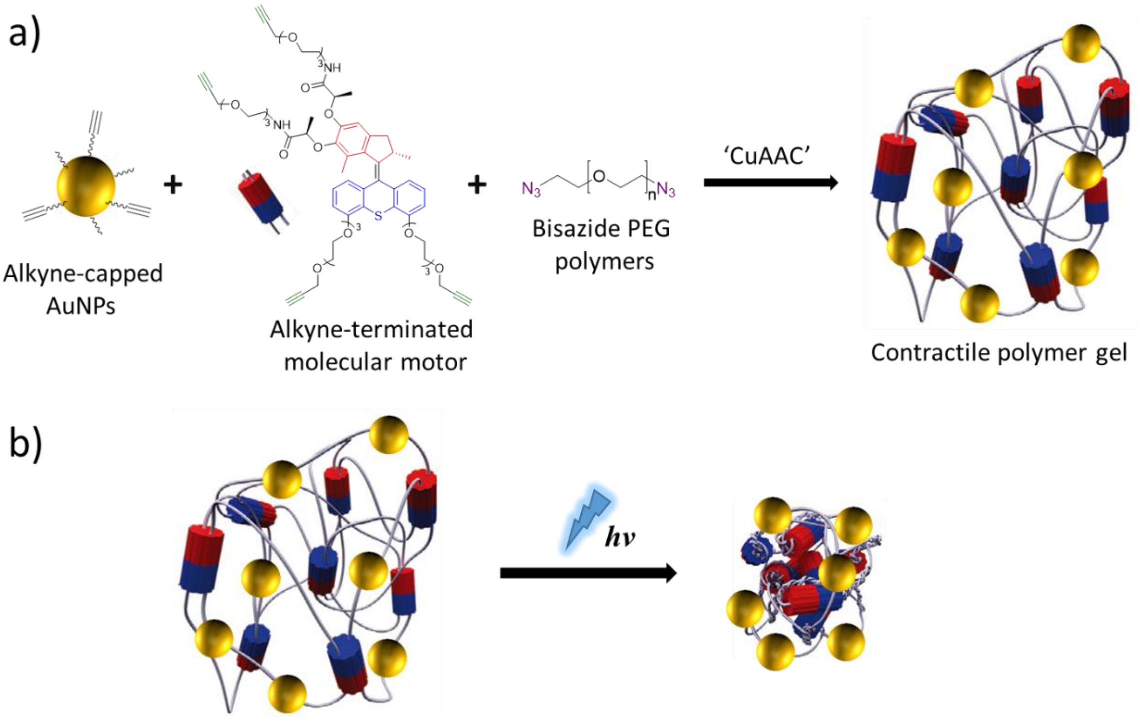

Figure 3.17 (a) Schematic representation of preparation of a motorized gel composed of PEG polymers, AuNPs, and molecular motors; (b) Schematic illustration of light-triggered contraction of motorized gel, accompanied by the tunable plasmonic coupling behavior.

3.3.2 Synthesis of molecular motor, bisazide PEG, and AuNPs

Synthesis of alkyne-terminated molecular motor and bis-azide PEG

Synthesis of the target molecular motor started from preparations of monoalkyne-terminated compounds **14** and **18** (Scheme 3.1), which are used to functionalize the lower half and upper half of the molecular motor, respectively. Starting from triethylene glycol, alkyne **13** was obtained in good yield, and further reacted with TsCl affording tosylated alkyne **14** in excellent yield. Product **18** was also prepared from triethylene glycol in four steps. First, compound **15** was obtained via a tosylation reaction, albeit in low yield as an excess of triethylene glycol was used to avoid the formation of bistosylated byproduct. Then, monoazide **16** was prepared in almost quantitative yield via nuleophilic substitution reaction with sodium azide. Afterwards, product **17** was obtained in excellent yield following the protocol developed for the synthesis of compound **13**. Finally, the azide group on intermediate **17** was reduced with triphenylphosphine to give target product **18** in very good yield.

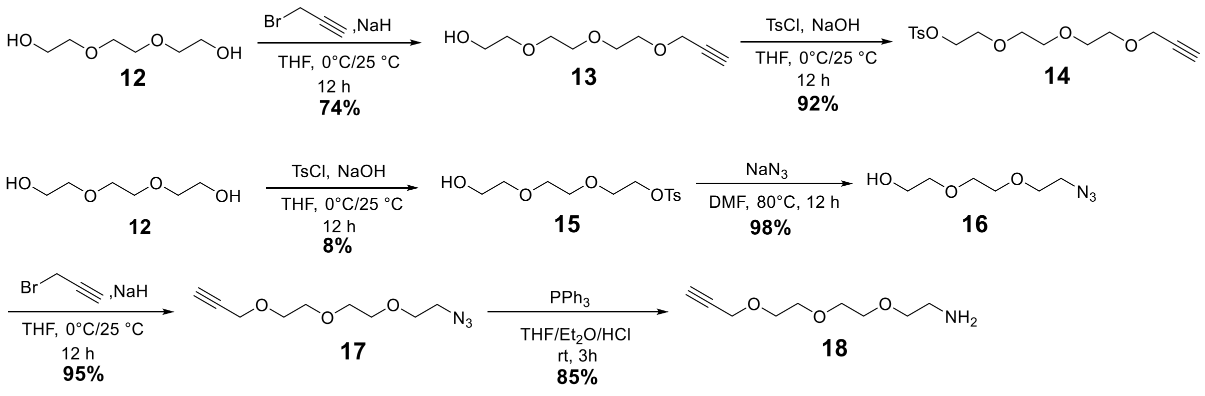

Scheme 3.1 Synthesis of alkyne-terminated compounds **14** and **18**.

Based on the design of Feringa's second generation molecular motor, our group developed a new molecular motor which can be functionalized differently on the lower and upper halves.[144] The presence of two stereogenic centers on the upper half of this molecular motor allows to separate the two isomers (*R* and *S*) of episulfide **19** by flash silica column chromatography. In addition, the gram-scale synthesis of this molecular motor has been readily achieved. Thanks to efforts from my colleagues, Dr. Xuyang Yao, Alexis Perrot, and Joakim Heiser, gram quantities of episulfide **19** (*S*) were available, which I could use as precursor for molecular motor **24** (Scheme 3.2).

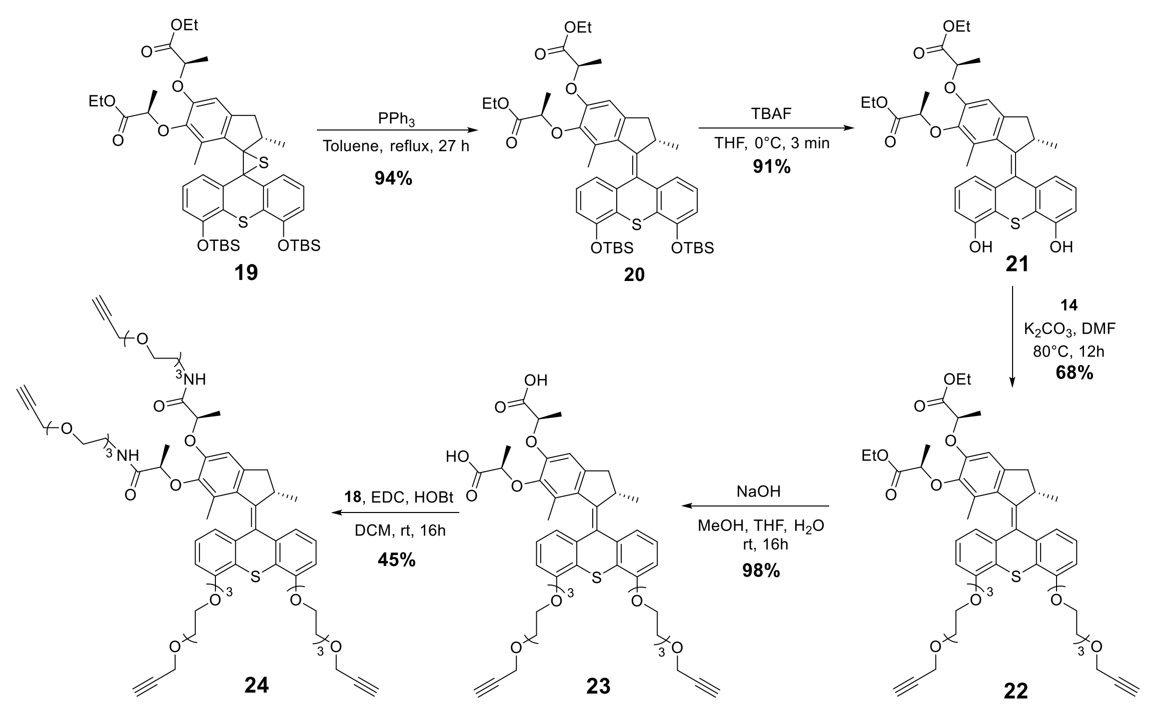

Scheme 3.2 Synthesis of alkyne-terminated molecular motor **24**.

First, episulfide **19** underwent desulfurization with PPh_3 in toluene at 120°C providing molecular motor **20** in excellent yield. Then TBS groups on the lower half were removed in the presence of TBAF at 0°C, affording bisphenol molecular motor **21** in 3 minutes and excellent yield. The resulting product was further engaged in a nucleophilic substitution reaction with tosylated alkyne **14** in DMF, resulting in the formation of bisalkyne **22** in good yield. In all these reactions, ester bonds were stable enough, so that no cleavage occurred. Saponification of ester bonds took place in a 1:1 THF/MeOH mixture using an aqueous solution of NaOH, affording bisazide **23** in almost quantitative yield after acidification with a 1M HCl solution. As the polarity of acid **23** is high and the reaction was almost quantitative, no further purification was necessary. Finally, by using EDC and HOBt as coupling reagents, amidation reaction of acid **23** with previously prepared compound **18** afforded tetra-alkyne molecular motor **24** in moderate yield.

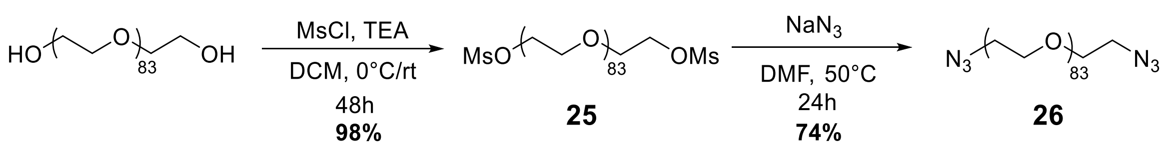

Scheme 3.3 Synthesis of bisazide PEG **15**.

Synthesis of bis-azide PEG polymer occurred in two steps from commercially available polymers. PEG polymer was first bis-functionalized with mesyl groups in excellent yield. Importantly, the use TsCl instead of MsCl for this reaction only led to monotosylated PEG, probably because of the larger steric hindrance of TsCl as opposed to MsCl. In the last step, compound **25** was used to react with sodium azide in DMF for 24 hours at 50°C providing bis-azide PEG **26** in good yield.

Synthesis, functionalization, and characterization of AuNPs

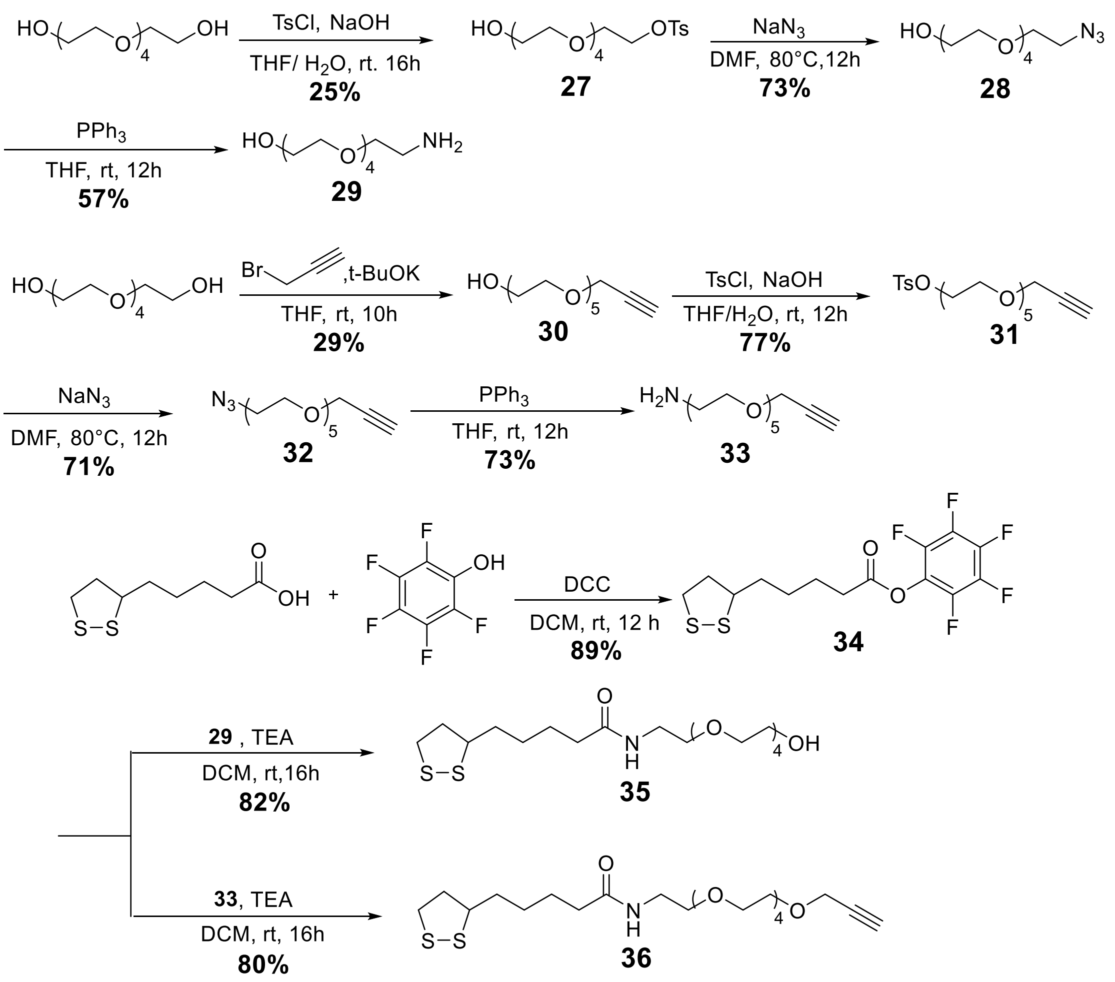

Scheme 3.4 Synthesis of disulfide **35** and **36**.

To integrate AuNPs into the polymeric networks via covalent bonds, AuNPs had to be functionalized with alkyne-terminated functional ligands. In addition, we also synthesized a hydroxyl-terminated background ligand, in order to adjust the density of functional ligands on the gold surface. Starting from pentaethylene glycol, amine **29** and **33** were prepared according to the protocols previously optimized for the synthesis of compound **18**. Then lipoic acid was reacted with pentafluorophenol to give pentafluorophenyl ester **34** in good yield. Next, by employing triethylamine as a base, active ester **34** was subsequently reacted with a solution of previously obtained amines **29** or **33** for 16 hours at room temperature affording disulfide **35** and **36** in good yield, respectively.

Water-soluble AuNPs **I** were synthesized by following the classical Turkevich method (Scheme 3.5).[145] This method is easy to operate and readily produces NPs of ~ 15 nm diameter. To get uniform AuNPs, the flask and stir bar were washed with aqua regia before use. $HAuCl_4$ was dissolved in milli-Q water and the mixture was boiled under vigorous stirring. Then an aqueous solution of sodium citrate (reductant) was added quickly, leading to a change in color of the solution turned from yellow to colorless, which eventually turned to wine red, as an indication of the successful formation of citrate-coated AuNPs.

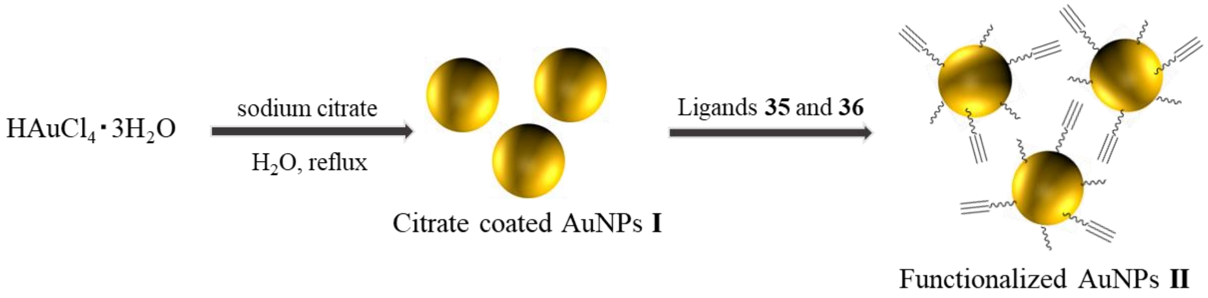

Scheme 3.5 Synthesis and functionalization of AuNPs **I**.

Characterization of freshly prepared AuNPs **I** was performed using several techniques. The UV-Vis spectrum of AuNPs **I** shows a LSPR band with a maximum absorption intensity at 520 nm (Figure 3.18a). Moreover, this absorption band is narrow, indicating highly uniform and monodisperse of AuNPs. This was confirmed by STEM image, which did not show the presence of large aggregates of AuNPs, but nanospheres with similar size of ~14 nm. This observation is in very good agreement with UV-Vis spectrum. Furthermore, DLS experiments confirmed these measurements with an average size of 13.81 nm and a relatively low polydispersity index (PDI, 0.19).

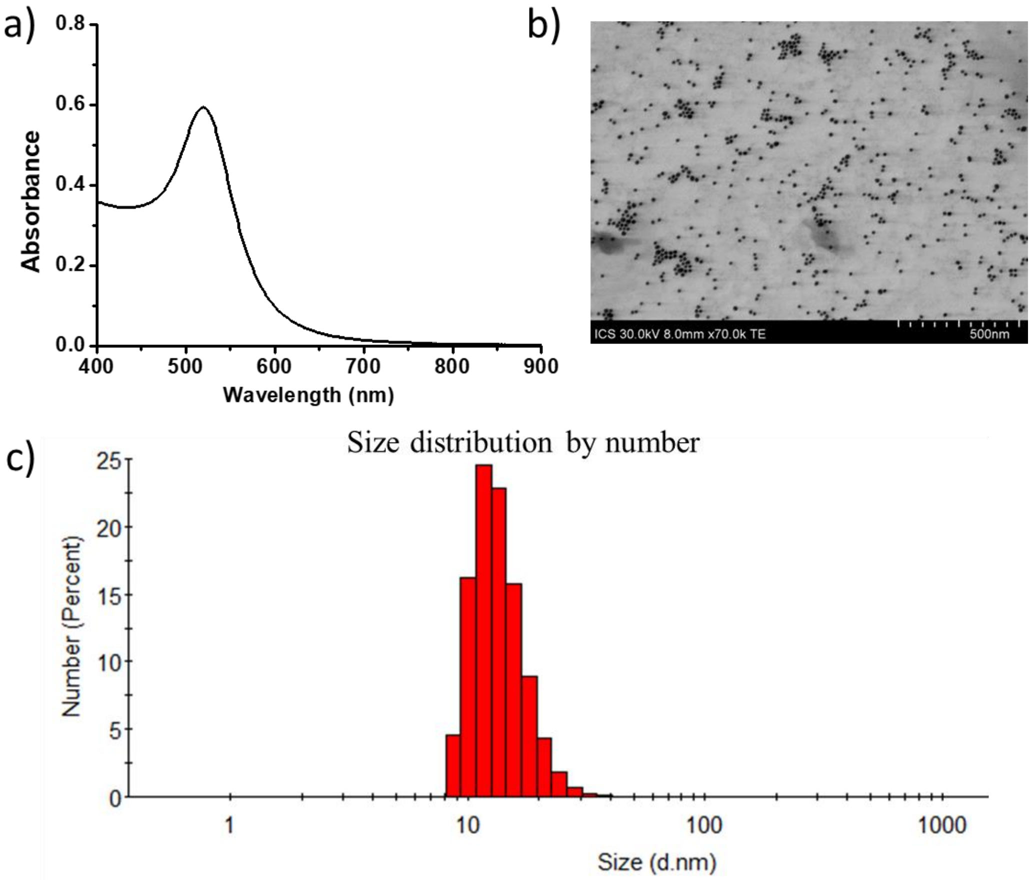

Figure 3.18 Characterization of citrate-coated AuNPs **I**. (a) UV-Vis spectrum of an aqueous solution of AuNPs **I** (3×10^{-10} M); (B) STEM image of AuNPs **I**; (c) DLS measurement of an aqueous solution of AuNPs **I**.

After confirming the formation of uniform AuNPs, we then turned their functionalization with functional and background ligands **35** and **36** (Scheme 3.5). In order to avoid the undesired aggregation of AuNPs during the functionalization process, the pH of the AuNPs solution was first adjusted to 9 with an aqueous solution of NaOH. Later, a methanol solution of ligands **35** and **36** with a ratio of 4:1 was added. After slightly shaking for 24 hours, the solution was centrifuged providing a black precipitate at the bottom of the vial. After removal of the supernatant, the black powder was washed with milli-Q water and eventually redissolved in DMF to give alkyne-capped AuNPs **II**.

To verify the successful modification of AuNPs, we carried out UV-Vis spectroscopy, STEM, and DLS experiments (Figure 3.19). AuNPs **II** displays a LSPR band at the wavelength of 530 nm, which is broaden and redshifted compared to the one of AuNPs **I**. This spectral change normally is caused either by aggregation or by a size increase of the nanoparticles. According to STEM image, we found that AuNPs are still well-dispersed, so the addition of disulfide ligands did not lead to serious aggregation. On the other hand, the average size of AuNPs **II** determined by DLS is 15.13 nm with a narrow size distribution. Undoubtedly, these results demonstrate that the change in LSPR band arises from a size increase, suggesting the successful modification of AuNPs.

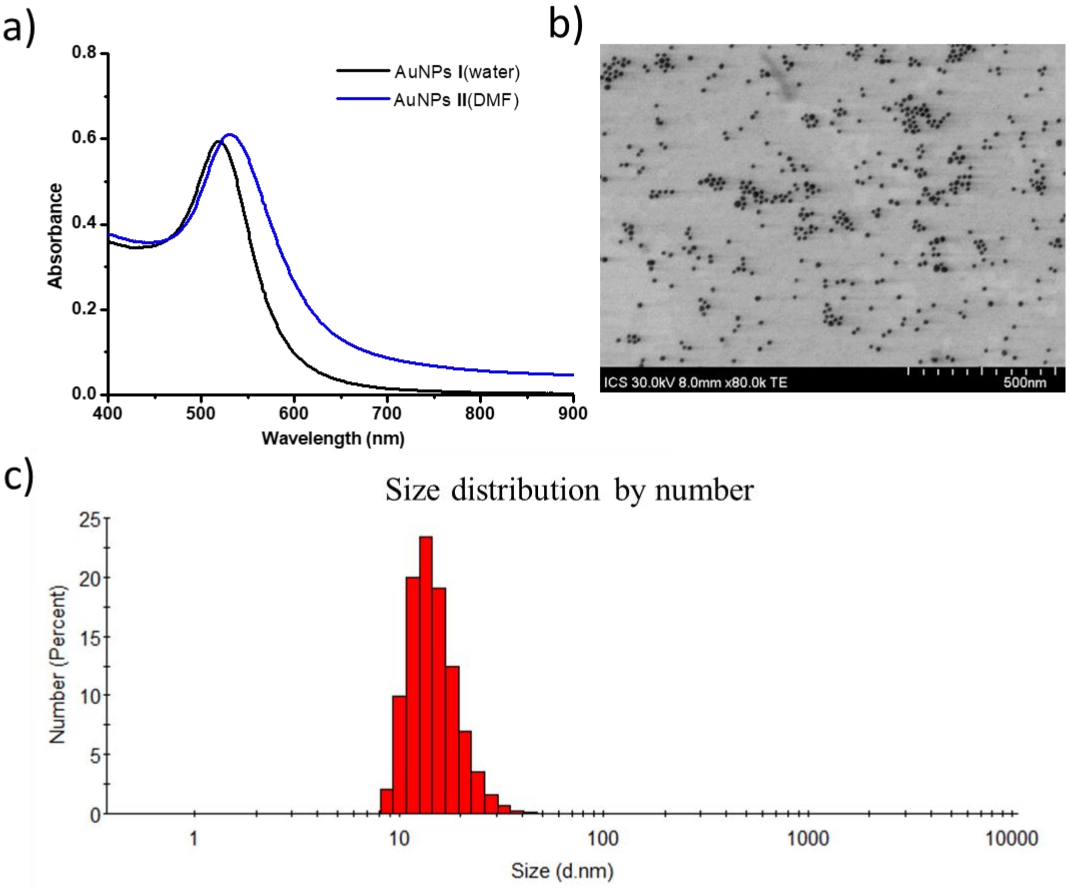

Figure 3.19 Characterization of ligand-modified AuNPs **II**. (a) UV-Vis spectra of an aqueous solution of AuNPs **I** (3×10^{-10} M) and a DMF solution of AuNPs **II** (3×10^{-10} M); (B) STEM image of AuNPs **II**; (c) DLS measurement of a DMF solution of AuNPs **II**.

3.3.3 Gelation, irradiation, and characterization

Integration of molecular motors, PEG, and AuNPs into gels

Motorized gels containing AuNPs were synthesized via copper-catalyzed ‘click’ reaction (Figure 3.20a). Precisely, catalyst CuBr and PMDETA were added to a DMF solution of precursor **24**, **26**, and functionalized AuNPs **II**. Then the mixture was transferred to a rheology mold to get a material with precise dimensions (2 cm×2 cm×458 µm) (Figure 3.20b(*i*)). The gelation process was performed at room temperature rather than 80°C as previously reported on motorized gel,[134,135] because high temperature could lead to aggregation of AuNPs. After 12 hours, a chemical gel was obtained thanks to successful couplings between the different components. In order to remove the excess of organic compounds and copper catalyst, the gel was washed three times by immersion in an aqueous EDTA solution. Finally, the gel was immersed in water. By varying the proportion of AuNPs during the gelation process, five gels named Gel **0, 1, 2, 3,** and **4** were obtained (Figure 3.20c). As shown in Figure 3.20b, the gel without AuNPs is colorless (Figure 3.20b(*ii*)), while gels containing AuNPs are purple (Figure 3.20b(*iii*)).

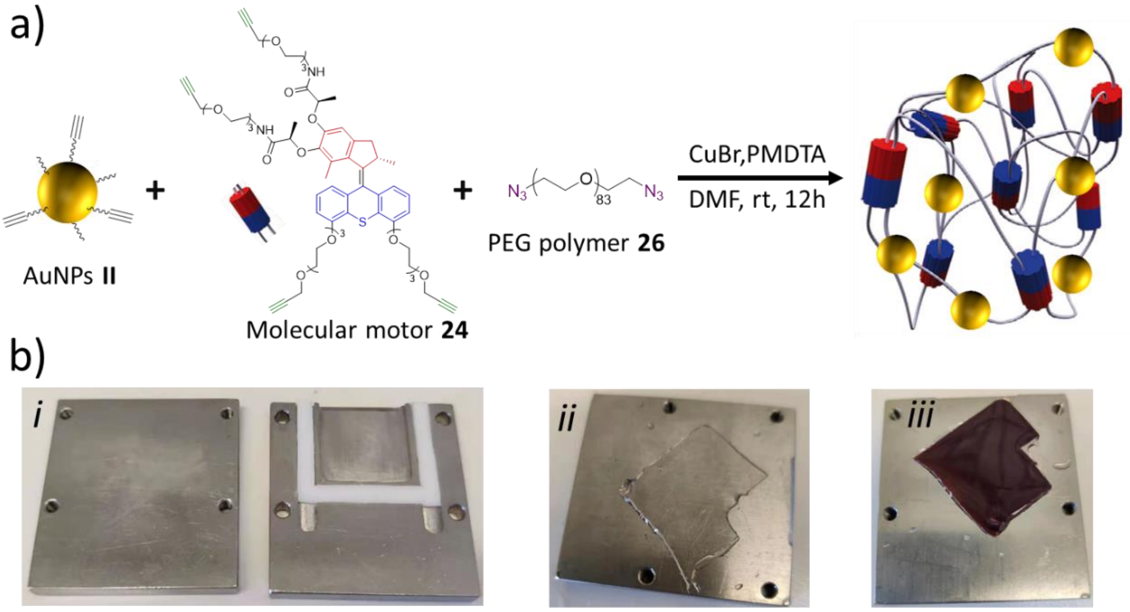

c)

Gel	Gel **0**	Gel **1**	Gel **2**	Gel **3**	Gel **4**
AuNPs (g/L)	0	0.8	1.6	2.0	4.0

Figure 3.20 (a) Synthetic pathway for the formation of motorized gels containing AuNPs; (b) Photographs of (i) the rheology mold, (ii) a motorized gel without AuNPs, and (iii) a motorized gel with AuNPs; (c) Proportion of AuNPs **II** in motorized gels.

Irradiation

By using a razor blade, gels were cut into small pieces, and one-piece gel was brought to a sample holder. Meanwhile, the gel was immersed in argon-degassed water, then the holder was covered with a cap and screwed to avoid leakage. Afterwards, the piece of gel was placed between the light beam and the camera (Figure 3.21). So that the irradiation process could be recorded. Then, light irradiation was carried out using an optical fiber at a wavelength of 365 nm. Under UV light irradiation, the light-triggered collective rotary motion of molecular motors led to a macroscopic contraction of the gel, as shown in the Figure 3.21. The light irradiation was then stopped when no more contraction was observed.

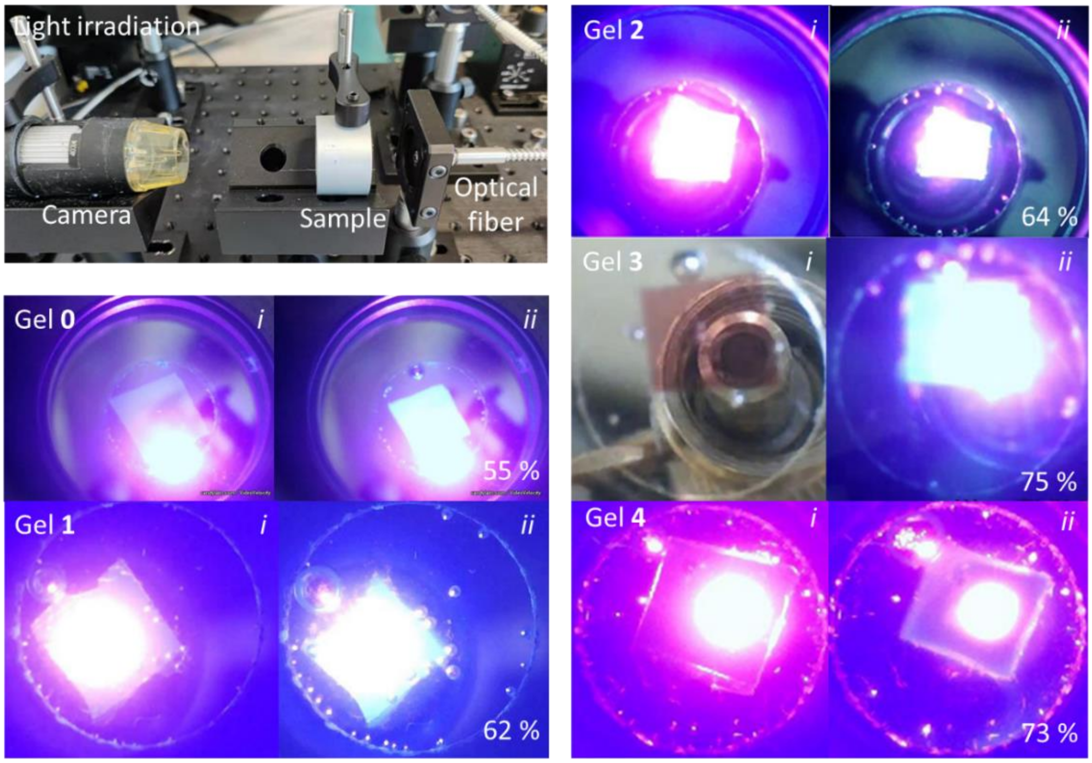

Figure 3.21 Photographs of the UV light irradiation system (top left) and snapshots of videos recording the contraction of gels.

The contraction in volume was quantified by image J software using the surface area. Because the gel thickness is thin and the light beam is powerful, the contraction of gels was considered homogenous over the whole volume. Thus, the relative volume could be estimated by the following equation:

$$V_r = \left(\frac{A_a}{A_b}\right)^{\frac{3}{2}}$$

where V_r is the relative volume of the gel after light irradiation, A_a is the surface area of the contracted gel and A_b is the surface area of gel before irradiation. According to videos, we observed that all gels reached a minimum volume after approximately one and a half hour of light irradiation. Photographs of gels before and after light irradiation are presented in Figure 3.21. After calculation, we determined that the relative volumes of gels range from 55% to 73%. More precisely, the relative volume of Gel **0** decreased from 100% to 55%, which is the smallest among all gels. After irradiation, the relative volumes of Gel **3** and **4** were 75% and 73%, respectively, that are larger than those of gels **1** and **2**. The difference in relative volumes can be explained by the various proportions of AuNPs. In motorized gels, AuNPs serve as reticulating points and thus as crosslinks in the polymeric networks. So Gel **3** and **4** with higher proportions of AuNPs contain more reticulating points, resulting in higher robustness and less contraction of gels.

Spectroscopic characterization of motorized gels containing AuNPs

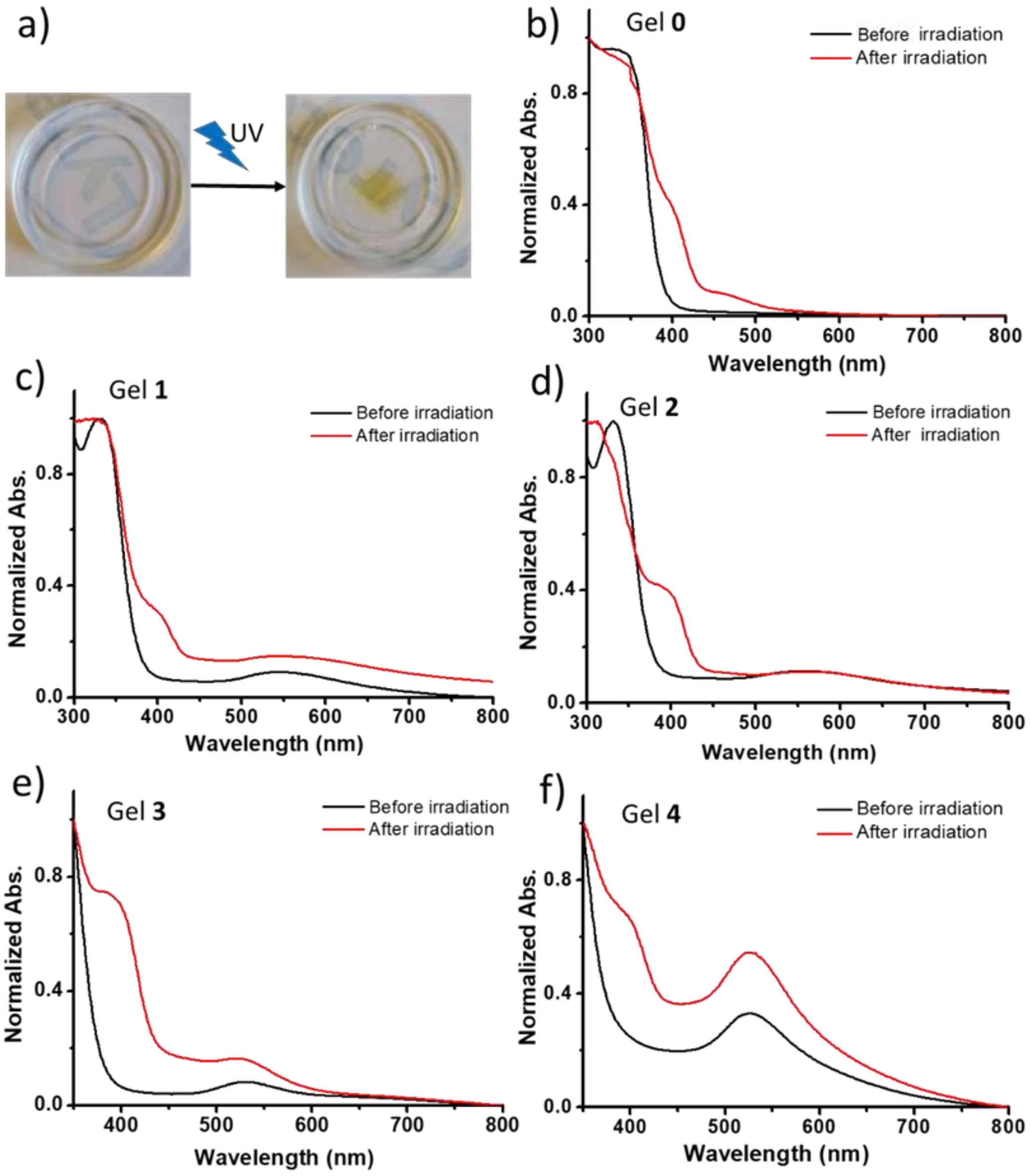

Figure 3.22 (a) Photographs of Gel **0** before and after irradiation; (b-f) UV-Vis spectra of Gel **0** (b), Gel **1** (c), Gel **2** (d), Gel **3** (e), and Gel **4** (f) before (black) and after (red) light irradiation.

As our objective is to tune the optical properties of motorized gels containing AuNPs by controlling irradiation time, we carried out UV-Vis spectroscopy on gels before and after UV light irradiation to evaluate their LSPR behavior (Figure 3.22). Before light irradiation, all gels except Gel **0** displayed a pronounced LSPR band ranging from 530 nm to 550 nm. The absorption wavelengths are similar to that observed in the absorption spectrum of a DMF solution of AuNPs **II** (Figure 3.19a), indicating a good dispersity of the AuNPs in gels. After 1.5 hours of light irradiation, all gels show an absorption band at 400 nm that do not exist in original gels, which probably arises from the degradation (oxidation) of the molecular motors as evidenced by the yellow color of the gels after long irradiation time (Figure 3.22a). Regarding to the LSPR bands in Gel **1**, **2**, **3**, and **4**, unfortunately, no noticeable redshift after light-induced contraction was observed, meaning that the contraction did not lead to significant proximity or aggregation of AuNPs. Indeed, with relatively large relative volumes, it is hard to reach an interparticle distance which can shift plasmonic coupling.

As our AuNPs are hydrophilic, they are able to aggregate in nonpolar solvents. Alternatively, we planned to transfer gels from water to toluene. In doing so, the interparticle distance is efficiently shorten due to aggregation of the AuNPs. Gel **2** was first transferred to acetonitrile, then was immersed in a mixture of acetonitrile:toluene (1:1), finally was brought to toluene. This organic gel is blue and displays a very broad band at 550 nm (Figure 3.23b), suggesting severe aggregation of AuNPs. Subsequent light irradiation was carried out in degassed toluene. After 1 hour irradiation, the relative volume of Gel **2** decreased down to 65% (Figure 3.23a). However, with this relative volume, we still did not observe any redshift of the LSPR band. This might be explained by the severe aggregation of AuNPs, in which AuNPs are so closed that further contraction cannot to vary the interparticle distance sufficiently.

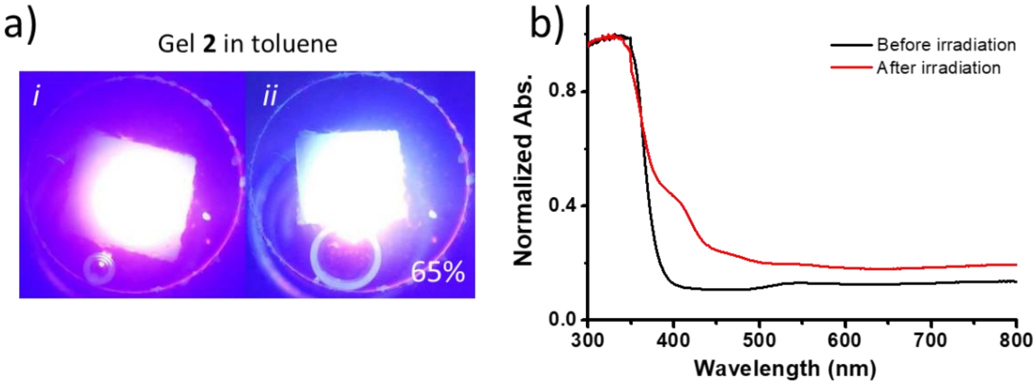

Figure 3.23 (a) Snapshots of a video recording the contraction of Gel **2** before (*i*) and after (*ii*) 1 hour light irradiation; (b) UV-Vis spectra of Gel **2** before (black) and after (red) light irradiation.

3.3.4 Conclusion

In this work, we first synthesized tetra-alkyne terminated molecular motor, bis-aizde PEG chains, and alkyne-coated AuNPs. Subsequent copper-catalyzed ‘click’ reaction of these components afforded chemical gels containing various proportions of AuNPs. Upon exposure to UV light irradiation, all gels showed macroscopic contraction as a result of braiding of PEG chains due to the collective rotary motion of molecular motors. Then the plasmonic properties of these gels before and after contraction were investigated by UV-Vis spectroscopy. Unfortunately, after several attempts, we did not observe any shift of plasmonic band in the contracted gels compared to ones before irradiation. This might be explained by the limited alteration of interparticle distance, which is not enough to give rise to plasmonic coupling of the AuNPs. One possible way to resolve this issue would be to increase the proportion of AuNPs in motorized gels. However, we found that a high proportion of AuNPs results in less contraction of the gels, thus limiting the possibility to reach interparticle distance leading to plasmonic coupling.

Chapter IV. Mechanically-induced Emission Enhancement of Molecular Motors

4.1 Bibliography

4.1.1 Aggregation-caused quenching (ACQ), aggregation-induced emission (AIE), and the working mechanisms

Nowadays, luminescent materials have raised increasing attention due to a variety of applications, ranging from sensors[146] to OLED[147], even for bioimaging[148] and theranostics[149]. The exploration of luminophores is a fascinating but challenging topic. In particular, high intensity, emission tunability (emission wavelength from UV to NIR region), and high stability are of crucial importance in practical applications.

To evaluate the emissive properties of luminescent compounds, characterizations are initially carried out in solution. However, the emissive properties we gained in solution are sometimes different from the ones in aggregate state. A typical illustration on perylene scaffold[150,151] is shown in Figure 4.1a. The emission of perylene in pure THF is strong under UV light irradiation. However, gradually increasing the fraction of poor solvent (e.g. water) reduces its emission intensity. Notably, when the fraction of water is up to 90%, the emission is totally quenched due to the formation of aggregates. This phenomenon is referred as ‘aggregation-caused quenching’ (ACQ), which constitutes one class of concentration quenching effect first discovered by Förster in 1954.[152] ACQ widely exists in aromatic luminophores. In dilute solution, luminophores exhibit an intense light emission intensity. However, in aggregated state, strong π-π stacking interactions between adjacent luminophores populate the non-radiative decay pathway when excitons return to ground state, quenching the emission. In fact, the ACQ process is undesired in real-world applications because luminophores are usually used as aggregates in optoelectronic devices. For instance, luminophores are processed into thin films or crystals for the applications in OLEDs and OFETs that usually require high light emission intensity. Moreover, in the biological applications (e.g. biological imaging), the aggregation of organic luminophores is inevitable in physiological environment or aqueous media.

The discovery of the aggregation-induced emission (AIE)[153] phenomenon brought opportunities for circumventing of ACQ. The concept of AIE was first established by the research group of Tang in 2001. When exploring highly emissive linear and hyperbranched polymers, they accidently found that the 1-methyl-1,2,3,4,5-pentaphenylsilole displayed unusual emissive properties, that is the light emissive intensity in the solid state is much higher than in diluted solution. AIE phenomenon associated with hexaphenylsilole (HPS) is clearly shown in Figure 4.1b, the dilute solution emits negligible fluorescence, while a dramatic emission enhancement is observed when the fraction of water is up to 80%.

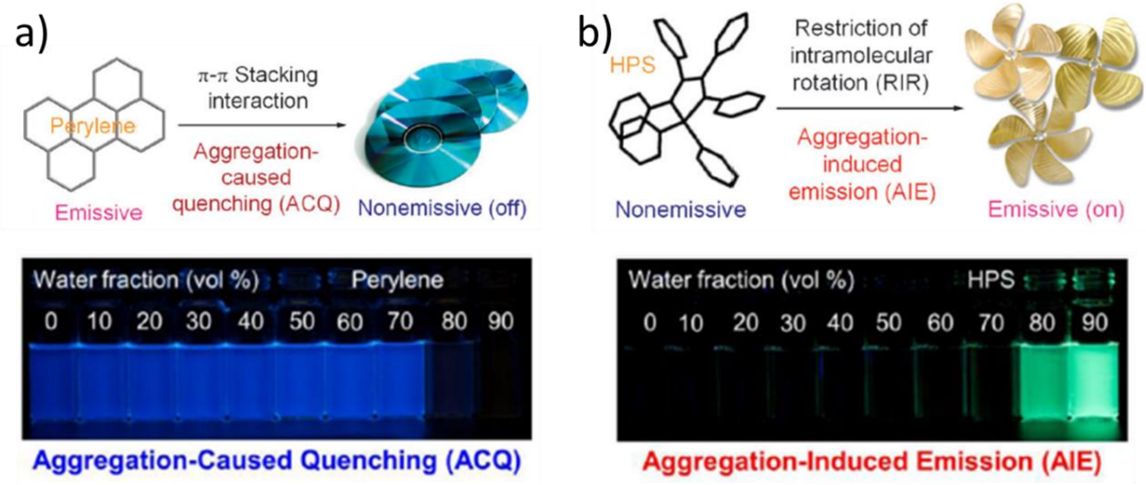

Figure 4.1 (a) Schematic representation aggregation-caused quenching (ACQ) mechanism of perylene, photographs of the fluorescence of THF solution of perylene with various water fraction is shown below; (b) Schematic representation of the aggregation-induced emission (AIE) mechanism of HPS, photographs of the fluorescence of THF solution of HPS with various water fraction is shown below. This figure is adapted from ref.[150].

Since the discovery of the AIE behavior, chemists have focused on unveil its working mechanism. In early researches, AIE behavior was attributed to the restriction of intramolecular rotation (RIR).[150,151,153] For example, the free rotation of phenyl rings of HPS in dilute solution is regarded as the main non-radiative deactivation pathway of excitons. While, in solid state, such propeller-shaped structure of HPS does not only preclude π-π stacking interactions between HPSs, but also restricts the rotation of phenyl rings, thereby emitting intense fluorescence (Figure 4.1b). Progresses on AIE luminogens (AIEgens) have shown that the RIR mechanism is not universal to explain the AIE behavior in particular for AIEgens without rotatable units. In this case, the strong fluorescence in the aggregated state is ascribed to restrictions of molecular vibration (RIV).[154] Nowadays, these two mechanisms of AIE have been merged as restriction of molecular motion (RIM)[150] that is the generally accepted explanation for AIE phenomenon.

In the past two decades, AIEgens have evolved from tedious silole derivatives into a wide variety of molecules, including simple hydrocarbon compounds,[155] heteroatom-containing compounds,[156] organometallic compounds,[157] covalent or supramolecular polymers[158] and so forth[159,160]. Furthermore, with the vigorous development of AIE, AIEgens have became versatile molecules used in diverse applications. For example, AIEgens are extensively exploited in chemical or biological sensors, biomedical areas, stimuli-responsive luminescent materials, and optoelectronic devices (e.g. OLEDs and organic optical waveguides).[150]

4.1.2 Emission of AIEgens in dilute solution

As presented before, strong emission from AIEgens typically exists in the aggregated state. Combining the mechanism of AIE, by internally hindering the intramolecular motion of AIEgens via structural control, high intensity luminescence can be achieved in diluted solutions. In 2005, the group of Tang studied how steric hindrance affect the luminescent properties of HPS derivatives (Figure 4.2a).[161] For instance, isopropyl groups have been attached on phenyl rings of HPS to provide steric hindrance aiming at hindering intramolecular motion. As anticipated, compared with HSP-1 and HSP-2, HSP-3 which displays the highest intramolecular motion (IMM) barrier is the most luminescent, and shows a quantum yield in acetone up to 83%. Similarly, Zhu and collaborators extended this strategy to tetraphenylethene (TPE) derivatives (Figure 4.2b).[162] The introduction of methyl groups on phenyl rings successfully enhances the light emission of TPE in THF solution.

Alternatively, immobilizing AIEgens into confined space proved to be another efficient strategy to achieve strong emission in dilute solutions. The group of Tang reported a host-guest system,[163] in which guest TPE was covalently linked with hosts α-, β-, or γ-CD (Figure 4.3a). In dilute DMSO solution, the TPE moiety was included in α- or β-CD host, and this complexation resulted in strong light emission. In addition, compared with bare TPE, a blueshift in fluorescence was observed for TPE-α-CD and TPE-β-CD, and attributed to a twisted conformation of the encapsulated TPE units. In sharp contrast to α- and β-CD, the large cavity of γ-CD does not allow for the complexation of TPE moieties, thus resulting in only very weak emission in dilute solution.

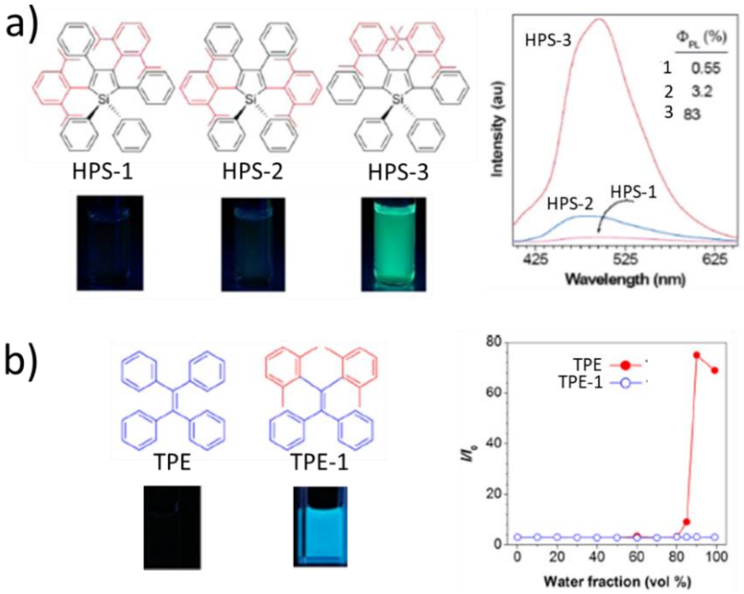

Figure 4.2 Steric hindrance induced emission of (a) HPS in acetone; and (b) TPE in THF. This figure is reproduced from ref.[161,162].

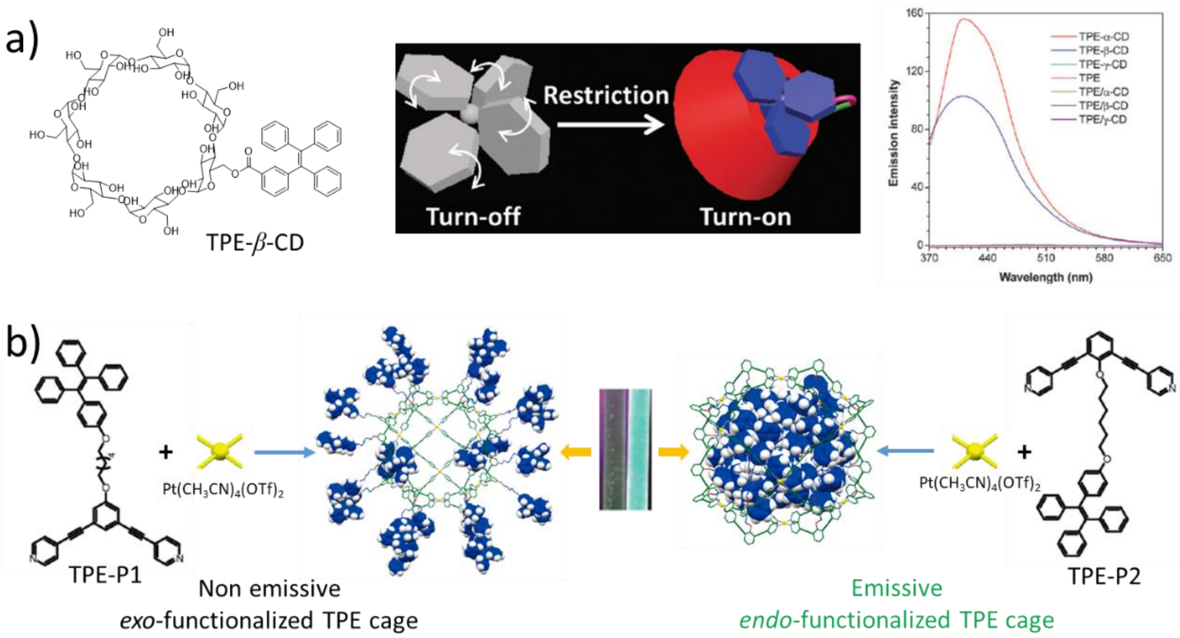

Figure 4.3 (a) Host-guest complexation induced emission of TPE; (b) Formation of *exo*- and *endo*-functionalized TPE cage and their corresponding emissive properties. This figure is adapted from ref.[163,164].

Inspired by the emission mechanism of green fluorescent proteins, Stang and collaborators reported a highly emissive system based on a supramolecular cage (Figure 4.3b).[164] In this work, two distinct *endo*- and *exo*- functionalized TPE cages were synthesized via metal-ligand coordination. In the *exo*-functionalized conformation, TPE subunits are located outside the cage, leading to free molecular motion of the TPEs and thus weak emitting fluorescence. On contrary, in the *endo*-functionalized configuration, the cage serves as a confined environment to encapsulate TPE subcomponents and restricts molecular motion, resulting in bright green emission.

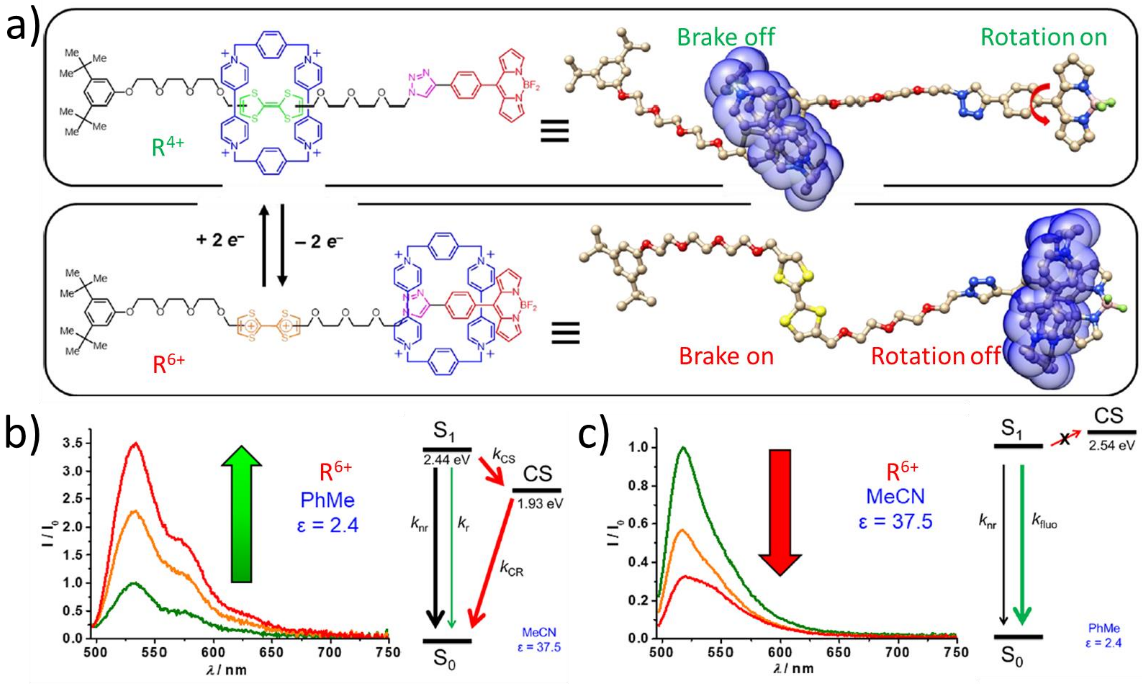

Figure 4.4 Switchable emission of electrochemically-responsive [2]rotaxane. (a) Chemical structure of reduced and oxidized rotaxanes; Corresponding luminescent properties (b) in toluene and (c) in MeCN. This figure is adapted from ref.[165].

Very recently, mechanical bonding induced emission enhancement of AIEgens has been achieved by Stoddart and collaborators (Figure 4.4).[165] The entire system is based on an electrochemically responsive [2]rotaxane in which AIEgen 8-phenyl-substituted boron dipyrromethene (BODIPY) is used as bulky stopper of the axle subcomponent. In the initial state, π-electron poor cyclobis(paraquat-*p*-phenylene) ($CBPQT^{4+}$) macrocycle encircled the π-electron rich tetrathiafulvalene (TTF) unit, leaving free rotation to the BODIPY and thus weak fluorescence. Upon electrochemical oxidation of TTF to TTF^{2+} in toluene, the strong electrostatic repulsion forced $CBPQT^{4+}$ to shuttle towards the BODIPY unit, resulting in an enhancement of emission due to the hindered rotation of BODIPY (Figure 4.4b). Interestingly, in a polar solvent (acetonitrile), charge-transfer process between $CBPQT^{4+}$ and BODIPY occurs by the non-radiative decay of excitons, resulting in a noticeable decrease in fluorescence (Figure 4.4c).

4.2 Emission enhancement of 8-shaped molecular motors

4.2.1 Objectives

In our previously reported study on contractile gels based on light-driven molecular motors, we found that, after UV light irradiation, the contracted gels emitted stronger fluorescence (Figure 4.5).[134] This intriguing phenomenon encouraged us to unveil the underlying mechanism. Considering the structural features of molecular motors, we postulated that the irradiation-induced emission enhancement is probably related to the aggregation-induced emission (AIE) property of molecular motors.[166] Before UV light irradiation, molecular motors are in a relatively ‘free’ state, meaning that excitons could decay in a non-radiative pathway (intramolecular motion), thereby giving rise to weak emission (Figure 4.5a). However, after irradiation, the braided polymer chains endow molecular motors with structural strain. In this case, the intramolecular motion becomes sufficiently restricted and lead to emission enhancement (Figure 4.5b).

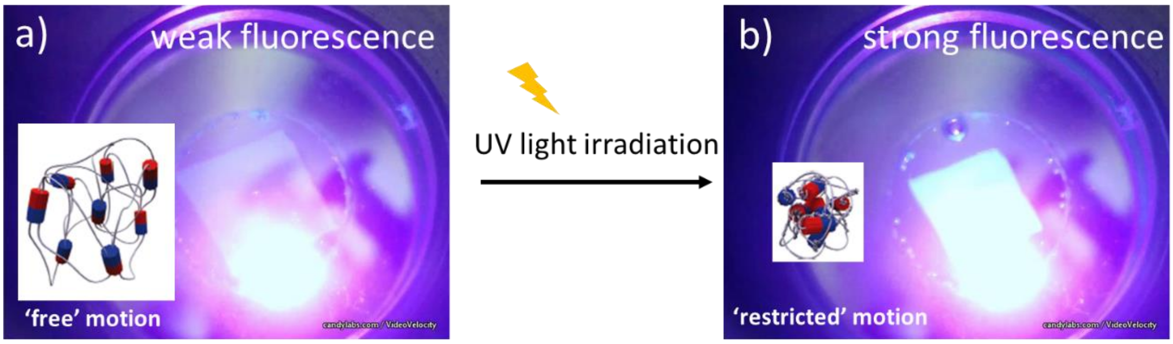

Figure 4.5 Snapshots of a video recording of the contraction process of a contractile gel. Insets correspond to schematic illustrations of motorized gels before and after 1 h irradiation in water.

This observation prompted us to explore the AIE property of molecular motor to develop an emission-tunable system. For that, we designed an 8-shaped molecular motor in which azide-terminated PEG chains on the upper half of the molecular motor are intramolecularly linked with the alkyne-terminated PEG chains on the lower half via ‘CuAAC’ click reaction (Figure 4.6). According to our previous description,[134] UV light irradiation should trigger the continuous rotation of 8-shaped molecular motors, and mechanically enforce coiling of self-entangled PEG chains. As a result of PEG chains entanglement, the ‘free’ molecular motion in twisted molecular motor could be efficiently reduced, resulting in stronger fluorescence through a so-called ‘mechanically-induced emission enhancement’ (MIEE) mechanism.

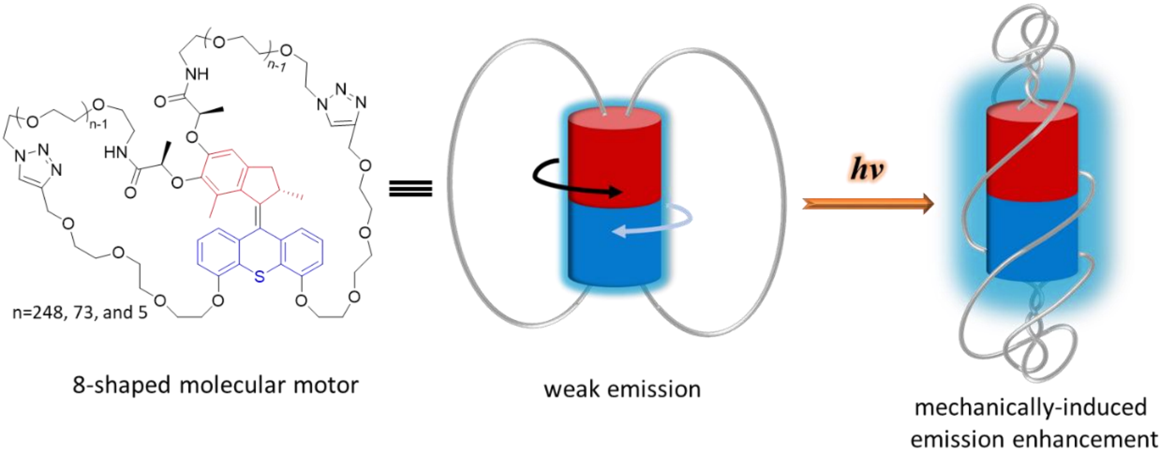

Figure 4.6 Chemical structure of 8-shaped molecular motor and schematic representation of the mechanically-induced emission enhancement.

4.2.2 Synthesis and characterization of 8-shaped molecular motors

To study the MIEE behavior, we designed 8-shaped molecular motors with 3 different chain lengths (n = 248, 73 and 5 (number of ethylene glycol units per chain)). For that, compounds N_3-PEG$_{10000}$-NH_2, N_3-PEG$_{3000}$-NH_2, and N_3-PEG$_{300}$-NH_2 were used to functionalize the upper half of molecular motor. While N_3-PEG$_{10000}$-NH_2 and N_3-PEG$_{3000}$-NH_2 are commercially available, N_3-PEG$_{300}$-NH_2 was synthesized in 3 steps from hexaethylene glycol. Upon addition of an excess of tosyl chloride in the presence of triethylamine, the ditosylate intermediate was formed and then reacted with an excess of sodium azide at 80°C to give the corresponding bisazide compound. Without further purification, the formed bisazide intermediate was directly dissolved in a mixture of Et_2O/THF/1M HCl (5/1/5), then a solution of triphenylphosphine in Et_2O was slowly added dropwise, leading to the formation of N_3-PEG$_{300}$-NH_2 with a good yield.

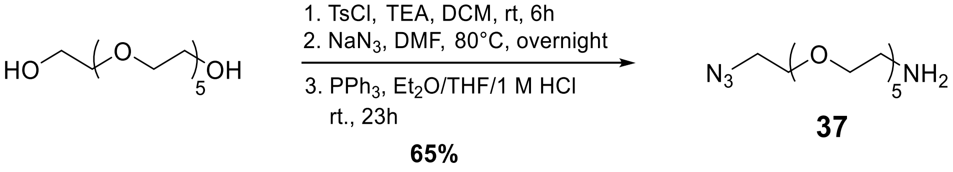

Scheme 4.1 Synthetic route for N_3-PEG$_{300}$-NH_2.

Amidation reaction between molecular motor **23** (synthesized in chapter III) and N_3-PEG-NH_2 allowed the formation of star-shaped compounds **S1**, **S2**, and **S3**. First, HOBt and EDC were added to a highly concentrated solution of compound **23** in dichloromethane affording the corresponding benzotriazole activated ester. Then N_3-PEG_{10000}-NH_2, N_3-PEG_{3000}-NH_2, or N_3-PEG_{300}-NH_2 was added, and star-shaped compounds were obtained after stirring at room temperature overnight. For products **S1** and **S2**, purification was performed by reversed-phase chromatography due to their high polarity. In contrast, compound **S3** was obtained after flash silica column chromatography in excellent yield.

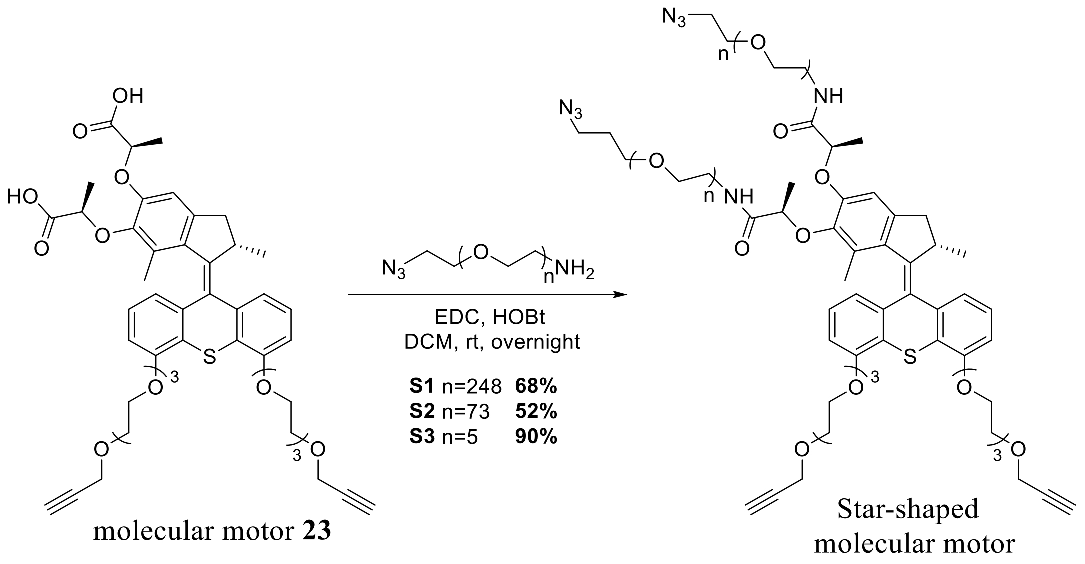

Scheme 4.2 Synthetic route for star-shaped molecular motors **S1**-**S3**.

8-shaped molecular motors were synthesized according to the protocol described in our previous work.[134] In order to avoid intermolecular 'CuAAC' click reaction, the reaction was performed in highly diluted condition. First, copper catalyst and PMEDTA were dissolved in DMF (degassed with three freeze-thaw cycles). Then a solution of star-shaped molecular motor **S1**, **S2**, or **S3** in degassed DMF was slowly added dropwise into above mixture using syringe pump at a rate of 0.75 mL/h. After addition completion, the mixture was stirred at 95°C for 12 hours affording 8-shaped molecular motors **E1**, **E2**, or **E3**, respectively. Similar to star-shaped molecular motors, **E1** and **E2** with long PEG chains were purified by reversed-phase column chromatography, while **E3** was purified by high performance liquid chromatography (HPLC).

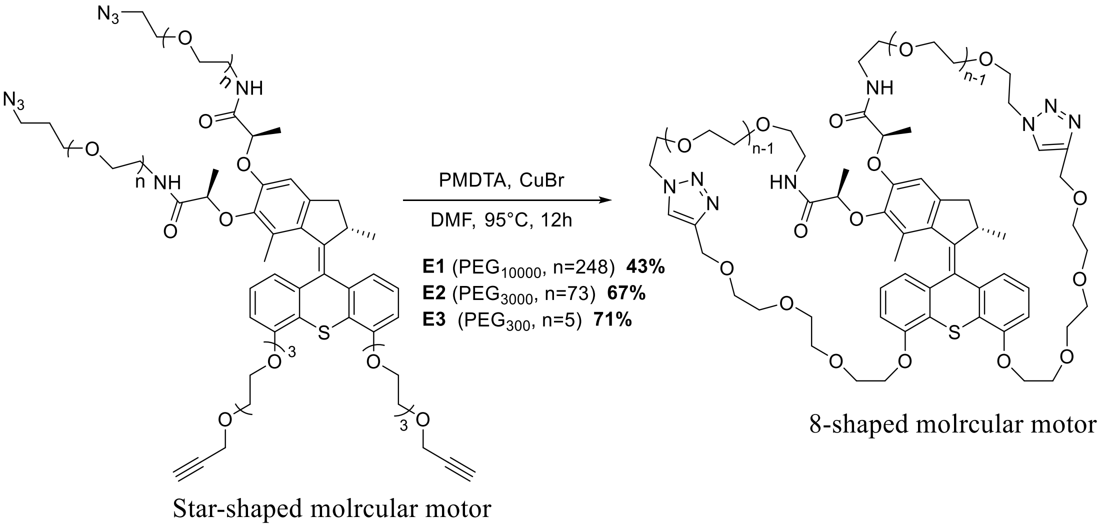

Scheme 4.3 Synthetic route for 8-shaped molecular motors **E1**, **E2**, and **E3**.

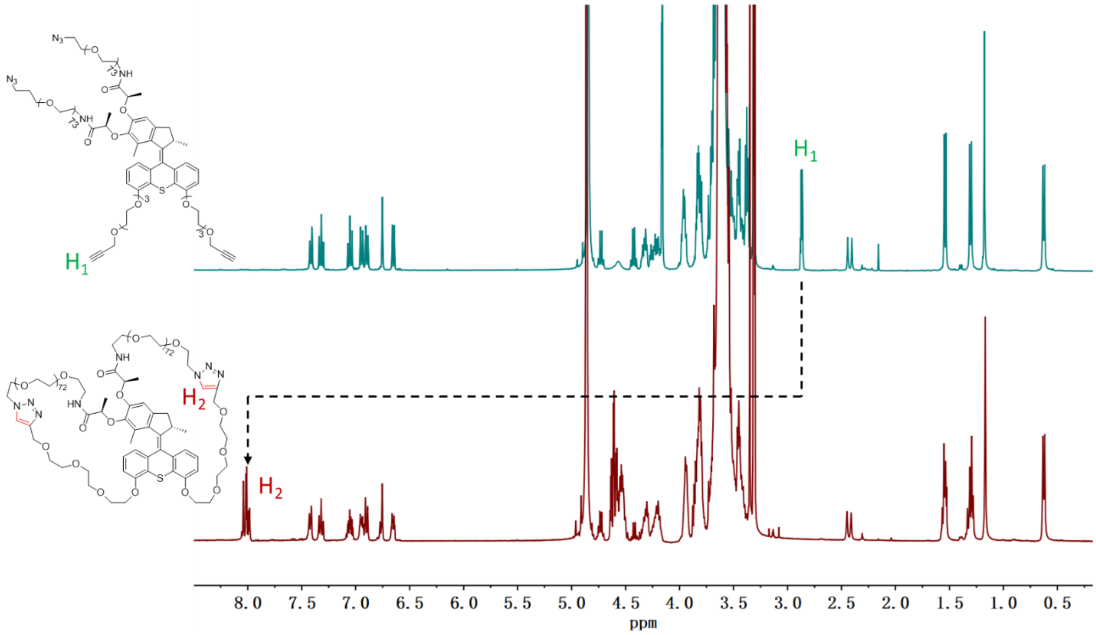

Figure 4.7 ^1H NMR spectra of **S2** (top) and **E2** (bottom) in CD_3OD.

The successful formation of 8-shaped molecular motors **E1**, **E2** and **E3** was confirmed by ^1H NMR and mass spectra. As shown in Figures 4.7 and 4.8, the signal corresponding to proton H_1 (2.8 ppm) on the alkyne group of motor **S2** and **S3** disappeared after reaction, and a signal corresponding to H_2 as multiple peaks at downfield chemical shift was observed in **E2** and **E3**, indicating the successful formation of the triazole moiety via click reaction. Similarly to **E2** and

E3, **E1** showed the same change in ^{1}H NMR spectrum (annexes section). In addition, HRMS (ESI+) experiment further confirmed the formation of the 8-shaped molecular motor **E3** (see experimental section).

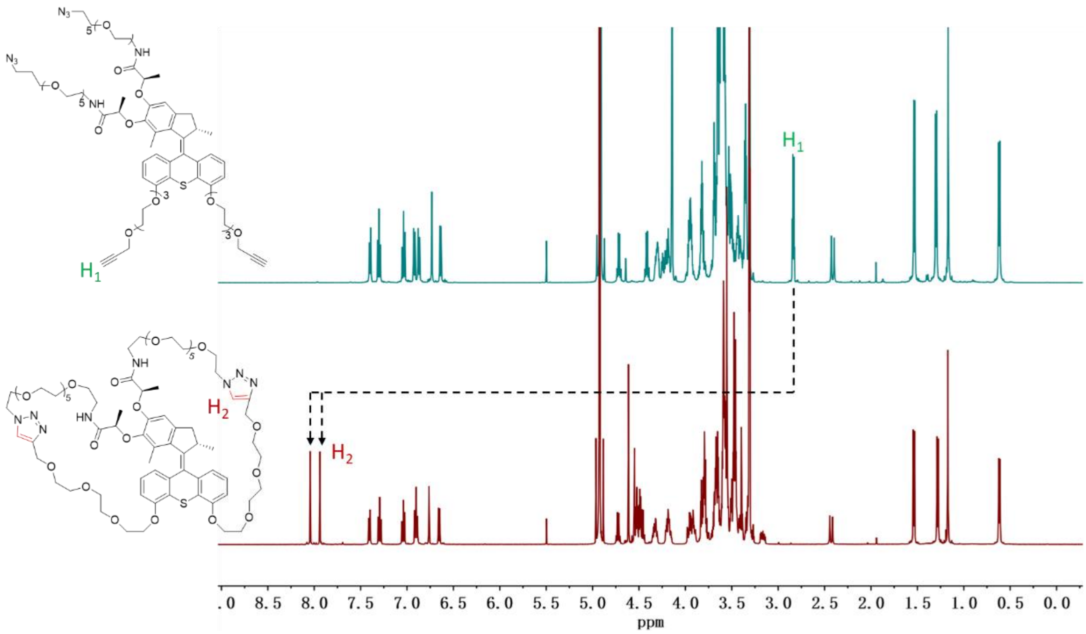

Figure 4.8 ^{1}H NMR spectra of **S3** (top) and **E3** (bottom) in CD_3OD.

4.2.3 Aggregation-induced emission (AIE) of molecular motor

As our 8-shaped system is designed according to a possible AIE property of molecular motors, we first established whether or not molecular motor **M1** (Figure 4.9a) displays AIE behavior. As shown in Figure 4.9b, a solution of **M1** in pure THF exhibits negligible light emission under 366 nm light irradiation. By adding water, a poor solvent for **M1**, stronger light emission is directly observed by naked eyes. In particular, when the fraction of water is up to 90%, the solution emits bright blue fluorescence. Besides visual observations, the AIE behavior of **M1** was also studied by photoluminescence spectroscopy. As shown in Figure 4.9c, in pure THF, **M1** displays a weak emission band at 465 nm. When the water fraction reaches 80%, the emission is significantly enhanced without change in the spectral profile. By further increasing the water fraction to 90%, a blueshift in emission occurs, suggesting the formation of large aggregates of **M1**. In this case, the intramolecular motion of **M1** is sufficiently suppressed, and the emission intensity increases by 20-time compared to that of dilute solution. These results confirm that molecular motor **M1** manifests AIE characteristics.

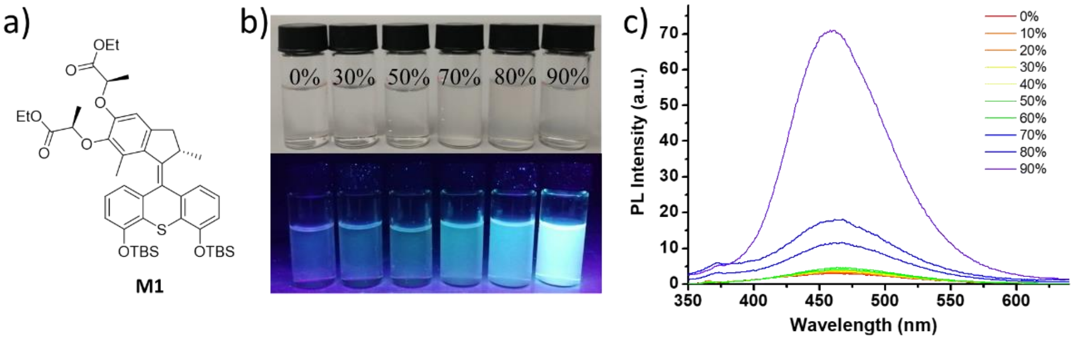

Figure 4.9 (a) Chemical structure of **M1**; (b) Photographs of **M1** in THF and THF/H_2O mixtures (water fraction: 0, 30, 50, 70, 80 and 90%). Top: under sunlight, bottom: under 366 nm irradiation; (c) Emission spectra of **M1** in THF and THF/H_2O mixtures (water fraction: 0-90%) (c=0.1 mM, λ_{ex}=330 nm).

4.2.4 Irradiation and characterization of 8-shaped molecular motors

4.2.4.1 Unidirectional rotation of molecular motor

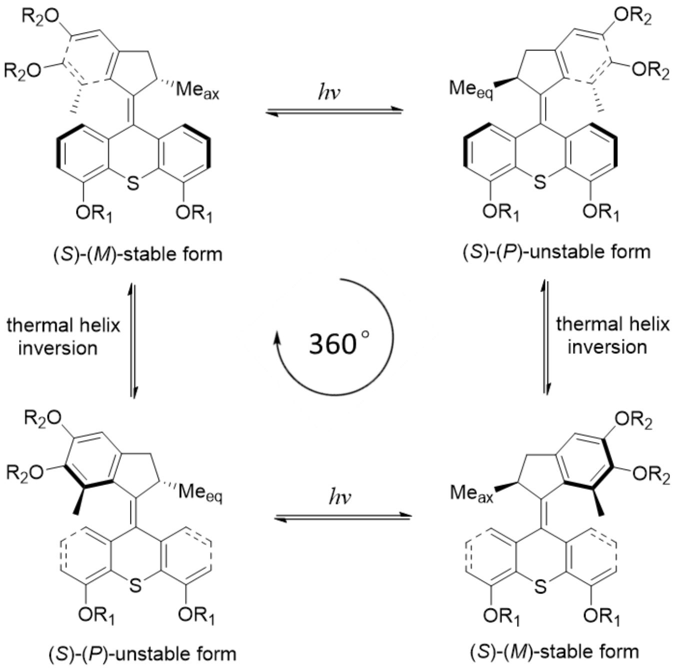

Figure 4.10 Schematic representation of a rotation cycle of molecular motor. This figure is reproduced from ref.[134].

To well understand the MIEE of 8-shaped molecular motors, we recall the rotation process of molecular motor used in this project (Figure 4.10). A complete 360° rotation of our molecular motor consists in four successive steps (two photo-isomerization processes and two THI processes), which are identical to Feringa's motors presented in chapter III. We found previously, at room temperature, the rotation speed of our molecular motor is up to megahertz according to DFT calculation.[134] This means that the rate-limiting step (THI process) could take place in a very short time at room temperature and preclude to observe the unstable form during rotation. In addition, the two stable forms have the same configuration due to the symmetry of the lower half. Thus, during rotation process, the ^{1}H NMR, UV-Vis, and emission spectra of this motor remain unchanged.

4.2.4.2 Influence of lamp power

After confirming the AIE behavior of molecular motor **M1**, we then initiated UV light irradiation experiments. Considering that light beam with a strong power might cause decomposition of molecular motors, so we first studied the influence of the lamp power aiming at looking for the optimal power. A solution of 8-shaped molecular motor **E1** in degassed toluene (0.03 mM) was used towards this goal. First, the solution in a quartz cuvette was irradiated with a LED fiber with a power output of 5 mW/cm^2. The time-dependent optical properties under light irradiation were investigated by UV-Vis absorption spectroscopy and photoluminescence spectroscopy.

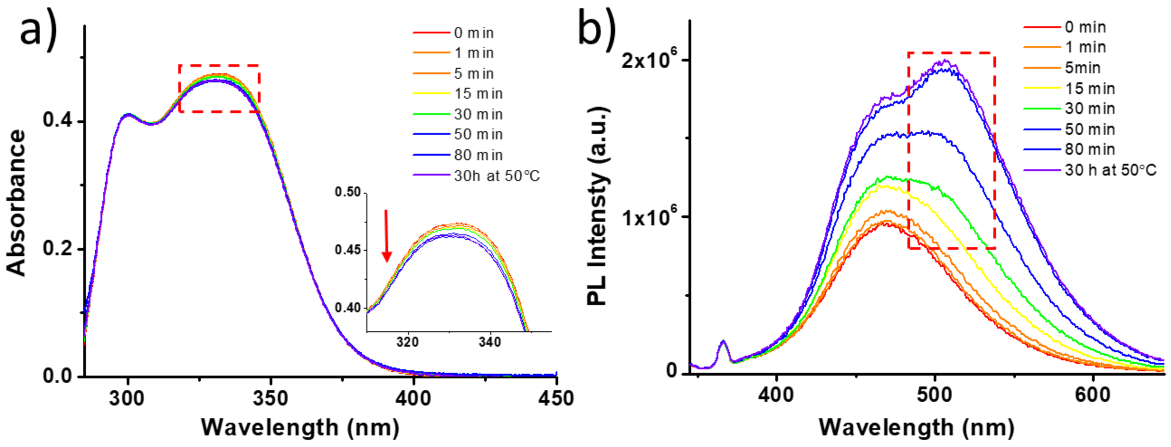

Figure 4.11 Optical properties of **E1** in toluene during UV light irradiation (*c*=0.03 mM, lamp power=5 mW/cm^2) (a) UV-Vis absorption spectra; (b) Emission spectra, λ_{ex}=330 nm.

As presented in Figure 4.11, during the first 15 minutes of irradiation, the absorption band of **E1** at 330 nm remains essentially unchanged and the emission intensity gradually increases without spectral profile change, suggesting there is no conformational change in the molecular motor core. This can be explained by the MIEE behaviour of 8-shaped motor. For irradiation time longer than 15 minutes, a decrease in absorption intensity and a broadening of the emission band, accompanied by the appearance of a small emission band at 520 nm occurs. This phenomenon can be explained ether by the 'trap' of unstable state or by the degradation of molecular motors. To get a clear insight into these spectral changes, we heated the solution for 30 hours at 50 °C aiming to accomplish THI process to reach again the stable state. Unfortunately, we did not observe any change in the optical spectra, and thus attributed these spectral changes to decomposition of the molecular motors induced by the strong power of the lamp.

To avoid such degradation, we then lowered the lamp power output to 1.2 mW/cm^2. With this weaker power, the UV-Vis spectrum of **E1** remained unchanged even after 130 minutes of irradiation. While the emission intensity increased without spectral profile change (Figure 4.12). Moreover, the emission intensity reached a plateau after 100 minutes of irradiation. This optical behaviour is ascribed to the light-driven rotation of molecular motors, which only resulted in braiding of the PEG chains without structural change in molecular motors. In this case, molecular motors are confined in a small space where the molecular motion is hindered, leading to emission enhancement.

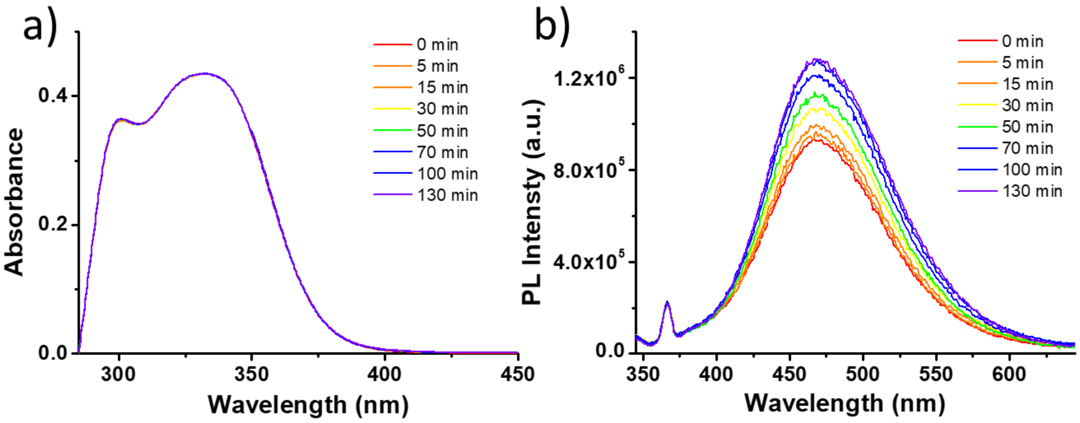

Figure 4.12 Optical properties of **E1** in toluene during UV light irradiation (*c*=0.03 mM, lamp power=1.2 mW/cm^2) (a) UV-Vis absorption spectra; (b) Emission spectra, λ_{ex}=330 nm.

To verify this hypothesis, we investigated the optical properties of star-shaped molecular motor **S1** under UV light irradiation. As shown in Figure 4.13, after 90 minutes of irradiation, the absorption and emission spectra of **S1** essentially remain unaltered, suggesting unchanged molecular structure after irradiation. Indeed, in such 'open' conformation, the PEG chains could not braid upon continuous rotation of the motor. Hence we prove that the emission enhancement of 8-shaped molecular motors originates from mechanical coiling of the PEG chains.

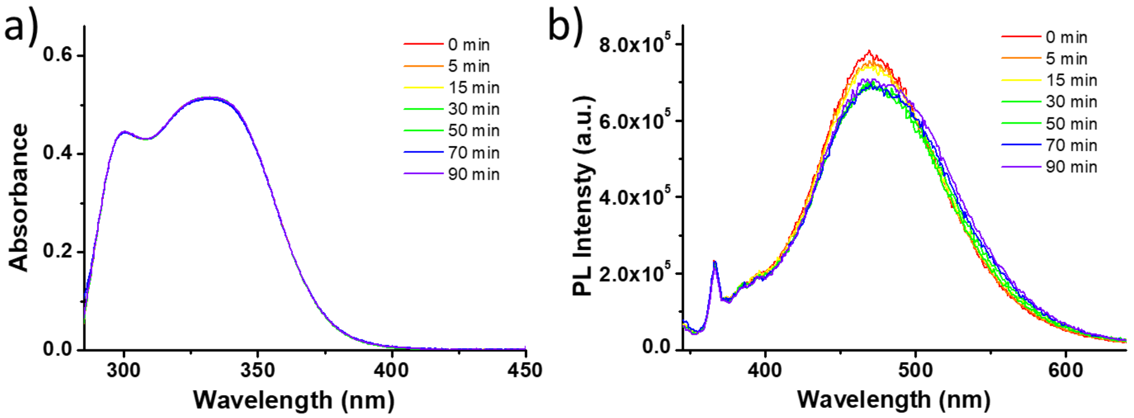

Figure 4.13 Time-dependent optical properties of star-shaped molecular motor **S1** under UV light irradiation (c=0.03 mM, lamp power=1.2 mW/cm^2). (a) UV-Vis absorption spectra; (b) Emission spectra, λ_{ex}=330 nm.

Based on these results, the lamp power output was fixed at 1.2 mW/cm^2 for the following irradiation experiments.

4.2.4.3 Influence of solvent

Although the fluorescence of **E1** can be enhanced by UV light irradiation, it only increased by 0.3 times in toluene. As described in the literature, one way to enhance the emission intensity of AIEgens is to increase the viscosity of solvents.[167,168] In order to improve the emission enhancement in our system, three solvents including toluene, THF, and H_2O were used to investigate the effect of solvent on MIEE. As shown in Figure 4.14, before UV light irradiation, the emission intensity of **E1** is dependent on the viscosity of solvents. More precisely, the fluorescence in toluene (0.56 cP, viscosity) is much weaker than that in water (0.89 cP, viscosity), but is stronger than in THF (0.46 cP, viscosity).

We then carried out irradiation experiments on these solutions. As suggested by Figure 4.14, after long time irradiation, the absorption spectrum of 8-shaped molecular motor **E1** in THF or toluene remains unchanged. Meanwhile, the emission intensities of **E1** in toluene and THF increases gradually during irradiation, and is eventually enhanced by 0.3 times and 0.5 times, respectively. On the other hand, absorption intensity of aqueous solution of **E1** decreases slightly during irradiation, which probably arises from the degradation of **E1**. Compared to the toluene or THF solution, after 140 minutes of irradiation, the emission intensity essentially remains unchanged. We first assumed that **E1** did not rotate in aqueous solution, but that is against the contraction of motorized gel in water (presented in Chapter III). Another rational explanation is that, in highly viscous solution, the emission intensity of **E1** is dominated by the viscosity and the braiding of PEG chains no longer contribute to emission enhancement. According to these observations, we decided to use THF as solvent for further experiments.

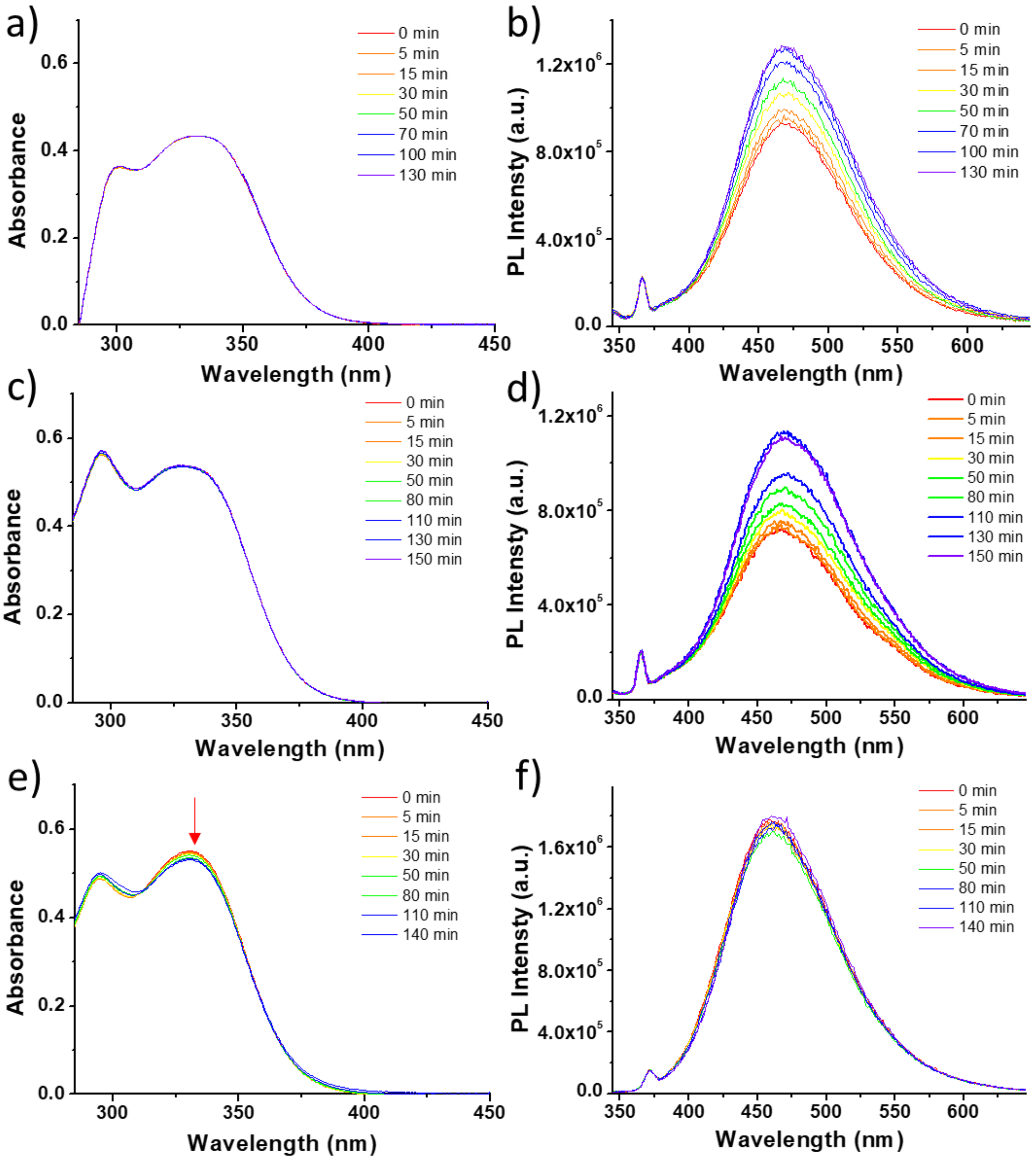

Figure 4.14 Time-dependent (a, c, e) absorption and (b, d, f) emission spectra of **E1** under UV light irradiation in (a, b) toluene, (c, d) THF, and (e, f) H_2O. *c*=0.03 mM, lamp power=1.2 mW/cm^2, λ_{ex}=330 nm.

4.2.4.4 Influence of the PEG chains length

In our previous studies on motorized gels, the PEG chains length shows influence on the macroscopic contraction and mechanical behaviour.[134,169] Thus, we were wondering whether the PEG chains length could affect the MIEE preopeties of 8-shaped molecular motors. To get a better insight into that, we thoroughly studied the optical properties of 8-shaped molecular motors **E1**, **E2**, and **E3** during UV light irradiation by UV-Vis and photoluminescence spectroscopies.

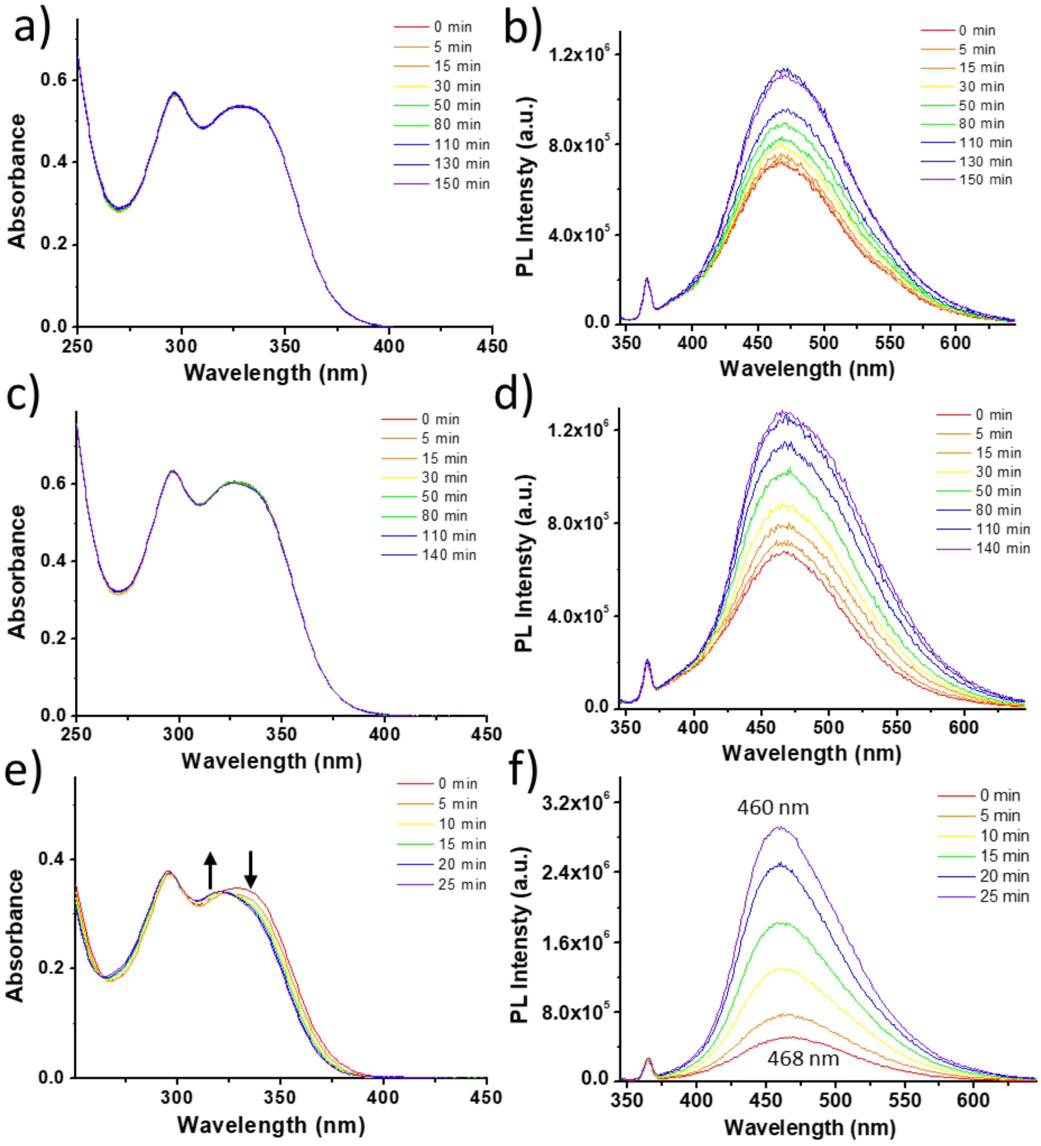

Figure 4.15 Time-dependent optical properties of THF solutions of 8-shaped molecular motors **E1** (0.03 mM), **E2** (0.03 mM), and **E3** (0.02 mM) under UV light irradiation. (a) UV-Vis absorption spectra of **E1**; (b) Emission spectra of **E1**; (c) UV-Vis absorption spectra of of **E2**; (d) Emission spectra of of **E2**; (e) UV-Vis absorption spectra of **E3**; (f) Emission spectra of **E3**. Lamp power=1.2 mW/cm^2, λ_{ex}=330 nm.

Upon UV light irradiation, the emission intensity of **E1** (PEG_{10000}) increases continuously without spectral profile change, and reaches a maximum value with a 0.5 time increase (Figure 4.15b). Meanwhile, there was no change in the UV-Vis spectra of **E1**. Similarly to the optical behaviour of **E1**, UV-Vis spectra of **E2** remained overlapped during irradiation. However, a 0.9-times emission enhancement was observed after 110 minutes. These results suggest that, with such long lengths, the conformation of molecular motor core remains unchanged after braiding of the PEG chains.

Before irradiation, the absorption and emission spectral profiles of **E3** (PEG_{300}) are similar to those of **E1** and **E2**. As presented in Figure 4.15e, the UV-Vis spectrum displays two absorption bands at 330 nm and 296 nm, respectively. The emission peak is observed at a wavelength of 468 nm (Figure 4.15f). However, during irradiation, the optical properties of **E3** differ from **E1** and **E2**. Upon UV light irradiation, the absorption intensity of **E3** at 330 nm decreases and, after 25 minutes, the photostationary state (PSS) is reached. Meanwhile, the absorption band at 330 nm shifts to 320 nm. These spectral changes can be explained by a conformational change of **E3**. In other words, **E3** is in a 'tensed' state which has highly conformational strain due to the braiding of PEG chains. In this case, the intramolecular motion of 'tensed' **E3** should be severely suppressed. As a result, after 25 minutes of irradiation, the emission intensity of **E3** increases by 5-times, which is much higher than those of **E1** and **E2**. Moreover, the emission band of such 'tensed' **E3** shows a blueshift due to its twisted conformation.[163]

To gain a deep insight into the conformational changes in 8-shaped molecular motors during UV light irradiation, circular dichroism (CD) experiments were performed. As shown in Figure 4.16a and 4.16b, before light irradiation, the CD signals of **E1** and **E2** are identical, indicating that the molecular motors possess the same chirality. After irradiation, the CD spectra of **E1** and **E2** remains unchanged compared to the ones before irradiation, indicating there is no change in chirality. Interestingly, due to significant differences in PEG length, **E3** exhibits a different behaviour during the irradiation process. As presented in Figure 4.16c, upon irradiation, the CD signal at 340 nm gradually decreases, associated with the braiding of PEG chains. The CD signal reaches a plateau after 25 minutes of irradiation, which is agreement with the observations from UV-Vis and emission spectra (Figure 4.16e and 4.16f). It should be noted that we did not observe any inversion of CD signals or dramatic decrease in CD signals for **E3** during irradiation process. Hence we concluded that irradiation only results in the stable state of **E3** rather than its unstable state.

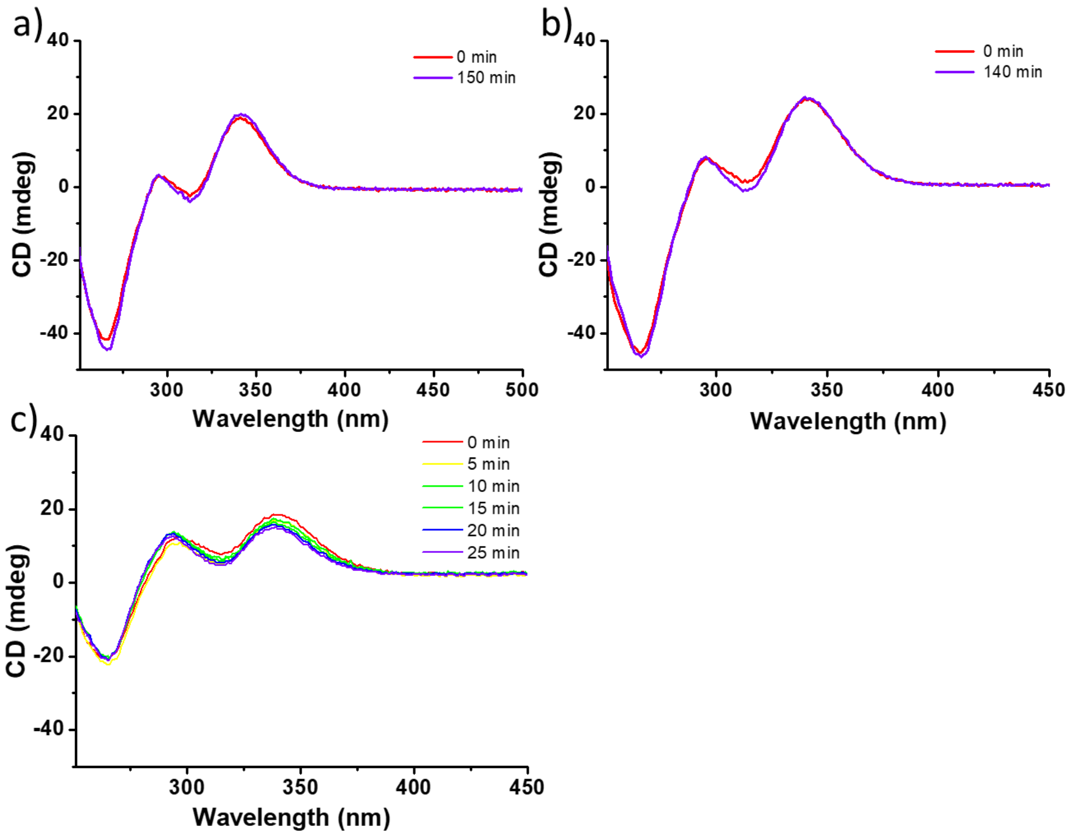

Figure 4.16 CD spectra of (a) **E1** (0.03 mM), (b) **E2** (0.03 mM), and (c) **E3** (0.02 mM) as a function of irradiation time. Lamp power=1.2 mW/cm^2.

4.2.5 Mechanically-induced emission enhancement of 8-shaped molecular motor E3

4.2.5.1 Characterization of the light-driven rotation of E3

In comparison to **E1** and **E2**, molecular motor **E3** shows a large emission enhancement and considerable spectral change in absorption and CD spectra during UV light irradiation. These unique optical properties encouraged us to focus on investigation on **E3**.

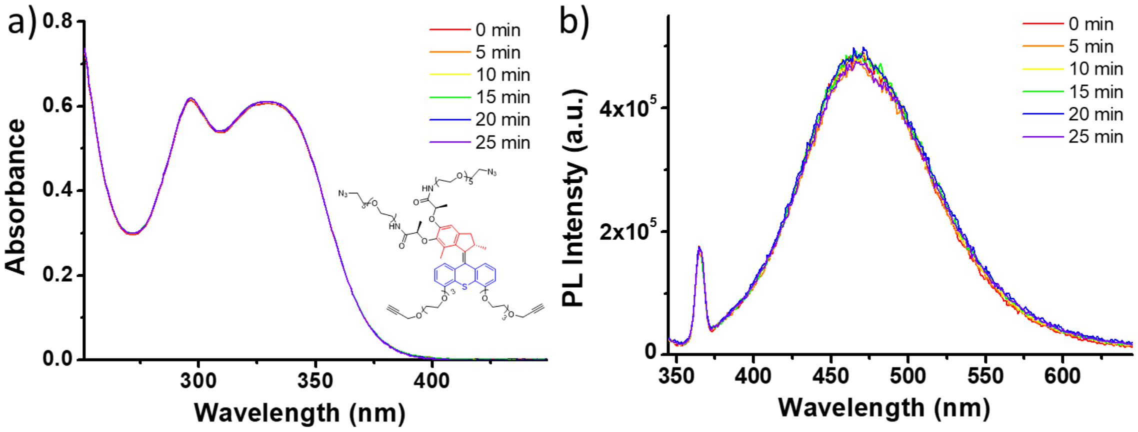

Figure 4.17 Time-dependent optical properties of 0.03 mM solution of **S3** in THF under UV light irradiation. (a) UV-Vis spectra. Inset is the chemical structure of reference compound **S3**; (b) Emission spectra, λ_{ex}=330 nm. Lamp power=1.2 mW/cm^2.

As a control experiment, the optical properties of reference compound **S3** were studied. As presented in Figure 4.17, after 25 minutes of irradiation, the UV-Vis and emission spectra of star-shaped **S3** remain unchanged, which is very different from those of 8-shaped **E3**. These experiments suggest that the conformation of **S3** does not change upon UV irradiation, which was further verified by Ultra Performance Liquid Chromatography (UPLC). Indeed, as shown in Figure 4.18, the composition of **S3** does not change after 25 minutes irradiation. These observations indicate that the optical properties of star-shaped molecular motor **S3** do not vary upon light irradiation.

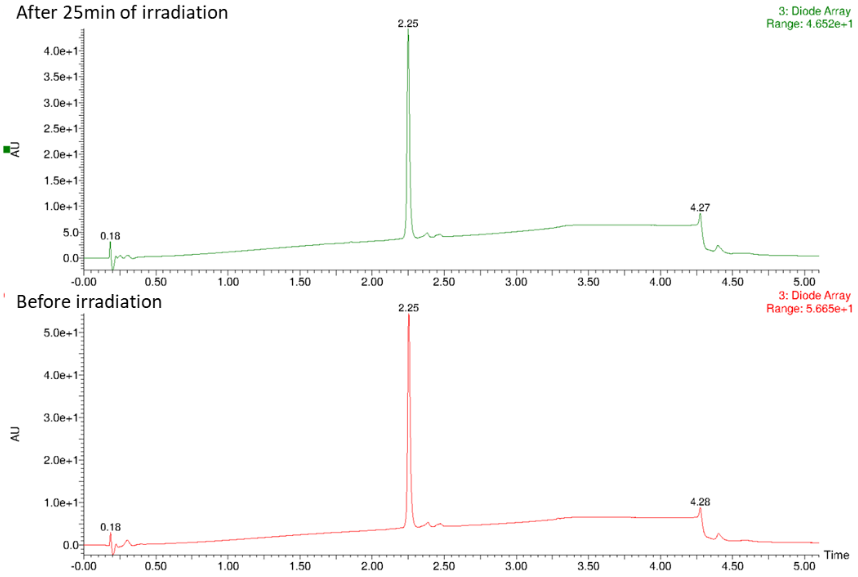

Figure 4.18 UV chromatograms of **S3** before irradiation (bottom) and after irradiation for 25 minutes (top).

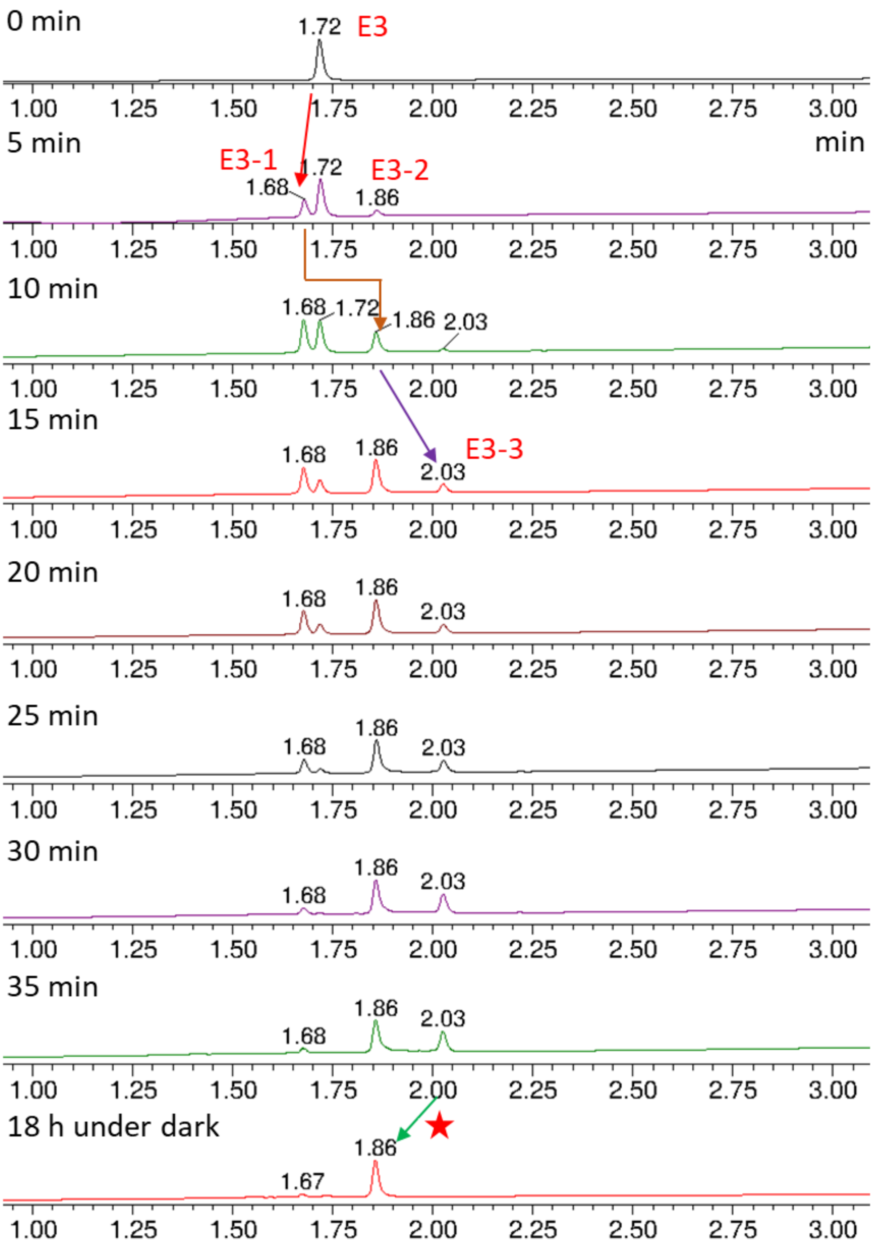

Figure 4.19 UV chromatograms of **E3** for different irradiation times and after 18 h in the dark. Lamp power=1.2 mW/cm^2.

We also monitored the rotation process of 8-shaped **E3** by UPLC (Figure 4.19). Before UV light irradiation, the retention time of **E3** is 1.72 min. Upon light irradiation, new species **E3-1** and **E3-2** (retention time 1.68 and 1.86 min, respectively) appeared, which possess the same mass as **E3**. Subsequent irradiation led to an increase in proportions of **E3-1** and **E3-2**, along with the decrease of **E3**. Furthermore, for 15 to 35 minutes irradiation, the **E3-1**/**E3-2** ratio gradually decreased over time and **E3-2** became the main component. It uncovers that **E3-2** comes directly from **E3-1** rather than from **E3**. After 10 minutes irradiation, a small amount of **E3-3** (retention time 2.03 min) appeared as a fourth component in the system. Moreover, the proportion of **E3-3** continuously increased accompanied by a decrease in **E3-2**. After 35 minutes irradiation, the proportion of **E3-3** reached a plateau. According to these experiments, the transformation of **E3** upon light irradiation can be clearly established, that is **E3** → **E3-1** → **E3-2** → **E3-3**. It should be highlighted that all components observed by UPLC showed the same mass, indicating that **E3** did not undergo decomposition and that newly formed components stemmed from the light-driven rotation of the molecular motor core.

Unexpectedly, **E3-3** could transform back to **E3-2** in the dark via thermal relaxation at room temperature. This interesting phenomenon might be explained by the highly conformational strain of **E3-3**. Compared to other components, **E3-3** is in a highly 'tensed' state owing to more braiding turns of the PEG chains. In this case, it could spontaneously relax to relatively 'stable' **E3-2** by relieving the conformational strain.

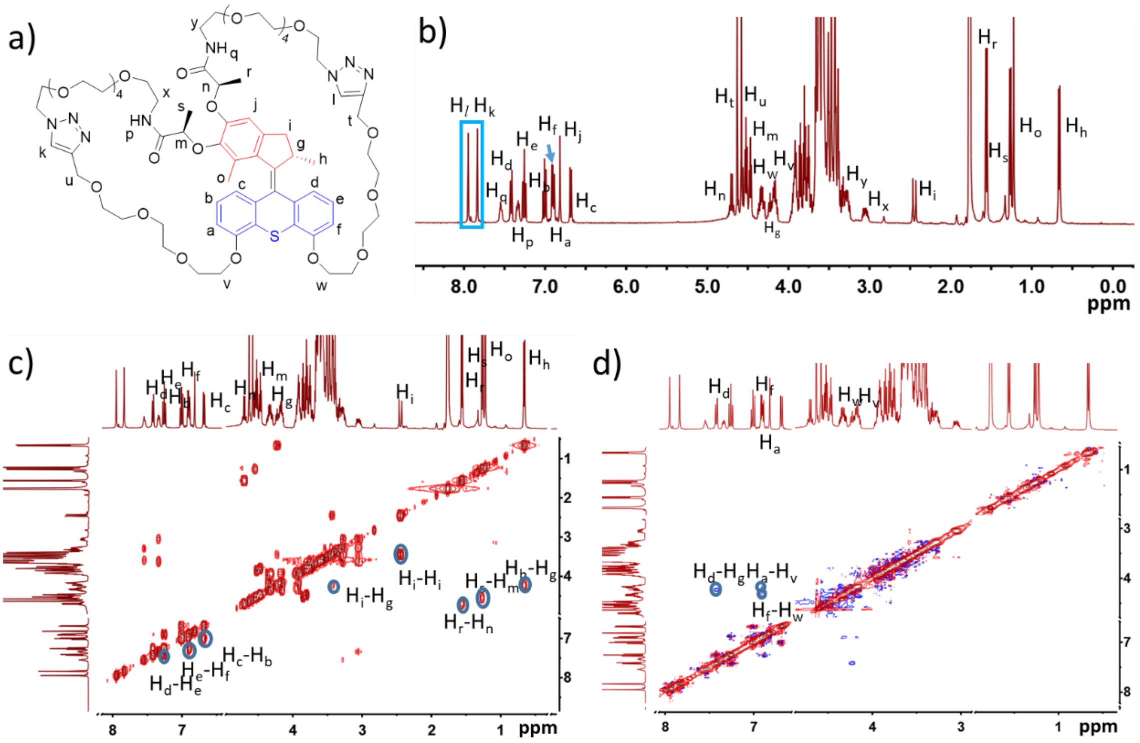

Figure 4.20 NMR analysis of non-irradiated **E3** (400 MHz, THF-d_8, 298K). (a) Chemical structure of **E3**; (b) ^{1}H NMR spectrum; (c) ^{1}H-^{1}H COSY NMR spectrum; (d) 2D NOESY NMR spectrum.

To elucidate the light-triggered rotation process of **E3**, we recorded ^{1}H NMR spectra during light irradiation. In order to avoid the photo-oxidation, irradiation experiments were conducted in a Young's NMR tube. Assignment of protons in non-irradiated **E3** was accomplished (Figure 4.20b) with the help of two-dimensional NMR (2D NMR, Figure 4.20c and 4.20d).

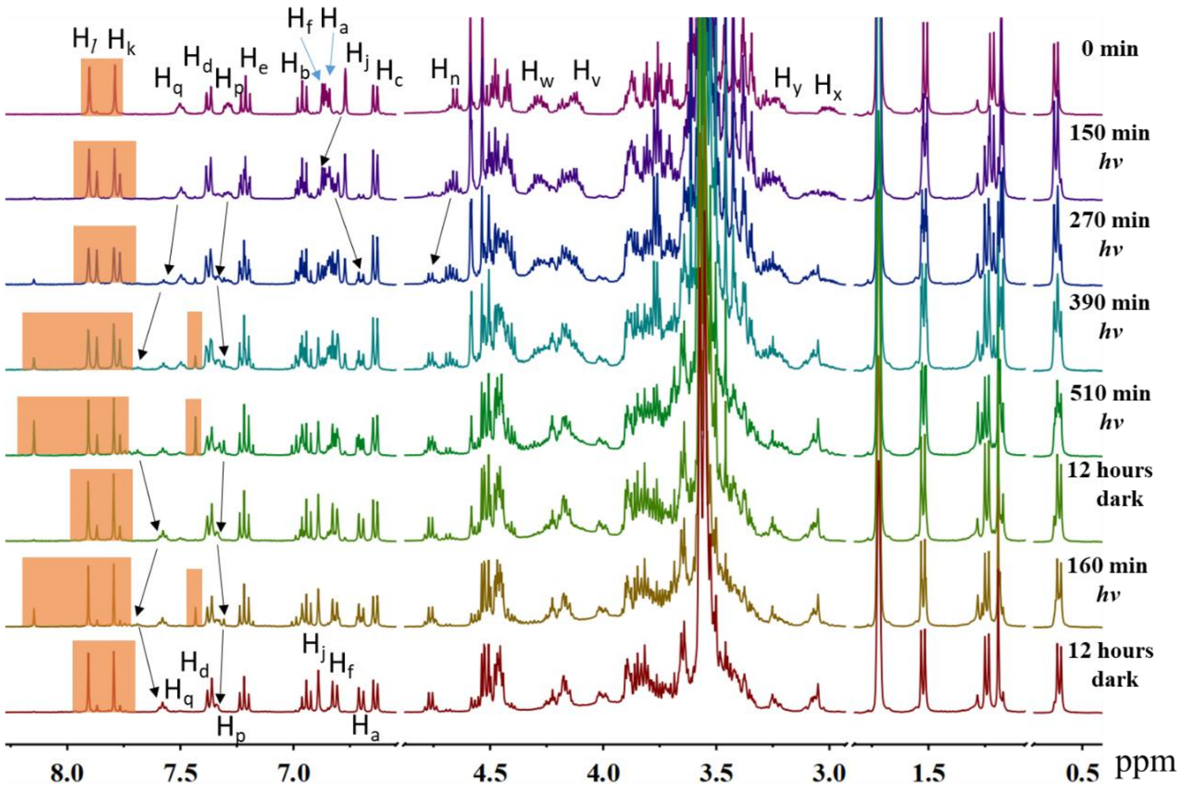

Figure 4.21 ^1H NMR spectra of **E3** for different irradiation times and after relaxation in the dark (400 MHz, THF-d_8, 298K, *c*=10 mM, lamp power=1.2 mW/cm^2).

Upon exposure of an **E3** solution to UV light, the proton signals of H_l and H_k on the triazole units split, and the aromatic proton H_j on the upper half of motor core shifted downfield. These distinctive shifts correspond to the formation of **E3-1**. After 270 minutes of irradiation, proton signals of H_q, H_p on amide bonds shifted downfield, indicating the generation of **E3-2**. Irradiating the solution for another 120 minutes yielded **E3-3** in which the protons H_l and H_k on triazole moieties dramatically shifted downfield. The proton signal of H_p also shifted downfield as opposed to H_q. As suggested by Figure 4.19, **E3-3** is able to transform back to **E3-2** via thermal relaxation in the dark. Likewise, the relaxation from **E3-3** to **E3-2** was also observed by ^1H NMR. After 510 minutes of irradiation, the solution of **E3** was kept in the dark for 12 hours at room temperature, leading to the recovery of proton signals of H_l, H_k, H_p and H_q. Further irradiation for 160 minutes led to the regeneration of **E3-3**, which transformed to **E3-2** after 12 hours in the dark as evidenced by ^1H NMR, indicating the reversible and reproducible transformation of **E3-2**.

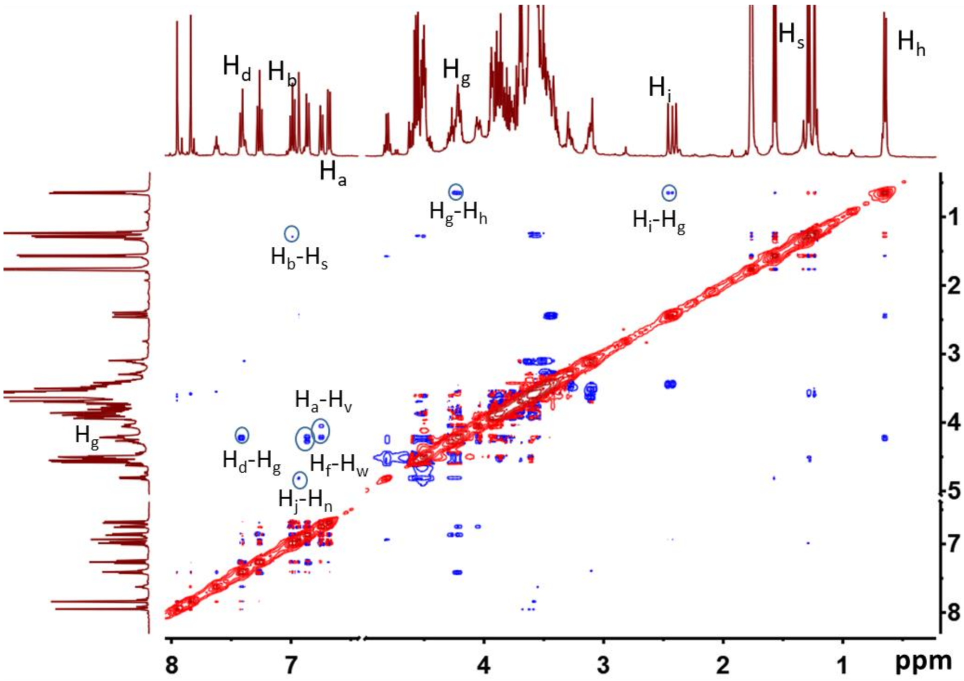

Figure 4.22 2D NOESY spectrum of **E3-2** (400 MHz, THF-d_8, 298K, c=10 mM).

To gain deeper insight into the conformation of **E3** after irradiation, we conducted 2D NOESY NMR with product **E3-2**. Similarly to **E3**, **E3-2** shows the cross-peaks of H_d-H_g, H_a-H_v, and H_f-H_w (Figure 4.22). In addition, it displays also additional signals, such as cross-peaks of H_b-H_s and H_j-H_n which only could be explained by the mechanical braiding of the PEG chains, suggesting a 'tensed' conformation for **E3-2**.

4.2.5.2 Tunable emission of 8-shaped molecular motor E3

In the previous section, we established that the conformational strain in **E3**, **E3-1**, **E3-2**, and **E3-3** is gradually increasing. Hence we postulated the conversion from highly 'tensed' **E3-3** to relatively 'stable' **E3-2** accompanied by a release of conformational strain could give rise to changes in optical properties. To verify this hypothesis, we first recorded the UV-Vis absorption spectra of **E3** as a function of irradiation time (Figure 4.23a). Upon UV light irradiation, the absorption band at 322-400 nm decreased notably corresponding to the stepwise transformation from **E3** to **E3-3**. After 25 minutes, there was no further spectral change under subsequent irradiation, indicating the 'PSS' is reached. This also means that all **E3-3** transformed into **E3-2**. Afterwards, the irradiated solution was kept in the dark for 21 hours, leading to a slight recovery of the absorption spectrum as a consequence of the transformation from **E3-3** to **E3-2** (Figure 4.23b). Subsequent UV light irradiation for 6 minutes resulted in a full recovery of the UV-Vis spectrum corresponding to **E3-3** (Figure 4.23b). As we expected, the emission intensity could be reversibly varied associated with the transformation between **E3-3** and **E3-2**. As evidenced by emission spectra (Figure 4.23c), after 21 hours in the dark, the fluorescence intensity is reduced by 37%. Impressively, further irradiation for 6 minutes led to a recovery of the emission spectrum. This behaviour is identical to the one recorded by UV-Vis spectroscopy. Importantly, the reversible emission showed a good fatigue resistance during irradiation/dark processes, which could be at least repeated over three cycles (Figure 4.23d).

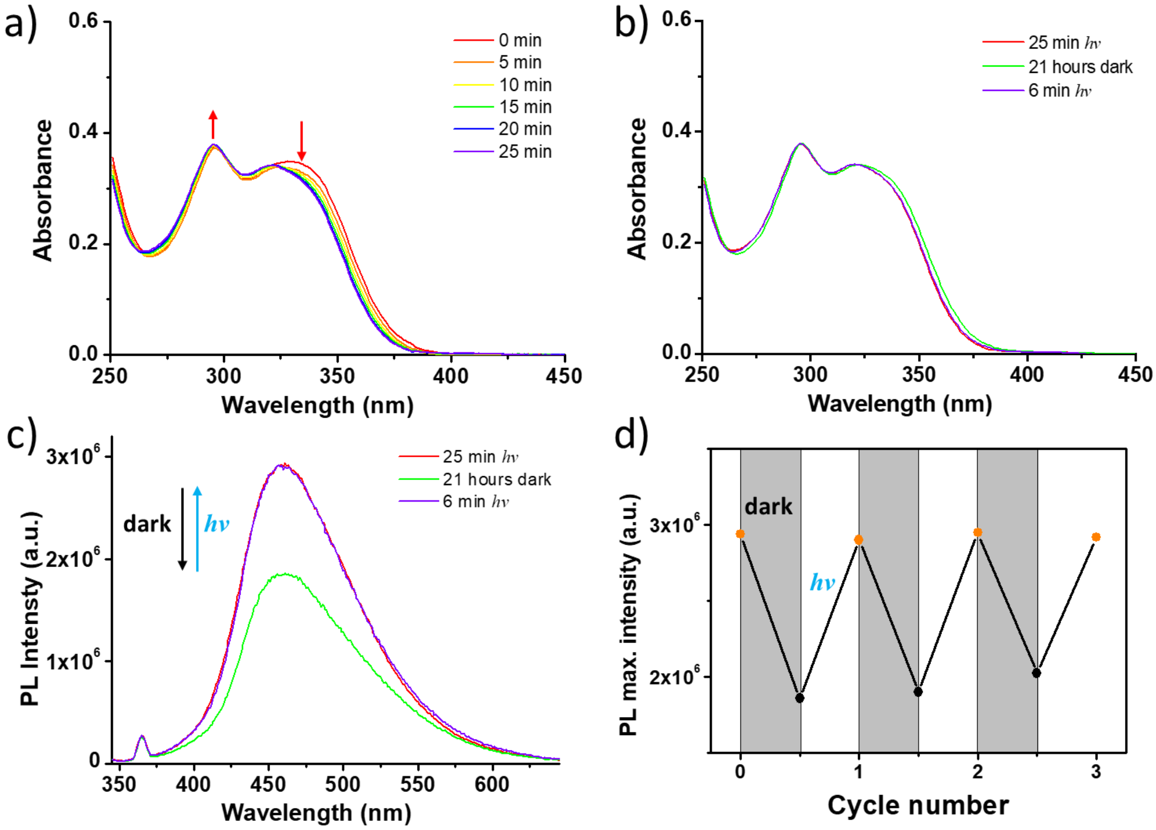

Figure 4.23 Tunable optical properties of **E3** in THF (0.02 mM). (a) UV-Vis absorption spectrum of **E3** as a function of irradiation time; (b) Evolution of UV-Vis absorption spectrum of **E3**. Red line: after 25 min irradiation, green line: in the dark for 21 h, and purple line: after another 6 min irradiation; (c) Evolution of the emission spectrum of **E3**. Red line: after 25 min irradiation, green line: in the dark for 21 h, and purple line: after another 6 min irradiation, λ_{ex}=330 nm; (d) Changes in maximum emission intensity during three irradiation/dark cycles. Lamp power=1.2 mW/cm^2.

The CD spectra were also recorded to study possible helical changes in molecular motor during dark/irradiation cycles. As suggested by Figure 4.24, the CD spectrum of the solution remains unchanged during dark/irradiation cycles, indicating that **E3-3** displays the same chirality as **E3-2**.

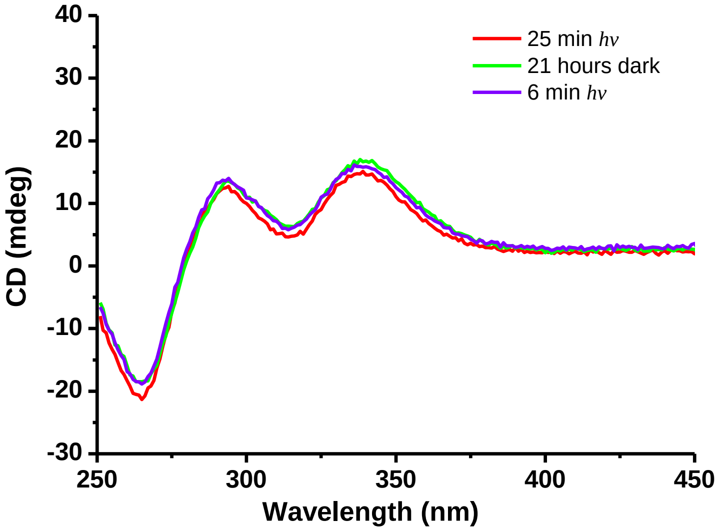

Figure 4.24 CD spectra of **E3**. Red line: after 25 min irradiation, green line: in the dark for 21 h, and purple line: after another 6 min irradiation.

All these experiments related to the rotation process and tunable optical properties of **E3** allowed us to propose a graphical representation of mechanically-induced emission enhancement of 8-shaped molecular motor **E3**. As presented in Figure 4.25, braiding of PEG chains induced by the light-driven rotation of molecular motor **E3** can be divided into two stages. First, UV light irradiation leads to the transformation of starting molecule **E3** into **E3-2** accompanied by an emission enhancement, this process is irreversible at room temperature. Then, prolonged irradiation resulted in the formation of highly 'tensed' **E3-3** with stronger emission, which could spontaneously relax to the relatively 'stable' **E3-2** in the dark, leading to a decrease in emission intensity.

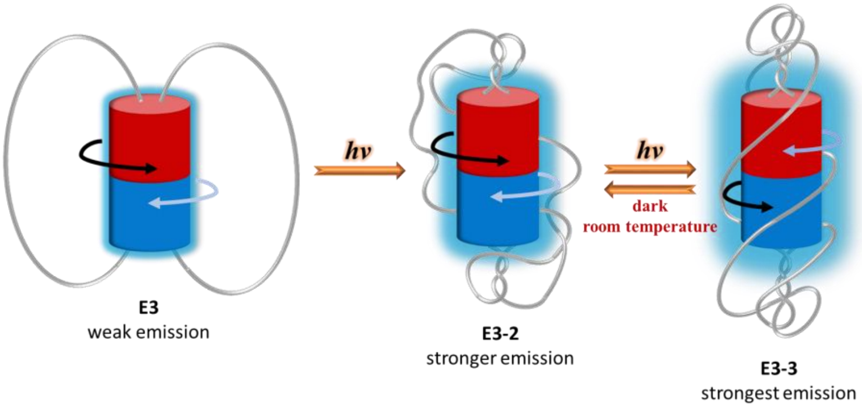

Figure 4.25 Graphical representation of mechanically-induced emission enhancement of 8-shaped molecular motor **E3**.

4.2.5.3 Kinetics study on E3-3

To better understand the thermal relaxation process occurring between **E3-3** and **E3-2**, the kinetics was investigated by UPLC. Specifically, a THF solution of **E3** was irradiated with UV light for 25 minutes to generate the ‘tensed’ **E3-3**, and then the decay of **E3-3** was monitored over time at four temperatures (298, 303, 308 and 313K). During relaxation process, the concentration of the solution was kept unchanged, thus the concentration of **E3-3** can be determined by integrating the area of its UV absorption band. Finally, a decay curve of **E3-3** was plotted as a function of time (Figure 4.26a). After data fitting according to a first-order kinetic model, the rate constant k of decay of **E3-3** was determined at each temperature, after which the activation parameters were obtained (Figure 4.26b) by using Eyring equation:

$$\ln\frac{k}{\mathrm{T}} = \frac{-\Delta \mathrm{H}}{R}\frac{1}{\mathrm{T}} + \ln\frac{k_B}{h} + \frac{\Delta \mathrm{S}}{R}$$

where R, h, and k_B correspond to the gas, Planck, and Boltzmann constants, respectively. The Gibbs energy of activation $\Delta^{\ddagger}$G (20 °C) is determined as 96.6 kJ mol^{-1}, which corresponds to a half time ($t_{1/2}$) of 5.2 hours according to equation of (ln2)/k.

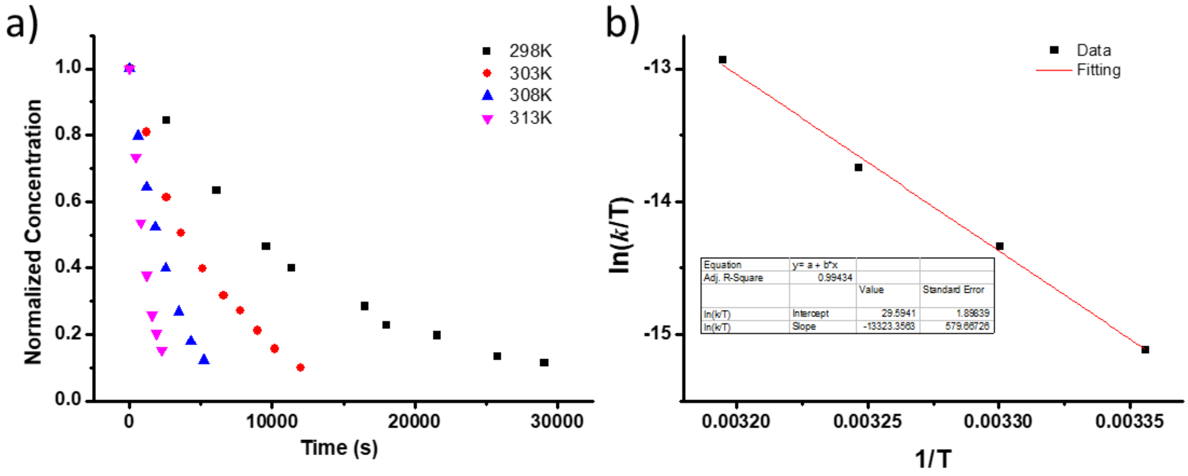

Equation	y= a + b*x		
Adj. R-Square	0.99434		
		Value	Standard Error
ln(k/T)	Intercept	29.5941	1.89839
ln(k/T)	Slope	-13323.3563	579.66726

Figure 4.26 (a) Time-dependent concentrations of **E3-3** in the dark at 25, 30, 35 and 40 °C as monitored by UPLC; (b) Eyring plot of the thermal relaxation of **E3-3** in THF. Activation parameters: $\Delta^{\ddagger}$G (20 °C) = 96.6 kJ mol^{-1}, ΔH = 110.8 kJ mol^{-1}, ΔS = 48.5 J mol^{-1} K^{-1}, $t_{1/2}$ = 5.2 h.

At the time of writing, we found that high temperature could allow the transformation from **E3-2** to **E3-1** and **E3**. As suggested by UPLC (Figure 4.27), at 40°C, **E3-2** slowly relaxed back to **E3-1**, which further transformed into **E3**. Kinetics on each thermal relaxation step are ongoing.

Considering the slow conversions from **E3-2** to **E3-1** and from **E3-1** to **E3**, we expect that the activation energies required for these thermal relaxations should be larger than that corresponding to the transformation from **E3-3** to **E3-2**.

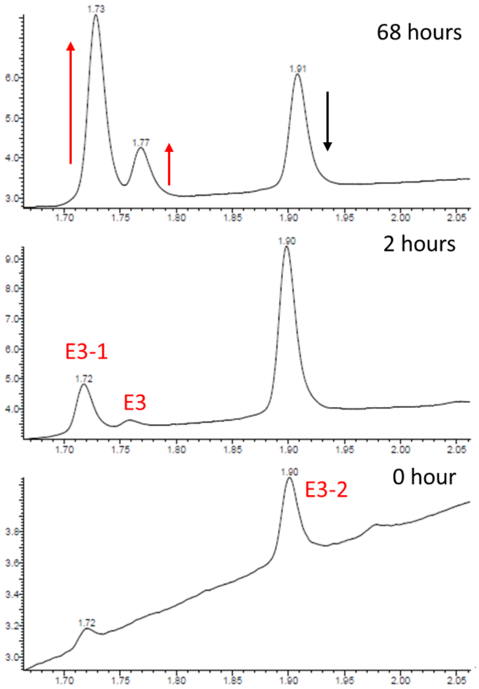

Figure 4.27 Evolution of UV chromatograms for a solution of **E3-2** in the dark at 40°C as a function of time.

4.2.6 Conclusion and Perspectives

Taking the inspiration from the light-induced emission enhancement of motorized gels, the aggregation-induced emission (AIE) behaviour of molecular motor was first demonstrated. Then, 8-shaped molecular motors **E1**, **E2**, and **E3** with various PEG chains were successfully synthesized via intramolecular ‘click’ reaction. We then proved that these molecular motors could rotate and mechanically braid PEG chains in response to UV light irradiation. As a result of mechanical coiling of PEG chains, the intramolecular motion was suppressed, leading to an emission enhancement. Here we defined this novel phenomenon occurring in our system as mechanically-induced emission enhancement (MIEE).

In comparison to **E1** and **E2**, **E3** bearing short PEG chains displayed improved emission enhancement at the photostationary state (PSS). Furthermore, using UPLC, ^{1}H NMR, UV-Vis, and emission spectroscopy, we monitored and investigated the stepwise rotation process of **E3**. Upon exposure to UV light, **E3** sequentially transformed to **E3-1**, **E3-2**, and **E3-3**, accompanied by a gradual emission enhancement due to the increasing conformational strain. More importantly, to release the elastic energy (conformational strain) stored in the ‘tensed’ molecular motors, **E3-3** was able to relax back to **E3-2** in the dark at room temperature. This release of elastic energy leads to a 37% decrease of the fluorescence intensity. Moreover, at higher temperature, **E3-2** could slowly transform to **E3** after undergoing two successive thermal relaxation processes.

Although this work is still ongoing to gain a clear insight into the activation energy required for each thermal relaxation process, all results describe the first example of an out-of-equilibrium emission system which uses the ‘reversible’ rotary motion of unidirectional light-driven molecular motors to tune its fluorescence.

Based on the aforementioned observations, we can extend this system to other luminescent materials. For example, the 8-shaped molecular motors could be prepared via supramolecular interactions (e.g. intramolecular hydrogen bond) or dynamic bonds (e.g. imine bond). In these cases, the elastic energy could be released by applying an external stimuli, leading to a rapid and reversible switching of fluorescence. Another possible application could be inkless writing and self-erasing materials by integrating molecular motor **E3** into gels.

GENERAL CONCLUSIONS

In this manuscript, we aimed to develop novel optical materials and nano-devices by taking advantage of previous works reported by our research group on the functions of triarylamine-based supramolecular polymers and on light-driven molecular motors.

In Chapter I, we synthesized a new triarylamine trisamide derivative, featuring with a 4-bromo-1,8-naphthalimide as phosphorescent unit on one of its side chains, to obtain supramolecular polymers with pure organic phosphorescence at room temperature. In various solvents, such as CH_2Cl_2, THF, and DMF, the molecule was able to self-assemble into supramolecular fibrillar networks with the phosphorescent units confined in the structures. Different from the diluted solution, self-assemblies in solid state displayed red phosphorescence at ambient conditions due to the restriction of intramolecular motion of 4-bromo-1,8-naphthalimide.

In chapter II, we prepared triarylamine trisacetamide based supramolecular nanoparticles and preliminarily investigated their plasmonic properties. In chloroform, triarylamine trisacetamide was able to be oxidized to form radical cations under visible light irradiation. Supramolecular nanoparticles with a crystalline nature were obtained via a precipitation method. In addition, by altering the volume of mother solution, the size of the nanoparticles could be varied. Thanks to the presence of positive radical cations, these nanoparticles presented unique UV absorption bands, the wavelength of which appeared redshift with increasing size. This optical behaviour is highly consistent with so-called localized surface plasmon resonance (LSPR) typically observed in metal plasmonic nanoparticles. Further studies will be addressed to prove the plasmonic property of our supramolecular nanoparticles.

In chapter III, the macroscopic contraction of motorized gels was exploited in order to tune plasmonic coupling of AuNPs. We demonstrated that light-responsive contractile gels containing AuNPs could be obtained by crosslinking light-driven molecular motors, PEG polymers, and AuNPs. Upon exposure to UV light, the collective rotary motion of molecular motors resulted in the contraction of the gels. However, after several attempts, we did not observe shifts of the LSPR band corresponding to AuNPs due to the limited relative volumes. Towards our goal, further investigation might be conducted in the direction of improving macroscopic contraction.

Featured with AIE property, second generation molecular motors display strong fluorescence in aggregated state due to the restriction of intramolecular motion (RIM). In the last chapter, we use this RIM mechanism to develop an emission-tunable system based on an 8-shaped molecular motor. Upon UV light irradiation, RIM was achieved by the mechanical coiling of the PEG chains, leading to emission enhancement. Influences of the lamp power, solvents, and the length of PEG chains were investigated. Intriguingly, in 8-shaped molecular motor bearing short PEG chains, the braiding of PEG chains was shown to be unwound owing to the high conformational strain in the molecular motor, accompanied by a reduced fluorescence.

To conclude, the work presented in this thesis demonstrates the possibilities that triarylamine-based supramolecular structures and molecular motors can offer to build unconventional optical materials. In particular, achievements reported in chapter II might be the first step towards organic plasmonic nanoparticles via a bottom-up strategy. On the other hand, we believe that the system of 8-shaped molecular motor presented in the last chapter will bring a new insight into the design of out-of-equilibrium tunable optical materials.

EXPERIMENTAL SECTION

a. Solvents and Chemical Reagents

All reagents and solvents were purchased at the highest commercial quality and used without further purification unless otherwise noted. Dry solvents were obtained using a double column SolvTech purification system. Water was deionized by using a milli gradient system (Millipore, Molsheim, France). All reactions were performed under atmosphere of argon unless otherwise indicated.

b. Chromatographic Methods

Thin Layer Chromatographies were performed using silica on TLC Aluminum foils (silica gel matrix with fluorescent indicator 254 nm, thickness: 500 µm, Sigma-Aldrich). In most cases, irradiation using a *Bioblock VL 4C* UV Lamp (6 W, 254 nm and/or 365 nm) as well as *p*-anisaldehydeanisaldehyde, phosphomolybdic acid and Cerium ammonium molybdate stainings, were used for visualization. *Preparative Adsorption Flash Column Chromatographies* were performed using silica gel (60 Å, 230 - 400 mesh, 40 - 63 µm, Sigma-Aldrich). *Ultra-Performance Liquid Chromatographies coupled to Mass Spectroscopy (UPLC MS)* were carried out on a Waters Acquity UPLC SQD apparatus equipped with a PDA detector (190 500 nm, 80Hz and a SQD spectrometer), using a reverse phase column (Waters, BEH C18 1.7 µm, 2.1 × 50 mm or CSH Fluoro Phenyl Column, 130Å, 1.7 µm, 2.1 mm × 100 mm), the MassLynx 4.1 XP software and a gradient (water acetonitrile + 0.1% TFA) as eluent. *Reversed-phase Chromatographies* were performed with reversed-phase silica gel (Lichroprep RP-18, 25-40 µm, Merck). *Preparative High Performance Liquid Chromatographies* were performed using a *Waters AutoPurify* system equipped with a UV detector (set at 300 nm, 500 nm or 600 nm), a *3100* mass spectrometer, a reverse phase column (Waters, Sun Fire Prep C_{18} 5.0 µm, 19 × 150 mm) running with a gradient (0.08% TFA water/acetonitrile) as eluent, and the MassLynx 4.1 – XP software.

c. Analytical Methods and Instruments

1. Nuclear Magnetic Resonance (NMR)

^{1}H NMR spectra were recorded either on a Bruker Avance III HD 500 MHz spectrometer equipped with a CPPBBO « Prodigy » cryo-probe at 298K or on a Bruker Avance III HD 400 MHz spectrometer equipped with a BBFO probe at 298K. ^{13}C NMR spectra were recorded either on a Bruker Avance 400 spectrometer at spectra at 100 MHz or on a Bruker Avance III HD spectrometer at 125 MHz. For ^{1}H NMR assignments, the chemical shifts are given in ppm. Coupling constants *J* are given in Hz. Peaks are described as singlet (s), doublet (d), triplet (t), quartet (q), doublet of doublets (dd), triplet of triplets (tt), multiplet (m) and broad (br).

2. Mass Spectrometry

Electrospray ionization (ESI) *mass spectrum* was recorded on a SQD mass spectrometer from Waters either by direct injection or after chromatography.

3. UV-Vis Spectroscopy

UV-Vis spectra were recorded either on Lambda 25 spectrophotometer from PerkinElmer or on a Cary 5000 spectrophotometer from Agilent Technologies.

4. Fluorescence Spectroscopy and Quantum Yield.

Fluorescence emission spectra were recorded on a FluoroMax-4 spectrofluorometer from Horiba Jobin-Yvon. Temperature was controlled using a Peltier system. Absolute quantum yields were measured using an integrating sphere.

5. Dynamic Light Scattering (DLS)

Dynamic light scattering was recorded on a Zetasizer Nano from Malvern Instruments Ltd. (UK).

6. Circular Dichroism Spectroscopy (CD)

CD spectra were recorded on a Jasco J-1700 spectropolarimeter. Quartz cells with a path length of 10 mm were used for the experiments.

7. Transmission Electron Microscopy (TEM)

TEM imaging was performed using a CM12 Philips microscope equipped with a MVIII (SoftImaging System) CCD camera. Samples were analyzed in Bright Field Mode with a LaB6 cathode and 120 kV tension. Image treatments were performed by using analySIS (Soft Imaging System) software. Samples were prepared by dropping a solution of the compound onto a carbon-coated copper grid placed on a filter paper.

8. Scanning Electron Microscopy (SEM)

SEM imaging was performed using a SU8000 Hitachi microscope. Samples were prepared by dropping a solution of the compound onto a carbon-coated copper grid or silicon wafer.

9. Atomic Force Microscopy (AFM)

AFM images were obtained by scanning the samples using a Nanoscope 8 (Bruker) operated in peak-force tapping mode. Ultra-sharp silicon cantilevers (ScanAsyst 0.4 N.m-1) with a nominal tip radius < 5 nm were used. AFM images were acquired under an air atmosphere at room temperature. The force was reduced in order to avoid dragging of molecules by the tip. Integral gain was adjusted to give sharp images. Images were taken without on-line filtering and were subsequently processed only by flattening to remove the background slope. Samples were prepared by dropping a solution of the compound onto one side of silicon wafer or mica.

10. X-ray Scattering (SAXS and WAXS)

Small angle/Wide angle X-ray scattering experiments were performed at the Institut Charles Sadron by using a diffractometer developed by Molecular Metrology (Elexience in France), which operates with a pinhole collimation of the X-ray beam and a two-dimensional gas-filled multiwire detector. The monochromatic (λ= 1.54 Å with Dl/l < 4%) and focused X-ray beam is obtained through a multilayer optic designed and fabricated by Osmic. The size of the incident beam on the sample was close to 700 µm. The sample to detector distance was set at 0.81 m and 0.1 m for SAXS and WAXS, respectively, allowing to explore scattering vectors ranging from q = 0.01 Å^{-1} to 3 Å^{-1}, with $q = 4\pi\sin(\theta/2)/\lambda$, where λ and θ are the wavelength of the incident beam and the scattering angle, respectively. The *q*-resolution related to the beam size on the sample and the beam divergence was close to 0.005 Å^{-1}. Cells of 1 mm thickness and calibrated Mica windows were used as sample holders. Measurements were performed at room temperature. All data were treated according to standard procedures for isotropic small angle X-ray scattering. After radial averaging, the spectra were corrected from electronic noise of the detector, empty cell, absorption and sample thickness. A ^{55}Ir source was used for the corrections of geometrical factors and detector cells efficiency as well as a Silver Behenate sample, for the *q*-calibration. After all these data treatments, the scattered intensities were corrected from the scattering of the solvent. According to such a procedure, the scattered intensity I(*q*) containing all the structural information is obtained for each sample.

11. Electron Paramagnetic Resonance Spectroscopy (EPR)

EPR measurements were carried out on EMX spectrometer at X-band (Bruker Biospin GmbH, Germany). Quantitative EPR experiments were performed by comparing with the integrated EPR spectra of the TEMPO standard. All experiments were performed at room temperature.

d. Irradiation methods

Visible light irradiation experiments were carried out with a halogen lamp from IKEA (12 V, 20W). The samples were positioned 5 cm from the sample (10 W/cm^2).

All UV irradiation experiments were performed with a Thorlabs model M356FP1 fiber-coupled LED (365 nm). Samples of motorized gel were irradiated under a power of 50 mW/cm^2. The solutions of molecular motor were irradiated under a power of 5mW/cm^2 or 1.2 mW/cm^2.

Lamp powers were measured using a handheld digital optical power meter PM100D from Thorlabs.

Synthesis

Compound **1**

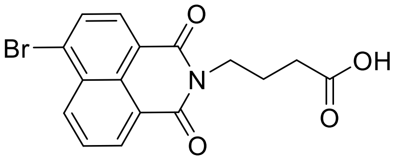

To a solution of 4-bromo-1,8-napthallic anhydride (500 mg, 1.81 mmol) in ethanol (25 mL) was added 4-aminobutyric acid (206 mg, 2.0 mmol). The mixture was stirred for 10 h under reflux. After cooling down to room temperature, the mixture was poured into ice water (100 mL). The precipitates were collected, and washed with water. Further drying under high vacuum afforded compound **1** as white solid (569 mg, 87%).

Characterizations are in agreement with the literature.[61]

^{1}H NMR (DMSO-d_6, 400 MHz, 298 K): δ 8.59 (dd, J = 9.2, 1.2 Hz, 1H), 8.56 (dd, J = 9.6, 0.8 Hz, 1H), 8.34 (d, J = 8.0 Hz, 1H), 8.23 (d, J = 8.0 Hz, 1H), 8.01 (dd, J = 8.8, 7.6 Hz, 1H), 4.09 (t, J = 6.8 Hz, 2H), 2.31 (t, J = 7.6 Hz, 2H), 1.95-1.85 (m, 2H).

^{13}C NMR (DMSO-d_6, 100 MHz, 298 K): δ 174.0, 163.1, 163.0, 132.6, 131.6, 131.4, 131.0, 129.8, 128.8, 122.9, 122.2, 31.3, 22.9.

ESI-MS: calculated for $C_{16}H_{12}BrNO_4$ $[M-H]^-$ 361.99 found 361.93.

Compound **(*S*)-2**

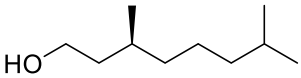

(3S)-3,7-dimethyloct-6-en-1-ol (5.0 g, 31.7 mmol) was dissolved in a 1:1 mixture of ethyl acetate (50 mL) and methanol (50 mL) in a 250 mL round bottom flask. The solution is passed through an H-cube reactor (*THALESNANO H-Cube HC 2-SS Continuous Flow Hydrogenation Reactor With CatCart*) equipped with a 10% Pd/C cartridge at 70°C, in full H_2 mode and with a 0.1mL/min flow. The reaction is monitored by NMR and the process is repeated several times in case of some starting material is remaining. The solvent was evaporated under reduced pressure, and the resulting residue was dried to give compound **(*S*)-2** (4.9 g, 98 %) as a colorless oily liquid, which was clean enough to be used in the next step without purification.

Characterization are in agreement with the literature.[39]

^{1}H NMR ($CDCl_3$, 400 MHz, 298 K): δ 3.74-3.60 (m, 2H), 1.65-1.45 (m, 3H), 1.42-1.33 (m, 1H), 1.33-1.20 (m, 4H), 1.19-1.06 (m, 3H), 0.92-0.80 (m, 9H).

^{13}C NMR ($CDCl_3$, 100 MHz, 298 K): δ 61.4, 40.2, 39.4, 37.5, 29.6, 28.1, 24.8, 22.8, 22.7, 19.8.

Compound **(*S*)-3**

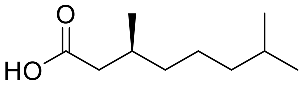

Periodic acid (7.2 g, 31.4 mmol) was dissolved in acetonitrile (100 mL) under vigorous stirring at room temperature for 40 min. Then, pyridinium chlorochromate (60 mg, 0.278 mmol) was added. The solution was cooled down to 0°C using an ice bath and compound **(*S*)-2** (2.2 g, 13.9 mmol) in acetonitrile (30 mL) was added dropwise. The reaction mixture was stirred for 1 hour at 0 °C and for 3 hours at room temperature. Then, acetonitrile was evaporated under reduced pressure. Ethyl acetate (200 mL) was added, and the organic layer was extracted with water/brine 1:1 v/v (400 mL), saturated $NaHSO_3$ (300 mL) and brine (500 mL). The organic phase was dried over Na_2SO_4, filtered and evaporated under vacuum. The resulting crude liquid was distilled using the kugelrohr to give compound **(*S*)-3** (2.2 g, 92 %) as a colorless viscous liquid.

Characterizations are in agreement with the literature.[39]

^{1}H NMR ($CDCl_3$, 400 MHz, 298 K): δ 2.35 (dd, *J* = 14.9, 5.8 Hz, 1H), 2.15 (dd, *J* = 14.9, 8.2 Hz, 1H), 2.01-1.90 (m, 1H), 1.60-1.46 (m, 1H), 1.38-1.10 (m, 6H), 0.97 (d, *J* = 6.7 Hz, 3H), 0.87 (d, *J* = 6.7 Hz, 6H).

^{13}C NMR ($CDCl_3$, 100 MHz, 298 K): δ 179.5, 41.3, 39.1, 36.8, 30.1, 27.7, 24.5, 22.6, 22.3, 19.8.

Compound **(*S*)-4**

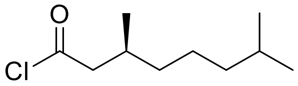

Compound **(*S*)-3** (2.2 g, 12.8 mmol) was dissolved in chloroform (10 mL) and thionyl chloride (5 mL, 68.9 mmol) was added. The reaction mixture was stirred at reflux for 3 hours. Next, it was cooled down to room temperature, solvent was removed under reduced pressure and compound **(*S*)-4** (2.4 g, 99 %) was obtained as a colorless oil after distillation using the kugelrohr.

Characterizations are in agreement with the literature.[39]

^{1}H NMR ($CDCl_3$, 400 MHz, 298 K): δ 2.88 (dd, *J* = 16.0, 5.8 Hz, 1H), 2.68 (dd, *J* = 16.0, 8.0 Hz, 1H), 2.14-2.01 (m, 1H), 1.60-1.46 (m, 1H), 1.38-1.10 (m, 6H), 0.99 (d, *J* = 6.6 Hz, 3H), 0.87 (d, *J* = 6.6 Hz, 6H).

^{13}C NMR ($CDCl_3$, 100 MHz, 298 K): δ 173.4, 54.4, 39.0, 36.5, 30.9, 3.03, 24.6, 22.8, 22.7, 19.4.

Compound **5**

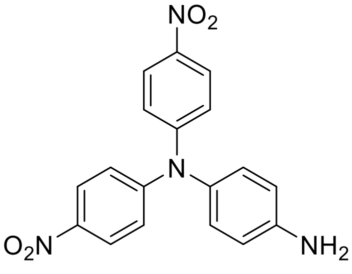

To a solution of 1, 4-benzenediamine (3.5 g, 32.4 mmol) and potassium carbonate (17.9 g, 129 mmol) in dry DMSO (50 mL) in a 250 mL Schleck flask was added 4-fluoronitrobenzene (6.87 mL, 64.7 mmol). The mixture was heated for 3 days at 90 °C. After that time, the solution was cooled down to room temperature and further diluted with water (300 mL) resulting in the formation of a dark red precipitate. The solid was filtered, washed with water (5 × 50 mL) and then dried to afford compound **5** as a dark red solid (10.4 g, 92%).

^{1}H NMR ($CDCl_3$, 400 MHz, 298 K): δ 8.12 (d, *J* = 8.6 Hz, 4H), 7.13 (d, *J* = 8.6 Hz, 4H), 6.96 (d, *J* = 8.6 Hz, 2H), 6.73 (d, *J* = 8.6 Hz, 2H), 3.84 (brs, 2H).

^{13}C NMR ($CDCl_3$, 100 MHz, 298 K): δ 152.2, 146.1, 142.3, 135.2, 129.1, 125.6, 121.6, 116.6.

ESI-MS: m/z calculated for $C_{18}H_{14}N_4O_4$ 351.10 $[M+H]^+$; found 351.29.

Compound **6**

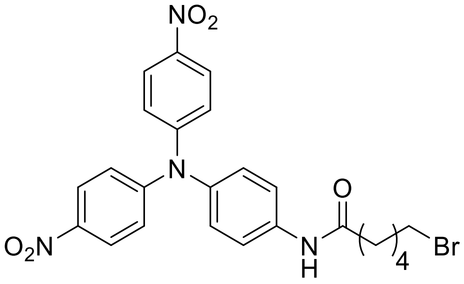

To a solution of compound **5** (520 mg, 1.48 mmol) in dry dichloromethane (50 mL) was added triethylamine (0.248 mL, 1.78 mmol), and the mixture was cooled down to 0 °C on an ice bath. Then, 6-bromohexanoyl chloride (348 mg, 1.63 mmol) was added dropwise to above solution under vigorous stirring. The reaction was left to regain room temperature and further stirred for 1 hour. Then, the solution was diluted with dichloromethane (50 mL) and washed with a saturated solution of $NaHCO_3$ (3 ×100 mL). The organic phase was dried over anhydrous Na_2SO_4 and concentrated under vacuum. The crude residue was purified by flash column chromatography (SiO_2, cyclohexane/ethyl acetate = 100/0→4/1) to obtain compound **6** (620 mg, 79%) as a yellowish solid.

^{1}H NMR ($CDCl_3$, 400 MHz, 298 K): δ 8.11 (d, *J* = 9.2 Hz, 4H), 7.60 (d, *J* = 8.5 Hz, 2H), 7.45 (s, 1H), 7.11-6.96 (m, 6H), 3.40 (t, *J* = 6.8 Hz, 2H), 2.40 (t, *J* = 7.4 Hz, 2H), 1.89 (tt, *J* = 7.4

Hz, 2H), 1.76 (tt, *J* = 7.5 Hz, 2H), 1.52-1.38 (m, 2H).

^{13}C NMR ($CDCl_3$, 100 MHz, 298 K): δ 171.3, 151.8, 142.7, 140.4, 137.0, 127.9, 125.5, 122.1, 121.6, 37.4, 33.7, 32.5, 27.7, 24.5;

ESI-MS: m/z calculated for $C_{24}H_{23}BrN_4O_5$ $[M+H]^+$ 528.38, found 528.18.

Compound **7**

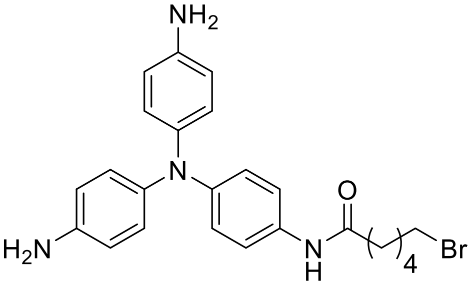

Compound **6** (600 mg, 1.19 mmol) was dissolved in ethyl acetate (50 mL) and tin chloride (2.25 g, 11.89 mmol) was added. The solution was stirred for 12 hours at 80 °C under argon atmosphere. Then, the solution was cooled down to room temperature and diluted with ethyl acetate (20 mL). The organic phase was washed with a saturated solution of $NaHCO_3$ (4 × 300 mL) and with brine (2 × 150 mL), dried over Na_2SO_4, filtered and the solvent was concentrated to a reduced volume (~10 ml). This solution was used in the next step without further purification.

Compound **8**

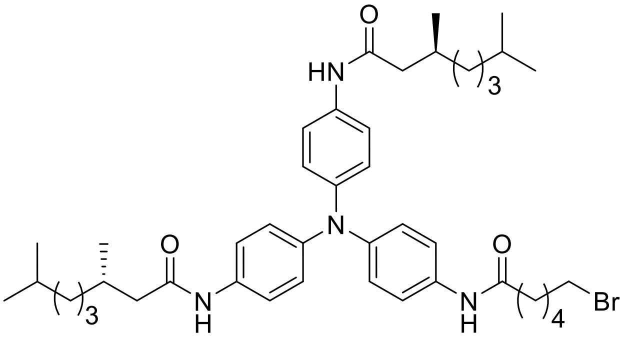

The solution of compound **7** from previous step was diluted with dichloromethane (40 mL), then triethylamine (0.45 mL, 325 mg, 3.21 mmol) was added and the mixture cooled down to 0 °C on an ice bath. Compound **(*S*)-4** (567 mg, 2.98 mmol) was then added. The solution was heat up slowly to room temperature and stirred for 4 hours. After that time, the solution was diluted with dichloromethane (50 mL) and washed with a saturated solution of $NaHCO_3$ (3 × 150 mL) and with brine (2×150 mL), dried over Na_2SO_4, filtered and the solvent was evaporated under reduced pressure. The crude product was recrystallized from diethyl ether (20 mL), the precipitate was filtered with a glass filter, washed with cold diethyl ether (20 mL) and dried under vacuum to obtain compound **8** (670 mg, 73%) over two steps as a white solid.

^{1}H NMR ($CDCl_3$, 400 MHz, 298 K): δ 7.35 (d, *J* = 8.8 Hz, 6H), 7.17 (s, 1H), 7.12 (s, 2H), 6.88 (d, *J* = 8.8 Hz, 6H), 3.42 (t, *J* = 6.4 Hz, 2H), 2.40-2.29 (m, 4H), 2.16-2.01 (m, 2H), 1.97-1.86 (m, 2H), 1.81-1.71 (m, 2H), 1.55-1.49 (m, 4H), 1.39-1.13 (m, 14H), 0.99 (d, *J* = 6.4 Hz, 2H), 0.86 (dd, *J* = 6.8, 1.2 Hz, 12H).

^{13}C NMR (DMSO-*d*$_6$, 100 MHz, 298 K): δ 171.2, 170.8, 151.7, 143.2, 140.3. 134.7, 124.0, 122.0, 120.7, 44.6, 39.2, 36.9, 36.6, 35.5, 32.5, 30.7, 27.9, 27.7, 24.8, 24.6, 23.1, 22.9, 20.0.

ESI-MS: m/z calculated for $C_{44}H_{63}BrN_4O_3$ $[M+H]^+$ 775.41, found 775.53.

Compound **9**

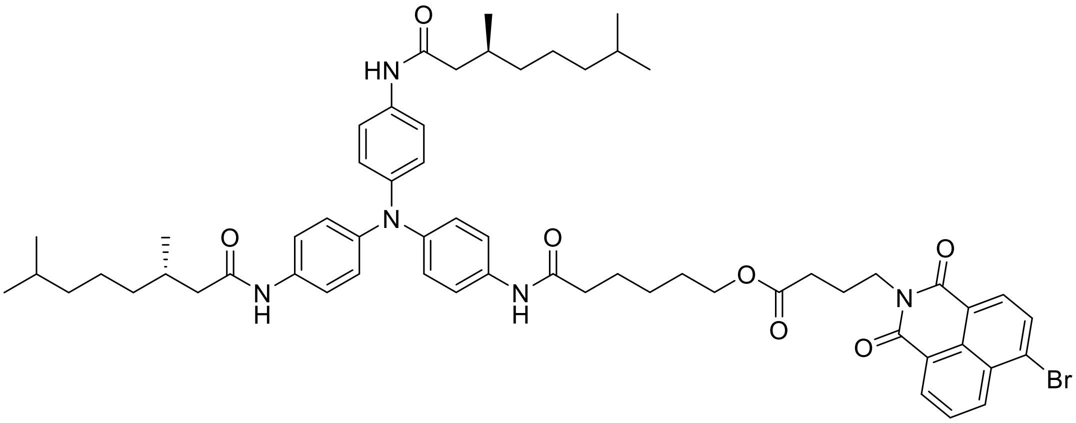

To a solution of compound **8** (200 mg, 0.26 mmol) in dry DMF (10 mL) was added compound **1** (140 mg, 0.39 mmol) and then K_2CO_3 powder (71.3 mg, 0.52 mmol). The solution was stirred for 12 hours at room temperature. After that time, the solution was filtered to remove the remaining K_2CO_3 solid and concentrated under reduced pressure. After adding ethyl acetate (10 mL), the suspension was sonicated for 10 minutes. After filtration, the solid was further washed with ethyl acetate (5 × 20 mL) to obtain compound **9** (168.9 mg, 62%) as a yellowish solid.

^{1}H NMR (DMSO-*d*$_6$, 400 MHz, 298 K): δ 9.78 (s, 3H), 8.58 (dd, *J* = 7.2, 0.8 Hz, 1H), 8.55 (dd, *J* = 8.8, 1.2, Hz, 1H), 8.34 (dd, *J* = 8.0 Hz, 2H), 8.22 (dd, *J* = 8.4, 7.2 Hz, 2H), 7.51-7.42 (m, 6H), 6.92-6.83 (m, 6H), 4.08 (t, *J* = 6.8 Hz, 2H), 3.91 (t, *J* = 6.4 Hz, 2H), 3.48-3.37 (m, 5H), 2.39 (t, *J* = 7.2 Hz, 2H), 2.95-2.12 (m, 4H), 2.12-2.03 (m, 2H), 1.99-1.87 (m, 4H), 1.60-1.46 (m, 6H), 1.35-1.22 (m, 8H), 0.88 (d, *J* = 6.4 Hz, 6H), 0.84 (d, *J* = 6.4 Hz, 12H).

^{1}H NMR (toluene-*d*$_8$:CD$_3$OD = 3:1, 400 MHz, 298 K): δ 8.35 (d, *J* = 7.2 Hz, 1H), 8.18 (d, *J* = 7.2 Hz, 1H), 8.03 (d, *J* = 8.0 Hz, 1H), 7.62-7.53 (m, 6H), 7.49 (d, *J* = 7.6 Hz, 1H), 7.28 (t, *J* = 7.6 Hz, 1H), 7.07 (s, 6H), 4.04 (t, *J* = 7.2 Hz, 2H), 3.91 (t, *J* = 7.2 Hz, 2H), 2.36-2.18 (m, 6H), 2.14-2.08 (m, 4H), 2.01-1.91 (m, 2H), 1.70-1.58 (m, 2H), 1.54-1.40 (m, 4H), 1.38-1.08 (m, 14H), 0.98 (d, *J* = 6.0 Hz, 6H), 0.87-0.79 (m, 12H).

^{13}C NMR (toluene-*d*$_8$:CD$_3$OD = 3:1, 125 MHz, 298 K): δ 173.6, 172.9, 172.8, 163.9, 163.8, 144.7, 144.6, 134.3, 133.2, 132.1, 131.4, 131.3, 131.0, 130.2, 124.8, 124.7, 124.6, 123.6, 122.7, 121.8, 121.7, 68.1, 64.8, 45.3, 40.0, 39.7, 37.8, 37.3, 32.1, 31.6, 28.9, 28.5, 26.1, 25.9, 25.8, 25.4, 23.9, 22.9, 22.8.

ESI-HRMS: m/z calculated for $C_{60}H_{74}BrN_5O_7$ $[M+H]^+$ 1056.4844 found 1056.4850.

Compound **10**

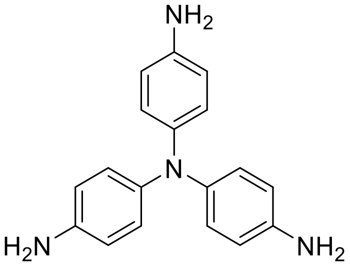

Compound **5** (11.0 g, 31.4 mmol) was dissolved in a 2:1 mixture of ethanol (200 mL) and dioxane (100 mL). Then palladium on carbon (0.83 g, 1.67 mmol) was added to above solution under argon atmosphere. After heating up to 80 °C, hydrazine hydrate (64-65%, 35 mL) was added dropwise under vigorous stirring over a period of 2 hours. The solution was further stirred under reflux for overnight. After cooling down to room temperature, the solution was filtered through a pad of Celite® and washed with ethanol (200 mL). After concentration under reduced pressure, the crude residue was recrystallized from boiling ethanol (50 mL) affording compound **10** (4.1 g, 45%) as purple solid.

^{1}H NMR (DMSO-*d*$_6$, 400 MHz, 298 K): δ 6.58 (d, *J* = 8.8 Hz, 6H), 6.43 (d, *J* = 8.8 Hz, 6H), 4.69 (brs, 6H)

^{13}C NMR (acetone-*d*$_6$, 100 MHz, 298 K): δ 143.9, 140.7, 125.3, 116.0.

ESI-MS: m/z calculated for $C_{18}H_{18}N_4$ $[M+H]^+$, 291.16; found 291.38.

Compound **11**

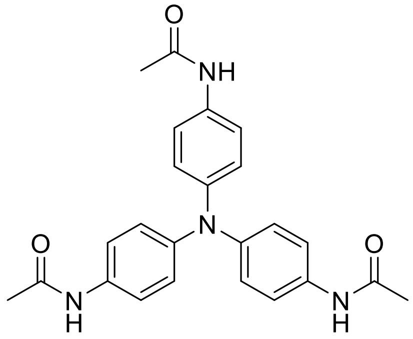

Compound **11** (2.54 g, 8.74 mmol) and triethylamine (4.86 mL, 35 mmol) were dissolved in THF (250 mL). The solution was cooled down to 0 °C in an ice-bath. Then a solution of acetyl chloride (2.74g, 2.5 mL, 35 mmol) in THF (15 mL) was added. After addition, the ice-bath was removed and the reaction was stirred for 3 additional hours. Afterwards the crude product was retrieved by filtration through a patch of Celite®. After recrystallization from boiling ethanol (40 mL) and further purification by flash column chromatography (SiO_2, ethyl acetate/methanol = 100/0→95/5), compound **11** (1.67 g, 46%) was obtained as small white crystals.

^{1}H NMR (DMSO-*d*$_6$, 400 MHz, 298 K): δ 9.95 (s, 3H), 7.46 (d, *J* = 8.9 Hz, 6H), 6.87 (d, *J* = 8.9 Hz, 6H), 2.01 (s, 9H).

^{13}C NMR (CD_3OD, 100 MHz, 298 K): δ 171.5, 145.5, 134.8, 125.2, 122.6, 23.7.

ESI-MS: *m/z* calculated for $C_{24}H_{25}N_4O_3$ $[M+H]^+$ 417.18; found 417.44.

Compound **13**

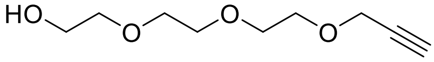

To a solution of triethylene glycol (19.64 g, 130.1mmol) in THF (50 mL) was added *t*-BuOK (7.34 g, 65.4 mmol) under argon at room temperature. The mixture was stirred for 30 min at room temperature and then propargyl bromide (9.73 g, 65.4 mmol, 80% in toluene) diluted in THF (20 mL) was added dropwise. The final mixture was stirred at room temperature for 15 h. Then the mixture was filtered through celite and washed with dichloromethane (50 mL). After concentration under reduced pressure, the resulting residue was purified by flash column chromatography (SiO_2, cyclohexane/ethyl acetate = 1/1→0/1) affording product **13** as a slight yellow oil (18.1 g, 74%).

Characterization are in agreement with the literature.[134]

^{1}H NMR ($CDCl_3$, 400 MHz, 298 K): δ 4.11 (d, J = 2.4 Hz, 2H), 3.72-3.65 (m, 10H), 3.38 (t, J = 5.2 Hz, 2H), 2.42 (t, J = 2.4 Hz, 1H).

^{13}C NMR ($CDCl_3$, 100 MHz, 298 K) δ 79.2, 74.4, 72.1, 70.1, 69.8, 61.0, 57.8.

ESI-MS: calculated for $C_9H_{17}O_4$ $[M+H]^+$ 189.11, found 189.33.

Compound **14**

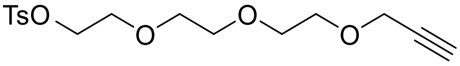

To a solution of compound **13** (7.1 g, 37.72 mmol) in THF (30 mL) was added tosyl chloride

(8.63 g, 45.27 mmol) at 0°C, then a NaOH aqueous solution (10 mL, 11.3 mol/L) was added slowly. The mixture was stirred at 0 °C for 12 hours. Then the mixture was poured into iced water (30 mL) and extracted with dichloromethane (50 mL). The combined organic phase was dried over Na_2SO_4 and purified by flash column chromatography (SiO_2, cyclohexane/ethyl acetate = 30/1→3/1) affording compound **14** (11.88 g, 92%) as a colorless oil.

Characterization are in agreement with the literature.[134]

^{1}H NMR (CDCl$_3$, 400 MHz, 298 K): δ 7.77 (d, *J* = 8.4 Hz, 2H), 7.32 (d, *J* = 8.4 Hz, 2H), 4.16 (d, *J* = 2.4 Hz, 2H), 4.14 (t, *J* = 4.8 Hz, 2H), 3.72-3.60 (m, 6H), 3.57 (s, 4H), 2.45-2.39 (m, 4H).

^{13}C NMR (CDCl$_3$, 100 MHz, 298 K): δ 144.7, 133.0, 129.7, 127.9, 79.6, 74.5, 70.6, 70.5, 70.4, 69.2, 69.0, 68.6, 58.3, 21.6.

ESI-MS (m/z): calculated for $C_{16}H_{22}O_6S$ $[M+H]^+$ 343.12, Found 343.49.

Compound **15**

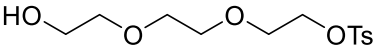

To a solution of tetraethylene glycol (50.0 g, 332.95 mmol) in THF (100 mL) was added the solution of sodium hydroxide (2.13 g, 53.27 mmol) in water (3 mL) at 0 °C. A solution of tosyl chloride (6.35 g, 33.29 mmol) in THF (50 mL) was added dropwise over 40 min and the solution was stirred for 12 hours at room temperature. Then, the solution was poured into iced water (30 mL) and extracted with dichloromethane (3 × 50 mL), and the combined organic layers were washed with distilled water (2 × 50 mL), and dried over Na_2SO_4. After concentration under reduced pressure, compound **15** (8.3 g, 8%) was obtained as yellowish oil, which was used in the next step without further purification

Compound **16**

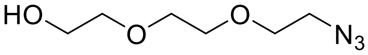

To a solution of compound **15** (6.00 g, 19.71 mmol) in DMF (20 mL) was added sodium azide (2.56 g, 39.43 mmol), the solution was stirred for 12 h at 80 °C. After cooling down to room temperature, the mixture was diluted with ethyl acetate (30 mL), and washed with brine (3 × 15 mL). The organic phase was dried over $NaSO_4$, and concentrated under reduced pressure to afford compound **16** (3.38 g, 98%) as yellowish oil.

^{1}H NMR ($CDCl_3$, 400 MHz, 298 K): δ 3.75-3.62 (m, 8H), 3.61-3.59 (m, 2H), 3.37 (t, *J* = 5.2 Hz, 2H).

ESI-MS (m/z): calculated for $C_6H_{13}N_3O_3$ $[M+H]^+$ 176.10, found 176.33.

Compound **17**

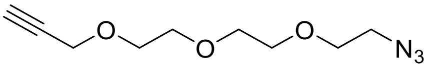

To a solution of compound **16** (1.00 g, 5.71 mmol) in THF (15 mL) was added sodium hydride (0.205 g, 8.56 mmol) at 0 °C, then propargyl bromide (1.36 g, 11.42 mmol) was added and the mixture was stirred for 12 h at room temperature. Then, the solution was diluted with water (10 mL), and the mixture was extracted with dichloromethane (3 × 10 mL). The combined organic phase was dried over $NaSO_4$ and purified by flash column chromatography (SiO_2, cyclohexane/ethyl acetate = 40/3→7/3) to afford compound **17** (1.18 g, 95%) asa yellow oil.

^{1}H NMR ($CDCl_3$, 400 MHz, 298 K): δ 4.19 (d, *J* = 2.4 Hz, 2H), 3.71-3.63 (m, 10H), 3.38 (t, *J* = 5.2 Hz, 2H), 2.42 (t, *J* = 2.4 Hz, 1H).

^{13}C NMR ($CDCl_3$, 100 MHz, 298K): δ 78.7, 76.4, 70.4, 70.1, 70.0, 69.5, 69.2, 60.3, 51.0.

ESI-MS (m/z): calculated for $C_9H_{15}N_3O_3$ $[M+H]^+$ 214.11, found 214.12.

Compound **18**

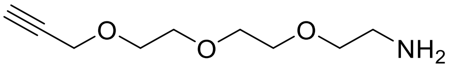

To a solution of compound **17** (1.00 g, 4.69 mmol) in a mixture of Et_2O/THF/1 M HCl (30 mL, v/v/v = 5/1/5) was added triphenylsphine (1.5 g, 5.72 mmol), and the mixture was stirred for 12 hours at room temperature. The organic phase was removed, and the aqueous layer was washed with Et_2O (3 × 20 mL). The pH of the aqueous was then adjusted to 14 using a 0.5 M NaOH solution (1 mL). The basic aqueous solution was extracted with dichloromethane (3 × 20 mL). The combined organic layers were dried over anhydrous Na_2SO_4 and further concentration under reduced pressure afforded compound **18** (745 mg, 85%) as a yellowish oil.

^{1}H NMR ($CDCl_3$, 400 MHz, 298 K): δ 4.19 (d, *J* = 2.4 Hz, 2H), 3.72-3.58 (m, 10H), 3.49 (t, *J* = 5.2 Hz, 2H), 2.41 (t, *J* = 2.4 Hz, 1H).

^{13}C NMR ($CDCl_3$, 100 MHz, 298K): δ 78.7, 76.4, 72.9, 70.4, 70.1, 69.5, 69.2, 60.3, 41.6.

ESI-MS (m/z): calculated for $C_9H_{17}NO_3$ $[M+H]^+$ 189.12, found 189.13.

Compound **20**

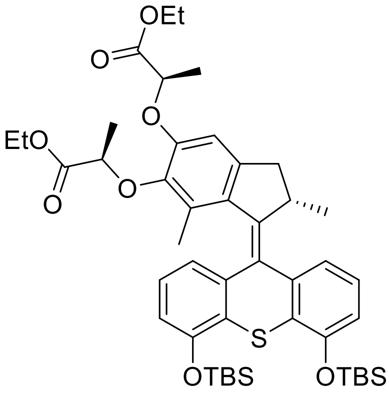

To a solution of precursor episulfide **19** (470 mg, 0.54 mmol) in toluene (20 mL) was added triphenylphosphine (2.14 g, 8.16 mmol). The mixture was stirred at 120 °C for 27 h. After that, the mixture was concentrated under reduced pressure and further purified by flash column chromatography (SiO_2, toluene/ethyl acetate = 100/0→50/1) to afford compound **20** (425.4 mg, 94 %) as a yellow solid.

^{1}H NMR (CDCl$_3$, 400 MHz, 298 K): δ 7.29 (d, *J* = 7.6 Hz, 1H), 7.12 (dd, *J* = 8.0, 8.0 Hz, 1H), 6.86 (dd, *J* = 8.0, 8.0 Hz, 1H), 6.69 (dd, *J* = 8.0, 0.8 Hz, 1H), 6.64 (dd, *J* = 7.6, 1.2 Hz, 1H), 6.62 (dd, *J* = 7.6, 1.2 Hz, 1H), 6.53 (s, 1H), 4.79-4.70 (m, 2H), 4.29-4.07 (m, 5H), 3.38-3.28 (m,1H), 2.31 (d, *J* = 15.2 Hz, 1H), 1.61 (d, *J* = 6.8 Hz, 3H), 1.44 (d, *J* = 6.8 Hz, 3H), 1.26-1.17 (m, 9H), 1.09 (d, *J* = 3.2 Hz, 18H), 0.61 (d, *J* = 6.8 Hz, 3H), 0.32-0.23 (m, 12H).

^{13}C NMR (CDCl$_3$, 100 MHz, 298 K): δ 172.4, 171.9, 152.7, 152.2, 149.6, 145.5, 144.4, 141.9, 141.8, 138.3, 133.4, 130.8, 128.1, 127.7, 127.1, 126.4, 126.1, 120.9, 120.2, 116.3, 115.5, 108.1, 76.9, 72.9, 61.2, 60.6, 39.4, 37.9, 25.9, 18.9, 18.5, 18.4, 14.4, 14.1, 14.0, -3.9, -4.0, -4.3, -4.4.

ESI-MS (m/z): calculated for $C_{46}H_{65}O_8SSi_2$ $[M+H]^+$ 833.39, found: 833.58.

Compound **21**

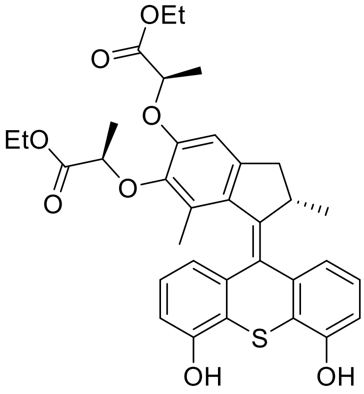

To a solution of motor **20** (200 mg, 0.24 mmol) in THF (5 mL) was added TBAF (0.50 mL, 1M in THF, 0.50 mmol) at 0 °C. The mixture was stirred at 0 °C for 1 min. Then a saturated solution of NH_4Cl (10 mL) was added and the mixture was extracted with dichloromethane (3 × 20 mL). The combined organic layers were dried over Na_2SO_4 and concentrated in vacuum. Further purification by flash column chromatography (SiO_2, dichloromethane/methanol = 50/1→10/1) afforded compound **21** (132.6 mg, 91%) as a yellow solid.

^{1}H NMR (CDCl$_3$, 400 MHz, 298 K): δ 7.31 (d, *J* = 7.6 Hz, 1H), 7.22 (dd, *J* = 8.0, 8.0 Hz, 1H), 6.95 (dd, J = 7.6, 7.6 Hz, 1H), 6.82 (dd, J = 8.0, 1.2 Hz, 1H), 6.74 (dd, J = 8.0, 1.2 Hz, 1H), 6.65 (dd, J = 7.6, 1.2 Hz, 1H), 6.56 (s, 1H), 4.81 (q, J = 6.8 Hz, 1H), 4.77 (q, J = 6.8 Hz, 1H), 4.30-4.08 (m, 5H), 3.37 (dd, J = 15.0, 6.1 Hz, 1H), 2.37 (d, J = 15.0 Hz, 1H), 1.62 (d, J = 6.8 Hz, 3H), 1.46 (d, J = 6.8 Hz, 3H), 1.32 (s, 3H), 1.23 (t, J = 7.1 Hz, 3H), 1.20 (t, J = 7.1 Hz, 3H), 0.71 (d, J = 6.7 Hz, 3H).

^{13}C NMR (CD$_3$OD, 100 MHz, 298 K): δ 174.2, 173.5, 155.7, 155.2, 151.1, 146.5, 145.5, 143.8, 143.5, 140.2, 134.7, 131.9, 130.2, 127.9, 127.8, 124.0, 123.3, 120.5, 120.0, 113.2, 113.1, 109.4, 77.9, 74.1, 62.4, 62.0, 40.4, 39.3, 19.3, 18.9, 18.7, 15.0, 14.5, 14.4.

ESI-HRMS (m/z): calculated for $C_{34}H_{36}O_8S$ [M+H]$^+$ 605.71, found 605.62.

Compound **22**

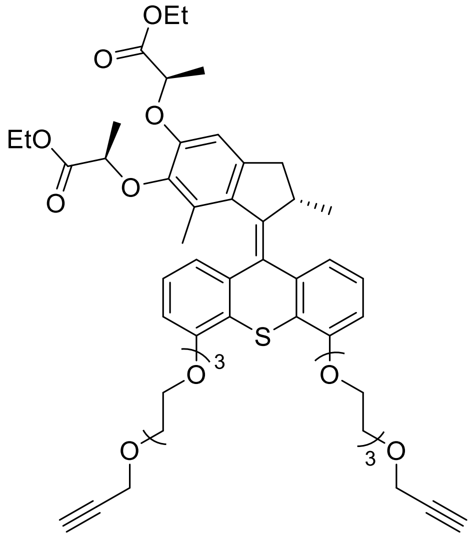

To a mixture of bis-phenol motor **21** (150 mg, 0.25 mmol) and K_2CO_3 (102.5 mg, 0.74 mmol) in DMF (10 mL) was added a solution of compound **14** (253.9 mg, 0.74 mmol) in DMF (1.5 mL). The mixture was stirred at 80 °C for 72 hours. Then the mixture was diluted with water (10 mL) and extracted with dichloromethane (3×20 mL). The combined organic phase was dried over Na_2SO_4, then concentrated under reduced pressure. The crude residue was further purified by flash column chromatography (SiO_2, cyclohexane/ethyl acetate = 10/1→1/1) to afford compound **22** (160 mg, 68 %) as a yellowish solid.

^{1}H NMR (CDCl$_3$, 400 MHz, 298 K): δ 7.33 (d, *J* = 7.6 Hz, 1H), 7.21 (dd, *J* = 8.0, 8.0 Hz, 1H), 6.93 (dd, *J* = 8.0, 8.0 Hz, 1H), 6.76 (d, *J* = 7.6 Hz, 1H), 6.69 (dd, *J* = 8.0, 1.0 Hz, 1H), 6.64 (dd, *J* = 7.6, 1.2 Hz, 1H), 6.53 (s, 1H), 4.79 (q, *J* = 6.8 Hz, 1H), 4.76 (q, *J* = 6.8 Hz, 1H), 4.35- 4.08 (m, 13H), 4.03-3.91 (m, 4H), 3.88-3.80 (m, 4H), 3.78-3.61 (m, 12H), 3.37-3.32 (m, 1H), 2.45-2.39 (m, 2H), 2.32 (d, *J* = 14.9 Hz, 1H), 1.61 (d, *J* = 6.8 Hz, 3H), 1.46 (d, *J* = 6.8 Hz, 3H), 1.22 (t, *J* = 7.1 Hz, 3H), 1.19 (s, 3H), 1.19 (t, *J* = 7.1 Hz, 3H), 0.62 (d, *J* = 6.7 Hz, 3H).

^{13}C NMR (CDCl$_3$,100 MHz, 298 K): δ 172.5, 172.0, 155.8, 155.3, 149.6, 145.9, 144.4, 141.9, 141.7, 138.2, 133.4, 131.0, 127.6, 126.7, 126.4, 124.9, 124.6, 120.9, 120.3, 109.5, 109.0, 108.0, 79.7, 77.2, 76.8, 74.5, 72.9, 71.1, 70.8, 70.4, 69.7, 69.6, 69.1, 68.8, 61.2, 60.7, 58.4, 39.5, 38.1, 18.9, 18.6, 18.4, 14.5, 14.1, 14.0.

ESI-MS (m/z): calculated for $C_{52}H_{64}O_{14}S$ $[M+H]^+$ 945.41, found 945.77.

Compound **23**

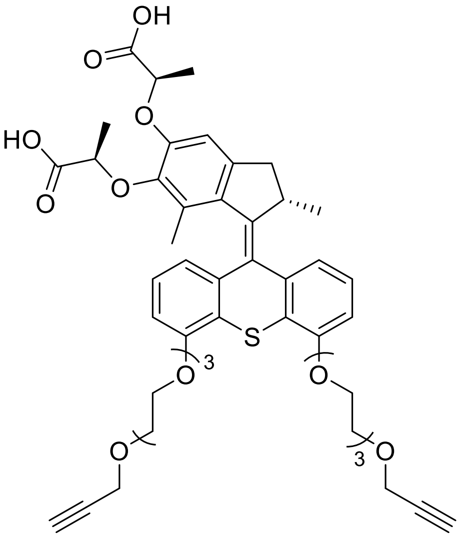

To a solution of compound **22** (160 mg, 0.17 mmol) in a 1:1 mixture of THF/MeOH (2 mL/2 mL) was added a NaOH (41 mg, 1.025 mmol) aqueous solution (2 mL). The mixture was stirred at room temperature for 16 hours, and quenched with 1 M HCl (5 mL) at 0 °C. The mixture was then washed with dichloromethane (3 × 10 mL). The combined organic phase was dried over Na_2SO_4. After removal of solvent, compound **23** (148 mg, 98 %) was afforded as a yellowish solid.

^{1}H NMR (CD_3OD, 400 MHz, 298 K): δ 7.37 (d, *J* = 7.6 Hz, 1H), 7.27 (dd, *J* = 8.0, 8.0 Hz, 1H), 6.98 (dd, *J* = 8.0, 8.0 Hz, 1H), 6.87 (d, *J* = 7.6 Hz, 1H), 6.81 (d, *J* = 7.6 Hz, 1H), 6.67 (s, 1H), 6.60 (dd, *J* = 8.0, 1.2 Hz, 1H), 4.81 (q, *J* = 7.2 Hz, 1H), 4.62 (q, *J* = 6.8 Hz, 1H), 4.30-4.10 (m, 9H), 3.92-3.89 (m, 4H), 3.78-3.77 (m, 4H), 3.66-3.60 (m, 12H), 3.40-3.35 (m, 1H), 2.80 (t, *J* = 2.4 Hz, 1H), 2.79 (t, *J* = 2.4 Hz, 1H), 2.36 (d, *J* = 15.2 Hz, 1H), 1.60 (d, *J* = 6.8 Hz, 3H), 1.38 (d, *J* = 6.8 Hz, 3H), 1.17 (s, 3H), 0.60 (d, *J* = 6.8 Hz, 3H).

^{13}C NMR (CD_3OD, 100 MHz, 298 K): δ 176.1, 175.5, 157.4, 156.8, 151.5, 147.2, 145.5, 143.8, 143.2, 139.5, 134.5, 131.9, 129.3, 128.0(2C), 126.4, 125.6, 122.0, 121.3, 110.8, 110.6, 109.5, 80.7, 78.4, 76.0, 74.3, 73.7, 72.1, 71.7, 71.6, 71.4, 70.9, 70.8, 70.2, 70.1, 62.3, 59.1, 40.4, 39.3, 19.3, 19.1, 18.8, 15.2.

ESI-MS (m/z): calculated for $C_{48}H_{56}O_{14}S$ $[M-H]^-$ 887.33, found 887.63.

Compound **24**

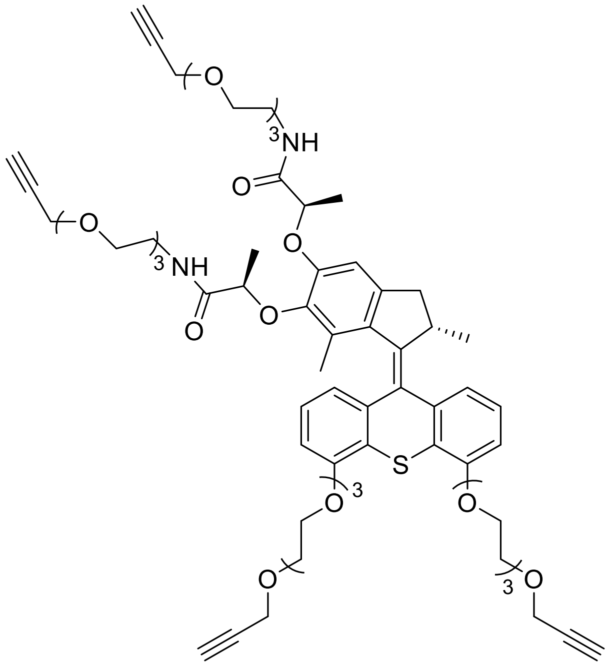

To a solution of motor **23** (160 mg, 0.18 mmol) in dichloromethane (2 mL) was added HOBt (146 mg, 1.08 mmol) and EDC (207 mg, 1.08 mmol). After 15 min, a solution of compound **18** (101 mg, 0.54 mmol) in dichloromethane (2 mL) was added, the reaction mixture was stirred at room temperature for 16 hours. After concentrating under reduced pressure, the residue was t purified by flash column chromatography (SiO_2, dichloromethane/methanol = 200/1→20/1) affording compound **24** (99.4 mg, 45%) as a yellow oil.

^{1}H NMR ($CDCl_3$, 400 MHz, 298 K): δ 7.51 (brs, 1H), 7.34 (d, *J* = 7.6 Hz, 1H), 7.23 (dd, *J* = 8.0, 8.0 Hz, 1H), 7.04 (brs, 1H), 6.96 (dd, *J* = 8.0, 8.0 Hz, 1H), 6.78 (d, *J* = 8.0 Hz, 1H), 6.72 (d, *J* = 7.6 Hz, 1H), 6.68 (s, 1H), 6.66 (s, 1H), 4.67 (q, *J* = 6.8 Hz, 1H), 4.44 (q, *J* = 6.8 Hz, 1H), 4.33-4.26 (m, 2H), 4.23-4.10 (m, 10H), 4.00-3.91 (m, 4H), 3.84 (t, *J* = 4.4 Hz, 4H), 3.74-3.66 (m, 13H), 3.65-3.32 (m, 24H), 2.45-2.44 (m, 3H), 2.37 (d, *J* = 15.2 Hz, 1H), 1.59 (d, *J* = 6.8 Hz, 3H), 1.33-1.22 (m, 5H), 1.14 (s, 3H), 0.63 (d, *J* = 6.8 Hz, 3H).

^{13}C NMR ($CDCl_3$, 100 MHz, 298 K): δ 172.6, 172.1, 156.2, 155.5, 149.9, 145.5, 143.8, 143.0, 141.6, 137.9, 134.3, 131.1, 128.5, 126.8, 126.7, 125.1 120.3, 109.7, 109.3, 109.2, 79.8, 79.7, 79.1, 76.3, 74.8, 74.7, 71.2, 70.9, 70.6, 70.5, 70.4, 70.3, 69.9, 69.8, 69.3, 69.2, 69.0, 68.9, 58.5, 58.4, 39.8, 39.0, 38.1, 19.2, 19.1, 18.4, 15.4.

ESI-MS (m/z): calculated for $C_{66}H_{86}N_2O_{18}S$ $[M+H]^+$ 1227.57, found 1227.16.

Compound **25**

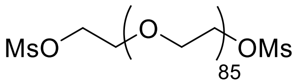

Polyethylene glycol (3.0 g, 0.75 mmol, M_n = 4000 g/mol) was dissolved in dichloromethane (10 mL) and trimethylamine (0.76 g, 7.55 mmol) was added. Then a solution of mesyl chloride in dichloromethane (20 mL) was added dropwise over 1 hour at 0 °C. The mixture was stirred for 2 days at room temperature. Afterwards, the solution was concentrated under vacuum, and the crude was poured into cold isopropanol (20 mL) leading to a white precipitate. After filtration, the white powder was collected and dried to afford compound **25** (3.04 g, 98%) as a withe powder.

^{1}H NMR (toluene-d_8, 400 MHz, 298 K): δ 3.97 (t, *J* = 4.4 Hz, 4H), 3.54-3.22 (m, 349H).

Compound **26**

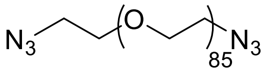

To a solution of compound **25** (2.5 g, 0.6 mmol) in DMF (50 mL) was added sodium azide (0.39 g, 6.0 mmol). The mixture was stirred for 24 hours at 50 °C. After that time, the mixture was cooled down to room temperature, poured into cooled diethyl ether (30 mL) to precipitate polymers which were further dissolved in dichloromethane (10 mL). After filtration, excess sodium azide was removed. Then the filtrate was poured into cold diethyl ether (25 mL) to precipitate the polymer again. The precipitates were washed with cold diethyl ether (20 mL) and dried to compound **26** (1.81 g, 74%) as a white solid.

^{1}H NMR (toluene-*d*$_8$, 400 MHz, 298 K): δ 3.55-3.548 (m, 345H), 3.27 (t, *J* = 6.8 Hz, 4H), 2.86 (t, *J* = 5.2 Hz, 4H).

Compound **27**

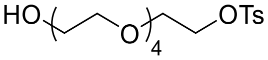

Pentaethylene glycol (2.0 g, 8.39 mmol) was first dissolved in THF (10 mL), the solution was then cooled down to 0 °C. A solution of NaOH (0.45 g, 2.8 mmol) in distilled water (2 mL) was subsequently added dropwise at the same temperature. Then, a solution of *p*-toluenesulfonyl chloride in THF (15 mL) was added dropwise over 40 min and the solution was stirred for 16 h at room temperature. The solution was diluted with water and the aqueous layer was extracted with dichloromethane (3 × 10 mL). The combined organic layers were dried over Na_2SO_4, the solvent was removed under reduced pressure. Then the crude was purified by flash column chromatography (SiO_2, dichloromethane/methanol = 100/0→100/1) affording COMPOUND **27** (0.9 g, 27%) as yellow oil.

^{1}H NMR ($CDCl_3$, 400 MHz, 298 K): δ 7.78 (d, *J* = 8.0 Hz, 2H), 7.72 (d, *J* = 8.0 Hz, 2H), 4.19-4.10 (m, 2H), 3.74-3.54 (m, 19H), 2.53 (s, 1H), 2.43 (s, 2H).

ESI-MS (m/z): calculated for $C_{17}H_{28}O_8$ $[M+H]^+$ 393.15, found 393.53.

Compound **28**

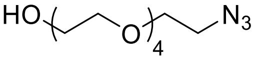

To a solution of compound **27** (840 mg, 2.14 mmol) in DMF (5 mL) was added sodium azide (209 mg, 3.21 mmol), and the mixture was stirred at 80°C for 12 h. Then the solution was diluted with ethyl acetate (10 ml) and washed WITH brine (3 × 10 mL). The organic layer was dried over Na_2SO_4. After concentration under reduced pressure, the crude residue was purified by flash column chromatography (SiO_2, dichloromethane/methanol = 100/0→100/1) affording compound **28** (410 mg, 73%) as a yellow oil.

^{1}H NMR ($CDCl_3$, 400 MHz, 298 K): δ 3.75-3.56 (m, 18H), 3.37 (t, *J* = 5.2 Hz, 2H), 2.64 (s, 1H).

^{13}C NMR ($CDCl_3$, 100 MHz, 298 K): δ 72.6, 70.8, 70.7, 70.6, 70.4, 70.1.

ESI-MS (m/z): calculated for $C_{10}H_{21}N_3O_5$ $[M+H]^+$ 264.15, found 264.99.

Compound **29**

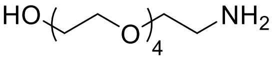

To a solution of compound **28** (410 mg, 1.56 mmol) in THF (5 mL) was added triphenylphosphine (613 mg, 2.34 mmol), and the mixture was stirred for 12 hours at room temperature. Then water (10 mL) was added into the mixture, and the aqueous phase was washed with toluene (3 × 10 mL). Evaporation of the aqueous layer under reduced pressure yielded compound **29** as a yellow oil (210 mg, 57%).

^{1}H NMR (D_2O, 400 MHz, 298 K): δ 3.65-3.57 (m, 15H), 3.55-3.50 (m, 2H), 3.48 (t, *J* = 5.2

Hz, 2H), 2.74 (t, *J* = 5.2 Hz, 2H).

^{13}C NMR (D_2O, 100 MHz, 298 K): δ 73.7, 73.5, 71.6, 71.5, 71.4, 71.2, 62.2, 42.1.

ESI-MS (m/z): calculated for $C_{10}H_{23}NO_5$ $[M+H]^+$ 238.16, found 238.52.

Compound **30**

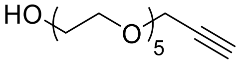

To a solution of pentaethylene glycol (3.0 g, 12.59 mmol) in THF (75 mL) was added t-BuOK (1.41 g, 12.59 mmol). The mixture was stirred for 30 min at room temperature, then a solution of propargyl bromide (1.5 g, 1.085 mL, 12.59 mmol) and t-BuOK (1.41 g, 12.59 mmol) in THF (40 mL) was added dropwise. After 15 hours, the mixture was filtered through celite and washed with dichloromethane (50 mL). After concentration under reduced pressure, further purification by flash column chromatography (SiO_2, cyclohexane/acetate = 10/1→0/1) afforded compound **30** (1 g, 29 %) as a slight yellow oil.

^{1}H-NMR data are in accordance with the literature.[170]

^{1}H NMR ($CDCl_3$, 400 MHz, 298 K): δ 4.17 (d, *J* = 2.4 Hz, 2H), 3.70-3.56 (m, 20H), 2.69 (s, 1H), 2.41 (t, *J* = 2.4 Hz, 1H).

ESI-MS (m/z): calculated for $C_{10}H_{24}NO_6$ $[M+K]^+$ 315.12, found 315.49.

Compound **31**

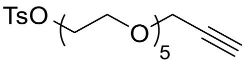

To a solution of compound **30** (1 g, 3.62 mmol) in THF (10 mL) was added tosyl chloride (0.83 g, 4.34 mmol) at 0 °C, then a solution of NaOH (0.43 g, 10.86 mmol) in water (2 mL) was

added slowly. The mixture was stirred at room temperature for 2 h. After that, the mixture was poured into iced water (20 mL) and extracted with dichloromethane (3 × 10 mL). The combined organic phase was dried over Na_2SO_4 and purified by flash column chromatography (SiO_2, cyclohexane/ethyl acetate = 20/1→2/1) to afford compound **31**(1.2 g, 77%) as a yellow oil.
^{1}H-NMR data are in accordance with the literature.[170]

^{1}H NMR ($CDCl_3$, 400 MHz, 298 K): δ 7.77 (d, *J* = 8.0 Hz, 2H), 7.32 (d, *J* = 8.0 Hz, 2H), 4.17 (d, *J* = 2.4 Hz, 2H), 4.13 (t, *J* = 4.8 Hz, 2H), 3.68-3.58 (m, 14H), 3.56 (s, 4H), 2.42 (brs, 3H), 2.41 (t, *J* = 2.4 Hz, 1H).

ESI-MS (m/z): calculated for $C_{20}H_{30}O_8$ $[M+H]^+$ 431.17, found 431.53.

Compound **32**

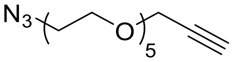

To a solution of compound **31** (1.2 g, 2.79 mmol) in DMF (5 mL) was added sodium azide (0.27 g, 4.18 mmol), the mixture was stirred for 12 hours at 80 °C. Then the solution was diluted with ethyl acetate (10 mL) and washed with brine (3 × 10 mL). The organic layer was dried over Na_2SO_4. After concentration under reduced pressure, the crude residue was purified by flash column chromatography (silica gel, cyclohexane/ethyl acetate = 20/1→2/1) to yield compound **32** (0.6 g, 71%) as a yellow oil.

^{1}H-NMR data are in accordance with the literature.[170]

^{1}H NMR ($CDCl_3$, 400 MHz, 298 K): δ 4.16 (d, *J* = 2.4 Hz, 2H), 3.69-3.56 (m, 18H), 3.35 (t, *J* = 5.2 Hz, 2H), 2.41 (t, *J* = 2.4 Hz, 1H).

ESI-MS (m/z): calculated for $C_{13}H_{23}N3O_5$ $[M+H]^+$ 302.17, Found 302.49.

Compound **33**

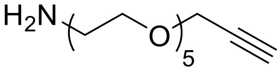

To a solution of compound **32** (600 mg, 1.99 mmol) in a mixture of Et_2O/THF/1 M HCl (20 mL, v/v/v = 5/1/5) was added triphenylphosphine (783 mg, 2.99 mmol), and the mixture was stirred for 12 h under room temperature. After that time, the organic phase was removed, and the aqueous layer was washed with Et_2O (3×20 mL). The pH of the aqueous solution was then adjusted to 14 using a 0.5M NaOH (2 mL). The basic aqueous solution was extracted with dichloromethane (3 × 20 mL). The combined organic layers were dried over anhydrous Na_2SO_4 and further concentration under reduced pressure yielded the compound **33** (400 mg, 73%) as a yellowish oil.

^{1}H-NMR data are in accordance with the literature.[170]

^{1}H NMR ($CDCl_3$, 400 MHz, 298 K): δ 4.20 (d, *J* = 2.0 Hz, 2H), 3.70-3.58 (m, 18H), 2.43 (t, *J* = 2.4 Hz, 1H), 1.24 (brs, 2H).

ESI-MS (m/z): calculated for $C_{13}H_{25}NO_5$ $[M+H]^+$ 276.18, found 276.57.

Compound **34**

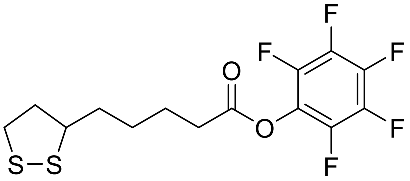

To a solution of lipoic acid (2.0 g, 9.69 mmol) in dichloromethane (20 mL) was added DCC (2 g, 9.69 mmol), then the mixture was stirred for 15 min. After that, a solution of pentafluorophenol (1.78 g, 9.69 mmol) in dichloromethane (5 mL) was added dropwise. After stirring for overnight, the mixture was filtered and the filtrate was washed with water (3 × 10 mL). The organic layer was dried over Na_2SO_4. After concentration under reduced pressure, the crude residue was purified by flash column chromatography (SiO_2, cyclohexane/ethyl acetate = 20/1→2/1) affording compound **34** (3.2 g, 89%) as a yellowish solid.

Characterization are in accordance with the literature.[171]

^{1}HNMR ($CDCl_3$, 400MHz, 298K): δ 3.62-3.54 (m, 1H), 3.21-3.08 (m, 2H), 2.69 (t, J = 7.2 Hz, 2H), 2.52-2.42 (m, 1H), 1.96-1.87 (m, 1 H), 1.86-1.64 (m, 4H), 1.64-1.46 (m, 2H).

^{13}C NMR ($CDCl_3$, 100MHz, 298K): δ 169.4, 142.5, 140.0, 139.9, 138.7, 56.2, 40.3, 38.6, 34.6, 33.2, 28.6, 24.6.

Compound **35**

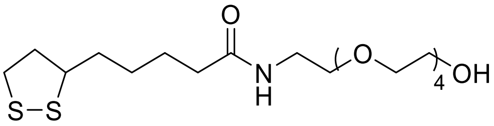

To a solution of compound **34** (359 mg, 1.06 mmol) and compound **29** (210 mg, 0.88 mmol) in dichloromethane (10 mL) was added triethylamine (269 mg, 0.37 mL, 2.65 mmol). The mixture was stirred for 16 hours at room temperature. After that time, the mixture was washed with water (3 × 10 mL) and the organic layer was dried over Na_2SO_4. The crude residue was purified by flash column chromatography (SiO_2, dichloromethane/methanol = 100/0→80/1) affording compound **35** (309 mg, 82%) as a yellow oil.

^{1}H NMR ($CDCl_3$, 400 MHz, 298 K): δ 6.55 (s, 1H), 3.72-3.52 (m, 19H), 3.43 (brs, 2H), 3.215-3.05 (m, 2H), 2.96 (s, 1H), 2.45 (t, J = 6.4 Hz, 1H), 2.19 (t, J = 7.6 Hz, 2H), 1.89 (dt, J = 6.4 Hz, 1H), 1.76-1.59 (m, 4H), 1.54-1.41 (m, 2H).

^{13}C NMR ($CDCl_3$, 100 MHz, 298 K): δ 173.1, 72.7, 70.7, 70.6, 70.4, 70.3, 70.2, 61.8, 56.6, 40.4, 39.3, 38.6, 36.4, 34.8, 29.1, 25.5.

ESI-MS (m/z): calculated for $C_{18}H_{36}NO_6S_2$ $[M+H]^+$ 426.19, found 426.65.

Compound **36**

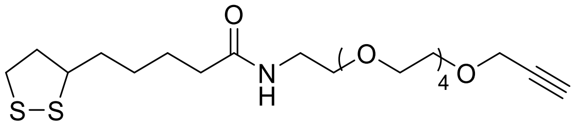

To a solution of compound **34** (400 mg, 1.074 mmol) and compound **33** (354.93 mg, 1.29 mmol) in dichloromethane (10 mL) was added triethylamine (217.4 mg, 0.3 mL, 2.15 mmol). The mixture was stirred for 16 h at room temperature. After that time, the mixture was washed with water (3 × 10 mL) and the organic layer was dried over Na_2SO_4. The crude residue was purified by flash column chromatography (SiO_2, dichloromethane/methanol = 100/0→100/1) affording compound **36** (398.4 mg, 80%) as a yellow oil.

^{1}H NMR ($CDCl_3$, 400 MHz, 298 K): δ 6.15 (s, 1H), 4.19 (d, *J* = 2.4 Hz, 2H), 3.71-3.52 (m, 19H), 3.43 (t, *J* = 5.2 Hz, 2H), 3.21-3.05 (m, 2H), 2.49-2.41 (m, 2H), 2.19 (t, *J* = 7.6 Hz, 2H), 1.89 (t, *J* = 6.4 Hz, 1H), 1.76-1.59 (m, 4H), 1.54-1.41 (m, 2H).

^{13}C NMR ($CDCl_3$, 100 MHz, 298 K): δ 172.9, 79.8, 74.7, 70.8, 70.7, 70.5, 70.4, 70.0, 69.2, 58.5, 56.6, 40.4, 39.3, 38.6, 36.5, 34.8, 29.1, 25.5.

ESI-MS (m/z): calculated for $C_{21}H_{37}NO_6S_2$ $[M+H]^+$ 464.21, found 464.33.

Synthesis of citrate-coated AuNPs **I**

A solution of chlorauric acid (39.4 mg, 0.1 mmol) in milli-Q water (90 mL) was heated to reflux, and a solution of sodium citrate (102.9 mg, 0.35 mmol) in milli-Q water (10 mL) was added very rapidly under vigorous stirring. Then the color of the mixture turned from yellow to red-wine. Afterwards, the solution was stirred for 10 min at the same temperature to yield citrate-coated AuNPs **I**.

Functionalization of AuNPs **I**

To avoid aggregation of AuNPs, the pH of the solution (5mL) of AuNPs **I** was adjusted to 9 using an aqueous solution of NaOH (0.5M, 40 μL). Then a methanol solution containing compound **36** (0.01 M, 100 μL), compound **35** (0.01 M, 400 μL), and TBAB (60 mM, 100 μL) was added into the AuNPs solution. The mixture was then shaken gently for 24 hours at room temperature. After that time, the mixture was centrifuged (6000 rpm). The precipitates were washed with milli-Q water (10 mL) to remove un-grafted ligands. Finally, the solids were re-dispersed in DMF to yield functionalized AuNP **II** with concentrations of 0.8, 1.6, 2.0 and 4.0 g/L, respectively.

Gels preparation

Every gel was prepared in a home-made metal mold (2 cm × 2 cm × 458 μm).

Typical procedure: in a vial, alkyne-terminated molecular motor **24** (1.5 mg, 0.0012 mmol) and bis-azide PEG **26** (9.2 mg, 0.0024 mmol) were dissolved in a DMF solution of AuNPs **II** (0.2 mL). Then CuBr (1.40 mg, 0.0098 mmol) and PMDETA (0.24 μL, 0.0098 mmol) were added. The mixture was then transferred into rheology mold and the mold was kept for 12 hours at room temperature. After unmolding, the formed gel was washed with aqueous solution of EDTA (200 mL) and water (200 mL). Finally the gel was brought into milli-Q water (200 mL).

Compound **37**

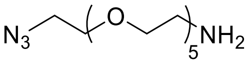

The synthesis of compound **37** contains three successive steps. First, to a solution of hexaethylene glycol (1.0 g, 3.54 mmol) in dichloromethane (10 mL) was added triethylamine (1.13 mL, 8.15 mmol) and tosyl chloride (1.55 g, 8.15 mmol). The mixture was stirred at room temperature for 6 h. After that, the mixture was washed with saturated $NaHCO_3$ solution (3 × 10 mL) and water (3 × 10 mL). The organic phase was dried over anhydrous Na_2SO_4. After concentration under reduced pressure, a yellow oil was obtained, which was directly used in the next step without further purification. The product was dissolved in DMF (10 mL). Then sodium azide (660 mg, 10.16 mmol) was added. The mixture was stirred overnight at 80 °C. After cooling down to room temperature, the mixture was diluted with ethyl acetate (30 mL) and washed with brine (3 × 30 mL). Then the organic phase was dried over anhydrous Na_2SO_4. After removal of solvent, the crude residue was dissolved in a mixture of Et_2O/THF/1 M HCl (30 mL, v/v/v = 5/1/5). A solution of triphenylphosphine (0.93 g, 3.54 mmol) in Et_2O (8mL) was added dropwise to above mixture over 3 h. After the addition was completed, the reaction mixture was allowed to stir at room temperature for another 20 h. The organic phase was removed, and the aqueous layer was washed with Et_2O (3×20 mL). The pH of the aqueous was then adjusted to 14 using a 0.5M NaOH solution (2 mL). The basic aqueous solution was extracted with dichloromethane (3 × 20 mL). The combined organic layers were dried over anhydrous Na_2SO_4 and further concentrated under reduced pressure to yield compound **37** (710 mg, 65 %) as a yellowish oil.

Data are in agreement with the literature.[172]

^{1}H NMR ($CDCl_3$, 400 MHz, 298 K): δ 3.69-3.58 (m, 18H), 3.48 (t, *J* = 5.2 Hz, 2H), 3.36 (t, *J* = 4.8 Hz, 2H), 2.83 (t, *J* = 5.2 Hz, 2H), 1.36 (brs, 2H).

^{13}C NMR ($CDCl_3$, 100 MHz, 298 K): δ 73.6, 70.8, 70.7, 70.4, 70.1, 50.7, 41.9.

ESI-MS (m/z): m/z calculated for $C_{12}H_{26}N_4O_5$ $[M+H]^+$ 307.198; found: 307.198.

Compound **S1**, **S2**, and **S3**

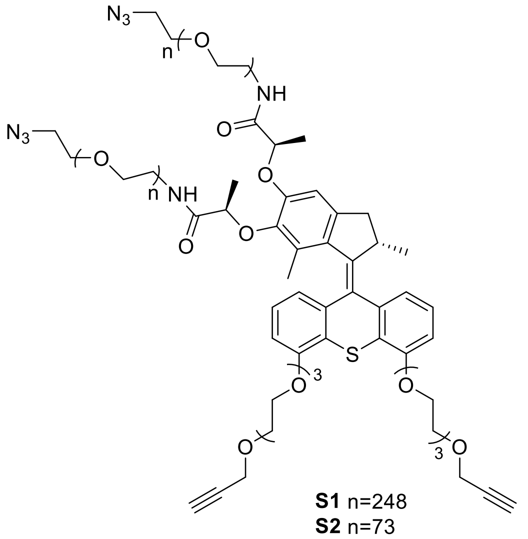

S1 n=248
S2 n=73
S3 n=5

PEG_{10000} Star-shaped motor **S1** (n=248): To a solution of compound **23** (10.0 mg, 0.011 mmol) in dichloromethane (1 mL) was added HOBt (5.1 mg, 0.037 mmol) and EDC (16.8 mg, 0.088

mmol) at room temperature. After 15 min, N_3-PEG-NH_2 (M_w = 10022 g/mol, 236.7 mg, 0.024 mmol) was added. The mixture was stirred at room temperature for 16 hours. After removal of the solvent, the residue was purified by reserved phase column chromatography (C18, Merck, methanol/water = 3/7→7/3) affording compound **S1** (160.0 mg, 68%) as a white powder.

^{1}H NMR (CD_3OD, 400 MHz, 298 K): δ 7.41 (d, *J* = 8.0 Hz, 1H), 7.32 (dd, *J* = 8.0, 8.0 Hz, 1H), 7.05 (dd, *J* = 8.0, 8.0 Hz, 1H), 6.94 (d, *J* = 8.0 Hz, 1H), 6.89 (d, *J* = 8.0 Hz, 1H), 6.75 (s, 1H), 6.65 (d, *J* =8.0 Hz, 1H), 4.73 (q, *J* = 6.8 Hz, 1H), 4.42 (q, *J* = 6.8 Hz, 1H), 4.37-4.14 (m, 9H), 4.05-3.92 (m, 4H), 3.87-3.78 (m, 15H), 3.76-3.34 (m, 1848 H), 2.89-2.83 (m, 2H), 2.42 (d, *J* = 15.2 Hz, 1H), 1.54 (d, *J* = 6.8 Hz, 3H), 1.30 (d, *J* = 6.8 Hz, 3H), 1.18 (s, 3H), 0.62 (d, *J* = 6.8 Hz, 3H).

PEG_{3000} Star-shaped motor **S2** (n=73): To a solution of compound **23** (20.0 mg, 0.022 mmol) in dichloromethane (1 mL) was added HOBt (10.2 mg, 0.074 mmol) and EDC (33.6 mg, 0.176 mmol) at room temperature. After 15 min, N_3-PEG-NH_2 (M_w = 2996 g/mol, 141.6 mg, 0.047 mmol) was added. The mixture was stirred at room temperature for 16 h. After removal of the solvent, the residue was purified by reserved phase column chromatography (C18, Merck, methanol/water = 3/7→7/3) affording compound **S2** (80 mg, 52%) as a white powder.

^{1}H NMR (CD_3OD, 400 MHz, 298 K): δ 7.41 (d, *J* = 8.0 Hz, 1H), 7.32 (dd, *J* = 8.0, 8.0 Hz, 1H), 7.05 (dd, *J* = 8.0, 8.0 Hz, 1H), 6.94 (d, *J* = 8.0 Hz, 1H), 6.89 (d, *J* = 8.0 Hz, 1H), 6.75 (s, 1H), 6.65 (d, *J* = 8.0 Hz, 1H), 4.73 (q, *J* = 6.8 Hz, 1H), 4.42 (q, *J* = 6.8 Hz, 1H), 4.37-4.13 (m, 9H), 4.01-3.91 (m, 4H), 3.87-3.77 (m, 8H), 3.73-3.34 (m, 584 H), 2.89-2.83 (m, 2H), 2.42 (d, *J* = 15.2 Hz, 1H), 1.54 (d, *J* = 6.8 Hz, 3H), 1.30 (d, *J* = 6.8 Hz, 3H), 1.18 (s, 3H), 0.62 (d, *J* = 6.8 Hz, 3H).

PEG_{300} Star-shaped motor **S3** (n=5): To a solution of compound **23** (25.0 mg, 0.028 mmol) in dichloromethane (2 mL) was added HOBt (12.7 mg, 0.092 mmol) and EDC (42 mg, 0.22 mmol) at room temperature. After 15 min, compound **37** (18.1 mg, 0.059 mmol) was added. The mixture was stirred at room temperature for 16 hours. The solution was diluted with dichloromethane (5 mL), and washed with saturated $NaHCO_3$ (3 × 5mL) and brine (3 × 5mL). The organic phase was dried over anhydrous Na_2SO_4. After concentration under reduced pressure, the residue was purified by flash column chromatography (methanol/dichloromethane = 1/100→1/25) affording compound **S3** (37 mg, 90%) as a yellowish oil.

^{1}H NMR (CD$_3$OD, 500 MHz, 298 K): δ 7.40 (d, *J* = 8.0 Hz, 1H), 7.30 (dd, *J* = 8.0, 8.0 Hz, 1H), 7.04 (dd, *J* = 8.0, 8.0 Hz, 1H), 6.92 (d, *J* = 8.0 Hz, 1H), 6.87 (dd, *J* = 8.0, 0.5 Hz, 1H), 6.73 (s, 1H), 6.64 (dd, *J* = 8.0, 1.0 Hz, 1H), 4.72 (q, *J* = 6.5 Hz, 1H), 4.42 (q, *J* = 6.5 Hz, 1H), 4.33-4.13 (m, 9H), 3.99-3.90 (m, 4H), 3.86-3.78 (m, 4H), 3.74-3.33 (m, 61H), 2.86-2.82 (m, 2H), 2.42 (d, *J* = 15.0 Hz, 1H), 1.53 (d, *J* = 7.0 Hz, 3H), 1.30 (d, *J* = 6.5 Hz, 3H), 1.17 (s, 3H), 0.62 (d, *J* = 6.5 Hz, 3H).

^{13}C NMR (CD$_3$OD, 125 MHz, 298 K): δ 175.1, 174.6, 157.5, 156.8, 151.5, 146.8, 145.3, 144.2, 143.1, 139.3, 134.8, 131.9, 129.6, 128.0, 126.3, 125.4, 121.9, 121.2, 110.6, 110.4, 109.9, 80.7, 80.3, 76.5, 76.0, 72.1, 71.7, 71.6, 71.5, 71.4, 71.3, 71.2, 70.8, 70.5, 70.1, 59.0, 51.8, 40.5, 40.1, 39.3, 19.5, 19.4, 19.1, 15.5.

ESI-HRMS: m/z calculated for $C_{72}H_{104}N_8O_{22}$ [M+H]$^+$ 1465.7064; found: 1465.6992.

Compound **E1**, **E2**, and **E3**

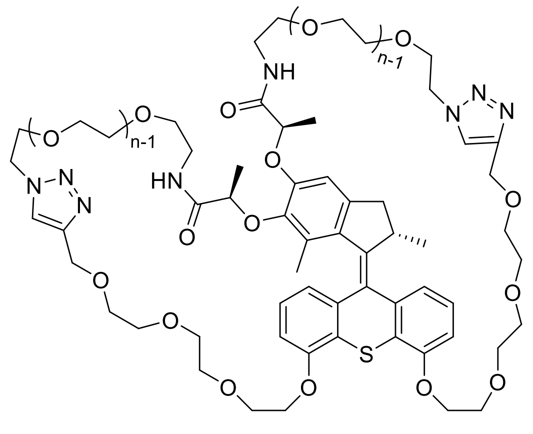

E1 n=248
E2 n=73
E3 n=5

PEG$_{10000}$ 8-shaped motor **E1** (n=248): To DMF (110 mL, degassed with freeze-pump-thaw cycles) was added PMDETA (0.42 mL, 2.01 mmol) and CuBr (288 mg, 2.01 mmol). The reaction mixture was heated up to 95 °C. Then a solution of compound **S1** (140 mg, 0.0067 mmol) in degassed DMF (12 mL) was added dropwise using a syringe pump at a rate of 0.75 mL/h. After 12 hours, DMF was evaporated under reduced pressure and the mixture was suspended in dichloromethane (20 mL), washed with a 1 M EDTA solution (3 × 20 mL) to remove copper. Then the organic phase was dried over Na_2SO_4. After concentration under reduced pressure, the residue was purified by reversed phase column chromatography (C18, Merck, methanol/water = 3/7→7/3) affording compound **E1** (60 mg, 43%) as a white solid.

^{1}H NMR (CD_3OD, 400 MHz, 298 K): δ 8.05-7.96 (m, 2H), 7.42 (d, *J* = 7.8 Hz, 1H), 7.32 (dd, *J* = 7.6, 7.6 Hz, 1H), 7.09-7.01 (m, 1H), 6.97-6.92 (m, 1H), 6.90 (d, *J* = 8.4 Hz, 1H), 6.78-6.73 (m, 1H), 6.68-6.62 (m, 1H), 4.65-4.49 (m, 11H), 4.36-4.14 (m, 5H), 4.01-3.38 (m, 1901H), 2.43 (d, *J* = 15.2 Hz, 1H), 1.60-1.51 (m, 3H), 1.36-1.26 (m, 3H), 1.17 (s, 3H), 0.63 (d, *J* = 6.8 Hz, 3H).

PEG_{3000} 8-shaped motor **E2** (n=73): To DMF (120 mL, degassed with freeze-pump-thaw cycles) was added PMEDTA (0.42 mL, 2.01 mmol) and CuBr (288 mg, 2.01 mmol). The reaction mixture was heated to 95 °C. Then a solution of compound **S2** (46 mg, 0.0067 mmol) in degassed DMF (12 mL) was added dropwise using a syringe pump at a rate of 0.75 mL/h. After 12 hours, DMF was evaporated under reduced pressure and the mixture was suspended in dichloromethane (20 mL), washed with a 1 M EDTA solution (3 × 20 mL) to remove copper. Then the organic phase was dried over Na_2SO_4. After concentration under reduced pressure, the residue was purified by reversed phase column chromatography (C18, Merck, methanol/water = 3/7→7/3) affording compound **E2** (31 mg, 67%) as a white solid.

^{1}H NMR (CD_3OD, 400 MHz, 298 K): δ 8.08-7.97 (m, 2H), 7.42 (d, *J* = 7.6 Hz, 1H), 7.32 (dd, *J* = 7.6, 7.6 Hz, 1H), 7.10-7.01 (m, 1H), 6.98-6.92 (m, 1H), 6.90 (d, *J* = 8.4 Hz, 1H), 6.80-6.73 (m, 1H), 6.69-6.63 (m, 1H), 4.66-4.49 (m, 9H), 4.37-4.15 (m, 5H), 3.99-3.40 (m, 575H), 2.43 (d, *J* = 15.6 Hz, 1H), 1.59-1.50 (m, 3H), 1.35-1.26 (m, 3H), 1.17 (s, 3H), 0.63 (d, *J* = 6.4 Hz, 3H).

PEG_{300} 8-shaped motor **E3** (n=5): To DMF (150 mL, degassed with freeze-pump-thaw cycles) was added PMEDTA (0.56 mL, 4.09 mmol) and CuBr (587 mg, 4.09 mmol). The reaction mixture was heated up to 95 °C. Then a solution of compound **S3** (20 mg, 0.014 mmol) in degassed DMF (12 mL) was added dropwise using syringe pump at a rate 0.75 mL/h. After 12 hours, DMF was evaporated under reduced pressure and the mixture was suspended in dichloromethane (20 mL), washed with a 1 M EDTA solution (3 × 20 mL) to remove copper. Then the organic phase was dried over anhydrous Na_2SO_4. After concentration under reduced pressure, the residue was purified by High-performance liquid chromatography (Waters, Sun

Fire Prep C_{18} 5.0 µm, 19 × 150 mm, running with a gradient (0.08% TFA water/acetonitrile) as eluent) affording compound **E3** as a yellowish oil (14 mg, 71%).

^{1}H NMR (CD_3OD, 500 MHz, 298 K): δ 8.04 (s, 1H), 7.94 (s, 1H), 7.40 (d, *J* = 8.0 Hz, 1H), 7.30 (dd, *J* = 8.0, 8.0 Hz, 1H), 7.04 (dd, *J* = 8.0, 8.0 Hz, 1H), 6.91 (dd, *J* = 7.5, 1.0 Hz, 1H), 6.89 (dd, *J* = 7.5, 1.0 Hz), 6.76 (s, 1H), 6.65 (dd, *J* = 8.0, 1.5 Hz, 1H), 4.72 (q, *J* = 6.5 Hz, 1H), 4.61 (s, 2H), 4.58-4.43 (m, 7H), 4.38-4.29 (m, 2H), 4.22-4.14 (m, 3H), 4.00-3.33 (m, 65H), 3.22-3.12 (m, 1H), 2.42 (d, *J* = 15.5 Hz, 1H), 1.53 (d, *J* = 6.5 Hz, 3H), 1.28 (d, *J* = 7.0 Hz, 3H), 1.17 (s, 3H), 0.62 (d, *J* = 7.0 Hz, 3H).

^{13}C NMR (CD_3OD, 125 MHz, 298 K): δ 180.8, 175.0, 174.5, 157.5, 156.8, 151.6, 146.9, 145.0, 144.5, 143.2, 139.3, 134.7, 131.9, 129.7, 128.1, 126.2, 126.0, 125.8, 125.3, 122.0, 121.1, 110.9, 110.5, 80.0, 76.8, 71.6, 71.5, 71.4, 65.1, 65.0, 51.5, 51.4, 40.6, 40.1, 39.3, 28.6, 23.1, 19.6, 19.4, 19.05, 15.8.

ESI-HRMS: m/z calculated for $C_{72}H_{104}N_8O_{22}$ $[M+H]^+$ 1465.7064; found: 1465.7111.

ANNEXES

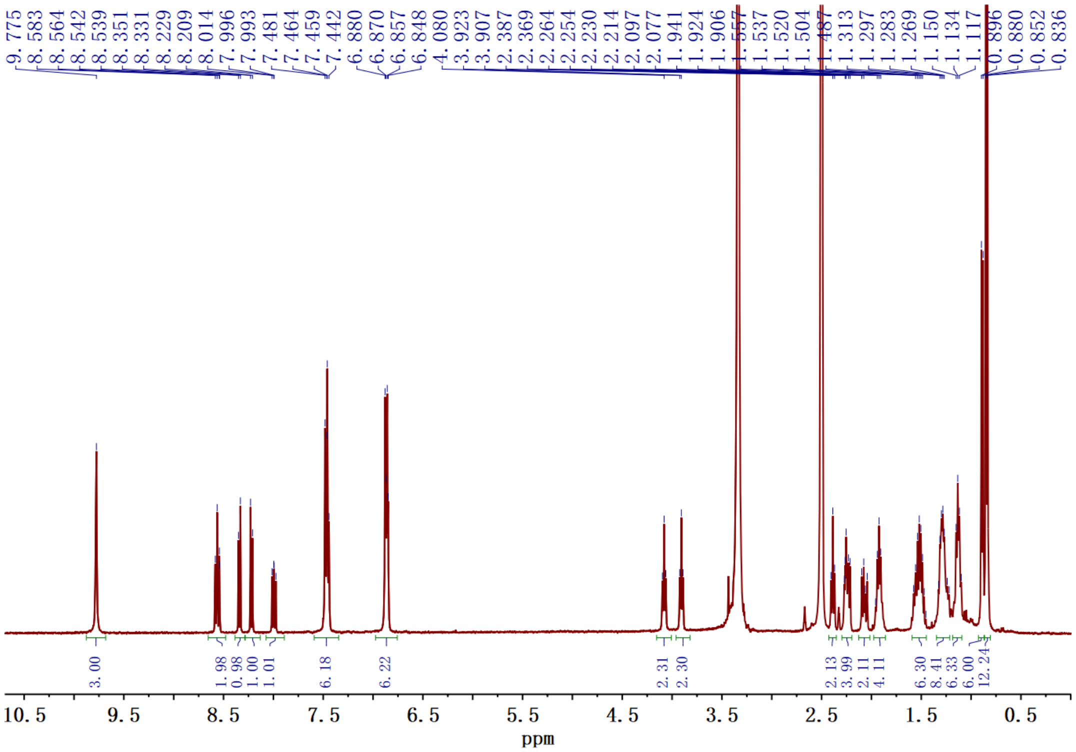

^{1}H NMR spectrum of compound **9** in $CDCl_3$

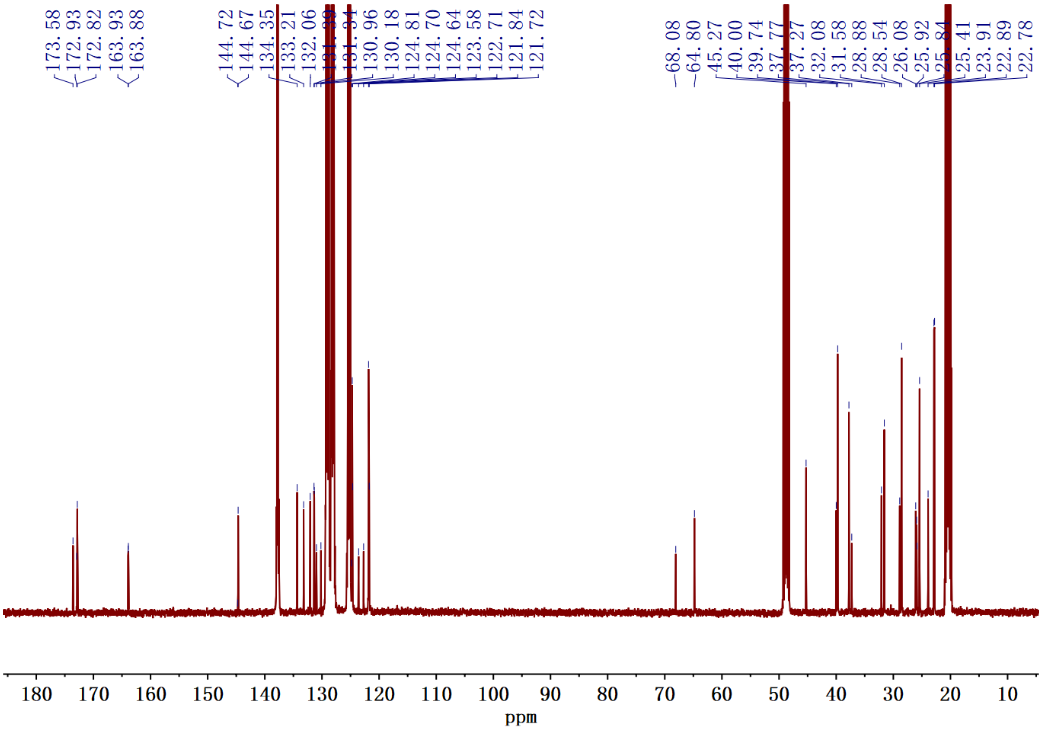

^{13}C NMR spectrum of compound **9** in toluene-d_8/CD_3OD (3/1)

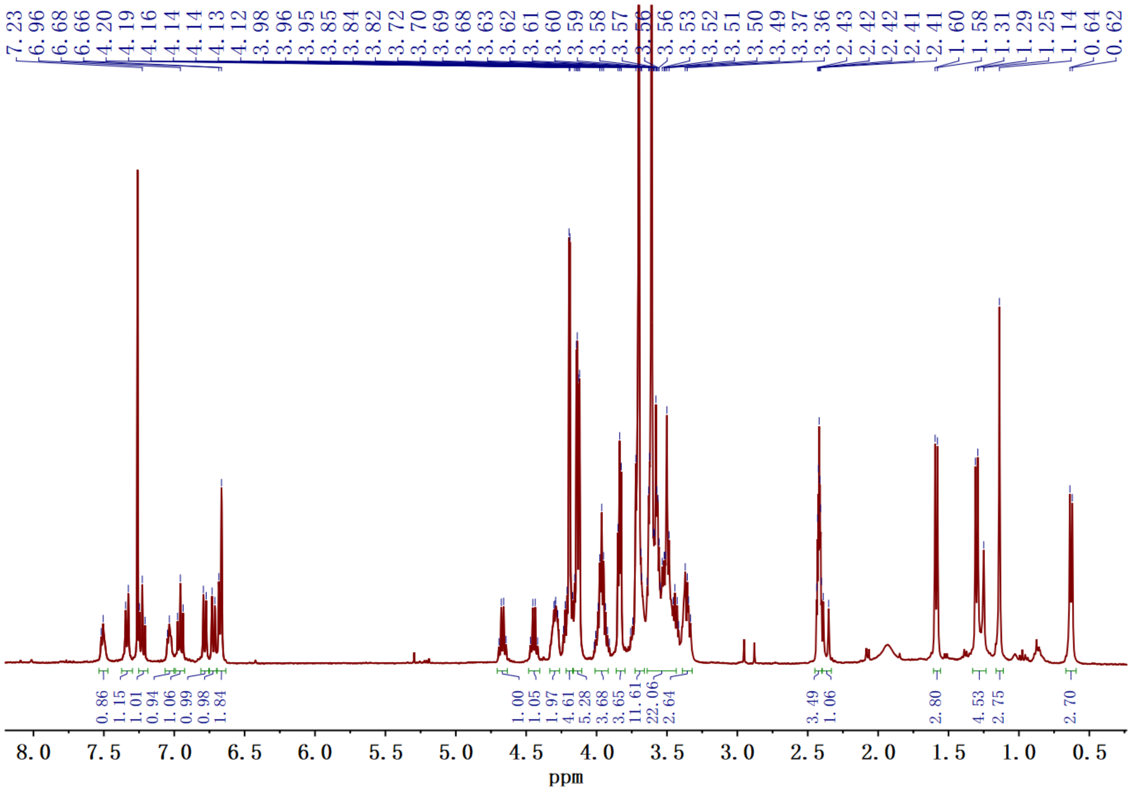

^{1}H NMR spectrum of compound **24**

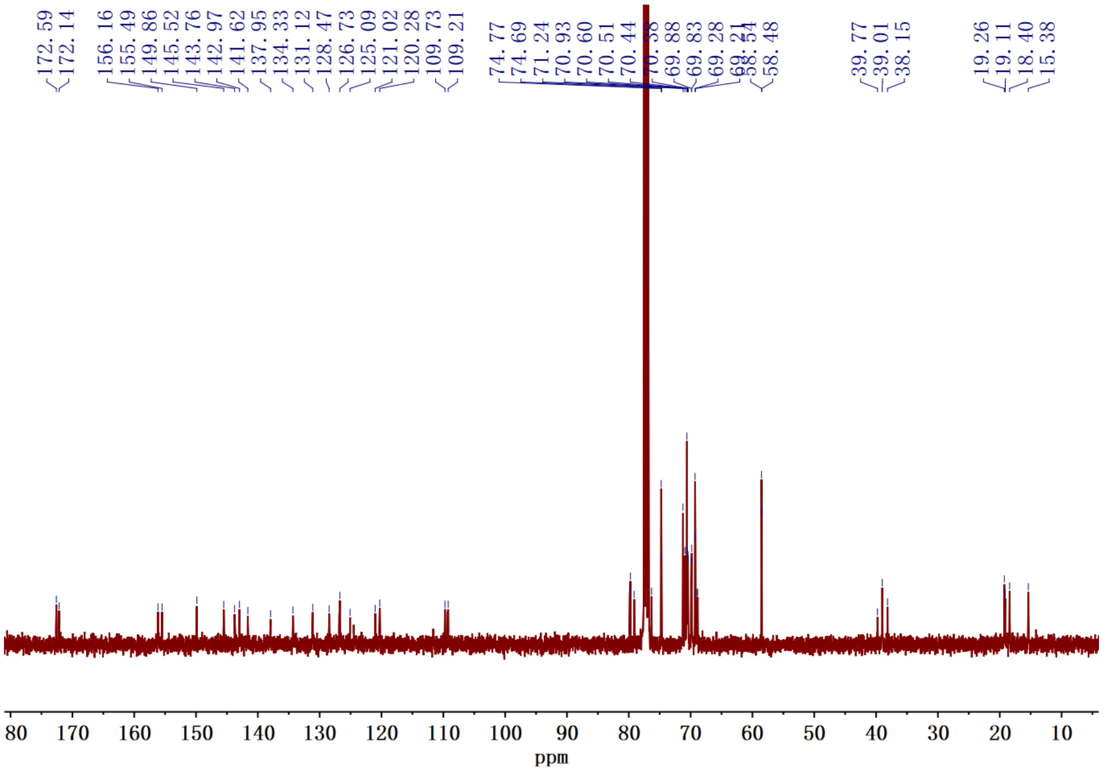

^{13}C NMR spectrum of compound **24**

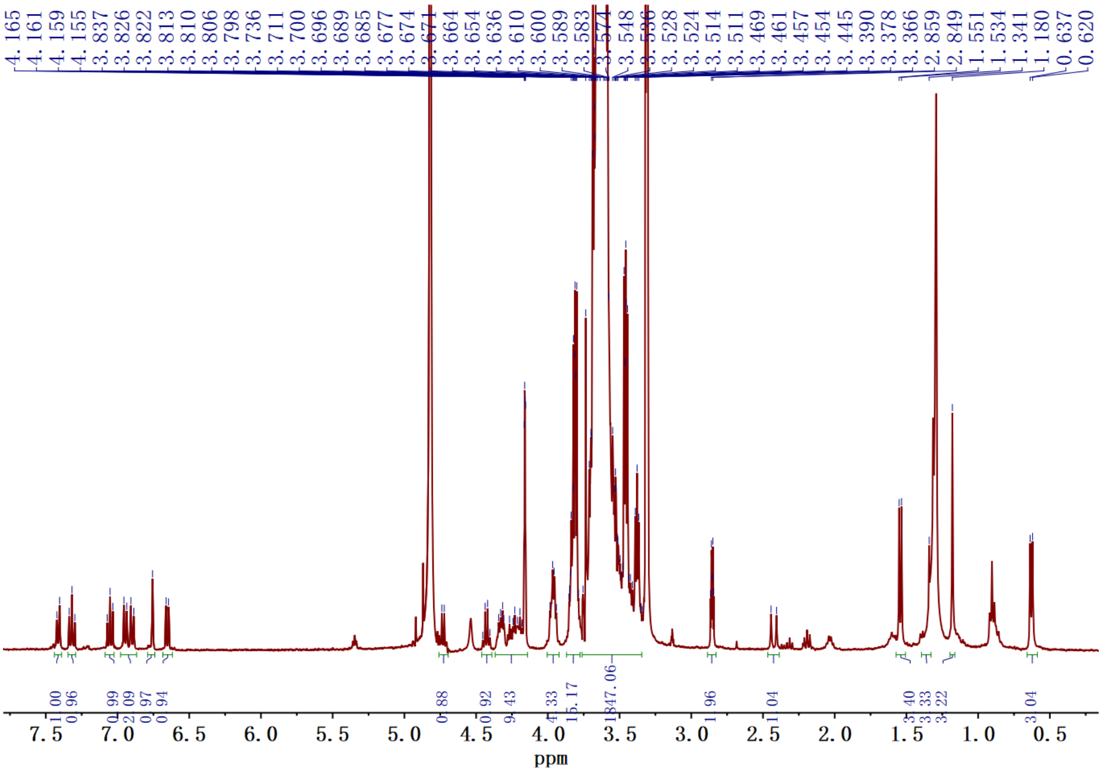

^{1}H NMR spectrum of compound **S1**

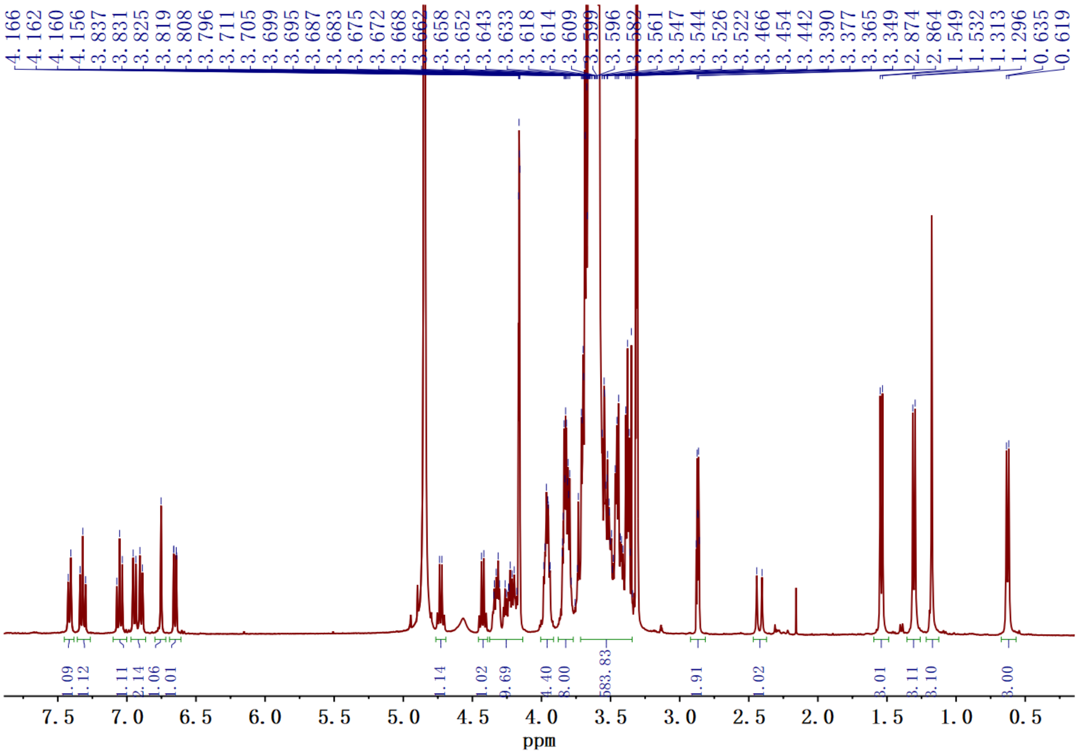

^{1}H NMR spectrum of compound **S2**

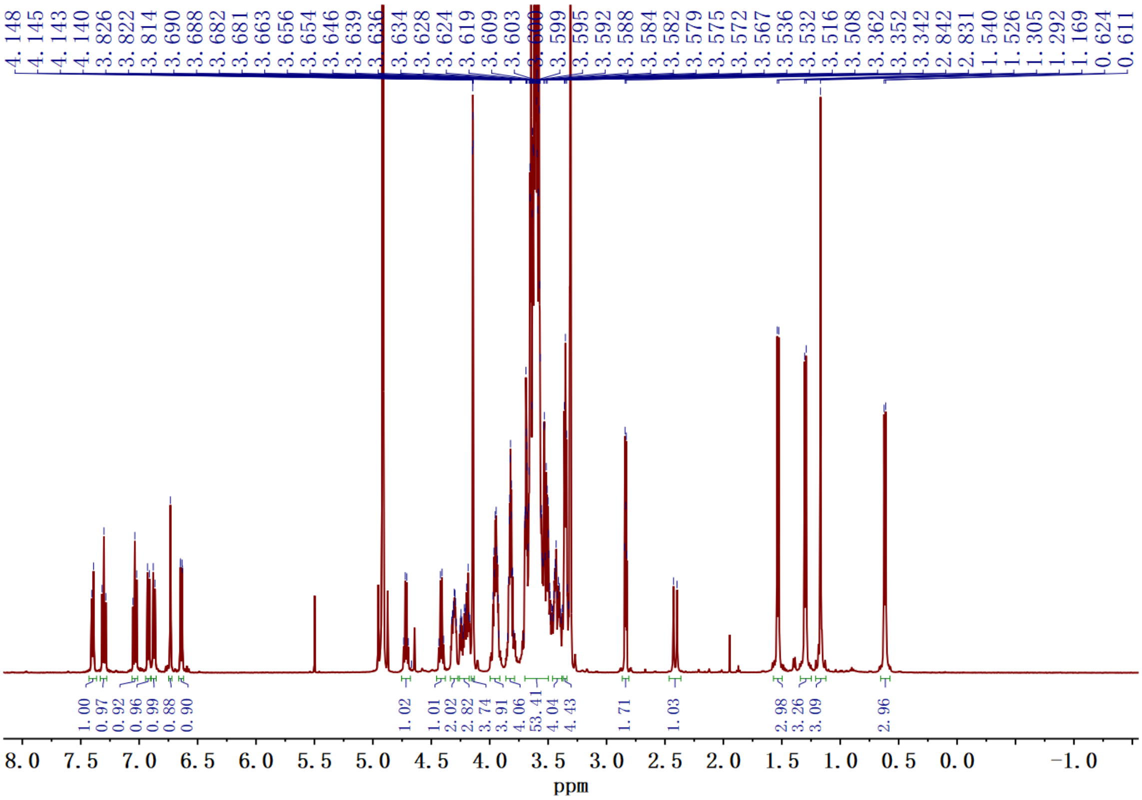

^{1}H NMR spectrum of compound **S3**

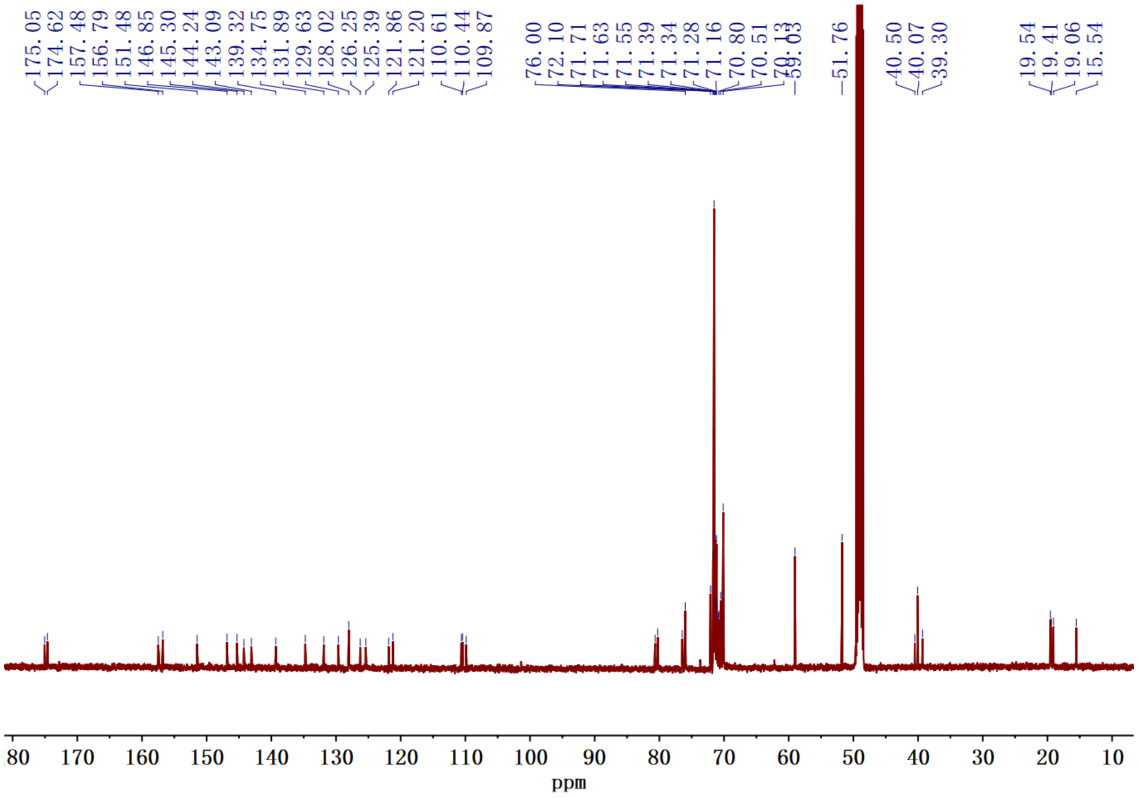

^{13}C NMR spectrum of compound **S3**

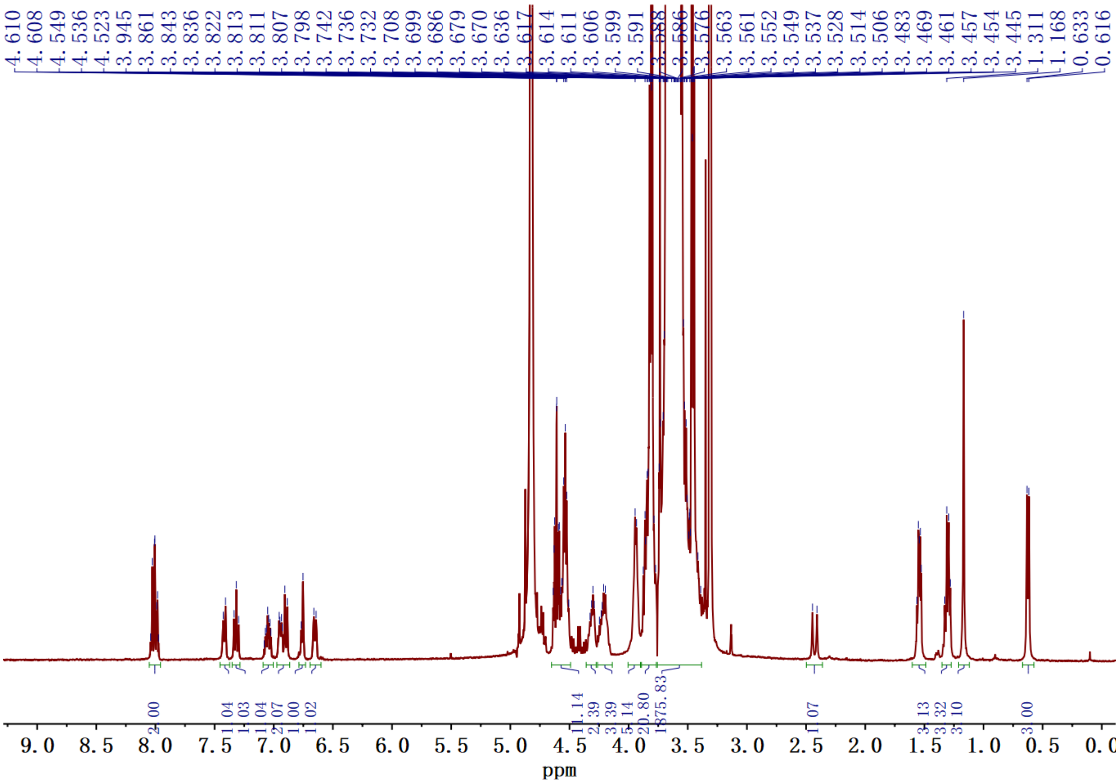

^{1}H NMR spectrum of compound **E1**

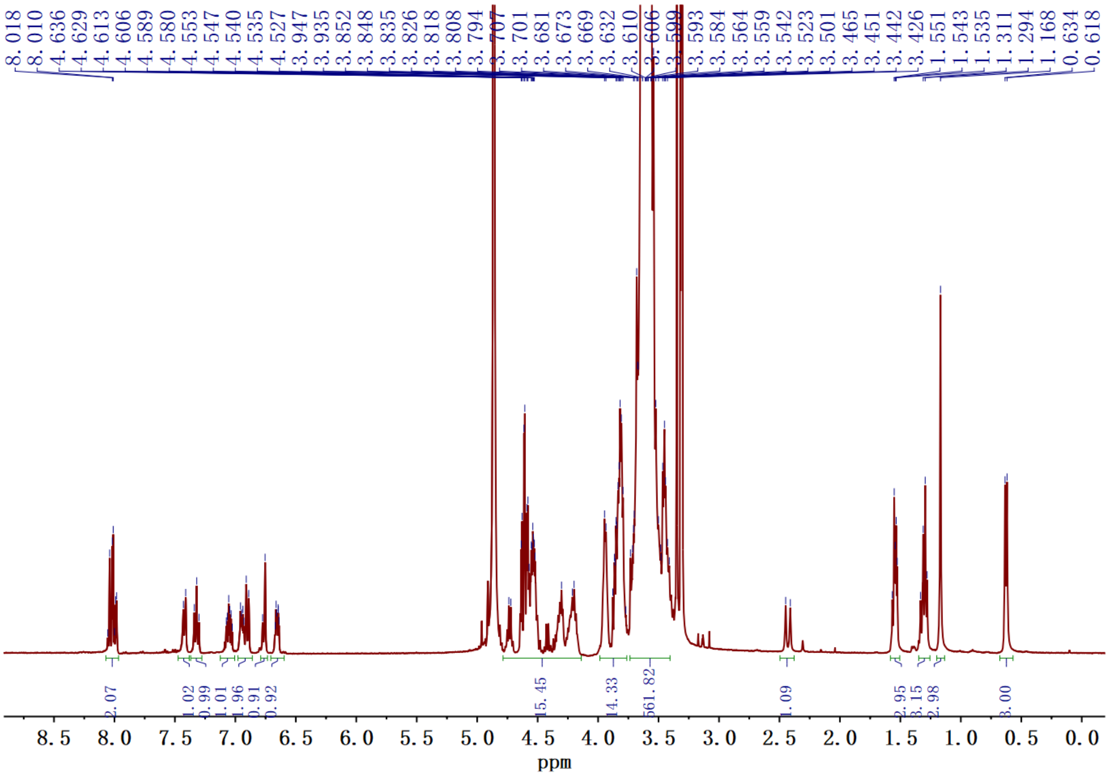

^{1}H NMR spectrum of compound **E2**

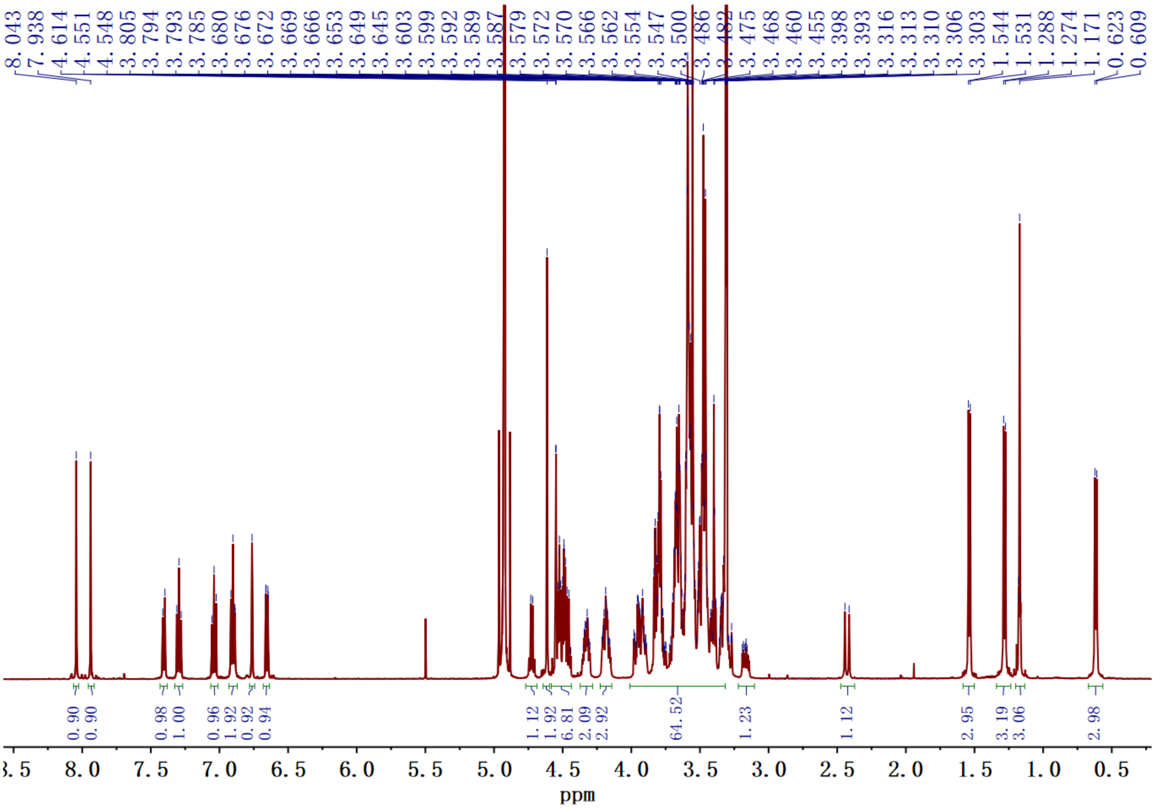

^{1}H NMR spectrum of compound **E3**

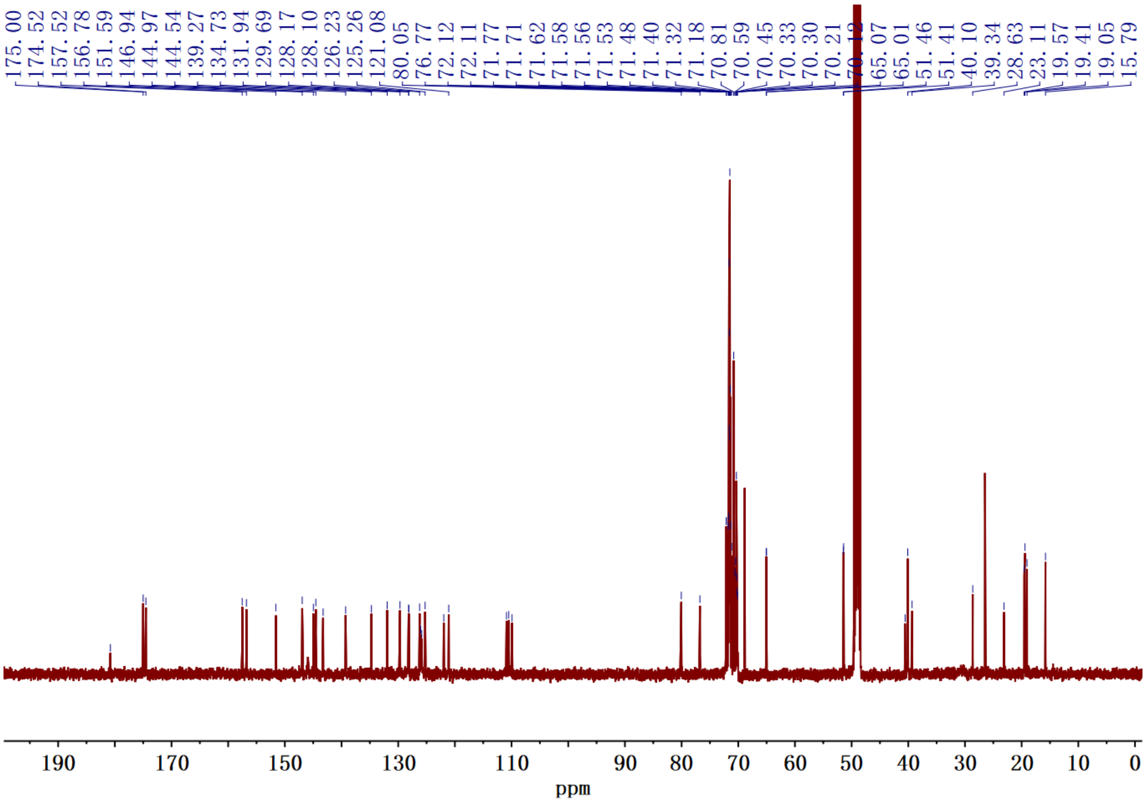

^{13}C NMR spectrum of compound **E3**

REFERENCES

[1] Cias, P.; Slugovc, C.; Gescheidt, G. Hole Transport in Triphenylamine Based OLED Devices: From Theoretical Modeling to Properties Prediction. *J. Phys. Chem. A* **2011**, *115* (50), 14519–14525.

[2] Madec, M.-B.; Morrison, J. J.; Sanchez-Romaguera, V.; Turner, M. L.; Yeates, S. G. Organic Field Effect Transistors from Ambient Solution Processed Poly(Triarylamine)–Insulator Blends. *J. Mater. Chem.* **2009**, *19* (37), 6750.

[3] Wang, J.; Liu, K.; Ma, L.; Zhan, X. Triarylamine: Versatile Platform for Organic, Dye-Sensitized, and Perovskite Solar Cells. *Chem. Rev.* **2016**, *116* (23), 14675–14725.

[4] Moulin, E.; Niess, F.; Maaloum, M.; Buhler, E.; Nyrkova, I.; Giuseppone, N. The Hierarchical Self-Assembly of Charge Nanocarriers: A Highly Cooperative Process Promoted by Visible Light. *Angew. Chem. Int. Ed.* **2010**, *49* (39), 6974–6978.

[5] Moulin, E.; Armao, J. J.; Giuseppone, N. Triarylamine-Based Supramolecular Polymers: Structures, Dynamics, and Functions. *Acc. Chem. Res.* **2019**, *52* (4), 975–983.

[6] Merz, V.; Weith, W. Vermischte Mittheilungen. *Berichte der Dtsch. Chem. Gesellschaft* **1873**, *6* (2), 1511–1520.

[7] Goldberg, I.; Nimerovsky, M. Über Triphenylamin Und Triphenylamin-carbonsäure. *Berichte der Dtsch. Chem. Gesellschaft* **1907**, *40* (2), 2448–2452.

[8] Zhao, Y.; Wang, Y.; Sun, H.; Li, L.; Zhang, H. Ullmann Reaction in Tetraethyl Orthosilicate: A Novel Synthesis of Triarylamines and Diaryl Ethers. *Chem. Commun.* **2007**, *30*, 3186-3188.

[9] Paul, F.; Patt, J.; Hartwig, J. F. Palladium-Catalyzed Formation of Carbon-Nitrogen Bonds. Reaction Intermediates and Catalyst Improvements in the Hetero Cross Coupling of Aryl Halides and Tin Amides. *J. Am. Chem. Soc.* **1994**, *116* (13), 5969–5970.

[10] Różalska, I.; Kułyk, P.; Kulszewicz-Bajer, I. Linear 1,4-Coupled Oligoanilines of Defined Length: Preparation and Spectroscopic Properties. *New J. Chem.* **2004**, *28* (10), 1235–1243.

[11] Sobolev, A. N.; Belsky, V. K.; Romm, I. P.; Chernikova, N. Yu.; Guryanova, E. N. Structural Investigation of the Triaryl Derivatives of the Group V Elements. IX. Structure of Triphenylamine, C18H15N. *Acta Cryst.* **1985**, *41* (6), 967–971.

[12] Reva, I.; Lapinski, L.; Chattopadhyay, N.; Fausto, R. Vibrational Spectrum and Molecular Structure of Triphenylamine Monomer: A Combined Matrix-Isolation FTIR and Theoretical Study. *Phys. Chem. Chem. Phys.* **2003**, *5* (18), 3844–3850.

[13] Amthor, S.; Noller, B.; Lambert, C. UV/Vis/NIR Spectral Properties of Triarylamines and Their Corresponding Radical Cations. *Chem. Phys.* **2005**, *316* (1), 141–152.

[14] Quinton, C.; Alain-Rizzo, V.; Dumas-Verdes, C.; Miomandre, F.; Clavier, G.; Audebert, P. Redox-Controlled Fluorescence Modulation (Electrofluorochromism) in Triphenylamine Derivatives. *RSC Adv.* **2014**, *4* (65), 34332–34342.

[15] Richtol, H. H.; Fitzgerald, E. A.; Wuelfing, P. Photochemical Oxidation of Some Substituted Aromatic Amines in Chloroform. *J. Phys. Chem.* **1971**, *75* (18), 2737–2741.

[16] Heckmann, A.; Lambert, C. Organic Mixed-Valence Compounds: A Playground for Electrons and Holes. *Angew. Chem. Int. Ed.* **2012**, *51* (2), 326–392.

[17] Hush, N. S. Adiabatic Theory of Outer Sphere Electron-Transfer Reactions in Solution. *Trans. Faraday Soc.* **1961**, *57*, 557.

[18] Hush, N. S. Distance Dependence of Electron Transfer Rates. *Coordination Chemistry Reviews* **1985**, *64*, 135–157.

[19] Robin, M. B.; Day, P. Mixed valence chemistry-a survey and classification. Advances in Inorganic Chemistry and Radiochemistry **1968**, *10*, 247-422.

[20] Lambert, C.; Moos, M.; Schmiedel, A.; Holzapfel, M.; Schäfer, J.; Kess, M.; Engel, V. How Fast Is Optically Induced Electron Transfer in Organic Mixed Valence Systems? *Phys. Chem. Chem. Phys.* **2016**, *18* (28), 19405–19411.

[21] Krug, M.; Fröhlich, N.; Fehn, D.; Vogel, A.; Rominger, F.; Meyer, K.; Clark, T.; Kivala, M.; Guldi, D. M. Pre-Planarized Triphenylamine-Based Linear Mixed-Valence Charge-Transfer Systems. *Angew. Chem. Int. Ed.* **2021**, *60* (12), 6771–6777.

[22] Thelakkat, M. Star-Shaped, Dendrimeric and Polymeric Triarylamines as Photoconductors and Hole Transport Materials for Electro-Optical Applications. *Macromol. Mater. Eng.* **2002**, 287, 442–461.

[23] Shirota, Y.; Kobata, T.; Noma, N. Starburst Molecules for Amorphous Molecular Materials. 4, 4′, 4″-Tris (N, N-diphenylamino) triphenylamine and 4, 4′, 4″-Tris [N-(3-methylphenyl)-N-phenylamino] triphenylamine. *Chem. Lett.*, **1989**, *18* (7), 1145-1148.

[24] Ganzorig, C.; Suga, K.; Fujihira, M. *P* -Type Semiconductors of Aromatic Diamines Doped with $SbCl_5$. *Chem. Lett.* **2000**, *29* (9), 1032–1033.

[25] Mizoshita, N.; Inagaki, S. Template-Free Synthesis of Electroconductive Triphenylamine–Silica Nanotubes Exhibiting a Mixed-Valence State. *Adv. Funct. Mater.* **2018**, *28* (40), 1803116.

[26] Snaith, H. J.; Grätzel, M. Enhanced Charge Mobility in a Molecular Hole Transporter via Addition of Redox Inactive Ionic Dopant: Implication to Dye-Sensitized Solar Cells. *Appl. Phys. Lett.* **2006**, *89* (26), 262114.

[27] Abate, A.; Leijtens, T.; Pathak, S.; Teuscher, J.; Avolio, R.; Errico, M. E.; Kirkpatrik, J.; Ball, J. M.; Docampo, P.; McPherson, I.; Snaith, H. J. Lithium Salts as "Redox Active" p-Type Dopants for Organic Semiconductors and Their Impact in Solid-State Dye-Sensitized Solar Cells. *Phys. Chem. Chem. Phys.* **2013**, *15* (7), 2572.

[28] Dimitrakopoulos, C. D.; Malenfant, P. R. L. Organic Thin Film Transistors for Large Area Electronics. *Adv. Mater.* **2002**, *14* (2), 99-117.

[29] Kunihiro, M.; Nakasone, Y.; Matsuda, S.; Shironita, S.; Nagayama, N.; Umeda, M. Crystal Structure Oriented Carrier Transport Characteristic of Triphenylamine Derivative Single Crystal. *AIP Adv.* **2018**, *8* (3), 035324.

[30] Brunsveld, L.; Folmer, B. J. B.; Meijer, E. W.; Sijbesma, R. P. Supramolecular Polymers. *Chem. Rev.* **2001**, *101* (12), 4071–4098.

[31] Burattini, S.; Greenland, B. W.; Merino, D. H.; Weng, W.; Seppala, J.; Colquhoun, H. M.; Hayes, W.; Mackay, M. E.; Hamley, I. W.; Rowan, S. J. A Healable Supramolecular Polymer Blend Based on Aromatic π–π Stacking and Hydrogen-Bonding Interactions. *J. Am. Chem. Soc.* **2010**, *132* (34), 12051–12058.

[32] Tavenor, N. A.; Murnin, M. J.; Horne, W. S. Supramolecular Metal-Coordination Polymers, Nets, and Frameworks from Synthetic Coiled-Coil Peptides. *J. Am. Chem. Soc.* **2017**, *139* (6), 2212–2215.

[33] Wei, P.; Yan, X.; Huang, F. Supramolecular Polymers Constructed by Orthogonal Self-Assembly Based on Host–Guest and Metal–Ligand Interactions. *Chem. Soc. Rev.* **2015**, *44* (3), 815–832.

[34] Busseron, E.; Ruff, Y.; Moulin, E.; Giuseppone, N. Supramolecular Self-Assemblies as Functional Nanomaterials. *Nanoscale* **2013**, *5* (16), 7098.

[35] Nyrkova, I.; Moulin, E.; Armao, J. J.; Maaloum, M.; Heinrich, B.; Rawiso, M.; Niess, F.; Cid, J.-J.; Jouault, N.; Buhler, E.; Semenov, A. N.; Giuseppone, N. Supramolecular Self-Assembly and Radical Kinetics in Conducting Self-Replicating Nanowires. *ACS Nano* **2014**, *8* (10), 10111–10124.

[36] Armao, J. J.; Maaloum, M.; Ellis, T.; Fuks, G.; Rawiso, M.; Moulin, E.; Giuseppone, N. Healable Supramolecular Polymers as Organic Metals. *J. Am. Chem. Soc.* **2014**, *136* (32), 11382–11388.

[37] Ellis, T. K.; Galerne, M.; Armao, J. J.; Osypenko, A.; Martel, D.; Maaloum, M.; Fuks, G.; Gavat, O.; Moulin, E.; Giuseppone, N. Supramolecular Electropolymerization. *Angew. Chem. Int. Ed.* **2018**, *57* (48), 15749–15753.

[38] Kim, J.; Lee, J.; Kim, W. Y.; Kim, H.; Lee, S.; Lee, H. C.; Lee, Y. S.; Seo, M.; Kim, S. Y. Induction and Control of Supramolecular Chirality by Light in Self-Assembled Helical Nanostructures. *Nat. Commun.* **2015**, *6* (1), 6959.

[39] Osypenko, A.; Moulin, E.; Gavat, O.; Fuks, G.; Maaloum, M.; Koenis, M. A. J.; Buma, W. J.; Giuseppone, N. Temperature Control of Sequential Nucleation–Growth Mechanisms in Hierarchical Supramolecular Polymers. *Chem. Eur. J.* **2019**, *25* (56), 13008–13016.

[40] Weissleder, R. A Clearer Vision for in Vivo Imaging. *Nat. Biotechnol.* **2001**, *19* (4), 316–317.

[41] Xu, H.; Chen, R.; Sun, Q.; Lai, W.; Su, Q.; Huang, W.; Liu, X. Recent Progress in Metal–Organic Complexes for Optoelectronic Applications. *Chem. Soc. Rev.* **2014**, *43* (10), 3259–3302.

[42] Lewis, G. N.; Kasha, M. Phosphorescence and the Triplet State. *J. Am. Chem. Soc.* **1944**, *66* (12), 2100–2116.

[43] Lower, S. K.; El-Sayed, M. A. The Triplet State and Molecular Electronic Processes in Organic Molecules. *Chem. Rev.* **1966**, *66* (2), 199–241.

[44] Gu, L.; Shi, H.; Gu, M.; Ling, K.; Ma, H.; Cai, S.; Song, L.; Ma, C.; Li, H.; Xing, G.; Hang, X.; Li, J.; Gao, Y.; Yao, W.; Shuai, Z.; An, Z.; Liu, X.; Huang, W. Dynamic Ultralong Organic Phosphorescence by Photoactivation. *Angew. Chem. Int. Ed.* **2018**, *57*

(28), 8425–8431.

[45] Yao, X.; Wang, J.; Jiao, D.; Huang, Z.; Mhirsi, O.; Lossada, F.; Chen, L.; Haehnle, B.; Kuehne, A. J. C.; Ma, X.; Tian, H.; Walther, A. Room-Temperature Phosphorescence Enabled through Nacre-Mimetic Nanocomposite Design. *Adv. Mater.* **2021**, *33* (5), 2005973.

[46] Yu, Y.; Kwon, M. S.; Jung, J.; Zeng, Y.; Kim, M.; Chung, K.; Gierschner, J.; Youk, J. H.; Borisov, S. M.; Kim, J. Room-Temperature-Phosphorescence-Based Dissolved Oxygen Detection by Core-Shell Polymer Nanoparticles Containing Metal-Free Organic Phosphors. *Angew. Chem. Int. Ed.* **2017**, *56* (51), 16207–16211.

[47] Suárez, P. L.; García-Cortés, M.; Fernández-Argüelles, M. T.; Encinar, J. R.; Valledor, M.; Ferrero, F. J.; Campo, J. C.; Costa-Fernández, J. M. Functionalized Phosphorescent Nanoparticles in (Bio)Chemical Sensing and Imaging – A Review. *Anal. Chim. Acta* **2019**, *1046*, 16–31.

[48] Wang, T.; Su, X.; Zhang, X.; Nie, X.; Huang, L.; Zhang, X.; Sun, X.; Luo, Y.; Zhang, G. Aggregation-Induced Dual-Phosphorescence from Organic Molecules for Nondoped Light-Emitting Diodes. *Adv. Mater.* **2019**, *31* (51), 1904273.

[49] Zhao, W.; He, Z.; Tang, B. Z. Room-Temperature Phosphorescence from Organic Aggregates. *Nat. Rev. Mater.* **2020**, *5* (12), 869–885.

[50] Zhi, J.; Zhou, Q.; Shi, H.; An, Z.; Huang, W. Organic Room Temperature Phosphorescence Materials for Biomedical Applications. *Chem. Asian J.* **2020**, *15* (7), 947–957.

[51] Ma, X.; Wang, J.; Tian, H. Assembling-Induced Emission: An Efficient Approach for Amorphous Metal-Free Organic Emitting Materials with Room-Temperature Phosphorescence. *Acc. Chem. Res.* **2019**, *52* (3), 738–748.

[52] Kwon, M. S.; Lee, D.; Seo, S.; Jung, J.; Kim, J. Tailoring Intermolecular Interactions for Efficient Room-Temperature Phosphorescence from Purely Organic Materials in Amorphous Polymer Matrices. *Angew. Chem. Int. Ed.* **2014**, *53* (42), 11177–11181.

[53] Kwon, M. S.; Yu, Y.; Coburn, C.; Phillips, A. W.; Chung, K.; Shanker, A.; Jung, J.; Kim, G.; Pipe, K.; Forrest, S. R.; Youk, J. H.; Gierschner, J.; Kim, J. Suppressing Molecular Motions for Enhanced Room-Temperature Phosphorescence of Metal-Free Organic Materials. *Nat. Commun.* **2015**, *6* (1), 8947.

[54] Turro, N. J.; Bolt, J. D.; Kuroda, Y.; Kuroda. Y.; Tabushi, I. A study of the kinetics of inclusion of halognaphthalenes with ß-cyclodextrin via time correlated phosphorescence. *Photochem. Photobiol*. **1982**, *35*, 69-72.

[55] Ma, X.; Cao, J.; Wang, Q.; Tian, H. Photocontrolled Reversible Room Temperature Phosphorescence (RTP) Encoding β-Cyclodextrin Pseudorotaxane. *Chem. Commun.* **2011**, *47* (12), 3559.

[56] Zhang, Z.; Chen, Y.; Liu, Y. Efficient Room-Temperature Phosphorescence of a Solid-State Supramolecule Enhanced by Cucurbit[6]Uril. *Angew. Chem. Int. Ed*. **2019**, *58* (18), 6028–6032.

[57] Wang, J.; Huang, Z.; Ma, X.; Tian, H. Visible-Light-Excited Room-Temperature

Phosphorescence in Water by Cucurbit[8]Uril-Mediated Supramolecular Assembly. *Angew. Chem. Int. Ed.* **2020**, *59* (25), 9928–9933.

[58] Li, D.; Lu, F.; Wang, J.; Hu, W.; Cao, X.-M.; Ma, X.; Tian, H. Amorphous Metal-Free Room-Temperature Phosphorescent Small Molecules with Multicolor Photoluminescence via a Host–Guest and Dual-Emission Strategy. *J. Am. Chem. Soc.* **2018**, *140* (5), 1916–1923.

[59] Wang, Z.; Li, T.; Ding, B.; Ma, X. Achieving Room Temperature Phosphorescence from Organic Small Molecules on Amino Acid Skeleton. *Chin. Chem. Lett.* **2020**, *31* (11), 2929–2932.

[60] Zhang, T.; Wang, C.; Ma, X. Metal-Free Room-Temperature Phosphorescent Systems for Pure White-Light Emission and Latent Fingerprint Visualization. *Ind. Eng. Chem. Res.* **2019**, *58* (19), 7778–7785.

[61] Dai, Z.-R.; Ge, G.-B.; Feng, L.; Ning, J.; Hu, L.-H.; Jin, Q.; Wang, D.-D.; Lv, X.; Dou, T.-Y.; Cui, J.-N.; Yang, L. A Highly Selective Ratiometric Two-Photon Fluorescent Probe for Human Cytochrome P450 1A. *J. Am. Chem. Soc.* **2015**, *137* (45), 14488–14495.

[62] Appel, W. P. J.; Portale, G.; Wisse, E.; Dankers, P. Y. W.; Meijer, E. W. Aggregation of Ureido-Pyrimidinone Supramolecular Thermoplastic Elastomers into Nanofibers: A Kinetic Analysis. *Macromolecules* **2011**, *44* (17), 6776-6784.

[63] Aveline, B. M.; Matsugo, S.; Redmond, R. W. Photochemical Mechanisms Responsible for the Versatile Application of Naphthalimides and Naphthaldiimides in Biological Systems. *J. Am. Chem. Soc.* **1997**, *119* (49), 11785–11795.

[64] Goudappagouda; Manthanath, A.; Wakchaure, V. C.; Ranjeesh, K. C.; Das, T.; Vanka, K.; Nakanishi, T.; Sukumaran, S. B. Paintable Room Temperature Phosphorescent Liquid Formulations of Alkylated Bromonaphthalimide. *Angew. Chem. Int. Ed.* **2019**, *58* (8), 2284-2288.

[65] Pines, D.; Bohm, D. A Collective Description of Electron Interactions: II. Collective vs Individual Particle Aspects of the Interactions. *Phys. Rev.* **1952**, *85* (2), 338–353.

[66] Wang, L.; Hasanzadeh Kafshgari, M.; Meunier, M. Optical Properties and Applications of Plasmonic-Metal Nanoparticles. *Adv. Funct. Mater.* **2020**, *30* (51), 2005400.

[67] Cao, J.; Sun, T.; Grattan, K. T. V. Gold Nanorod-Based Localized Surface Plasmon Resonance Biosensors: A Review. *Sens. Actuat. B-Chem.* **2014**, *195*, 332–351.

[68] Naik, G. V.; Shalaev, V. M.; Boltasseva, A. Alternative Plasmonic Materials: Beyond Gold and Silver. *Adv. Mater.* **2013**, *25* (24), 3264–3294.

[69] Zhao, Y.; Pan, H.; Lou, Y.; Qiu, X.; Zhu, J.; Burda, C. Plasmonic Cu_{2-x} S Nanocrystals: Optical and Structural Properties of Copper-Deficient Copper(I) Sulfides. *J. Am. Chem. Soc.* **2009**, *131* (12), 4253–4261.

[70] Luther, J. M.; Jain, P. K.; Ewers, T.; Alivisatos, A. P. Localized Surface Plasmon Resonances Arising from Free Carriers in Doped Quantum Dots. *Nat. Mater.* **2011**, *10* (5), 361–366.

[71] Kriegel, I.; Rodríguez-Fernández, J.; Wisnet, A.; Zhang, H.; Waurisch, C.; Eychmüller,

A.; Dubavik, A.; Govorov, A. O.; Feldmann, J. Shedding Light on Vacancy-Doped Copper Chalcogenides: Shape-Controlled Synthesis, Optical Properties, and Modeling of Copper Telluride Nanocrystals with Near-Infrared Plasmon Resonances. *ACS Nano* **2013**, *7* (5), 4367–4377.

[72] Chen, S.; Kang, E. S. H.; Shiran Chaharsoughi, M.; Stanishev, V.; Kühne, P.; Sun, H.; Wang, C.; Fahlman, M.; Fabiano, S.; Darakchieva, V.; Jonsson, M. P. Conductive Polymer Nanoantennas for Dynamic Organic Plasmonics. *Nat. Nanotechnol.* **2020**, *15* (1), 35–40.

[73] Deng, T.-S.; Parker, J.; Yifat, Y.; Shepherd, N.; Scherer, N. F. Dark Plasmon Modes in Symmetric Gold Nanoparticle Dimers Illuminated by Focused Cylindrical Vector Beams. *J. Phys. Chem. C* **2018**, *122* (48), 27662–27672.

[74] Myroshnychenko, V.; Rodríguez-Fernández, J.; Pastoriza-Santos, I.; Funston, A. M.; Novo, C.; Mulvaney, P.; Liz-Marzán, L. M.; García de Abajo, F. J. Modelling the Optical Response of Gold Nanoparticles. *Chem. Soc. Rev.* **2008**, *37* (9), 1792.

[75] Jain, P. K.; El-Sayed, M. A. Plasmonic Coupling in Noble Metal Nanostructures. *Chem. Phys. Lett.* **2010**, *487* (4–6), 153–164.

[76] Jain, P. K.; Huang, W.; El-Sayed, M. A. On the Universal Scaling Behavior of the Distance Decay of Plasmon Coupling in Metal Nanoparticle Pairs: A Plasmon Ruler Equation. *Nano Lett.* **2007**, *7* (7), 2080–2088.

[77] Faramarzi, V.; Niess, F.; Moulin, E.; Maaloum, M.; Dayen, J.-F.; Beaufrand, J.-B.; Zanettini, S.; Doudin, B.; Giuseppone, N. Light-Triggered Self-Construction of Supramolecular Organic Nanowires as Metallic Interconnects. *Nat. Chem.* **2012**, *4* (6), 485–490.

[78] Bhattacharya, S.; Akande, A.; Sanvito, S. Spin Transport Properties of Triarylamine-Based Nanowires. *Chem. Commun.* **2014**, *50* (50), 6626–6629.

[79] Armao, J. J.; Domoto, Y.; Umehara, T.; Maaloum, M.; Contal, C.; Fuks, G.; Moulin, E.; Decher, G.; Javahiraly, N.; Giuseppone, N. Supramolecular Organic Nanowires as Plasmonic Interconnects. *ACS Nano* **2016**, *10* (2), 2082-2090.

[80] Armao, J. J.; Rabu, P.; Moulin, E.; Giuseppone, N. Long-Range Energy Transport via Plasmonic Propagation in a Supramolecular Organic Waveguide. *Nano Lett.* **2016**, *16* (4), 2800–2805.

[81] Unser, S.; Bruzas, I.; He, J.; Sagle, L. Localized Surface Plasmon Resonance Biosensing: Current Challenges and Approaches. *Sensors* **2015**, *15* (7), 15684–15716.

[82] Stewart, M. E.; Anderton, C. R.; Thompson, L. B.; Maria, J.; Gray, S. K.; Rogers, J. A.; Nuzzo, R. G. Nanostructured Plasmonic Sensors. *Chem. Rev.* **2008**, *108* (2), 494–521.

[83] Lemos de Souza, M.; Pereira dos Santos, D.; Corio, P. Localized Surface Plasmon Resonance Enhanced Photocatalysis: An Experimental and Theoretical Mechanistic Investigation. *RSC Adv.* **2018**, *8* (50), 28753–28762.

[84] Becerra, J.; Gopalakrishnan, V. N.; Quach, T.; Do, T. Plasmonic Materials: Opportunities and Challenges on Reticular Chemistry for Photocatalytic Applications. *ChemCatChem* **2021**, *13* (4), 1059–1073.

[85] Huang, X.; El-Sayed, M. A. Gold Nanoparticles: Optical Properties and Implementations in Cancer Diagnosis and Photothermal Therapy. *J. Adv. Res.* **2010**, *1* (1), 13–28.

[86] Kim, M.; Lee, J.; Nam, J. Plasmonic Photothermal Nanoparticles for Biomedical Applications. *Adv. Sci.* **2019**, *6* (17), 1900471.

[87] Lu, X.; Zhang, H.; Fei, G.; Yu, B.; Tong, X.; Xia, H.; Zhao, Y. Liquid-Crystalline Dynamic Networks Doped with Gold Nanorods Showing Enhanced Photocontrol of Actuation. *Adv. Mater.* **2018**, *30* (14), 1706597.

[88] Thoniyot, P.; Tan, M. J.; Karim, A. A.; Young, D. J.; Loh, X. J. Nanoparticle-Hydrogel Composites: Concept, Design, and Applications of These Promising, Multi-Functional Materials. *Adv. Sci.* **2015**, *2* (1–2), 1400010.

[89] Ghosh, P. N. Davydov Splitting and Multipole Interactions. *Solid State Commun.* **1976**, *19* (7), 639–642.

[90] Horák, M.; Šikola, T. Influence of Experimental Conditions on Localized Surface Plasmon Resonances Measurement by Electron Energy Loss Spectroscopy. *Ultramicroscopy* **2020**, *216*, 113044.

[91] Armao, J. J.; Nyrkova, I.; Fuks, G.; Osypenko, A.; Maaloum, M.; Moulin, E.; Arenal, R.; Gavat, O.; Semenov, A.; Giuseppone, N. Anisotropic Self-Assembly of Supramolecular Polymers and Plasmonic Nanoparticles at the Liquid–Liquid Interface. *J. Am. Chem. Soc.* **2017**, *139* (6), 2345–2350.

[92] Erbas-Cakmak, S.; Leigh, D. A.; McTernan, C. T.; Nussbaumer, A. L. Artificial Molecular Machines. *Chem. Rev.* **2015**, *115* (18), 10081–10206.

[93] Sauvage, J.-P. From Chemical Topology to Molecular Machines (Nobel Lecture). *Angew. Chem. Int. Ed.* **2017**, *56* (37), 11080–11093.

[94] Heard, A. W.; Goldup, S. M. Simplicity in the Design, Operation, and Applications of Mechanically Interlocked Molecular Machines. *ACS Cent. Sci.* **2020**, *6* (2), 117–128.

[95] Kistemaker, J. C. M.; Lubbe, A. S.; Feringa, B. L. Exploring Molecular Motors. *Mater. Chem. Front.* **2021**, *5* (7), 2900–2906.

[96] Kassem, S.; van Leeuwen, T.; Lubbe, A. S.; Wilson, M. R.; Feringa, B. L.; Leigh, D. A. Artificial Molecular Motors. *Chem. Soc. Rev.* **2017**, *46* (9), 2592–2621.

[97] The photo is from the official website of the Nobel Prize, and the cartoons of rotaxane and catenane are adapted from Nobel Lecture Slides- Jean-Pierre Sauvage.

[98] Kinbara, K.; Aida, T. Toward Intelligent Molecular Machines: Directed Motions of Biological and Artificial Molecules and Assemblies. *Chem. Rev*. **2005**, *105* (4), 1377–1400.

[99] Junge, W. ATP Synthase and Other Motor Proteins. *Proc. Natl. Acad. Sci. U.S.A.* **1999**, *96* (9), 4735–4737.

[100] Wang, J.; Feringa, B. L. Dynamic Control of Chiral Space in a Catalytic Asymmetric Reaction Using a Molecular Motor. *Science* **2011**, *331* (6023), 1429–1432.

[101] Chen, S.; Leung, F. K.-C.; Stuart, M. C. A.; Wang, C.; Feringa, B. L. Dynamic Assemblies of Molecular Motor Amphiphiles Control Macroscopic Foam Properties. *J. Am. Chem. Soc.* **2020**, *142* (22), 10163–10172.

[102] van Delden, R. A.; ter Wiel, M. K. J.; Pollard, M. M.; Vicario, J.; Koumura, N.; Feringa, B. L. Unidirectional Molecular Motor on a Gold Surface. *Nature* **2005**, *437* (7063), 1337–1340.

[103] Chen, K.-Y.; Ivashenko, O.; Carroll, G. T.; Robertus, J.; Kistemaker, J. C. M.; London, G.; Browne, W. R.; Rudolf, P.; Feringa, B. L. Control of Surface Wettability Using Tripodal Light-Activated Molecular Motors. *J. Am. Chem. Soc.* **2014**, *136* (8), 3219–3224.

[104] Danowski, W.; van Leeuwen, T.; Abdolahzadeh, S.; Roke, D.; Browne, W. R.; Wezenberg, S. J.; Feringa, B. L. Unidirectional Rotary Motion in a Metal–Organic Framework. *Nat. Nanotechnol.* **2019**, *14* (5), 488–494.

[105] García-López, V.; Chen, F.; Nilewski, L. G.; Duret, G.; Aliyan, A.; Kolomeisky, A. B.; Robinson, J. T.; Wang, G.; Pal, R.; Tour, J. M. Molecular Machines Open Cell Membranes. *Nature* **2017**, *548* (7669), 567–572.

[106] Koumura, N.; Zijlstra, R. W. J.; van Delden, R. A.; Harada, N.; Feringa, B. L. Light-Driven Monodirectional Molecular Rotor. *Nature* **1999**, *401* (6749), 152–155.

[107] Koumura, N.; Geertsema, E. M.; Meetsma, A.; Feringa, B. L. Light-Driven Molecular Rotor: Unidirectional Rotation Controlled by a Single Stereogenic Center. *J. Am. Chem. Soc*. **2000**, *122* (48), 12005–12006.

[108] Yasuda, R.; Noji, H.; Yoshida, M.; Kinosita, K.; Itoh, H. Resolution of Distinct Rotational Substeps by Submillisecond Kinetic Analysis of F1-ATPase. *Nature* **2001**, *410* (6831), 898–904.

[109] Noji, H.; Yasuda, R.; Yoshida, M.; Kinosita, K. Direct Observation of the Rotation of F1-ATPase. *Nature* **1997**, *386* (6622), 299–302.

[110] Klok, M.; Walko, M.; Geertsema, E. M.; Ruangsupapichat, N.; Kistemaker, J. C. M.; Meetsma, A.; Feringa, B. L. New Mechanistic Insight in the Thermal Helix Inversion of Second-Generation Molecular Motors. *Chem. Eur. J.* **2008**, *14* (35), 11183–11193.

[111] Lubbe, A. S.; Ruangsupapichat, N.; Caroli, G.; Feringa, B. L. Control of Rotor Function in Light-Driven Molecular Motors. *J. Org. Chem.* **2011**, *76* (21), 8599–8610.

[112] Pollard, M. M.; Klok, M.; Pijper, D.; Feringa, B. L. Rate Acceleration of Light-Driven Rotary Molecular Motors. *Adv. Funct. Mater.* **2007**, *17* (5), 718–729.

[113] García-López, V.; Liu, D.; Tour, J. M. Light-Activated Organic Molecular Motors and Their Applications. *Chem. Rev.* **2020**, *120* (1), 79–124.

[114] Klok, M.; Boyle, N.; Pryce, M. T.; Meetsma, A.; Browne, W. R.; Feringa, B. L. MHz Unidirectional Rotation of Molecular Rotary Motors. *J. Am. Chem. Soc*. ***2008***, *130* (32), 10484–10485.

[115] Kulago, A. A.; Mes, E. M.; Klok, M.; Meetsma, A.; Brouwer, A. M.; Feringa, B. L. Ultrafast Light-Driven Nanomotors Based on an Acridane Stator. *J. Org. Chem*. **2010**, *75* (3), 666–679.

[116] Vachon, J.; Carroll, G. T.; Pollard, M. M.; Mes, E. M.; Brouwer, A. M.; Feringa, B. L. An Ultrafast Surface-Bound Photo-Active Molecular Motor. *Photochem. Photobiol. Sci*. **2014**, *13* (2), 241–246.

[117] Bauer, J.; Hou, L.; Kistemaker, J. C. M.; Feringa, B. L. Tuning the Rotation Rate of Light-Driven Molecular Motors. *J. Org. Chem.* **2014**, *79* (10), 4446–4455.

[118] Kistemaker, J. C. M.; Štacko, P.; Visser, J.; Feringa, B. L. Unidirectional Rotary Motion in Achiral Molecular Motors. *Nat. Chem.* **2015**, *7* (11), 890–896.

[119] Kistemaker, J. C. M.; Štacko, P.; Roke, D.; Wolters, A. T.; Heideman, G. H.; Chang, M.-C.; van der Meulen, P.; Visser, J.; Otten, E.; Feringa, B. L. Third-Generation Light-Driven Symmetric Molecular Motors. *J. Am. Chem. Soc.* **2017**, *139* (28), 9650–9661.

[120] Berrocal, J. A.; Pfeifer, L.; Heijnen, D.; Feringa, B. L. Synthesis of Core-Modified Third-Generation Light-Driven Molecular Motors. *J. Org. Chem.* **2020**, *85* (16), 10670–10680.

[121] Guentner, M.; Schildhauer, M.; Thumser, S.; Mayer, P.; Stephenson, D.; Mayer, P. J.; Dube, H. Sunlight-Powered KHz Rotation of a Hemithioindigo-Based Molecular Motor. *Nat. Commun.* **2015**, *6* (1), 8406.

[122] Wilcken, R.; Schildhauer, M.; Rott, F.; Huber, L. A.; Guentner, M.; Thumser, S.; Hoffmann, K.; Oesterling, S.; de Vivie-Riedle, R.; Riedle, E.; Dube, H. Complete Mechanism of Hemithioindigo Motor Rotation. *J. Am. Chem. Soc.* **2018**, *140* (15), 5311–5318.

[123] Gerwien, A.; Mayer, P.; Dube, H. Photon-Only Molecular Motor with Reverse Temperature-Dependent Efficiency. *J. Am. Chem. Soc.* **2018**, *140* (48), 16442–16445.

[124] Lehn, J.-M. Conjecture: Imines as Unidirectional Photodriven Molecular Motors-Motional and Constitutional Dynamic Devices. Chem. Eur. J. **2006**, *12* (23), 5910–5915.

[125] Greb, L.; Lehn, J.-M. Light-Driven Molecular Motors: Imines as Four-Step or Two-Step Unidirectional Rotors. *J. Am. Chem. Soc.* **2014**, *136* (38), 13114–13117.

[126] Greb, L.; Eichhöfer, A.; Lehn, J.-M. Synthetic Molecular Motors: Thermal N Inversion and Directional Photoinduced C=N Bond Rotation of Camphorquinone Imines. *Angew. Chem. Int. Ed.* **2015**, *54* (48), 14345–14348.

[127] Kelly, T. R.; De Silva, H.; Silva, R. A. Unidirectional Rotary Motion in a Molecular System. *Nature* **1999**, *401* (6749), 150–152.

[128] Dahl, B. J.; Branchaud, B. P. 180° Unidirectional Bond Rotation in a Biaryl Lactone Artificial Molecular Motor Prototype. *Org. Lett.* **2006**, *8* (25), 5841–5844.

[129] Fletcher, S. P.; Dumur, D.; Pollard, M. M.; Feringa, B. L. A Reversible, Unidirectional Molecular Rotary Motor Driven by Chemical Energy. *Science* **2005**, *310* (5745), 80–82.

[130] Zhang, Y.; Chang, Z.; Zhao, H.; Crespi, S.; Feringa, B. L.; Zhao, D. A Chemically Driven Rotary Molecular Motor Based on Reversible Lactone Formation with Perfect Unidirectionality. *Chem* **2020**, *6* (9), 2420–2429.

[131] Kudernac, T.; Ruangsupapichat, N.; Parschau, M.; Maciá, B.; Katsonis, N.; Harutyunyan, S. R.; Ernst, K.-H.; Feringa, B. L. Electrically Driven Directional Motion of a Four-Wheeled Molecule on a Metal Surface. *Nature* **2011**, *479* (7372), 208–211.

[132] Dorel, R.; Feringa, B. L. Stereodivergent Anion Binding Catalysis with Molecular Motors. *Angew. Chem. Int. Ed.* **2020**, *59* (2), 785–789.

[133] Xu, F.; Pfeifer, L.; Crespi, S.; Leung, F. K.-C.; Stuart, M. C. A.; Wezenberg, S. J.; Feringa, B. L. From Photoinduced Supramolecular Polymerization to Responsive Organogels. *J.*

Am. Chem. Soc. **2021**, *143* (15), 5990–5997.

[134] Li, Q.; Fuks, G.; Moulin, E.; Maaloum, M.; Rawiso, M.; Kulic, I.; Foy, J. T.; Giuseppone, N. Macroscopic Contraction of a Gel Induced by the Integrated Motion of Light-Driven Molecular Motors. *Nat. Nanotechnol.* **2015**, *10* (2), 161–165.

[135] Foy, J. T.; Li, Q.; Goujon, A.; Colard-Itté, J.-R.; Fuks, G.; Moulin, E.; Schiffmann, O.; Dattler, D.; Funeriu, D. P.; Giuseppone, N. Dual-Light Control of Nanomachines That Integrate Motor and Modulator Subunits. *Nat. Nanotechnol*. **2017**, *12* (6), 540–545.

[136] Chen, J.; Leung, F. K.-C.; Stuart, M. C. A.; Kajitani, T.; Fukushima, T.; van der Giessen, E.; Feringa, B. L. Artificial Muscle-like Function from Hierarchical Supramolecular Assembly of Photoresponsive Molecular Motors. *Nat. Chem.* **2018**, *10* (2), 132–138.

[137] Hou, J.; Mondal, A.; Long, G.; Haan, L.; Zhao, W.; Zhou, G.; Liu, D.; Broer, D. J.; Chen, J.; Feringa, B. L. Photo-responsive Helical Motion by Light-Driven Molecular Motors in a Liquid-Crystal Network. *Angew. Chem. Int. Ed.* **2021**, *60* (15), 8251–8257.

[138] Zhang, Q.; Rao, S.-J.; Xie, T.; Li, X.; Xu, T.-Y.; Li, D.-W.; Qu, D.-H.; Long, Y.-T.; Tian, H. Muscle-like Artificial Molecular Actuators for Nanoparticles. *Chem* **2018**, *4* (11), 2670–2684.

[139] Lee, S.; Pérez-Luna, V. H. Surface-Grafted Hybrid Material Consisting of Gold Nanoparticles and Dextran Exhibits Mobility and Reversible Aggregation on a Surface. *Langmuir* **2007**, *23* (9), 5097–5099.

[140] Lian, X.; Jin, J.; Tian, J.; Zhao, H. Thermoresponsive Nanohydrogels Cross-Linked by Gold Nanoparticles. *ACS Appl. Mater. Interfaces* **2010**, *2* (8), 2261–2268.

[141] Bian, T.; Chu, Z.; Klajn, R. The Many Ways to Assemble Nanoparticles Using Light. *Adv. Mater.* **2020**, *32* (20), 1905866.

[142] Chen, Y.; Wang, Z.; He, Y.; Yoon, Y. J.; Jung, J.; Zhang, G.; Lin, Z. Light-Enabled Reversible Self-Assembly and Tunable Optical Properties of Stable Hairy Nanoparticles. *Proc. Natl. Acad. Sci. U.S.A.* **2018**, *115* (7), E1391–E1400.

[143] Kundu, P. K.; Samanta, D.; Leizrowice, R.; Margulis, B.; Zhao, H.; Börner, M.; Udayabhaskararao, T.; Manna, D.; Klajn, R. Light-Controlled Self-Assembly of Non-Photoresponsive Nanoparticles. *Nat. Chem.* **2015**, *7* (8), 646–652.

[144] Li, Q.; Foy, J. T.; Colard-Itté, J.-R.; Goujon, A.; Dattler, D.; Fuks, G.; Moulin, E.; Giuseppone, N. Gram Scale Synthesis of Functionalized and Optically Pure Feringa's Motors. *Tetrahedron* **2017**, *73* (33), 4874–4882.

[145] Turkevich, J.; Stevenson, P. C.; Hillier, J. A Study of the Nucleation and Growth Processes in the Synthesis of Colloidal Gold. *Discuss. Faraday Soc.* **1951**, *11*, 55.

[146] Mako, T. L.; Racicot, J. M.; Levine, M. Supramolecular Luminescent Sensors. *Chem. Rev.* **2019**, *119* (1), 322–477.

[147] Yu, T.; Liu, L.; Xie, Z.; Ma, Y. Progress in Small-Molecule Luminescent Materials for Organic Light-Emitting Diodes. *Sci. China Chem.* **2015**, *58* (6), 907–915.

[148] Ashton, T. D.; Jolliffe, K. A.; Pfeffer, F. M. Luminescent Probes for the Bioimaging of Small Anionic Species in Vitro and in Vivo. *Chem. Soc. Rev.* **2015**, *44* (14), 4547–4595.

[149] Xing, J.; Gong, Q.; Akakuru, O. U.; Liu, C.; Zou, R.; Wu, A. Research Advances in

Integrated Theranostic Probes for Tumor Fluorescence Visualization and Treatment. *Nanoscale* **2020**, *12* (48), 24311–24330.

[150] Mei, J.; Leung, N. L. C.; Kwok, R. T. K.; Lam, J. W. Y.; Tang, B. Z. Aggregation-Induced Emission: Together We Shine, United We Soar! *Chem. Rev.* **2015**, *115* (21), 11718–11940.

[151] Hong, Y.; Lam, J. W. Y.; Tang, B. Z. Aggregation-Induced Emission. *Chem. Soc. Rev.* **2011**, *40* (11), 5361.

[152] Förster, T.; Kasper, K. Ein Konzentrationsumschlag der Fluoreszenz. *Z. Phys. Chem. (Muenchen, Ger.)* **1954**, *1*, 275−277.

[153] Luo, J.; Xie, Z.; Lam, J. W. Y.; Cheng, L.; Tang, B. Z.; Chen, H.; Qiu, C.; Kwok, H. S.; Zhan, X.; Liu, Y.; Zhu, D. Aggregation-Induced Emission of 1-Methyl-1,2,3,4,5-Pentaphenylsilole. *Chem. Commun.* **2001**, *18*, 1740–1741.

[154] Luo, J.; Song, K.; Gu, F. long; Miao, Q. Switching of Non-Helical Overcrowded Tetrabenzoheptafulvalene Derivatives. *Chem. Sci.* **2011**, *2* (10), 2029.

[155] Hu, R.; Lam, J. W. Y.; Liu, Y.; Zhang, X.; Tang, B. Z. Aggregation-Induced Emission of Tetraphenylethene-Hexaphenylbenzene Adducts: Effects of Twisting Amplitude and Steric Hindrance on Light Emission of Nonplanar Fluorogens. *Chem. Eur. J.* **2013**, *19* (18), 5617–5624.

[156] Tu, Y.; Liu, J.; Zhang, H.; Peng, Q.; Lam, J. W. Y.; Tang, B. Z. Restriction of Access to the Dark State: A New Mechanistic Model for Heteroatom-Containing AIE Systems. *Angew. Chem. Int. Ed.* **2019**, *58* (42), 14911–14914.

[157] Zhao, K.-Y.; Shan, G.-G.; Fu, Q.; Su, Z.-M. Tuning Emission of AIE-Active Organometallic Ir(III) Complexes by Simple Modulation of Strength of Donor/Acceptor on Ancillary Ligands. *Organometallics* **2016**, *35* (23), 3996–4001.

[158] Hu, R.; Qin, A.; Tang, B. Z. AIE Polymers: Synthesis and Applications. *Prog. Polym. Sci.* **2020**, *100*, 101176.

[159] Feng, H.-T.; Yuan, Y.-X.; Xiong, J.-B.; Zheng, Y.-S.; Tang, B. Z. Macrocycles and Cages Based on Tetraphenylethylene with Aggregation-Induced Emission Effect. *Chem. Soc. Rev.* **2018**, *47* (19), 7452–7476.

[160] Zhu, L.; Zhu, B.; Luo, J.; Liu, B. Design and Property Modulation of Metal–Organic Frameworks with Aggregation-Induced Emission. *ACS Mater. Lett.* **2021**, *3* (1), 77–89.

[161] Li, Z.; Dong, Y.; Mi, B.; Tang, Y.; Häussler, M.; Tong, H.; Dong, Y.; Lam, J. W. Y.; Ren, Y.; Sung, H. H. Y.; Wong, K. S.; Gao, P.; Williams, I. D.; Kwok, H. S.; Tang, B. Z. Structural Control of the Photoluminescence of Silole Regioisomers and Their Utility as Sensitive Regiodiscriminating Chemosensors and Efficient Electroluminescent Materials. *J. Phys. Chem. B* **2005**, *109* (20), 10061–10066.

[162] Zhang, G.-F.; Chen, Z.-Q.; Aldred, M. P.; Hu, Z.; Chen, T.; Huang, Z.; Meng, X.; Zhu, M.-Q. Direct Validation of the Restriction of Intramolecular Rotation Hypothesis via the Synthesis of Novel Ortho-Methyl Substituted Tetraphenylethenes and Their Application in Cell Imaging. *Chem. Commun.* **2014**, *50* (81), 12058–12060.

[163] Liang, G.; Lam, J. W. Y.; Qin, W.; Li, J.; Xie, N.; Tang, B. Z. Molecular Luminogens Based on Restriction of Intramolecular Motions through Host–Guest Inclusion for Cell

Imaging. *Chem. Commun.* **2014**, *50* (14), 1725–1727.

[164] Yan, X.; Wei, P.; Liu, Y.; Wang, M.; Chen, C.; Zhao, J.; Li, G.; Saha, M. L.; Zhou, Z.; An, Z.; Li, X.; Stang, P. J. *Endo* - and *Exo* -Functionalized Tetraphenylethylene M 12 L 24 Nanospheres: Fluorescence Emission inside a Confined Space. *J. Am. Chem. Soc.* **2019**, *141* (24), 9673–9679.

[165] Wu, Y.; Frasconi, M.; Liu, W.-G.; Young, R. M.; Goddard, W. A.; Wasielewski, M. R.; Stoddart, J. F. Electrochemical Switching of a Fluorescent Molecular Rotor Embedded within a Bistable Rotaxane. *J. Am. Chem. Soc.* **2020**, *142* (27), 11835–11846.

[166] Franken, L.; Wei, Y.; Chen, J.; Boekema, E. J.; Zhao, D.; Stuart, M. C. A.; Feringa, B. L. Solvent Mixing to Induce Molecular Motor Aggregation into Bowl-Shaped Particles: Underlying Mechanism, Particle Nature and Application to Control Motor Behavior. *J. Am. Chem. Soc.* **2018**, *140* (25), 7860–7868.

[167] Yu, C.; Huang, Z.; Gu, W.; Wu, Q.; Hao, E.; Xiao, Y.; Jiao, L.; Wong, W.-Y. A Novel Family of AIE-Active *Meso* -2-Ketopyrrolyl BODIPYs: Bright Solid-State Red Fluorescence, Morphological Properties and Application as Viscosimeters in Live Cells. *Mater. Chem. Front.* **2019**, *3* (9), 1823–1832.

[168] Xu, L.; Ni, L.; Zeng, F.; Wu, S. Tetranitrile-Anthracene as a Probe for Fluorescence Detection of Viscosity in Fluid Drinks *via* Aggregation-Induced Emission. *Analyst* **2020**, *145* (3), 844–850.

[169] Colard-Itté, J.-R.; Li, Q.; Collin, D.; Mariani, G.; Fuks, G.; Moulin, E.; Buhler, E.; Giuseppone, N. Mechanical Behaviour of Contractile Gels Based on Light-Driven Molecular Motors. *Nanoscale* **2019**, *11* (12), 5197–5202.

[170] Tran, F.; Odell, A.; Ward, G.; Westwood, N. A Modular Approach to Triazole Containing Chemical Inducers of Dimerisation for Yeast Three-Hybrid Screening. *Molecules* **2013**, *18* (9), 11639–11657.

[171] Klinker, K.; Schäfer, O.; Huesmann, D.; Bauer, T.; Capelôa, L.; Braun, L.; Stergiou, N.; Schinnerer, M.; Dirisala, A.; Miyata, K.; Osada, K.; Cabral, H.; Kataoka, K.; Barz, M. Secondary-Structure-Driven Self-Assembly of Reactive Polypept(o)Ides: Controlling Size, Shape, and Function of Core Cross-Linked Nanostructures. *Angew. Chem. Int. Ed.* **2017**, *56* (32), 9608–9613.

[172] Li, X.; Martin, S. J. H.; Chinoy, Z. S.; Liu, L.; Rittgers, B.; Dluhy, R. A.; Boons, G.-J. Label-Free Detection of Glycan-Protein Interactions for Array Development by Surface-Enhanced Raman Spectroscopy (SERS). *Chem. Eur. J.* **2016**, *22* (32), 11180–11185.

Chuan GAO

Generation of Unconventional Optical Properties in Triarylamine-based Supramolecular Polymers and Molecular Motors-based Nanodevices

Résumé

Dans cette thèse, nous avons étudié les propriétés optiques non conventionnelles des polymères supramoléculaires à base de triarylamine et de matériaux à base de moteurs moléculaires, notamment la phosphorescence à température ambiante (RTP), la résonance plasmonique de surface localisée (LSPR) et l'émission modulable par un stimulus. Dans le premier projet, une émission dans le rouge a été observée à l'état solide pour les auto-assemblages à base de triarylamine, ce qui a été principalement attribué au RTP grâce à la rigidification du groupement BrNp. Dans le deuxième projet, nous avons étudié le comportement de photo-oxydation de triarylamines trisacétamides et préparé des nanoparticules supramoléculaires à base de TATA-Ac avec des tailles ajustables par précipitation. Les nanoparticules oxydées présentent des bandes d'absorption UV uniques, qui correspondent au processus LSPR dans les nanoparticules métalliques. Mes deux derniers projets sont liés aux moteurs moléculaires. Tout d'abord, les gels de moteurs contenant différentes fractions de nanoparticules d'or (AuNPs) ont été synthétisés, afin de réguler le couplage plasmonique entre AuNPs par irradiation lumineuse. Cependant, la contraction macroscopique limitée des gels n’a pour l’instant pas permis de moduler cette propriété. D'autre part, en s'inspirant d’observations réalisées sur des gels contractés, nous avons d'abord démontré l'émission induite par l'agrégation du moteur moléculaire. Ensuite, nous avons réussi à réguler l'intensité d'émission de moteurs moléculaires sous forme de 8 sous l’influence du stimulus lumineux. Ainsi, afin de soulager la contrainte conformationnelle élevée, les moteurs moléculaires à l'état tendu peuvent effectuer une rotation inversée via une voie thermiquement activée.

Mots-clés: Polymères supramoléculaires, auto-assemblage, phosphorescence à température ambiante, plasmonique organique, couplage plasmonique, moteurs moléculaires.

Résumé en anglais

In this thesis we have investigated the unconventional optical properties of triarylamine-based supramolecular polymers and molecular motor-based materials, including room-temperature phosphorescence (RTP), localized surface plasmonic resonance (LSPR), and stimuli-responsive emission. In the first project, red emission was observed in the solid state of triarylamine-based self-assemblies, which was primarily attributed to the RTP thanks to the rigidification of appendant phosphor BrNp. In the second project, we studied the photo-oxidation behavior of triarylamine trisacetamides (TATA-Ac) and prepared TATA-Ac-based supramolecular nanoparticles with tunable sizes via precipitation. The oxidized nanoparticles display unique UV absorption bands, which are in agreement with the LSPR in metal nanoparticles. My last two projects are related to molecular motors, first, the motorized gels containing different fractions of gold nanoparticles (AuNPs) were synthesized, aiming at regulating the plasmonic coupling between AuNPs by light irradiation. However, the limited macroscopic contraction of the gels preclueded this observation. On the other hand, taking inspiration from the emission enhancement of contracted gels, we first demonstrated the aggregation-induced emission of molecular motor. Then we succeeded in regulating the emission intensity of 8-shaped molecular motors via mechanically-induced emission enhancement. Interestingly, to relieve the high conformational strain, the molecular motors in the tensed state could perform backward rotation through a thermally-activated pathway.

Keywords: Supramolecular polymers, self-assembly, room-temperature phosphorescence, organic plasmonics, plasmonic coupling, molecular motors.